Soft x-ray spectroscopic study of methanol and glycine peptides in different physical environments

Dissertation zur Erlangung des naturwissenschaftlichen Doktorgrades
der Julius-Maximilians-Universität Würzburg

vorgelegt von

Andreas Benkert
aus Schweinfurt

Würzburg 2017

Eingereicht am: 18.08.2016
bei der Fakultät für Physik und Astronomie

1. Gutachter: Prof. Dr. Friedrich Reinert
2. Gutachter: Prof. Dr. Jean Geurts
der Dissertation

Vorsitzende(r): Prof. Dr. Vladimir Dyakonov
1. Prüfer: Prof. Dr. Friedrich Reinert
2. Prüfer: Prof. Dr. Jean Geurts
3. Prüfer: Prof. Dr. Björn Trauzettel
im Promotionskolloquium

Tag des Promotionskolloquiums: 10.02.2017

Doktorurkunde ausgehändigt am: ....

ZUSAMMENFASSUNG

Ionenspezifische Effekte treten in einer Vielzahl von wässrigen Lösungen aus Elektrolyten und größeren Molekülen wie Peptiden auf. Die Ionen bewirken dabei Änderungen in Eigenschaften wie z.B. der Viskosität, den Aktivitäten von Enzymen, der Stabilität von Proteinen und deren Ein- bzw. Aussalzverhalten. Typischerweise wird die ionenabhängige Ausprägung derartiger Effekte mithilfe der Hofmeister–Serie beschrieben, die ursprünglich Ionen nach ihrer Fähigkeit ordnete, die Löslichkeit von Hühnereiweis in Wasser zu steigern oder zu unterdrücken. Die empirische Abfolge der Ionen in der Hofmeister–Serie kann jedoch bis heute nicht zweifelsfrei erklärt werden. Trotz weitreichender Bemühungen, ein molekulares Verständnis dieses Phänomens zu schaffen, konnte bisher keine Einigung über die zugrundeliegenden Mechanismen und die genauere Bestimmung und Lokalisierung der Wechselwirkung erzielt werden.

Die resonante inelastische Weichröntgenstreuung (RIXS) kombiniert die beiden Methoden der Röntgenemissions– (XES) und Röntgenabsorptionsspektroskopie (XAS). So können mit RIXS Informationen sowohl über die besetzten als auch die unbesetzten elektronischen Zustände gesammelt und zu einem umfassenden Bild der elektronischen Struktur des Systems verknüpft werden, was diese Methode zu einem vielversprechenden Werkzeug macht, etwas mehr Licht auf die Thematik zu werfen.

Die in dieser Arbeit präsentierten Ergebnisse zielen deshalb darauf ab, ein verbessertes Verständnis der Wechselwirkungen zwischen Salzen und Peptiden in wässriger Lösung zu schaffen. Hierfür wird systematisch der Einfluss verschiedenster physikalischer Umgebungen auf die elektronische Struktur von kleinen Molekülen (Methanol und von Glycin abgeleitete Peptide) mittels Weichröntgenspektroskopie, unterstützt durch Dichtefunktionaltheorie (DFT) Rechnungen, untersucht.

In einem ersten Schritt werden isolierte Moleküle ohne jegliche Wechselwirkung zu ihrer unmittelbaren Umgebung anhand von Methanol in der Gasphase als Modelsystem untersucht. Hierbei wird insbesondere der lokale und elementspezifische Charakter von RIXS demonstriert und die lokale elektronische Struktur von Methanols Hydroxyl– und Methylgruppe untersucht. Mithilfe von DFT–Rechnungen werden die beobachteten Emissionslinien in den XES–Spektren der Emission bestimmter Molekülorbitale zugeordnet und deren relative Emissionsintensitäten erläutert. Für eine resonante Anregung der ersten Resonanz an der Sauerstoff–K–Absorptionskante werden starke Isotopeneffekte beobachtet, die durch dynamische Prozesse an der Hydroxylgruppe erklärt werden können. Dies dient als hervorragendes Beispiel für mögliche Auswirkungen, die eine lokale Änderung in der Geometrie oder Symmetrie des Moleküls auf dessen elektronische Struktur haben kann.

Im weiteren Verlauf dieser Arbeit wird das untersuchte Probensystem um die Aminosäure Glycin und deren kleinste Peptide Diglycin und Triglycin, vorerst in ihrer kristallinen Form als Festkörper, erweitert. Mithilfe von RIXS–Karten der Stickstoff– und Sauerstoff–K–Absorptionskanten wird erneut, unterstützt durch DFT–Rechnungen, ein umfassendes Bild der elektronischen Struktur der Moleküle gezeichnet. Ähnlich zum Fall von Methanol werden die Emissionsspektren an der Stickstoff–K–Kante stark von dynamischen Prozessen an der protonierten Aminogruppe der Moleküle beeinflusst. Zudem wird gezeigt, dass RIXS gezielt dazu verwendet werden kann, das Stickstoffatom in der Peptidbindung anzuregen und die elektronische Struktur in dessen lokaler Umgebung zu untersuchen. Desweiteren wird ein einfaches Baukastenprinzip für XES–Spektren dazu genutzt, die spektralen Anteile der Emission aus Übergängen an den beiden Stickstoffatomen in Diglycin zu isolieren.

In wässriger Lösung kann eine leichte Veränderung der elektronischen Struktur der Moleküle durch die Wechselwirkung mit benachbarten Wassermolekülen, vermutlich an den geladenen funktionellen Gruppen, beobachtet werden. Die Auswirkungen auf die XES–Spektren sind jedoch eher gering. Deutlich größere Veränderungen werden beobachtet, wenn man den Protonierungszustand der Moleküle über den pH–Wert der Lösung manipuliert. Sowohl die Protonierung der Carboxylgruppe für kleine pH–Werte als auch die Deprotonierung der Aminogruppe in basischer Lösung führen zu starken Veränderungen in den RIXS–Karten. In einer umfangreichen Untersuchung der XES–Spektren von Glycin als Funktion des pH–Wertes wird gezeigt, dass sich die Änderungen jedoch nicht nur örtlich begrenzt auf die Umgebung der manipulierten funktionellen Gruppe, sondern auch auf die elektronische Struktur in weiter entfernten Bereichen des Moleküls auswirken.

Als Beispiel für Systeme in denen Hofmeister–Effekte beobachtet werden, werden zu guter Letzt gemischte wässrige Lösungen aus Diglycin und verschiedenen Salzen untersucht. Um den Einfluss verschiedener Kationen auf die elektronische Struktur der Diglycin Moleküle zu erfassen wird eine Reihe unterschiedlicher Chloride verwendet, wohingegen eine Reihe von Kaliumsalzen für die Untersuchung verschiedener Anionen herangezogen wird. In beiden Fällen werden ionenspezifische Auswirkungen auf die XES–Spektren von Diglycin beobachtet, die qualitativ der Sortierung innerhalb der Hofmeister–Serie folgen. Die beobachteten Änderungen deuten dabei darauf hin, dass Kationen unterschiedlich stark mit dem Sauerstoff in der Peptidbindung und dessen unmittelbarer Umgebung wechselwirken, wohingegen Anionen eine gesteigerte Affinität zur Aminogruppe von Diglycin aufweisen.

ABSTRACT

Ion-specific effects occur in a huge variety of aqueous solutions of electrolytes and larger molecules like peptides, altering properties such as viscosity, enzyme activity, protein stability, and salting-in and salting-out behavior of proteins. Typically, these type of effects are rationalized in terms of the Hofmeister series, which originally orders cations and anions according to their ability to enhance or suppress the solubility of proteins in water. This empirical order, however, is still not understood yet. Quite some effort was made to gain a molecular level understanding of this phenomenon, yet no consensus has been found about the underlying mechanisms and the determination and localization of the interaction sites.

Resonant inelastic soft x-ray scattering (RIXS) combines x-ray emission (XES) and absorption spectroscopies (XAS), probing the partial local density of states of both occupied and unoccupied electronic states and is thus a promising candidate to shed more light onto the issue. The studies presented in this work are directed towards an improved understanding of the interaction between salts and peptides. In order to address this topic, the impact of different physical environments on the electronic structure of small molecules (i.e., methanol and glycine derived peptides) is investigated systematically using soft x-ray spectroscopic methods, corroborated with density functional theory (DFT) calculations.

In a first step, molecules without any interactions to the surrounding are investigated, using gas-phase methanol as a model system. Thereby, the local and element specific character of RIXS is demonstrated and used to separately probe the local electronic structure of methanol's hydroxyl and methyl group, respectively. The attribution of the observed emission features to distinct molecular orbitals is confirmed by DFT calculations, which also quantitatively explain the different relative intensities of the emission features. For resonant excitation of the O K pre-edge absorption resonance, strong isotope effects are found that are explained by dynamical processes at the hydroxyl group. This serves as an excellent example for possible consequences of a local change in the geometric structure or symmetry of a molecule on its electronic structure.

In the following, the sample system is expanded to the amino acid glycine and its smallest derived peptides diglycine and triglycine. As a first step, they are studied in their crystalline form in solid state. Again, a comprehensive picture of the electronic structure is developed by measuring RIXS maps at the oxygen and nitrogen K absorption edge, corroborated by DFT calculations. Similar to the case of methanol, dynamic processes at the protonated amino group of the molecules after exciting the nitrogen atom have a strong influence on the emission spectra. Furthermore, it is shown that RIXS can be used to selectively excite the peptide nitrogen to probe the electronic structure around it. A simple building block approach for XES spectra is applied to separate the contribution of the emission attributed to transitions into core holes at the peptide and the amino nitrogen, respectively.

In the aqueous solution, the surrounding water molecules slightly change the electronic structure, probably via interactions with the charged functional groups. The effects on the x-ray emission spectra, however, are rather small. Much bigger changes are observed when manipulating the protonation state of the functional groups by adjusting the pH value of the solution. A protonation of the carboxyl group at low pH values, as well as a deprotonation of the amino group at high pH values lead to striking changes in the shape of the RIXS maps. In a comprehensive study of glycine's XES spectra at varying pH values, changes in the local electronic structure are not only observed in the immediate surrounding of the manipulated functional groups but also in more distant moieties of the molecule.

Finally, the study is extended to mixed aqueous solutions of diglycine and a variety of different salts as examples for systems where Hofmeister effects are observed. To investigate the influence of different cations and anions on the electronic structure of diglycine, two series of chlorine and potassium salts are used. Ion-specific effects are identified for both cases. Some of the changes in the x-ray emission spectra of diglycine in the mixed solutions qualitatively follow the Hofmeister series as a function of the used salt. The observed trends thereby indicate an increased interaction between the electron density around the peptide oxygen with the cations, whereas anions seem to interact with the amino group of the peptide.

TABLE OF CONTENTS

Page

CHAPTER 1

INTRODUCTION

In the 1880s, the pharmacologist and chemist Franz Hofmeister discovered that adding salts to egg white protein can change its solubility. Depending on the sort of salt, he observed alterations in the salting-in and salting-out behavior, i.e., that the concentration of salt needed to precipitate the protein out of solution changes with the type of ions present in the solution [1–3]. With the available techniques at that time, he furthermore demonstrated the consequences of different salts on phenomena like swelling of biological material and osmotic pressures. Nowadays, it is known that ion-specific effects play a crucial role in nature and occur in a wide variety of aqueous solutions. Examples of this kind of phenomena are changes in viscosity [4], ionic liquids [5], optical rotation of amino acids [6], protein stability [7], enzyme activity [8], and many more. Especially the protein stability against aggregation is critical for therapeutic treatments dealing with neurodegenerative diseases such as Alzheimer's, Huntington's, and Parkinson's disease [9]. For more examples and an overview of the situation the reader is referred to a variety of review articles [10–15].

Interestingly, for many different ion-specific effects, a distinct ordering of the ions when classified with respect to the magnitude of the respective effect is found. Today, this ordering of ions is known as the Hofmeister series, with two distinct series for anions and cations, respectively. Limited to selected ions they can be written as [10]:

$$SO_4^{2-} - HPO_4^{2-} - CH_3COO^- - F^- - Cl^- - Br^- - NO_3^- - I^- - ClO_4^- - SCN^-$$

$$NH_4^+ - K^+ - Na^+ - Li^+ - Mg^{2+} - Ca^{2+}$$

However, this empirical ordering and the underlying ion-specific effects are not explained by standard theories of electrolytes [11, 16]. In the 1930s-1950s, a theory of structure-making and structure-breaking properties of different ions was developed [17, 18]. This model separates the ions in the series with respect to their ability to orientate water molecules on a long-range order beyond their first solvation shell. Accordingly, structure makers are found on the left side of the series given above and are also referred to as “kosmotropes”, whereas structure breakers (“chaotropes”) are found on the right.

In this model, kosmotropes are rather small and strongly hydrated ions and have a strong electric field which interacts with the permanent dipole moments of the surrounding water molecules, leading to a higher order in the nearby water molecules by charge-dipole interactions [11]. Thereby, they “steal” water molecules from the protein which leads to protein precipitation and a salting-out effect. The big and weaker hydrated chaotropes, however, only produce a weak electrostatic field which perturbs the dynamic hydrogen-bonded array in liquid water, thus making the surrounding water molecules more disordered [11]. As a reference point, the strength of water-water interactions is used [19]. A recent review about this theory can be found in [20].

This explanation of the ordering of Hofmeister ions, however, is not without doubt. New experimental and computational work showed that there is no long-range water ordering induced by ions [21, 22]. Furthermore, the fact that the peptide is not considered to play a role in this theory seems questionable. For instance, it can not be explained that there are examples of particular salts which show salting-in or salting-out behavior depending on the solute [23]. Furthermore, the Hofmeister series is observed to be reversed in certain cases and shows several exceptions [24–27]. This leads to the hypothesis that direct ion-peptide interactions are responsible for the observed phenomena [14]. Accordingly, already starting in the late 1950s, there has been a growing interest in understanding how proteins interact with ions in their surrounding, for the time being mostly based on thermodynamic studies for small model systems [28, 29] and solubility measurements [30–32]. As a general trend it was found that an interaction with the peptide backbone is especially observed for weakly hydrated anions and strongly hydrated cations.

For peptides, it seemed likely to investigate the mechanisms of the interaction for the backbone and the side chain separately [31, 32], an approach which was also widely used in later work [7, 33–36]. Based on the observation that for single charged ions there is a stronger attraction of similarly sized ions than for ions of different size in water, Kim Collins established his *law of matching water affinities* [37]. This law states that “*only oppositely charged ions with matching absolute free energies of hydration spontaneously form inner sphere ion pairs in free solution*” [37]. Accordingly, ions that possess similar hydration energies have matching water affinities, a measure of how strongly or weakly they bind to water. This approach is also considered to be applicable to the interaction between ions with charged functional groups [38, 39].

In more recent years, enabled by the improvement and development of new computational and experimental techniques, the ordering of Hofmeister ions in interaction with charged amino acid side-chains has been investigated by means of molecular dynamics [38–42] and spectroscopic methods [39, 43–48], partly with results challenging Collins findings [40]. Furthermore, it has been suggested that ions not only bind to proteins via specific ion-ion interactions but also a solvent assisted attraction to non-polar surface groups occurs [49]. Hence, a theory explaining the ordering of Hofmeister ions and the determination of the interaction between peptides and ions still is not found yet.

Soft x-ray emission (XES) and absorption spectroscopies (XAS), as well as resonant inelastic soft x-ray scattering (RIXS), have been demonstrated to give valuable insights into the electronic strucutre of liquids and solutions of both, occupied and unoccupied electronic states [50–54]. Aqueous solutions of small molecules have been investigated in a steadily increasing number of publications, also in our group [43, 55–62], resulting in a detailed picture of their electronic structure.

In this thesis, XES, XAS, and RIXS is used to shed more light on the electronic structure of the dipeptide diglycine in different aqueous salt solutions as a model system to demystify some of the secrets of the Hofmeister series. To disentangle the complex system of the peptide, the surrounding water, and the additional salt ions, a firm basis for the interpretation of the collected data is set in a step-by-step manner. For this purpose, this thesis is organized as follows: In chapter 2, the techniques of soft x-ray spectroscopy are introduced, together with a brief explanation of the computational methods which are used to calculate the collected x-ray emission and absorption spectra. Furthermore, the experimental setup is described and the investigated samples are listed in this chapter. Chapter 3-5 contain the experimental results. In chapter 3, the electronic structure of gas-phase methanol is discussed. On the basis of this example of a small isolated molecule, the origin of XES spectra and RIXS maps is explained and the local character of RIXS is demonstrated. Thereby, special attention is set to the discussion of methanol's hydroxyl group. This serves as a first reference for the investigation of bigger molecules in the subsequent chapters and demonstrates the impact of nuclear dynamics on the x-ray emission spectrum. Chapter 4 deals with the electronic structure of glycine and its smallest peptides in the solid state. Using the local character of RIXS, the different moieties of the molecules are probed selectively and a detailed picture of the diglycine's electronic structure, determined by its functional groups and the peptide bond, is given. Aqueous solutions of diglycine are then discussed in chapter 5. The influence of the aqueous environment on the electronic structure of diglycine is investigated in Sec. 5.1 by comparing the results to the solid-state measurements. Afterwards, the functional groups of diglycine are selectively manipulated by changing the pH of the solution and the changes to the electronic structure are monitored. In a last step in Sec. 5.3, salts with different anions and cations are added to the aqueous solution of diglycine, partially leading to ion-specific Hofmeister effects, which are discussed separately for anions and cations. Last, a conclusion of this thesis and an outlook is given.

CHAPTER 2

METHODOLOGY

In this thesis, the electronic structure of molecules in different environments is studied using soft x-ray photon-in-photon-out methods. While x-ray absorption spectroscopy (XAS) probes the unoccupied states, the occupied states can be studied using x-ray emission spectroscopy (XES). The technique of resonant inelastic (soft) x-ray scattering (RIXS) combines these two methods and provides the complete information about the electronic structure accessible with soft x-ray spectroscopies. The theoretical framework and the physical principles of soft x-ray spectroscopy is given in Sec. 2.1. To corroborate the experimental results, XES as well as XAS spectra are theoretically modeled in this thesis using density functional theory (DFT) calculations, which became a common tool for the description of the electronic structure of atoms, molecules, and even bigger systems. A short survey of the principles behind DFT calculations and how DFT is used in this thesis is given in Sec. 2.2. Last, the experimental setup is depicted in Sec. 2.3, together with detailed descriptions of the sample preparation routines.

2.1 Soft x-ray spectroscopy

Since this thesis focuses on the interpretation of the electronic structure of molecular systems, the description of the three spectroscopic methods used here, namely XAS, XES, and RIXS, is limited to systems with discrete electronic states. A detailed introduction into XAS can be found in [63]. Gel'mukhanov and Ågren give a thorough theoretical description of XES and RIXS in their work [64–66]. Even though a complete RIXS data set contains a multitude of XAS and XES spectra, making a differentiation between these experimental methods difficult, in the following it will be distinguished between XAS, XES, and RIXS to introduce the physics behind it step by step.

2.1.1 X-ray absorption and emission spectroscopy

X-ray absorption spectroscopy probes the unoccupied electronic states by measuring the absorption probability of a photon as a function of its energy hν_{in}. If the focus thereby lies on the electronic fine structure close to the absorption edge, as it is the case in this thesis, it is often referred to as near edge x-ray absorption fine structure (NEXAFS), in contrast to the extended x-ray absorption fine structure (EXAFS), which deals with energies higher above the absorption onset. XAS requires a light source with tunable energy, as it is found at 3rd generation synchrotron light sources. X-ray emission spectroscopy gives information about the occupied states by recording the emission probability as a function of hν_{out}.

A theoretical description of the emission and absorption of photons was given by Dirac in 1927 [67] and is nowadays known as Fermi's Golden Rule [68], which is given in equation 2.1:

$$W_{i\to f} \propto |\langle f|\mathbf{H'}|i\rangle|^2 \delta\left(E_f - E_i \pm h\nu\right). \tag{2.1}$$

In this formalism, $W_{i\to f}$ is the probability for a transition from the initial state $|i\rangle$ to the final state $\langle f|$ caused by a perturbation described by the Hamiltonian **H'**. Dirac's δ-function ensures energy conservation, with the minus sign being used for the absorption process and the plus sign for the emission process, respectively. E_f and E_i are the energies of the final and initial state, and $h\nu$ represents the energy of the participating photon.

Approximating the electric field to be constant over the spatial distribution of the electron wave functions relevant for the interaction (dipole approximation), and neglecting multi-photon processes, Fermi's Golden Rule can be written as:

$$W_{i\to f} \propto \left|\sum_k \langle f\left|\mathbf{p}_k \cdot \mathbf{A}\right| i\rangle\right|^2 \delta\left(E_f - E_i \pm h\nu\right). \tag{2.2}$$

The Hamiltonian is expressed as the product of the momentum operators of the electrons $\mathbf{p}_k$ and the vector potential $\mathbf{A}$. The sum accounts for all electrons which interact with the photon field. To obtain an expression for the measured intensities, one has to sum over all possible final states, which leads to

$$I_{XAS}(h\nu_{in}) \propto \left|\sum_f \sum_k \langle f\left|\mathbf{p}_k \cdot \mathbf{A}\right| i\rangle\right|^2 \rho_f(E_f) \text{ with } E_f = E_i + h\nu_{in}, \tag{2.3}$$

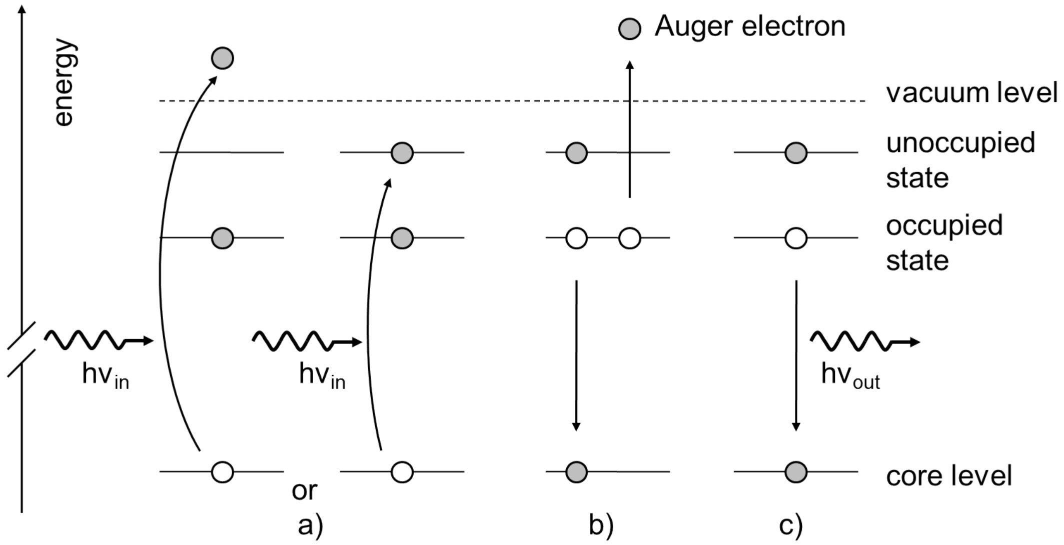

FIGURE 2.1. Schematic presentation of the (a) x-ray absorption process for non-resonant (left) and resonant (right) excitation, as well as the two possible decay channels by emitting Auger electrons (b) or photons (c).

$$I_{XES}(h\nu_{out}) \propto \left| \sum_f \sum_k \langle f \left| \mathbf{p}_k \cdot \mathbf{A} \right| i \rangle \right|^2 \rho_i(E_i) \text{ with } E_i = E_f + h\nu_{out} \tag{2.4}$$

for the absorption and the emission process, respectively. ρ_f and ρ_i represent the density of states of the unoccupied and occupied states. The dipole transition matrix element $|\langle f \left| \mathbf{p}_k \cdot \mathbf{A} \right| i \rangle|^2$ requires the dipole selection rules to be fulfilled to enable the transition to take place, imposing restrictions on the involved states. Furthermore, the spatial overlap between initial and final state is considered. Since the spectral intensities are weighted with the matrix elements, only the *local partial* density of states (LPDOS) is probed by XAS and XES.

A schematic illustration of the electronic transitions relevant for the two techniques applied to molecules is given in Fig. 2.1. The absorption process is shown in Fig. 2.1.a) for non-resonant (left) and resonant excitation (right). For non-resonant excitation, the sample is ionized by exciting a core electron above the vacuum level, whereas for resonant excitation the excitation energy is only sufficient to lift the core electron to an unoccupied state. In both cases, a core hole is created, which subsequently is filled by relaxation processes with the two different pathways shown in b) and c), respectively. In the non-radiative Auger decay (b), the energy gained by the relaxation process is transferred to another electron, which is excited and leaves the molecule. In the radiative fluorescence decay (c), a photon with a maximum energy given by the energy of the exciting photon is emitted. Both signals, Auger electrons (electron yield) and photons (fluorescence yield), can in principle be used to prove a previous absorption process. In this thesis only the fluorescence yield is used. For the experiments with gaseous or liquid samples using the available setup described below, this is the only possible technique since the inelastic mean free path is not high enough for the Auger electrons to penetrate the membrane used to separate the sample from the vacuum. Note, that for light elements the Auger decay is the dominant decay channel [69], which is why a bright light source and an efficient detector is needed for XES experiments.

2.1.2 Resonant inelastic soft x-ray scattering

In the previous section, the absorption and emission of a photon were treated separately to illustrate the physics behind the two processes step by step. However, this two-step model is only applicable for non-resonant, i.e., ionizing excitation. For resonant excitation, as it is outlined on the right side in Fig. 2.1.a), resonance effects occur and the now coherent absorption and emission processes have to be described in a one-step model. In this model, the incident photons can be considered to be inelastically scattered in the sample, which is why this technique is called resonant inelastic (soft) x-ray scattering (RIXS) or, due to the strong similarities to Raman spectroscopy, as resonant x-ray Raman scattering [66]. A schematic comparison of the two models is given in Fig. 2.2.

The theoretical description of RIXS as a photon scattering process requires second order perturbation theory, resulting in the Kramers-Heisenberg formalism [70]. The first application of this formalism to resonant effects in x-ray emission spectra was performed by Ma *et al.* for the C K edge of diamond [71]. Omitting the terms describing the non-resonant case and elastic scattering processes, the cross section of the RIXS process can be expressed as:

$$\frac{d^2\sigma(\nu_{in})}{d\nu_{out}d\Omega} \propto \sum_f \sum_m \frac{|\langle f|\mathbf{p}\cdot\mathbf{A}_{out}|m\rangle\,\langle m|\mathbf{p}\cdot\mathbf{A}_{in}|i\rangle|^2}{(E_m - E_i - h\nu_{in})^2 + \Gamma_m^2/4} \cdot \delta(h\nu_{in} - h\nu_{out} - E_f + E_i), \tag{2.5}$$

where i, m, and f are initial, intermediate, and final state. Since in the present case the initial state is always the ground state, only all possible intermediate and final states are summed up. The δ-function again ensures energy conservation, determining a relation between the energies of initial and final state, as well as the incoming and outgoing photon. Γ_m represents the lifetime broadening of the intermediate state and corresponds to the full width at half maximum (FWHM) of the Lorentzian broadening. This allows *on-resonance* excitation (e.g., $|E_m - E_i - h\nu_{in}| \le \Gamma_m$ [72]) into short-lived so-called *virtual* states even for a slightly detuned excitation energy. If this condition is met, resonance effects with high intensity can be observed, which can only be explained by a one-step scattering process.

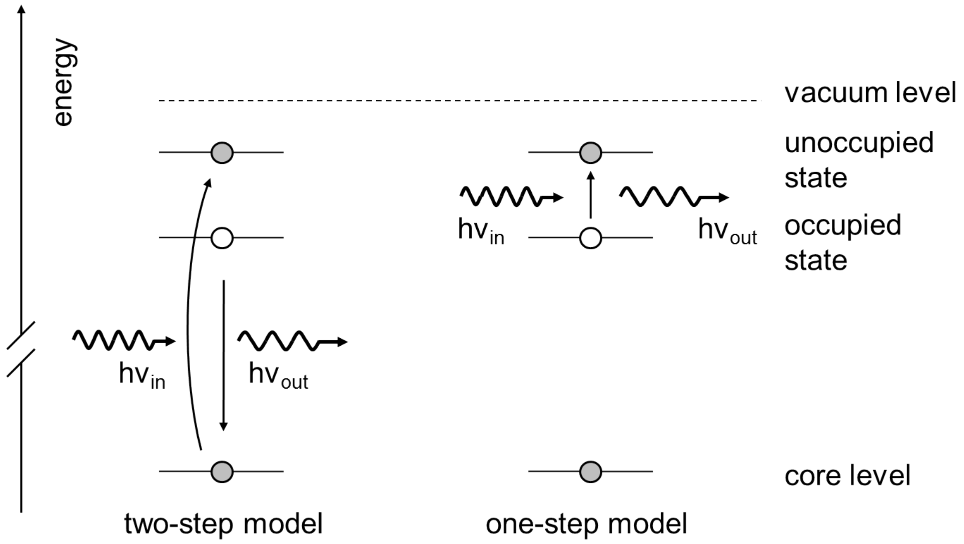

FIGURE 2.2. Schematic presentation of the RIXS process in the two-step model (left) and the one-step model (right).

The most important difference between the one-step model described by the Kramers-Heisenberg formalism and the simpler two-step model is the occurrence of a mixed second-order term. In the latter case, the two matrix elements are squared *before* multiplication, whereas in the Kramers-Heisenberg formalism they are squared *after* multiplication. This allows different intermediate states to interfere with each other, which can have a large effect on the total scattering cross section. The site-, species-, and symmetry-selective character of RIXS, however, can already be explained without interfering intermediate states. Examples which require the RIXS process to be treated with the one-step model are the applicability of parity selection rules for centro-symmetric molecules such as C_{60} [73] or the preservation of momentum in solid-state samples [71].

Observation of dynamic effects with RIXS

The finite lifetime of the intermediate state (i.e., the core hole) allows RIXS to investigate dynamics taking place on the same time scale using the so-called “core hole clock” approach. For the light elements relevant in this thesis this lifetime is of the order of several femtoseconds (3.5 fs for O 1s, 6.6 fs for C 1s, and 5.5 fs for N 1s [74]). Examples for such dynamics in this thesis are the dissociation of methanol molecules in chapter 3 and of the protonated amino groups of glycine and its smallest peptides in chapters 4 and 5. More examples can be found in literature [59, 60, 73, 75–78]. If the intermediate state is dissociative, the atoms in the molecule will start to move apart after the electronic excitation. This can especially be observed for hydrogen atoms, which can move sufficiently far during the core hole lifetime to lead to significant changes in the emission spectra. The duration time of the RIXS process can be shortened by detuning the excitation energy below the absorption resonance [66], which then reduces the influence of dynamic processes on the XES spectra (see, e.g. [79]).

2.2 Density functional theory

Since the chemical properties of a molecule are determined by its geometric and electronic structure, it seems obvious to look for a respective theoretical description for the latter. To do this, one needs to solve the Schrödinger equation with the Hamiltonian describing the molecule. However, an analytical solution of the Schrödinger equation is only possible for a single hydrogen atom. For every other system (containing more particles), only an approximative or iterative numerical solution can be obtained. Several different approaches have been developed for this purpose. One very prominent approach is the density functional theory (DFT), which became a common tool to describe the electronic structure of molecules, clusters, and solids. For an overview of the individual theory approaches, the reader is referred to standard quantum chemical textbooks [80, 81]. Detailed descriptions of the DFT technique can be found in numerous review articles [82–85] and in the lecture of Walter Kohn on the occasion of winning the Nobel Prize in Chemistry ("for his development of of the density functional theory") in 1998 [86]. In the following, a brief overview of the main principles of DFT is given, following the content and nomenclature of this lecture [86].

The density functional theory is an alternative approach to the theory of electronic structure, using the electron density distribution $n(r)$, rather than the many-electron wave function to solve the non-relativistic Schrödinger equation. One of the biggest advantages of this approach is the highly reduced number of parameters and thus computational time, making it suitable for the description of large systems with a large number of atoms. In this formalism, the electron density in the ground state completely describes the system. Furthermore, the Hohenberg-Kohn theorem states, that for a given $n(r)$ only one distinct external potential $v(r)$ for the Hamiltonian exists [87]. In this work, the authors also prove the existence of a universal functional $F[n(r)]$, which connects the ground state density $n(r)$ and the external potential $v(r)$ with the total energy E of the system: $E = \int v(r)n(r)dr + F[n(r)]$. This up to date not explicitly known functional $F[n(r)]$ requires no explicit knowledge of $v(r)$ and reproduces the correct electron density for a minimized total energy. For wave-function based methods, E can be calculated from the Rayleigh-Ritz principle,

$$E = min_{\tilde{\Psi}}(\tilde{\Psi}, H\tilde{\Psi}), \tag{2.6}$$

where $\tilde{\Psi}$ is a normalized trial function for the given number of electrons. Translating $\tilde{\Psi}$ in a trial electron density $\tilde{n}(r)$ results in the Hohenberg-Kohn minimum principle [87]:

$$E = min_{\tilde{n}(r)} E_v[\tilde{n}(r)] = min_{\tilde{n}(r)} \left[\int v(r)\tilde{n}(r)dr + F[\tilde{n}(r)] \right]. \tag{2.7}$$

Hence, instead of finding the minimum of $(\tilde{\Psi}, H\tilde{\Psi})$ with respect to the 3N-dimensional trial function $\tilde{\Psi}$, the problem has been significantly simplified to finding the minimum of $E_v[\tilde{n}(r)]$ with respect to the 3-dimensional trial function $\tilde{n}(r)$, significantly reducing computational time.

2.2.1 The Kohn-Sham equations

Finding the density $n(r)$ which minimizes the total energy became feasible by the introduction of the self-consistent Kohn-Sham equations [88]. These equations are based on a set of self-consistent single-particle equations proposed by Hartree [89], which describe the electronic structure of atoms based on non-interacting electrons in an effective single-particle potential. Kohn and Sham translated this formalism into a system of interacting electrons in an effective external potential $v_{eff}(r)$. Based on this, the minimizing density $n(r)$ can be obtained by solving the single-particle Schrödinger equation

$$\left(-\frac{1}{2}\nabla^2 + v_{eff}(r) - \epsilon_f \right) \phi_f(r) = 0. \tag{2.8}$$

Here, ϵ_f are the eigenvalues of the eigenfunctions $\phi_f(r)$, and the effective external potential is given by

$$v_{eff}(r) = v(r) + \int \frac{n(r')}{|r-r'|} dr' + v_{xc}(r), \tag{2.9}$$

with the *local* exchange-correlation potential

$$v_{xc}(r) = \frac{\delta}{\delta \tilde{n}(r)} E_{xc}[\tilde{n}(r)]|_{\tilde{n}(r)=n(r)}, \tag{2.10}$$

which depends on the entire density distribution $\tilde{n}(r)$. The second term in Eq. (2.9) describes the potential due to the average electronic density distribution $n(r)$. The minimizing electron density $n(r)$ is then obtained by

$$n(r) = \sum_{f=1}^{N} \left|\phi_f(r)\right|^2, \tag{2.11}$$

where the sum runs over the N lowest eigenvalues. The ground state energy then can be calculated as

$$E = \sum_j \epsilon_f + E_{xc}[n(r)] - \int v_{xc}(r) n(r) dv - \frac{1}{2} \int \frac{n(r)n(r')}{|r - r'|} dr dr'. \tag{2.12}$$

With the exact knowledge of $E_{xc}[n(r)]$ and $v_{xc}(r)$, in principle all many-body effects are included. Up to now, however, the exact shape of this functional is not known. Thus, the exchange correlation energy functional $E_{xc}[\tilde{n}(r)]$ has to be approximated in a way which is simple enough to limit computational time but at the same time sufficiently accurate to obtain reasonable results.

Approximations for E_{xc}

The basis of all approximate exchange correlation functionals is the *local density approximation* (LDA), which is based on the model of a uniform electron gas. The central idea of LDA is the assumption that $E_{xc}[n(r)]$ can be expressed in the form

$$E_{xc}^{LDA} = \int e_{xc}(n(r)) n(r) dr, \tag{2.13}$$

where $e_{xc}(n(r))$ is the exchange correlation energy per particle of a uniform electron gas of density n [88]. This energy per particle can be further split into an elementary exchange part e_x and correlation contributions e_c, which were first estimated by E. Wigner [90] and later with a precision of about ±1% by D. Ceperley [91]. Based on the assumption of a uniform electron gas, LDA is expected to only give reasonable results for slowly varying electron densities. Although these conditions are rarely satisfied, experience has shown that LDA gives extremely useful results for most applications. Bond lengths of molecules and solids typically are obtained with an accuracy of $\approx 2\%$, whereas dissociation energies of molecules and ionization energies of atoms are estimated with an accuracy of typically 10–20%. However, for systems which are dominated by electron-electron interactions, LDA is likely to fail due to the lacking resemblance to non-interacting electron gases.

One logical step to improve the results of LDA is the use of not only the density $n(r)$ as a parameter, but also the information about the gradient of the electron density $\nabla n(r)$ to account for the non-homogeneity of the true electron density. This is done in the *generalized gradient approximation* (GGA), based on the concept of the *average exchange correlation hole* distribution. The *physical exchange correlation hole*, $n_{xc}(r,r')$, around a given point r is given by $n_{xc}(r,r') = g(r,r') - n(r')$, with $g(r,r')$ being the conditional density at r' given that one electron is at r. One can think of $g(r,r')$ describing the "hole" the electron at point r digs in the surrounding density

$n(r')$ [86]. Expanding E_{xc} obtained from this concept around the point r leads to the equations [86]:

$$E_{xc}^{(0)} = \int \epsilon(n(r))n(r)dr \qquad (LDA), \tag{2.14}$$

$$E_{xc}^{(1)} = \int f^{(1)}(n(r), |\nabla n(r)|)n(r)dr \qquad (GGA), \tag{2.15}$$

$$E_{xc}^{(2)} = \int f^{(2)}(n(r), |\nabla n(r)|)\nabla^2 n(r)dr. \tag{2.16}$$

Equation (2.14) corresponds to the functional obtained for the LDA. The functional for the GGA comprises both the density $n(r)$ and its gradient $\nabla n(r)$. The higher orders of the series (Eq. (2.16)) contain also higher orders of the density gradient. Some GGA exchange correlation energy functionals, which are frequently used in DFT, can be found in [92–95]. Using GGA instead of LDA reduced errors of atomization energies of standard sets of small molecules by typically a factor 3–5 [86]. The remaining errors are typically about twice as high as for best established wave function methods. Together with the capability to deal with very large systems, DFT is now a significant method in quantum chemistry.

2.2.2 Theoretical modeling of x-ray spectra

After the brief outline of the theoretical principles of DFT, some details about how DFT is used to calculate XAS and XES spectra in this thesis are given in the following. As described by Fermi's Golden Rule, the intensity of the calculated transitions for XAS and XES are determined by the matrix element of two wave functions, describing the initial and final state, respectively (Eqs. (2.3) and (2.4)). Thus, a set of energy levels with a corresponding wave function has to be calculated to obtain both the energy difference and the cross sections of the two states. However, with this ground-state "frozen orbital" approach, final-state effects such as the existence of a core hole for the absorption or a valence hole for the emission are not considered. These effects have to be implemented separately for XAS and XES calculations to obtain reasonable transition energies.

For all calculations in this thesis, the StoBe-deMon DFT package was used [96]. This DFT code models the wave functions with a linear combination of Gaussian type orbitals to solve the Kohn-Sham DFT equations (2.8)–(2.12). The theory and numerical details of this realization can be found in Refs. [97, 98].

Used functionals and basis sets

Within this thesis, the gradient-corrected exchange and correlation functionals of Becke and Perdew were used [93, 95, 99]. It was shown that these functionals lead to reasonable results in good agreement to experiments of free and chemisorbed molecules [100–104].

To describe the valence electrons, a triple-zeta valence plus polarization basis [105] with a (7111/411/1) basis set for carbon, nitrogen, and oxygen, and a (41/1*) basis set for hydrogen were employed, respectively [105]. The auxiliary basis sets were comprised of five s and two spd-type Gaussians to fit the charge density as well as the exchange and correlation potentials for carbon, nitrogen, and oxygen, and of five s and one spd-type Gaussians for the hydrogen atoms. To localize the excitation to a specific atom and to obtain a better description of relaxation effects, the ionized atom was described by a IGLO-III basis [106]. For the remaining atoms of the same element, effective core potentials [107] were used, which describe the atoms after removing the core electrons to make them distinguishable from the excited atom.

Calculating transition energies and intensities

For XES, the transition probabilities were calculated based on the Kohn-Sham eigenstates in the “frozen orbital” approach. Even though core and valence relaxation effects are not considered by this approach, the errors luckily cancel out partially, leading to reasonable results [101]. The energies of the transitions were determined using a Δ(Kohn-Sham self-consistent field) (ΔSCF) approach, including differential relativistic effects associated with the removal of one electron from the 1s orbital. For this, the valence binding energies are calculated for a half-occupied core hole and half an electron in the valence state, whereas the remaining occupied orbitals of the same spin are populated by one electron each [101]. The ΔSCF correction calculates the core hole binding energy by calculating the difference of the total energies in the ground state and the core excited state, i.e., with one electron being removed from the 1s orbital. With this core hole binding energy the transition energies then can be corrected.

The transition probabilities for the XAS spectra were calculated using the “half core hole transition potential method” [100], in which half an electron is removed from the 1s orbital of the excited atom. With this approach, initial and final state effects are at least partially included, leading to a correct description of relaxation effects up to the second order. The transition probabilities and relative energies give reasonable results. The transition energy from the 1s orbital to the lowest unoccupied molecular orbital (LUMO) is then determined as the ΔSCF corrected total energy of the state with half a core hole and a half filled LUMO.

2.3 Experimental setup

To apply the soft x-ray spectroscopic methods introduced in Sec. 2.1, all parts of the experimental setup have to fulfill special needs. First of all, a light source with tunable energy is needed to be able to resonantly excite the sample or measure an absorption scan. In addition, a high photon flux is needed to achieve reasonable measurement times due to the small fluorescence yield for light elements (compared to the competing, non-radiative Auger decay). The bright, 3rd generation synchrotron light sources meet these requirements. All experiments presented in this thesis have been performed at the Advanced Light Source (ALS), Lawrence Berkeley National Laboratory in Berkeley, California, with electron energies of 1.9 GeV and a current of 500 mA in the storage ring. The endstation described below was attached to the open port of beamline 8.0, which is optimized to achieve a maximum photon flux for soft x-rays at the sample position. This beamline uses a 5-cm period undulator as insertion device, covering an energy range of 80 - 1250 eV, combined with a minimum amount of optical elements to minimize intensity losses due to absorption. After a first vertical condensing mirror, the light is monochromized, using three interchangeable spherical gratings for different energy ranges, with a resolving power of up to $E/\Delta E \approx 7000$. With one horizontal and a subsequent vertical refocusing mirror, a spotsize of $\approx 30\,\mu m \times 100\,\mu m$ is achieved. After the horizontal refocusing mirror, a gold mesh is installed for measuring a photo current, which is proportional to the beam intensity and thus can be used for normalization purposes. The attached SALSA (**S**olid **A**nd **L**iquid **S**pectroscopic **A**nalysis) endstation is equipped with a spherical electron analyzer (SPECS Phoibos 150 MCD), a high-transmission soft x-ray spectrometer [108], and a standard DN 150CF flange facing the beamline, which is used to attach the different measurement setups described below [109].

The custom-built soft x-ray spectrometer has been developed by Oliver Fuchs in our group. Details about the construction and the design can be found in Refs. [108, 110]. Originally, the spectrometer was designed for a maximum transmission in the energy range from 130 - 650 eV, with an energy resolution of $E/\Delta E > 1200$. The limit for low energies is set by the geometry of the optical elements and the detector and was recently lowered to 85 eV. The upper limit is defined by the reflectivity and absorption properties of the nickel coating of the optical elements. The principle design of the spectrometer is schematically shown in Fig. 2.3. The source spot is labeled “S” on the left. First, the emitted photons are collected with a spherical mirror (M) and reflected onto the energy dispersive element, a blazed plane variable line space grating (G). Finally, the x-rays are detected with an uncoated back-illuminated CCD camera with 2048 × 2048 pixels (1 inch × 1 inch) in normal incidence. The non-dispersive direction

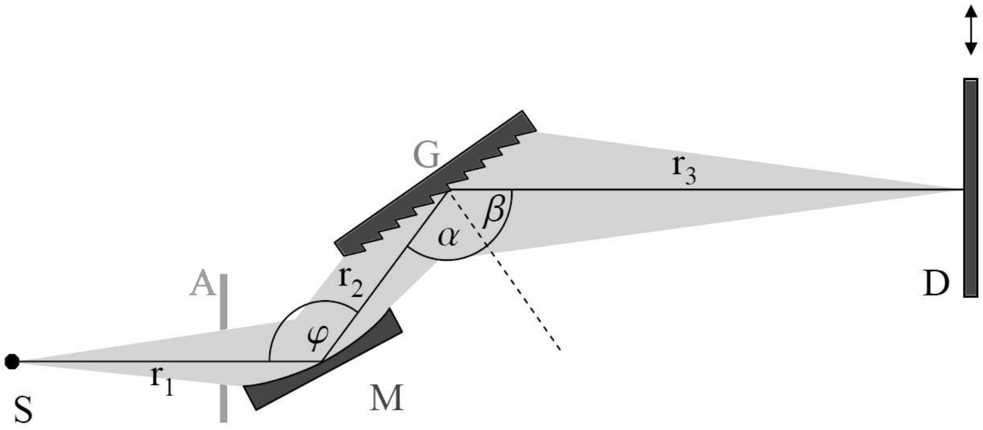

FIGURE 2.3. Schematic drawing of the soft x-ray spectrometer with sample spot “S”, an aperture “A” (which is only used to align the spectrometer), a spherical mirror “M”, a variable line space grating “G”, and a CCD detector “D”. The solid line shows the center path of the x-rays after proper alignment. [108]

of the two-dimensional CCD image is then integrated, resulting in an one-dimensional x-ray emission spectrum. The aperture “A” is only used to align the spectrometer. For the measurements, it is moved upwards such that the knife edge at its bottom blocks the direct path from the source spot to the detector.

As source, the spectrometer uses the focused synchrotron spot on the sample instead of an entrance slit, which helps to achieve a high transmission with the spectrometer. This reduces the exposure times needed to record meaningful spectra dramatically. Single x-ray emission spectra with reasonable signal-to-noise ratio can be acquired within five to twenty seconds, depending on the density of the sample and the investigated absorption edge. This allows to measure an emission spectrum on each step of a regular absorption scan within less than an hour, with almost the whole energy range of the spectrometer being measured simultaneously. The data is then presented in two-dimensional RIXS maps including all spectroscopic information.

Calibration

To calibrate the excitation energy of the beamline, reference XAS measurements of TiO_2 for the O K edge, N_2 for the N K edge, and HOPG for the C K edge were performed and compared to literature [111–113]. The XAS spectrum of gas-phase nitrogen bears a first absorption resonance at 400.88 eV [112]. At the beginning of every experimental run, the spectrometer is aligned and calibrated such that the elastically scattered light with this energy hits the CCD detector at certain pixels. Based on the design of the spectrometer, this emission feature appears twice in the emission spectrum (in different diffraction orders of the grating). The alignment is done for the two cells described below, which are at a fixed position relative to the analysis chamber. For solid-state experiments, the sample is carefully placed in the focus position of beamline and spectrometer by aligning emission features with known energy, e.g., the elastic peaks with an energy of 400.88 eV, to their known position on the emission energy scale of the CCD detector. For details the reader is referred to Ref. [110].

In general, once the emission energy axis is calibrated, it can be used for all measurements as long as the focus position of the beamline, the alignment of the spectrometer, and the sample position is not changed. However, small changes in the spot position on the sample with time can be observed, potentially caused by a slightly changed orbit of the electrons in the storage ring or a fluctuating heat load on the optical elements of the beamline, which slightly affect the spot position. Thus, all spectra taken are calibrated prior to any further data processing. For single spectra, the positions of the elastic lines for an excitation energy of 400.88 eV are used. In case of the aqueous solutions presented in this thesis, non-resonantly excited spectra of pure water were recorded frequently between the measurements and used to correct potential shifts in the position of distinct emission features on the detector. By fitting the spectrometer function (which attributes a certain pixel position on the detector to the respective calibrated emission energy) to the emission features and their position in the reference measurements, variations in the spot position can be corrected. For the two-dimensional RIXS maps, a more advanced routine is applied. Here, the position of the elastic peak(s) in each single spectrum of the RIXS map is read out together with its calibrated energy. By doing this, dozens of data pairs are generated, making the fit of the spectrometer function more accurate. With this procedure, the error in the absolute energy (for both excitation and emission) can be estimated to be below 0.1 eV, whereas the uncertainties in the relative energy scale are about 50 meV.

2.3.1 Setup for gaseous samples

In chapter 3, gas-phase methanol in its regular form H_3COH and its deuterated forms H_3COD and D_3COD is investigated. To make the gases accessible to soft x-ray spectroscopies, which require UHV conditions, a sophisticated setup was developed in the framework of the author's master thesis. A detailed description of this "gas cell" can be found in Ref. [114]. In this cell, which is mounted on the DN 150CF flange of SALSA, the sample gas is separated from the vacuum of the analysis chamber by a thin window membrane. The incoming photons from the beamline and the emitted photons penetrate through this membrane. This allows experiments to be performed

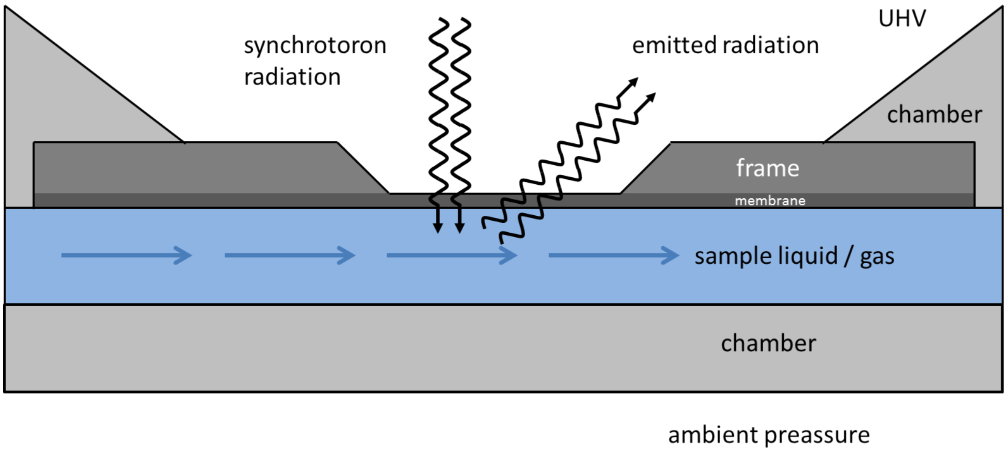

FIGURE 2.4. Schematic drawing of the membrane in the gas and liquid cell used to separate the sample gas or liquid from the UHV of the analysis chamber.

under atmospheric pressure conditions, while the gas can be continuously exchanged with a controlled mass flow. A schematic picture of the membrane is shown in Fig. 2.4.

The membranes have to meet certain requirements, e.g., they have to withstand the pressure difference between the sample gas and the vacuum of the analysis chamber. Furthermore, they should be as transparent as possible in the energy region of interest and non-degradable under intense x-ray radiation. The membranes used in this thesis were made of Si_3N_4 for measuring the C K edge, and SiC for measuring the O K edge, with thicknesses of 100 - 150 nm. Calculated transmission characteristics of the different membranes can be found in [115].

To bring methanol into its gaseous state, liquid methanol is filled into a reservoir and evaporated by heating it above its boiling point. The gas then expands into the evacuated tubing system of the gas cell that includes the central part of the cell (called “reactor”) with the membrane. To prevent condensation of the gas, the whole setup is heated via resistive heating elements both inside and outside the vacuum. In total five thermocouples allow to control the temperature at the crucial parts (especially the reactor) in the setup. Two pressure gauges indicate the pressure upstream and downstream of the reactor. The pressure in the reactor can thus be estimated by the mean value of these two readings. The outlet of the reactor is connected via a leak valve to a membrane or oil-free roughing pump that is used to evacuate the setup and to maintain a continuous gas flow during the measurement.

Preparation of gaseous samples

Methanol in its regular form H_3COH and its deuterated forms H_3COD and D_3COD was purchased from Sigma Aldrich with a purity of 99.8, 99.5, and 99.8 %, respectively. Prior to the experiments, the liquids were first degassed in an ultrasonic bath and subsequently by evacuating the liquid reservoir in the setup described above with an oil-free roughing pump to remove potential residual gases in the liquid. For the measurement, the complete setup was heated to $(80 \pm 5)\,^\circ$C to evaporate the liquids. To prevent condensation on the membrane, the reactor of the cell was kept at a slightly higher temperature than the rest of the setup. During the measurement, a gas flow through the cell was regulated to achieve both a base pressure of ≈ 1 bar in the cell with only small variations in the mbar range and a beam-damage free spectrum by constantly replenishing the sample volume.

2.3.2 Setup for solid-state measurements

In chapter 4, the amino acid glycine and its two smallest derived peptides diglycine and triglycine are investigated in solid sate. For this purpose, the gas cell described above is replaced by a solid-state manipulator, which can hold pressed powder samples. However, the molecules used in this studies are susceptible to beam damage by soft x-rays [116, 117], especially when irradiated with highly focused and intense synchrotron radiation. To minimize the influence of such degradation processes in the XES spectra and RIXS maps, the sample is continuously moved below the exciting beam. For this purpose, the three axes of the manipulator are motorized with computer controlled stepper motors. The scanning pattern is chosen such that every spot on the sample is illuminated only once to always obtain a completely fresh sample. By changing the scanning speed, the irradiation time per sample spot can be varied. When positioning the sample, special care was taken that the irradiated spot on the surface of the sample is always in the focus position of the spectrometer to prevent shifts in the measured spectra which can be attributed to a poorly aligned sample.

Preparation of solid samples

For the experiments discussed in chapter 4, glycine, diglycine, and triglycine were purchased from Alfa Aesar, all with a purity of better than 99% and used without further purification. For the measurements, the powders were pressed under ambient conditions into pellets with a hydraulic press (5 tons/cm^2), during which the powders only got in contact with clean teflon sheets. The resulting pellets were about 1 mm thick, 15 mm × 24 mm large, and were glued to the sample holder using carbon tape.

Afterwards, the samples were transferred into the load-lock and stored there until the measurement.

2.3.3 Setup for investigating aqueous solutions

In chapter 5, various aqueous solutions are investigated. Similar to the measurements of the gaseous samples, experiments including liquid samples require sophisticated setups. In this thesis, a liquid cell, which was designed in the PhD thesis of Monika Blum [115], is used. Also in this cell, the sample liquid is separated from the vacuum by a window membrane as was described above. For the measurements in chapter 5, only SiC membranes were used for both the experiments at the O K and the N K edge. The investigated liquid is pumped through a channel with a cross-section of 0.13 mm^2 behind the membrane with a typical pump rate of about 6 ml/min. With a beam size of 30 μm × 100 μm, this equals to a replenishing of the probed sample volume of about 5000 times per second. The liquid is collected in a reservoir with a volume of $\approx$ 30 ml and reused throughout the measurement. The reuse of the sample liquid did not have any influence on the measured XES spectra. Only a slight temperature increase of about 5 °C in the reservoir can be observed for longer measurements, e.g. RIXS maps, since the sample liquid simultaneously cools the membrane, which is prone to a high heat load by the synchrotron beam. A detailed description of the liquid cell, including technical drawings and further specifications, can be found in Refs. [109, 115].

Preparation of aqueous samples

All aqueous samples were prepared using ultra-pure water (Sigma Aldrich) as a solvent. Prior to the measurement, all samples were degassed in an evacuated chamber using a roughing pump. For the aqueous solutions at neutral pH values discussed in Sec. 5.1, a 1.7 M (=1.7 mol/liter) glycine solution was prepared by dissolving 12.5 g of the glycine powder also used for the solid-state samples in 100 ml water. Similarly, 6.6 g of the diglycine powder and 3.8 g of triglycine were dissolved in 100 ml water, resulting in solutions with a concentration of 0.5 M and 0.2 M, respectively. Note, that for all given and following concentrations the increase in volume by the solvent is neglected.

In Sec. 5.2, aqueous solutions of glycine and diglycine at different pH values are investigated. All pH values were measured using a pH meter equipped with a BlueLine electrode from Schott that was calibrated with pH = 1.0, 6.0, and 10.0 buffer solutions. The pH values at room temperature were adjusted either by adding aqueous HCl (50 %, Alfa Aesar) or NaOH (50 %, Alfa Aesar) to the base solution. For glycine, a 2 M base solution was prepared by dissolving 30 g glycine in 200 ml water. For diglycine, the 0.5 M solution described above was used as the base solution.

For the experiments of mixed solutions of diglycine and different salts in Sec. 5.3, a 0.5 M base solution of diglycine was prepared as described above. Then, specific amounts of salts were added to 30 ml of the 0.5 M diglycine solution, such that the salt concentration was also set to 0.5 M (again, neglecting the increase in the volume by the salt). The amounts were: KF: 0.87 g, KCl: 1.12 g, KI: 2.49 g, K_2SO_4: 2.61 g, KSCN: 1.46 g, KNO_3: 1.52 g, KBr: 1.79 g, LiCl: 0.64 g, NaCl: 0.88 g, NH_4Cl: 0.80 g, $MgCl_2$: 1.43 g, and $CaCl_2$: 1.66 g. All salts had a purity of >99% and where purchased from Sigma Aldrich or provided by the Advanced Light Source. In addition, reference samples for selected salt solutions were prepared with a concentration of 2 M. Therefore, 5.82 g KSCN, 6.07 g KNO_3, or 3.21 g NH_4Cl were added to 30 ml water, respectively.

In Sec. 4.2.2, reference measurements of acetic acid and acetamide are presented. The acetic acid was purchased from Sigma Aldrich as a 50 wt% aqueous solution and diluted to a 25 wt% solution with ultra-pure water. Then, the pH was adjusted to pH 12.8 by adding NaOH. Acetamide was purchased in form of small crystals from Sigma Aldrich (≈99%) and a 1 M aqueous solution was prepared by adding 1.77 g acetamide to 30 ml water.

CHAPTER

3

NUCLEAR DYNAMICS AND ISOTOPE EFFECTS IN THE RIXS MAPS OF GAS-PHASE METHANOL

The main goal of this thesis is to gain a better understanding of the interaction between molecules and ions in aqueous solution to shed more light onto the effects leading to the specific ordering of ions in the Hofmeister series. However, the multiplicity of different molecules and ions in such systems and an accordingly high number of possible interactions between these components lead to a very complex electronic structure. Hence, it is helpful to narrow down the number of parameters and start with a smaller system with less components. The smallest possible system and thus an ideal candidate to start with the investigation of the electronic structure is an isolated molecule, i.e., without any interactions with surrounding molecules. In general, these circumstances are found in the gas phase. The setup described in Sec. 2.3 allows for investigating gases at atmospheric pressures by separating the sample gas from the vacuum of the analysis chamber with a thin membrane. Furthermore, substances which are liquid at ambient conditions can be evaporated to measure the molecules in their gas phase. However, the setup is not designed to sublimate solid samples.

The molecule used in this thesis was chosen to be methanol, which is the smallest alcohol consisting of a methyl group (CH_3) and a hydroxy group (R-OH) (Fig. 3.1). The boiling point of liquid methanol at ambient pressure is at ≈65 °C [118], which is easily achievable with the gas cell described in Sec. 2.3 and Ref. [114]. Despite its simple chemical structure, it contains a carbon and an oxygen atom and thus provides two absorption edges in the relevant energy region of soft x-ray spectroscopies. This is particularly relevant for the study of bigger molecules in the following chapters,

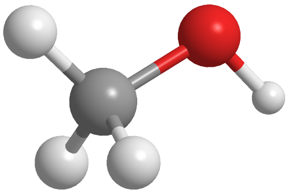

FIGURE 3.1. Chemical structure of methanol (H_3COH). White spheres represent hydrogen, gray carbon, and red oxygen atoms, respectively.

since the existence of different absorption edges enables the investigation of the local electronic structure with RIXS in different moieties of the molecule. Furthermore, methanol is commercially available not only in its normal form H_3COH, but also in its deuterated forms H_3COD and D_3COD, allowing for studies of isotope effects. Such isotope effects have been found to give valuable information about the electronic structure of gas-phase water [78] and in aqueous ammonia [59]. Hence, methanol is a promising candidate as a reference system for investigating the electronic structure of an isolated molecule which is performed in this chapter.

The main aspect thereby lies on the interpretation and the understanding of how the chemical structure and geometry of the molecule influence the molecular orbitals and thus the x-ray emission spectrum. X-ray absorption and non-resonantly excited x-ray emission spectra of normal methanol (H_3COH) at the O K and C K edge are discussed in Sec. 3.1. The resonant inelastic soft x-ray scattering (RIXS) maps of gas-phase methanol are addressed in Secs. 3.2 (O K edge) and 3.3 (C K edge). Special attention is set on isotope effects for resonant excitation after replacing the hydrogen atom of the hydroxy group with a deuterium atom (H_3COD) at the O K edge (Sec. 3.2). The C K RIXS maps of normal and completely deuterated methanol (D_3COD) are discussed in Sec. 3.3. The chapter is then summarized and discussed in Sec. 3.4 and has been published in parts in Ref. [119].

3.1 Review: Interpretation of soft x-ray spectra of an isolated methanol molecule

This section gives a brief review of experimental results which were collected prior to this thesis in the framework of the author's master thesis [120]. They form the basis of the discussion of the experimental data in the following sections of this chapter. The main result is that non-resonantly excited x-ray emission spectra of isolated molecules can be interpreted based on the symmetry and overlap of the molecular orbitals involved in the underlying electronic transitions.

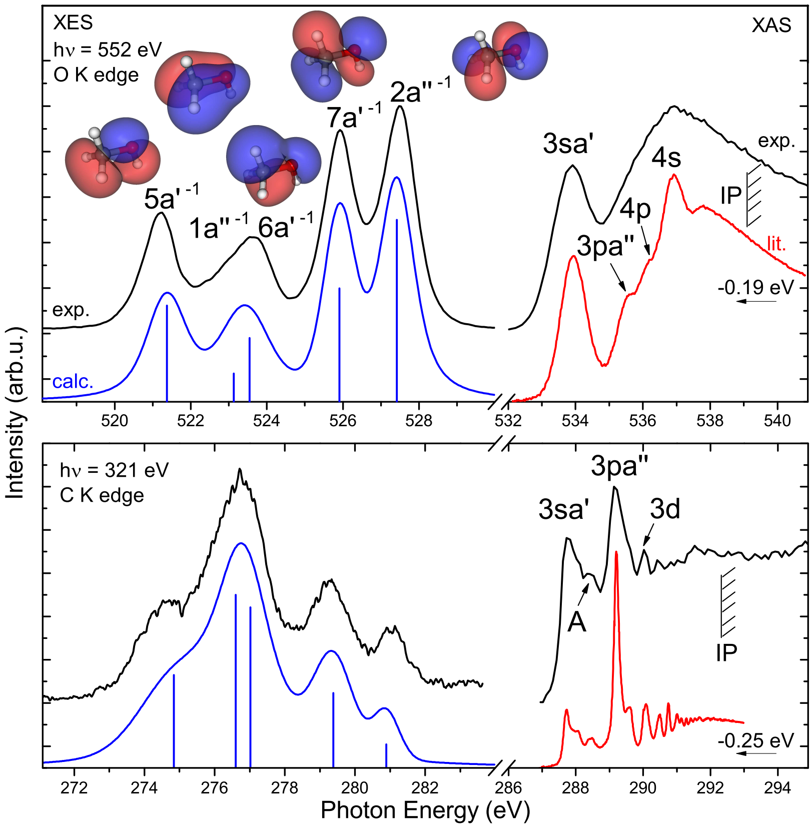

FIGURE 3.2. Left: Non-resonant XES spectra of gas-phase methanol at the O K (top) and C K (bottom) edge. Experimental data is shown in black, blue vertical bars represent DFT calculations resulting in the spectra shown in blue after broadening with Voigt profiles. Emission features are labeled with respect to the corresponding valence hole state (top). The five highest occupied molecular orbitals are displayed. Right: Partial fluorescence yield XAS spectra (black) in comparison with literature spectra [121] (red). The most prominent absorption resonances are labeled and the ionization potentials (O K: 539.1 eV, C K: 292.3 eV [122]) are given.

On the right side of Fig. 3.2, partial fluorescence yield XAS (PFY-XAS) spectra of gas-phase methanol at the oxygen K (top) and carbon K edge (bottom) are given. They were generated from the RIXS maps in Figs. 3.3 and 3.6 (discussed in Secs. 3.2 and 3.3) by integrating the emission intensity between emission energies of 518 eV and 530 eV (O K) and between 271 eV and 283 eV (C K) at each excitation energy, respectively. The PFY-XAS spectra are in good agreement with the high-resolution XAS spectra from Ref. [121] (displayed in red), showing all Rydberg derived resonances (3d, 4p, 4s), but suffering from the well-known saturation effects of fluorescence yield detection [123]. To align the most prominent absorption features, the literature spectra were shifted by -0.19 eV (O K) and -0.25 eV (C K). Following the nomenclature in Ref. [121], the identified absorption resonances are labeled. The absorption resonance at the C K edge marked “A” is attributed to an excitation into the 3sa’ state, in combination with a vibrational excitation of the symmetric stretch of the molecules‘s methyl group [121]. On the left side of Fig. 3.2, non-resonantly excited x-ray emission spectra at the oxygen K (top) and the carbon K edge (bottom) are shown in black. The O K spectrum was excited with 552.0 eV, the C K spectrum with 321.0 eV, hence far above the ionization potentials of 539.1 eV [121] and 292.3 eV [121, 122], labeled “IP” in the XAS spectra, respectively. They are in good agreement with spectra of gas-phase methanol available in literature, excited using x-rays [124] or electron impact [125, 126]. However, satellite structures at higher emission energies that can be observed for electronic excitation [125, 126] do not occur and the spectra presented here exhibit a better signal-to-noise ratio and resolution than was previously possible. Blue vertical lines below the x-ray emission spectra represent the results of DFT calculations for an isolated methanol molecule (for computational details see Sec. 2.2). After energy alignment, the calculation is in good agreement with the experimental spectra and calculations in literature [127]. To account for experimental and lifetime broadening as well as the vibrational fine structure, the calculation was broadened with Voigt profiles. Note, that the (unresolved) vibrational fine structure can lead to very complex and asymmetric line shapes, which usually can not be described by a simple Voigt profile. In the present case, however, only a slight asymmetry of the spectral lines can be observed. The results for both calculations (O K and C K) are shown as blue spectra in Fig. 3.2. Despite the simplified broadening, they are in excellent agreement with the measured spectra. The spectra exhibit four clearly separated emission features, with the emission feature around 523.5 eV (O K) and 276.5 eV (C K) being comprised of two emission lines, as the calculation confirms. The labels refer to the final states of the electronic transition with the superscript “-1” representing the missing electron in the respective orbital. They are based on the C_s symmetry (i.e., one existing mirror plane) of the methanol molecule [124]. Next to the x-ray emission spectrum in the top panel, isodensity surfaces of the ground state molecular orbitals (MOs) resulting from the performed DFT calculations are shown. As mentioned in Sec. 2.1, the matrix element in Fermi’s Golden Rule (Eq. 2.1) determines the emission intensity of a specific emission line for non-resonant excitation and depends on the wave function overlap and the symmetry of the participating MOs. Accordingly, the intensity distribution in the emission spectrum can qualitatively be understood by taking a closer look at the displayed MOs. For instance, the 1a” and 6a’ MOs have a significant p character around the carbon atom resulting in high emission intensities after creating a C 1s core hole and only a low intensity when an O 1s core hole was created. In contrast, the 2a” MO exhibits the highest emission intensity of all emission features after excitation of the oxygen K edge and only low intensity after creating a C 1s core hole. This can be understood by considering the 2p character of this orbital and its confinement around the oxygen atom. All statements given here regarding the character and localization of the discussed MOs are confirmed by other calculations [125–127].

3.2 Impact of nuclear dynamics on the electronic structure at the O K edge of gas-phase methanol

After developing an understanding how the symmetry and localization of molecular orbitals define the structure and shape of non-resonantly excited x-ray emission spectra in the previous section, the focus of this section is set on the resonant excitation of the oxygen K edge of gas-phase methanol. With partly and completely deuterated methanol (H_3COD and D_3COD, respectively), an additional parameter is introduced into the analysis. Compared to hydrogen, deuterium has an additional neutron, resulting in approximately double the mass of the hydrogen. Note that the electronic structure of the ground state is not affected by a molecule's mass. Nevertheless, isotope effects can be observed in the x-ray emission, which is shown based on the RIXS maps in Fig. 3.3 for excitation of the oxygen K edge.

In these maps, the emission intensity is displayed color coded as a function of excitation energy (ordinate) and emission energy (abscissa). The O K RIXS map of normal methanol is displayed in Fig. 3.3 a), whereas the maps of the deuterated samples are shown in Fig. 3.3 b) (H_3COD) and c) (D_3COD), respectively. For emission energies above 530 eV, the intensity is magnified by a factor 5. In this energy region, emission with the same excitation and emission energies is observed, which is assigned to elastically scattered (Rayleigh) light. The intensity of the Rayleigh line varies with excitation energy. Regions with increased intensities can be found at and around the different absorption resonances, which were identified in the XAS spectrum of H_3COH in Fig. 3.2 and are labeled on the left in Fig. 3.3 a). On the low (emission) energy side of the Rayleigh line, loss features occur, which can be attributed to excitations of molecular vibrations. Since the electron which was excited from a core level to an unoccupied state takes part in the following emission process, all features in this region are referred to as *participant* emission. Its complement is the so-called *spectator* emission, i.e., an electron of a different molecular orbital fills up the created core hole, whereas the excited electron "spectates" this process. The spectator emission is found at emission energies below approximately 528.5 eV. Emission features are labeled on the top in Fig. 3.3 a). One observes changes in relative emission intensity

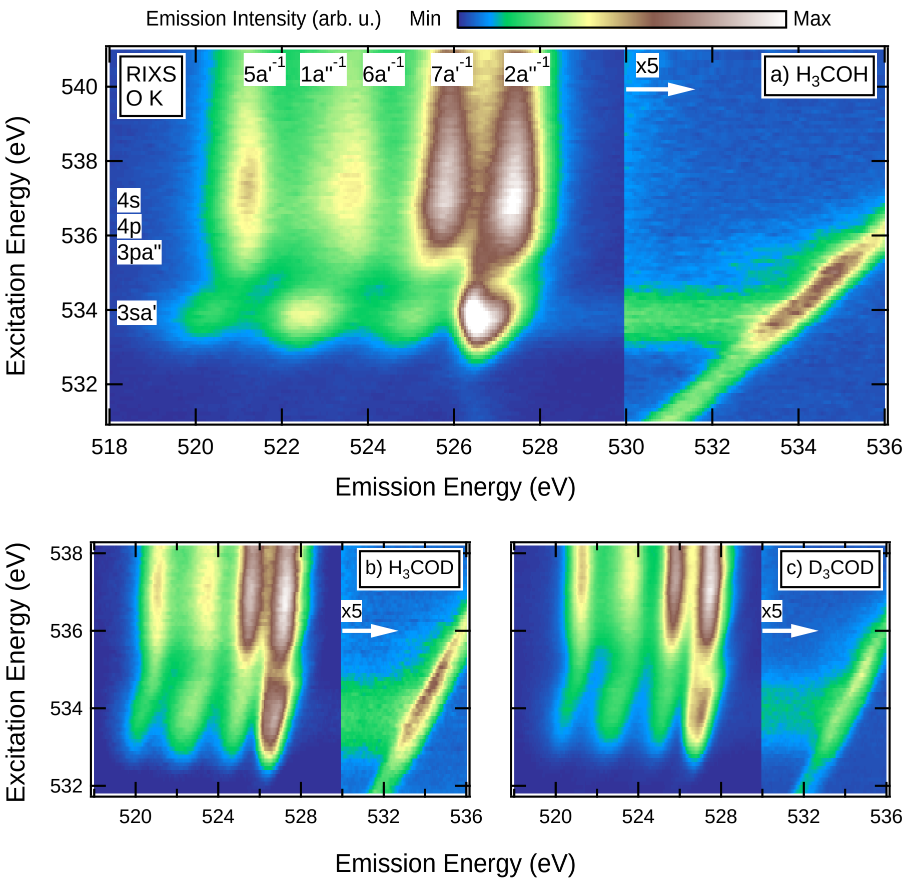

FIGURE 3.3. RIXS maps of gas-phase methanol at the O K edge of different methanol isotopes [a) H_3COH, b) H_3COD, and c) D_3COD]. Emission features are labeled at the top, selected absorption resonances at the left in panel a). For emission energies above 530 eV, the intensity is magnified by a factor 5.

and significant shifts of the emission features as a function of the excitation energy. Especially at the 3sa’ absorption resonance these changes are obvious when one compares, e.g., the relative intensities and emission energies of the 7a’$^{-1}$ and 2a”$^{-1}$ emission lines with the spectra taken at higher excitation energies. As expected, the overall shape of the RIXS maps is comparable between the different methanol isotopes. When taking a closer look, however, differences in peak shape can be found, especially for the 2a”$^{-1}$ emission feature at the 3sa’ resonance.

For a more detailed analysis, Fig. 3.4 shows a comparison of non-resonant x-ray emission spectra (a) and spectra resonantly excited at the 3sa’ absorption resonance (b) of the three isotopes. Spectra of normal methanol are displayed in black, H_3COD in red, and D_3COD in green. In addition to the emission features identified in Fig. 3.2 for H_3COH, the 3a’$^{-1}$ and 4a’$^{-1}$ emission lines are shown on a compressed energy scale

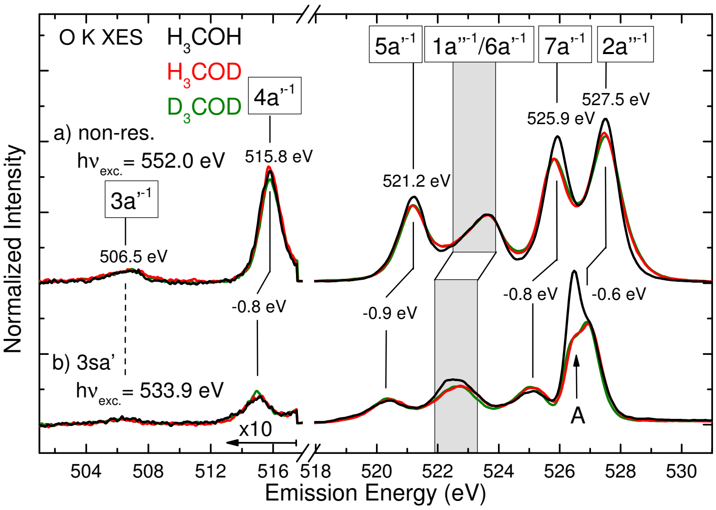

FIGURE 3.4. XES spectra of gas-phase methanol in its normal and deuterated forms [H_3COH (black), H_3COD (red), and D_3COD (green)] for non-resonant excitation (a) and excited at the 3sa' absorption resonance (b). Emission features are labeled at the top. Vertical lines illustrate center positions and spectator shifts for selected emission features (details see text). For the $3a'^{-1}$ line, the position for non-resonant excitation is shown as a dashed line. The gray shaded area specifies likely positions for the $1a''^{-1}$ and $6a'^{-1}$ line for non-resonant excitation with a speculative spectator-shift of -0.6 eV for resonant (3sa') excitation. Below an emission energy of 517.5 eV, the intensity is magnified (×10).

and with magnified intensity (×10) below emission energies of 517.5 eV. Vertical black lines indicate the center positions for selected emission features for H_3COH. Given energies refer to non-resonant excitation. All positions were determined by fitting the spectra with one Voigt profile for each emission feature. Note that there is an additional feature ("A" in Fig. 3.4), which can be attributed to nuclear dynamics on the time scale of the RIXS process (discussed in more detail below). Thus, the $2a''^{-1}$ feature was fitted with two Voigt profiles and the peak position was obtained from the high energy component.

For excitation at the 3sa' resonance (Fig. 3.4 b), shifts of up to -0.9 eV in the energy position of almost all emission features are observed as compared to the non-resonant excitation. Due to the weak intensity of the $3a'^{-1}$ line for resonant excitation, no reliable energy position could be determined. As a guide to the eye, the position for non-resonant excitation is shown as a dashed line instead. The overlapping emission of the $1a''^{-1}$ and $6a'^{-1}$ lines hinders an exact determination of their energetic position. The gray area covers likely positions based on the fit with Voigt profiles with an indicated (speculative) shift of -0.6 eV for the resonant excitation. Such shifts have previously been observed for a number of molecules in the gas phase (e.g., CO [128],

N_2 [129], and H_2O [78]) and can be explained by the presence/absence of the excited electron in the resonant/non-resonant case and its interaction with the remaining electronic system [130]. In this thesis, these shifts will be referred to as *spectator shifts*. Since the observed spectator shifts have been discussed in previous work and do not play a crucial role for the scope of this thesis, the reader is referred to Refs. [119] and [120] for more details.

Besides the spectator shifts, changes in the relative emission intensities occur with varying excitation energy as was already mentioned in conjunction with the RIXS maps in Fig. 3.3. One reason for these changes is the angular-anisotropic character of the RIXS process, which is observed for randomly orientated molecules upon resonant excitation [131] and can briefly be explained as follows. The absorption probability for a distinct transition is influenced by the symmetry of the intermediate state and the orientation of the molecule with respect to the incoming, linearly polarized light. Assuming that the molecule does not change its orientation before the x-ray emission process takes place, this leads to a defined angular distribution of the emitted photons, also depending on the symmetry of the final valence hole state. Since the O 1s core hole lifetime is of the order of only a few fs [132], this assumption holds. Luo *et al.* [131] give a detailed theoretical description of this angular anisotropy for the water molecule, which was applied to x-ray emission spectra of gas-phase water by our group [78].

A second reason for the changes in relative emission intensities can be developed by a comparison of the spectra of normal methanol (black) with H_3COD (red) and D_3COD (green). The small differences in the line shape between normal methanol and the deuterated isotopes in the non-resonant spectra (Fig. 3.4 a) can be explained by different vibrational structures caused by the different mass of deuterium and hydrogen. For resonant (3sa') excitation (Fig. 3.4 b), however, the isotope effect in the spectra becomes very strong. This can be most easily seen in the intensity of feature “A”, which is much more prominent for regular methanol compared to the deuterated molecules. Furthermore, normal methanol shows higher emission intensities at an emission energy of approximately 522.5 eV compared to the deuterated forms.

For a more detailed discussion of the isotope effect, the spectra excited at the 3sa' absorption resonance of H_3COH (black) and H_3COD (red) are displayed in Fig. 3.5. 1a) and b), normalized to the highest peak maximum, respectively. In analogy to the case of liquid and gas-phase water [77, 78, 133], the differences in the peak intensity of feature “A” in Fig. 3.4 will be analyzed in the following based on ultra-fast nuclear dynamics taking place on the time scale of the x-ray emission process. In a simple model, one can reproduce the emission spectra by a superposition of the emission of intact molecules and H_3CO^- fragments that were created before the emission process took place. Due to the higher mass of deuterium compared to hydrogen, the

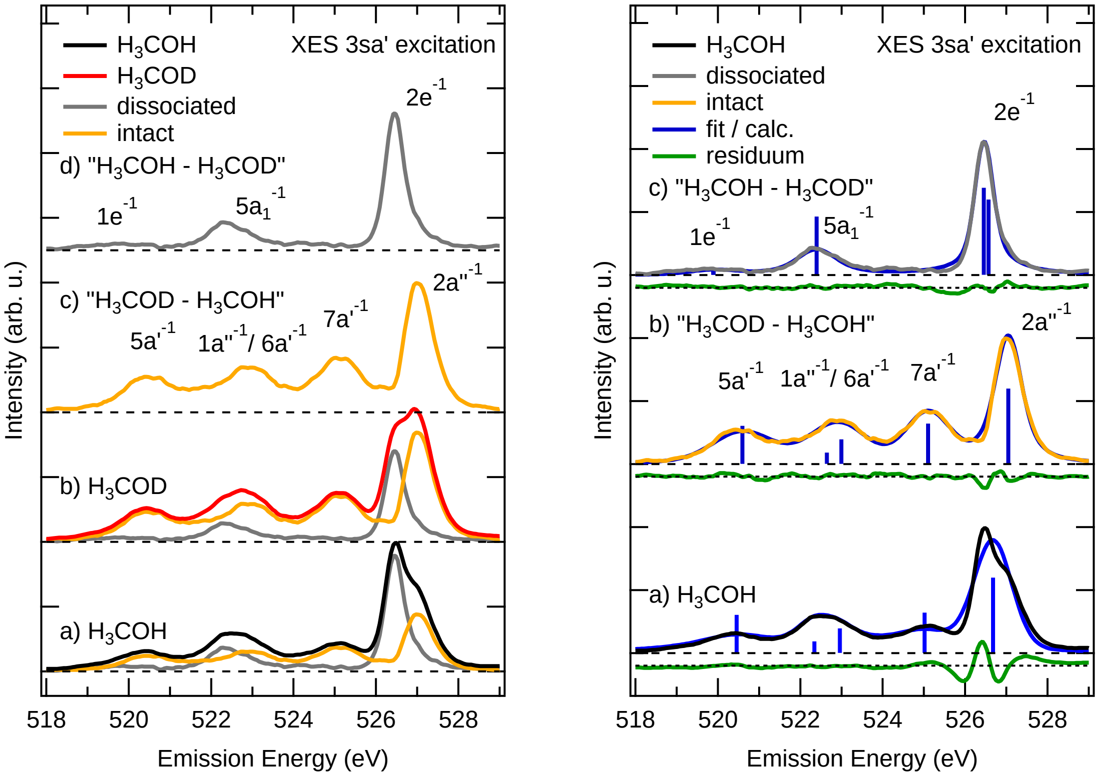

3.5.1 3.5.2

FIGURE 3.5. Left (3.5.1): XES spectra of gas-phase H_3COH (a, black) and H_3COD (b, red) for excitation of the 3sa' resonance at the O K edge. The difference spectrum generated by forming the subtraction of "H_3COD - 0.56 × H_3COH" (c, orange) represents the contribution of intact molecules, the contribution of dissociated molecules (d, gray) was obtained by the subtraction "H_3COH - 0.73 × H_3COD". Suitable weighted linear combinations of spectra c) and d) give exact reproductions of the measured spectra in a) (0.73:1) and b) (1:0.56). Emission features in a)-c) are labeled analog to Fig. 3.4, while for d), the nomenclature of the resulting C_{3v} point group was used. The measured and difference spectra are normalized to the peak maximum for presentation.
Right (3.5.2): Fits based on DFT calculations are plotted in blue, showing an excellent agreement with the spectra for intact (b, orange) and dissociated molecules (c, gray), but big deviations for the measured spectrum of H_3COH (a, black). The respective residua are displayed in green.

dissociation process is expected to be slower for H_3COD than for H_3COH and therefore the spectral weight of dissociated molecules will be lower for H_3COD than for H_3COH. In the model, this allows for separating the emission of dissociated molecules from the emission of intact molecules by calculating suitable difference spectra. Prior to the subtraction, the spectra were normalized to the integrated emission intensity in the emission energy range from 500 - 536 eV. For the contribution of intact molecules (orange, Fig. 3.5.1 c), the difference “H_3COD - 0.56 × H_3COH” was computed, for the emission of dissociated molecules the difference was “H_3COH - 0.73 × H_3COD” (gray, Fig. 3.5.1 d). In both cases, this corresponds to the maximal fraction not generating any negative intensity in the range from 500 - 524 eV. With these two difference spectra, the spectra of H_3COH and H_3COD can now be described by a superposition of the two fractions, as shown in Fig. 3.5.1 a) and b).

The difference spectrum associated with intact molecules still looks very similar to the measured spectra, except that it exhibits only a single line at the 2a”$^{-1}$ emission feature. The spectrum of dissociated molecules, however, is significantly different from all other spectra, which can be explained by the changes of the electronic structure of the molecule by removing the proton bound to the oxygen. The point group of the methanol molecule changes from C_s to C_{3v} symmetry, which leads to a redistribution of the electron density. As a consequence, two 2e MOs are formed by an energetic degeneration of the former 2a” and 7a’ MOs. Similar, the former MOs 1a” and 5a’ degenerate and form two 1e MOs. Whereas the two latter MOs show only a very small emission intensity, the strong p-like character and localization of the 2e MOs at the oxygen atom lead to a high relative emission intensity.

The comparison with the DFT calculations shown in Fig. 3.5.2 supports the interpretation of ultra-fast nuclear dynamics. In Fig. 3.5.2 a), the measured spectrum of H_3COH (black) is fitted in a similar way as it was performed for the non-resonant spectrum in Fig. 3.2 with a single Voigt profile for each emission feature based on the calculations presented in Fig. 3.2. However, to account for the angular anisotropy of the x-ray emission process, the relative emission intensities were corrected for resonant (3sa’) excitation with the equations in Ref. [131]. Using the dipole moments of all MOs extracted from the calculation and the geometry of the experimental setup (with an angle of 45° between spectrometer and the exciting beam), correction factors of 1.05, 0.90, 0.99, 1.05, and 1.01 (in decreasing energetic order from 2a”$^{-1}$ to 5a’$^{-1}$) are obtained. Even though the energetic position of the Voigt profiles used for the fit was used as a fitting parameter (albeit, with the energetic order staying untouched), the spectrum of H_3COH is not described satisfactorily. Especially in the energy region of the 2a”$^{-1}$ emission and feature “A”, big discrepancies are found as can be most easily seen when looking at the residuum of the fit shown in green below the spectrum.

For the spectrum of intact molecules (Fig. 3.5.2 b), the situation is different. Again, one Voigt profile for each emission feature was used, corrected for the angular anisotropy as described above. However, the relative emission energies were set according to the calculation with an additional shift of -0.2 eV for the 7a'$^{-1}$ peak, and -0.3 eV for the 5a'$^{-1}$ line with respect to the 2a"$^{-1}$ feature, to account for the difference in the spectator shifts observed in conjunction with Fig. 3.4. The corrected spectrum for intact molecules is described very well by the fit and much better as it is the case for the spectrum in a), although the number of fitting parameters was reduced. Likewise, the spectrum of H_3CO^- fragments is reproduced very well by the calculation of a H_3CO^- fragment (Fig. 3.5.2 c). The geometry and orientation of the H_3CO^- fragment corresponds to the one used for H_3COH, only the hydrogen bound to the oxygen was removed. The relative emission energies again were corrected for the angular anisotropy. The dipole moment of the intermediate state, however, was extracted from the lowest unoccupied molecular orbital (LUMO) of H_3COH, since the dissociation process is triggered by the resonant excitation of intact methanol molecules (i.e., no H_3CO^- fragments in ground state configuration are excited by the incoming photon beam in this model). With the dipole moments of the occupied MOs of the H_3CO^- fragment, correction factors for the emission intensities of 0.90, 1.05, 1.05, 0.91, and 1.05 (in decreasing energetic order from 2e^{-1} to 1e^{-1}) are calculated. For energy alignment, the calculation was shifted by +0.77 eV. Emission features are labeled with respect to the C_{3v} point group of the H_3CO^- molecule. Note, that the emission features 1e^{-1} and 2e^{-1} each consist of two emission lines, which are energetically degenerated. The result of the calculation, however, exhibits a splitting into two single emission lines with a separation in emission energy of ≈0.1 eV for the 2e^{-1} lines and 0.01 eV for the 1e^{-1} lines.

As the calculation confirms, the model that the measured spectra can be reproduced by a superposition of the spectra of intact and dissociated molecules is a good approximation. In Fig. 3.5.1 a) and b) one can see, that the relative contributions of intact and dissociated molecules to the spectra of H_3COH and H_3COD are quite different. These proportions can be used to determine an effective dissociation time τ_D for the two isotopes, as it was introduced in Ref. [134] for the dissociation of the H_2S molecule and applied to ammonia in Refs. [59, 135]: With the concept of an effective scattering time [66], τ being the lifetime of the core hole, and assuming that the decay of the excited state is reasonably well described by an exponential function, the fraction of remaining core holes n_{ch} at the time τ after the excitation at $t = 0$ is given by $n_{\text{ch}} = e^{-t/\tau}$. The rate of core hole decays, n_{decays}, is then given by the negative of the time derivative of n_{ch}: $n_{\text{decays}} = -\frac{d}{dt} n_{\text{ch}} = \frac{1}{\tau} e^{-t/\tau}$. For the definition of the dissociation time τ_D it is assumed, that the emitting molecule can be described as H_3COH (H_3COD) from the core excitation event at $t = 0$ up to $t = \tau_D$, and as H_3CO^- after τ_D [134]. The time integral of the decay rate from $t = 0$ to $t = \tau_D$ then gives the fraction of decay events in intact molecules, $n_{\text{decays,intact}}$, relative to the total number of decay events: $n_{\text{decays,intact}} = \int_0^{\tau_D} \frac{1}{\tau} e^{-t/\tau} dt = 1 - e^{-\tau_D/\tau}$. The dissociation time τ_D can then be calculated as $\tau_D = -\tau \ln\left(1 - n_{\text{decays,intact}}\right)$. The fractions of emitting intact molecules for H_3COH and H_3COD can be obtained by the intensity of the two contributions in Fig. 3.5.1 a) and b). By integrating the contributions for an emission energy range of 518 - 529 eV, decay fractions of intact molecules of ≈ 0.52 (H_3COH) and ≈ 0.73 (H_3COD) are obtained. For an O 1s core hole lifetime broadening Γ of $\approx$150 meV [136], the lifetime τ can be calculated to be $\tau = \hbar/\Gamma = (4 \pm 1)$ fs. Using this lifetime and the determined decay fractions, dissociation times of $\tau_{D,H_3COH} = (3 \pm 1)$ fs and $\tau_{D,H_3COD} = (6 \pm 1)$ fs can be estimated. For ammonia, the dissociation time was found to be 32 fs [135] for the gas phase, and (9 ± 2) fs and (12 ± 2) fs for aqueous NH_3 and ND_3, respectively. Schreck *et al.* [79] state for liquid methanol that after $\tau_{\text{dyn}} = (1.2 \pm 0.8)$ fs nuclear dynamics in the core-excited state have a measurable contribution to the RIXS spectra. Arguing, that the hydrogen-bonding environment in the aqueous solution with the attractive potential of neighboring molecules accelerates the dissociation process, the obtained dissociation times for gas-phase methanol seem to be reasonable.

In addition to the spectral changes discussed above, the RIXS maps in Fig. 3.3 show further spectral signatures of molecular dissociation in the participant emission. When examining the loss features on the low energy side of the Rayleigh line, one detects that these losses extend only a few eV down for the 3pa" resonance. At the 3sa' resonance, however, the full energy range down to the spectator emission exhibits some intensity for all isotopes. For normal methanol (Fig. 3.3 a), the intensity of this loss feature is more intense than for the deuterated samples. Assuming the final state for this feature includes a dissociated molecule and an outgoing proton, this continuous loss feature can be explained by a continuous amount of energy that can be transferred to the outgoing proton. This was already found previously for an aqueous solution of NH_3 [59].

Hence, one can state that changes in the molecular structure can change the symmetry of a molecule and thus have a strong effect on its electronic structure. In the case of gas-phase methanol, the changes in the x-ray emission spectrum for resonant excitation of the O K edge, i.e., the appearance of additional emission features in combination with a strong isotope effect, can be traced back to the removal of the hydrogen of the hydroxy group. This can be induced, e.g., by ultra-fast nuclear dynamics on the time scale of the x-ray emission process subsequent to the resonant excitation, as it was shown by comparing the spectra of regular and deuterated methanol.

3.3 The C K RIXS map of gas-phase methanol

After the discussion of the oxygen K edge of gas-phase methanol, this section discusses the C K edge data of normal and fully deuterated methanol in the gas phase. It will be shown that isotope effects are much less pronounced for the C K edge than it is the case at the O K edge. In particular, changes in the electronic structure as a consequence of a dissociation of the molecule after resonant excitation only play a minor role for the interpretation of the x-ray emission spectra at the C K edge. In general, resonance effects are less distinct after the creation of a C 1s core hole which will be discussed based on the RIXS maps of gas-phase methanol in Fig. 3.6.

The RIXS map of gas-phase H_3COH for excitation above the C K edge is shown in Fig. 3.6 a), while the data of fully deuterated methanol (D_3COD) is displayed in panel b). Emission features which were introduced for the non-resonantly excited spectrum in Fig. 3.2 are labeled at the top and selected absorption resonance on the left, respectively. Red vertical bars represent the excitation energies for which the emission intensity was integrated to obtain the x-ray emission spectra displayed in Fig. 3.7 (discussed below). The resonance at an excitation energy of 288.4 eV is attributed to an electronic excitation of the 3sa' absorption resonance in combination with a symmetric stretch vibrational excitation of the methyl group [137]. Similar to the O K RIXS maps in Fig. 3.3, the emission of the five highest valence orbitals is shown. However, the depicted emission features exhibit different relative intensities, which can be attributed to the differences in the wave function overlap of the valence orbitals with the C 1s and O 1s orbitals, as was discussed in Sec. 3.2. Furthermore, the symmetry of the involved orbitals lead to an angular anisotropic RIXS intensity, causing changes in relative emission intensities which are observed for resonant excitation. For excitation of the 3sa' and 3pa" absorption resonances, the intensity of the participant emission increases strongly and on the low energy side of the Rayleigh line vibrational loss structures can be detected. These loss structures are more distinct at the C K edge than at the O K edge. For excitation of the 3sa' resonance, a continuous loss feature between participant and spectator emission is visible, albeit with only very low intensity. For H_3COH (Fig. 3.6 a), additional emission intensity with an emission energy of $\approx$ 282.8 eV can be observed for excitation energies between $\approx$ 288.1 eV - 289.6 eV. Its origin, however, is unclear. Since this feature is not present for deuterated methanol it might be related to the vibrational structure in the spectra.

When comparing the RIXS maps of the two methanol isotopes one can state that isotope effects are not as prominent as it was the case for the O K edge. For a more detailed analysis, some selected resonant emission spectra are shown in Fig. 3.7 a)-c). They have been extracted from the RIXS maps by integrating the emission intensity in the excitation energy regions marked by the red vertical bars in Fig. 3.6. The

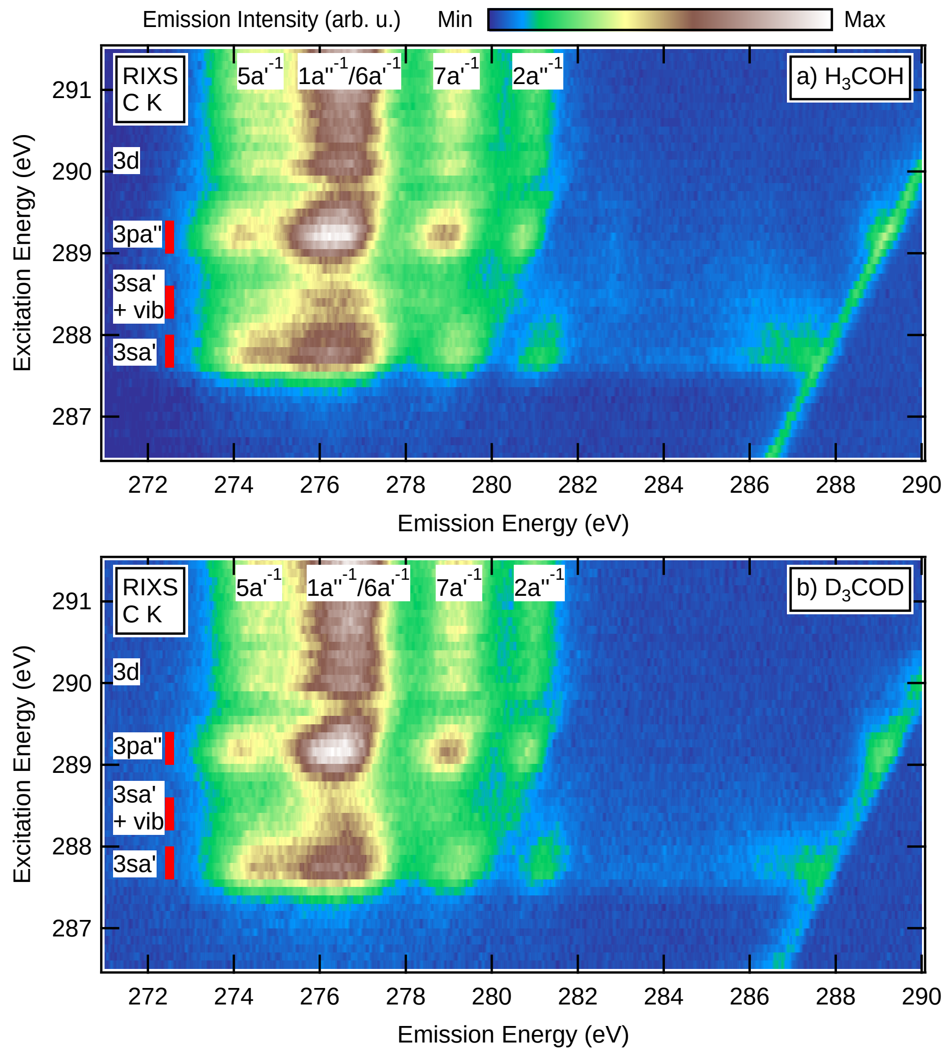

FIGURE 3.6. RIXS map of gas-phase methanol at the C K edge. Normal methanol (H_3COH) is shown in panel a), fully deuterated methanol (D_3COD) in panel b), respectively. Emission features are labeled at the top, selected absorption resonances on the left.

center energies of the intervals are given, the total width was chosen to be 0.4 eV to achieve a good signal-to-noise ratio. The spectra of normal methanol are displayed in black, fully deuterated methanol is shown in green. Spectra 3.7 a) and c) were excited at the two most prominent absorption resonances 3sa' and 3pa" [122, 137] (see XAS spectra in Fig. 3.2), whereas spectrum 3.7 c) was excited just above the 3sa' absorption resonance. In addition to the resonant 3sa' excitation, a symmetric stretch vibration of the methyl group is excited at this energy [137]. Spectra 3.7 d) represent the non-resonant excitation, which was already shown for H_3COH in Fig. 3.2. Emission features are labeled at the top. For the two highest emission lines, $7a'^{-1}$ and $2a''^{-1}$,

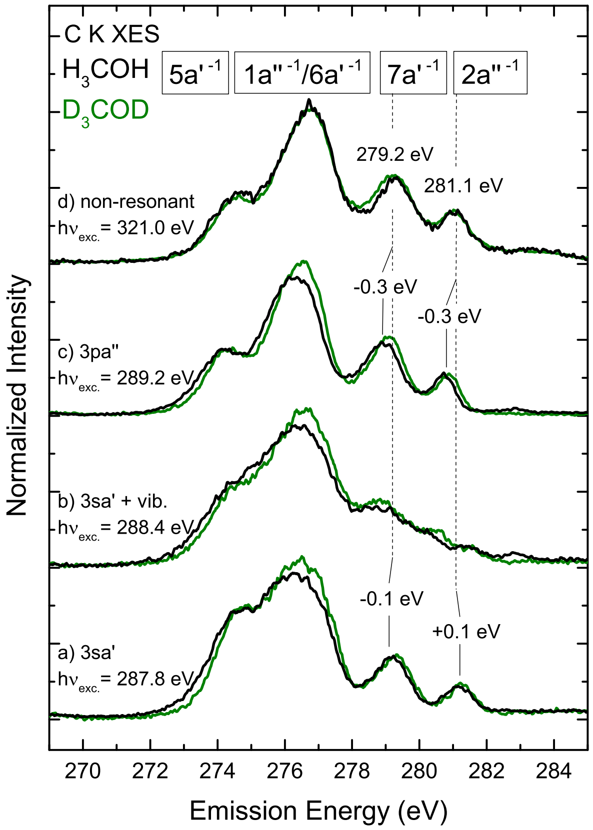

FIGURE 3.7. XES spectra of gas-phase H_3COH (black) and D_3COD (green) at the C K edge at selected excitation energies. Emission features are labeled at the top, vertical dashed lines represent the (given) energetic positions of the 7a'$^{-1}$ and 2a"$^{-1}$ line, solid lines show selected spectator shifts, respectively.

dashed vertical lines depict the (given) energy positions for non-resonant excitation for H_3COH. Due to the strong vibrational broadening and the resulting overlap of different emission features the exact determination of the energetic position of the other shown valence emission lines is difficult.

For non-resonant excitation, the two isotopes show only slight differences in the line shape, which can be attributed to a more pronounced vibrational progression for H_3COH due to the smaller mass of the hydrogen atoms compared to deuterium. For the resonantly excited x-ray emission spectra (a-c), the differences in the line shape between the two isotopes are also very small. Although a continuous loss feature can be observed between the participant and the spectator emission in the RIXS maps in Fig. 3.6, the depicted spectra do not show a strong isotope effect as it is the case at the O K edge.

The observed spectator shifts are smaller compared to the O K edge. For the 3pa” resonance, the two highest emission features shift by -0.3 eV to lower emission energies, as indicated by black solid lines. For excitation of the 3sa’ resonance, the $7a'^{-1}$ emission feature shifts by -0.1 eV, whereas the $2a''^{-1}$ line shifts by +0.1 eV with respect to their position for non-resonant excitation. The determination of the spectator shifts for the other valence emission features is difficult due to the mentioned vibrational broadening and overlapping features. However, the qualitative statement that the spectator shifts are most likely smaller than -0.5 eV can be made based on the data.

When comparing the relative intensities of the emission features for non-resonant and resonant (e.g., 3sa’) excitation, the effects of the angular anisotropy of the RIXS process can be observed. However, the overlapping emission features again hinder a detailed analysis, as it was performed for the O K edge in Sec. 3.2. Thus, only qualitative statements can be made. When comparing, e.g., the combined emission intensity of the two highest emission features with the other valence emission lines one can state that for resonant excitation the spectral weight shifts to lower emission energy. The overall shape of the spectra for the 3sa’ + vib excitation in Fig. 3.7 b) is strongly different from the other ones. Here, all emission features including the two highest emission lines are much broader compared to the other shown spectra. The excitation of the symmetric stretch mode of the methyl group at this excitation energy [137] might cause a bigger overlap with vibrational states in the final state which then leads to a broadening of the emission lines. In spectra b) and c) the additional emission feature with unknown origin at $\approx$ 282.8 eV is visible for H_3COH.

Overall one can state that for gas-phase methanol, the x-ray emission spectra after excitation of an C 1s core hole are less susceptible to isotope effects than it is the case at the O K edge. The excitation of vibrational modes in addition to an electronic excitation, however, can have a strong influence on the overall shape of a x-ray emission spectrum. Keeping in mind that the excited symmetric stretch mode of the molecule’s methyl group changes the local geometry and surrounding of the excited carbon atom, one can understand that the observed broadening is observed for the C K emission rather than for the O K emission. The fact that the spectator shifts tend to be smaller at the C K edge compared to the O K edge, especially for excitation of the 3sa’ resonance, might point towards a stronger localization of the respective molecular orbital around the oxygen atom, leading to stronger screening effects induced by the excited electron.

3.4 Summary and discussion

In this chapter, non-resonantly and resonantly excited x-ray emission spectra and x-ray absorption spectra at the O K and C K edge of gas-phase methanol in its normal (H_3COH) and deuterated forms (H_3COD, D_3COD) are presented. For the non-resonant spectra, each emission line can be attributed to a distinct molecular orbital. The relative emission intensities for the observed valence emission features can be explained by the localization and symmetry of the involved MOs. A strong O 2p character thus leads to a relatively high emission intensity at the O K edge (as it is the case, e.g., for the 2a" MO of methanol), whereas a strong C 2p character and primarily localization around the carbon atom leads to high emission intensities after excitation of a C 1s core hole (e.g., the 1a" and 6a' MOs). These findings are supported by DFT calculations for an isolated methanol molecule, showing an excellent agreement with the measured spectra.

For both absorption edges in the soft x-ray regime, the different isotopes of the methanol show slight deviations in the line shape of the x-ray emission spectra. This can likely be attributed to a different vibrational progression due to the higher mass of deuterium compared to hydrogen. A remarkably different overall line shape is observed at the C K edge for an excitation of the 3sa' resonance in combination with a vibrational excitation of the methyl group, leading to a much stronger broadening of the observed emission features.

The strongest isotope effect, however, is observed for resonant (3sa') excitation of the O K edge. A detailed comparison of the two methanol isotopes traces the changes (especially the appearance of additional emission features) back to nuclear dynamics on the time scale of the x-ray emission process. Based on a simple model that the measured spectra are a superposition of the emission of intact and dissociated molecules and assuming that the dissociation process is slower for the deuterium due to its bigger mass, the two components can be separated. A comparison with DFT calculations for a H_3CO^- fragment leads to an excellent agreement, which supports this interpretation. The fact that the emission spectrum of the dissociated molecules exhibits a very different shape compared to the intact molecule testifies that changes in the geometrical structure of a molecule can have enormous consequences for the electronic structure. In the discussed case, the removal of the hydrogen atom bound to the oxygen by nuclear dynamics leads to a change in the symmtery of the molecule. This is followed by a reorganisation of the electron density and the formation of new molecular orbitals, giving rise to different and new emission features in the x-ray emission spectrum.

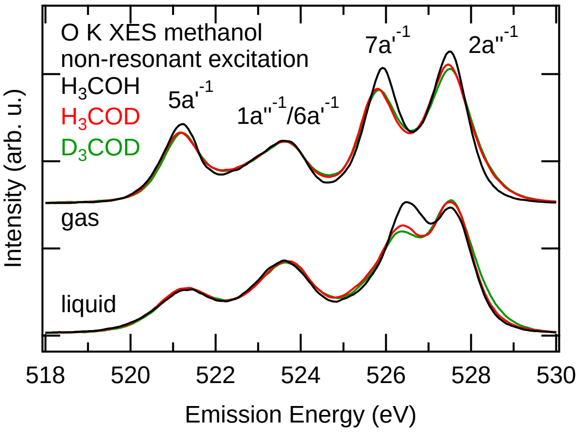

FIGURE 3.8. Comparison of the non-resonantly excited O K XES spectra of methanol in gas-phase (top) and in its liquid state (bottom), normalized to the integrated emission intensity in the shown energy region.

In the gas phase the molecule can be considered as isolated from its surrounding, making it a good starting point for the analysis of the influence the physical and chemical surrounding of a molecule can have on its electronic structure. Ideally, the next steps would be to “add” different kinds of surroundings to the molecule, e.g., by turning to the liquid phase, to look for changes in the electronic structure and relate them to distinct interactions. The liquid phase of methanol is accessible for the investigation with x-ray spectroscopies, e.g., with the liquid cell described in Sec. 2.3. A comparison between normal methanol in gas-phase and as a liquid was performed by the author of this thesis in [120]. The main conclusion which could be made based on the experimental data was that the x-ray emission spectra of the liquid are very similar to the spectra of the gas phase, i.e., the electronic structure is dominated by the gas phase, with only minor differences which can be attributed to the influence of the surrounding. A comparison of the non-resonant O K XES spectra of methanol in gas phase and as a liquid is displayed in Fig. 3.8. The spectra of liquid methanol in its deuterated forms were recorded in conjunction with this work.

The additional emission feature at the $2a"^{-1}$ line for resonant (3sa’) excitation of the O K edge was observed also in the liquid phase of methanol [120]. However, for excitation of the 3pa” resonance and in the non-resonant spectrum (shown in Fig. 3.8), a shift of the $7a'^{-1}$ emission feature towards higher emission energies (tentatively due to an overlap of an additional emission feature at slightly higher emission energy) and a lower relative emission intensity of the $5a'^{-1}$ line compared to the gas phase is found [120]. These findings suggest that in the liquid phase nuclear dynamics leading to a dissociation of the methanol molecule not only occur at the 3sa’ resonance. They might be promoted by hydrogen bonds between neighboring methanol molecules with the attractive potential of the neighboring molecule defining the pathway of the dissociating hydrogen atom [120]. This is corroborated by the strong isotope effect in the $7a'^{-1}/2a''^{-1}$ energy region, which follows the same trend as in the gas phase, i.e., the $7a'^{-1}$ emission feature is significantly weaker for the deuterated forms. Thus, nuclear dynamics are also crucial for the interpretation of the non-resonant spectra of liquid methanol. Spectator shifts were observed to be smaller for the liquid phase, pointing towards an enhanced screening of the excited electron by the surrounding molecules [120]. The findings are in concordance with a later RIXS study of liquid alcohols of Schreck *et al.*, including methanol in its normal and single deuterated form [79].

The role of hydrogen bonds in liquid methanol and their effect on the electronic structure is even more discussed in literature [79, 124, 137–144]. Several models have been proposed to describe a possible arrangement of methanol molecules in the liquid and in aqueous solution, ranging from cyclic hexamers [138] to rings and chains of different sizes [124, 137, 139–143]. However, up to now no consensus has been found.

Turning to the solid phase of methanol could be a next step towards a better understanding of how the surrounding affects the electronic structure. However, to analyze methanol as a solid with x-ray spectroscopies the sample has to be cooled down to its freezing point in ultra high vacuum conditions. This requires several experimental challenges to be met, which the setup described in Sec. 2.3 is not capable of. In literature only little work is published about x-ray spectroscopies applied to methanol ice [126, 145]. Moreover, the quality of the available data is not sufficient to compare it with the liquid or the gas phase.

Hence, for the following chapters of this thesis, the sample system was changed to something more easily treatable in the solid phase with the option to analyze aqueous solutions of the molecule. At the same time, the size of the molecule is increased and another absorption edge in the soft x-ray regime, the nitrogen K edge, is made available. The fact that also the dimer and trimer of the molecule, i.e., bigger molecules which consist out of two or three units of the primary molecule, respectively, are commercially available and thus can be analyzed further increases the parameter range of this thesis. The chosen sample system is the amino acid glycine, its dimer glycylglycine, and its trimer glycylglycylglycine. The electronic structure of these three molecules in solid phase is investigated in the following chapter. This sets the basis for the discussion of the electronic structure of diglycine in aqueous solution in chapter 5 and the observation of ion-specific effects when salts are added to the solution.

CHAPTER 4

GLYCINE AND ITS SMALLEST PEPTIDES IN THE SOLID PHASE

Glycine is the smallest of the 20 naturally occurring amino acids. Proteins and peptides consist of a chain of these basic amino acids [146], with the exact sequence of amino acids determining their structure and function [146]. Hence, these amino acids can be called the “building blocks” of life. Today, more than 500 different amino acids are known [147]. All amino acids contain both an amino and a carboxyl functional group, which are connected via a carbon atom (“α-carbon”). The side chain, which also connects to this carbon atom, however, is different for all amino acids. In the case of the smallest amino acid glycine, the side chain consists of a single hydrogen atom.

In Fig. 4.1, the *zwitterion* of glycine, which is by far the most common molecular species in the solid state (and in aqueous solution at pH 7) [146, 148] is displayed. In this configuration, the amino group of the molecule is “protonated”, i.e., an additional

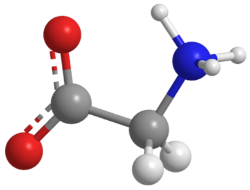

$COO^{-} - CH_2 - NH_3^{+}$

FIGURE 4.1. Chemical structure of the glycine molecule in its zwitterionic state, i.e., with a deprotonated carboxyl (COO^{-}) and a protonated amino (NH_3^{+}) group. Hydrogen atoms are presented in white, carbon in gray, oxygen in red, and nitrogen in blue, respectively.

proton is bound to the nitrogen, forming a NH_3^+ group and the carboxyl group is "deprotonated", i.e., the proton of the carboxyl group is removed, resulting in a COO^- group. Intermolecular interactions in the solid state favor this proton transfer from the carboxyl to the amino group [148]. In the gas phase, experimental studies show that glycine exists in a neutral form [149, 150]. The net charge of the molecule, however, is zero in both configurations. In aqueous solution, the charge state of an amino acid can be changed via the pH of the solution. This will be explained in more detail and applied in chapter 5 to study the effect of protonation and deprotonation of the functional groups on the electronic structure.

In literature, predominantly x-ray absorption studies of solid-state glycine [55, 151–157] and its derived peptides [55, 151–155] are available. Photoelectron spectroscopy (PES) was applied to solid glycine [158–160] and its small peptides [161, 162]. Only limited work on x-ray emission spectroscopy of glycine is available [163–165] for the solid state. The electronic structure of gas-phase glycine was investigated by XAS and PES [166–169], Feyer *et al.* reported the first PES data on gas-phase diglycine [166]. Due to technical developments, aqueous solutions of amino acids became accessible for soft x-ray spectroscopies, for example, using XAS or XPS on liquid jets [43, 55–57, 170]. The first x-ray emission studies of glycine in aqueous solution and at different pH values using a liquid cell are found in [58]. An extensive XES investigation in combination with dynamical DFT calculations of aqueous glycine solutions of different pH using the liquid cell described in Sec. 2.3 and Ref. [109] was performed by Blum *et al.* [60].

In this chapter, the electronic structure of glycine (Gly) and of its dimer glycylglycine (Gly-Gly, diglycine, or "Digly") and trimer glycylglycylglycine (Gly-Gly-Gly, triglycine, or "Trigly") in the solid phase is subject of a detailed analysis. The investigation of the solid phase as a homo-molecular sample system thereby sets the foundation for the discussion of hetero-molecular systems involving glycine and its dimer in the further course of this thesis. In particular, the complex system of diglycine in different aqueous salt solutions and the occurrence of ion-specific effects on the electronic structure of diglycine in conjunction with the Hofmeister series will be discussed in Sec. 5.3, which requires a good understanding of the involved individual components.

First, non-resonant x-ray emission spectra of glycine at the O K and N K edge are discussed in Sec. 4.1. The similarities and differences in the electronic structure of glycine and its smallest peptides are then addressed in Sec. 4.2, with the resonant and non-resonant excitation of the N K edge being discussed in Sec. 4.2.1, and a detailed analysis of the O K edge in Sec. 4.2.2. In Sec. 4.3, the results of this chapter are summarized and comprehensively discussed.

4.1 The x-ray emission spectrum of glycine

Fig. 4.2 shows x-ray emission spectra of a pressed glycine pellet, non-resonantly excited above the O K ($h\nu = 547.4\,\text{eV}$, Fig. 4.2.1) and N K absorption edges ($h\nu = 419.4\,\text{eV}$, Fig. 4.2.2). The measured data is plotted as a red curve. Vertical lines represent spectral intensities calculated using DFT for an isolated molecule in the zwitterionic charge state (as it is present for the solid-state sample [148]). As a geometric input for the calculation, the molecular structure of glycine as evaluated by powder diffraction measurements from Schreyer *et al.* [171] was used. For further computational details see Sec. 2.2. In the left panel, the used geometry is displayed with labels for the nitrogen and oxygen atoms. Black vertical bars ("O1") in Fig. 4.2.1 correspond to the transitions from the occupied molecular orbitals into a O1 1s core hole, red bars ("O2") to the transitions into a O2 1s core hole, respectively. Selected emission lines are labeled with respect to the involved molecular orbital. After a small (+0.4 eV) shift in energy, the calculation of the O K edge describes the measured spectrum very well. An energetic shift of $\approx 0.2\,\text{eV}$ in the calculation of the two O 1s binding energies is observed. For solid state XPS measurements, a splitting for the two core levels of 0.2 eV in the zwitterionic state can not be resolved (FWHM $\approx 2\,\text{eV}$) [161]. For the neutral glycine molecule in gas phase, a splitting of 1.8 eV between the two core levels is observed in XPS [168]. There, one oxygen in the carboxyl group is double bonded to the neighboring carbon, whereas the other oxygen has each a single bond to the carbon atom and to an additional hydrogen atom.

To emphasize the good agreement with the experimental data, the calculation was broadened with Gaussian profiles, resulting in the green spectrum. Based on the fact that the calculation of an isolated zwitterionic molecule reproduces the measurement of the solid state to such a high degree, one can state that the electronic structure of the solid-state sample is dominated by the electronic structure of the isolated molecule. The neighboring molecules in the crystal structure apparently only have a minor influence on the x-ray emission spectrum. Due to the lack of available x-ray emission data of gas-phase glycine (not to neglect the differences in electronic conformation between the two states), a direct comparison between the solid state and the gas-phase sample is not possible. A convolution of the calculation with a more complex peak shape (e.g., a potentially asymmetric Voigt profile to account for the Lorentzian line shape of lifetime broadening and the asymmetry in the vibrational progression) most likely would further improve the agreement but also introduce more parameters. For the sake of simplicity this was avoided, since the broadening with Gaussian profiles already describes the experimental spectrum to a satisfying amount.

The calculation reveals that the intense high emission energy feature at 526.8 eV stems from transitions from the highest occupied molecular orbital (HOMO) into the

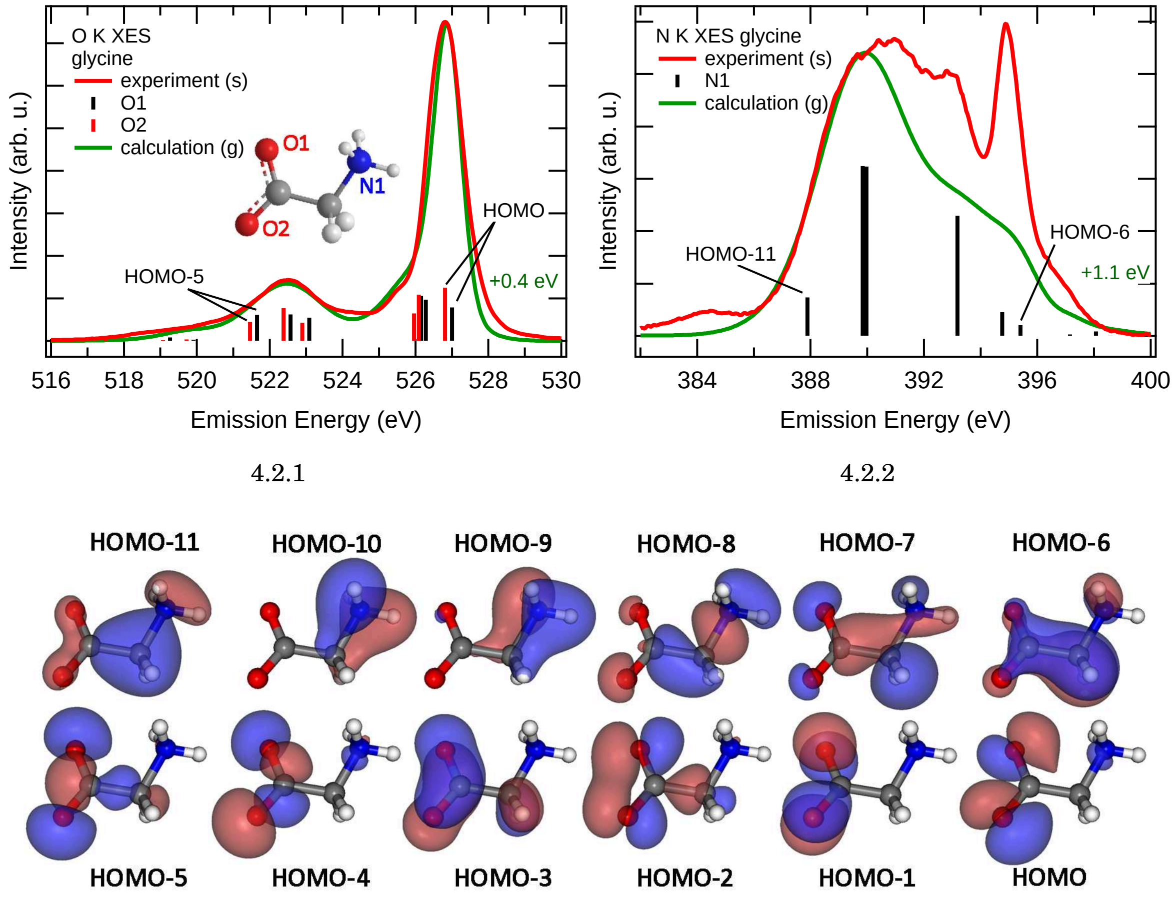

4.2.1

4.2.2

4.2.3

FIGURE 4.2. XES spectra of glycine, non-resonantly excited at the O K (4.2.1) and N K edge (4.2.2). Red curves represent the experimental data, vertical bars the results of a DFT calculation for an isolated glycine zwitterion ("gas phase"). The green curve represents the calculation, broadened with Gaussian profiles and shifted by the given values for comparison. The geometry of the molecule with partly labeled atoms is displayed in the top left panel. Selected calculated emission lines are labeled with respect to the involved occupied molecular orbitals displayed in Fig. 4.2.3.

oxygen 1s core levels. Thereby, the HOMO predominantly consists of the lone-pair orbitals of the two oxygen atoms. The shoulder on the low-energy side of this feature at about 525.5 eV can be attributed to the HOMO-1 and HOMO-2 transitions. The low-energy feature with its maximum at 522.5 eV is formed by transitions from the HOMO-3, -4, and -5, respectively. The lower lying molecular orbitals exhibit only low emission intensity at the O K edge, which can be explained by the small wave function overlap and the symmetry of the involved molecular orbitals.

Fig. 4.2.3 displays isodensity surfaces of the twelve highest occupied molecular orbitals of the glycine zwitterion in the ground state as they result from the performed DFT calculation. The six highest occupied MOs all exhibit a strong localization at the oxygen atoms of the carboxyl group. Combined with a strong O 2p character this results in comparatively high emission intensities for O K excitation. The deeper lying MOs barely show a wave function overlap with the oxygen 1s orbitals, thus having only small emission intensities. Note that the emission energies of the HOMO-9 and the deeper lying orbitals is below the displayed minimum emission energy of 516 eV in Fig. 4.2.1. Based on the calculated molecular orbitals some more qualitative statements can be made. The HOMO, for example, has mainly O 2p character with only very limited contribution of orbitals derived from the neighboring carbon atom. Thus, it will barely contribute to the C-O bond in the molecule and will be less susceptible to changes in the geometric structure of the carboxyl group induced by molecular vibrations. Accordingly, the envelope of the vibrational progression has a narrow line shape, leading to a comparatively narrow and intense emission of this orbital. The HOMO-3, -4, and -5, which make up the low-energy feature at ≈ 522.5 eV, however, exhibit a strong contribution of orbitals derived from both oxygens and the neighboring carbon atom and thus take part in the C-O bonds. Therefore, they are more susceptible to geometric changes through molecular vibrations and show a broader line shape.

For the N K edge, the interpretation of the measured spectrum only based on the emission of different molecular orbitals is not sufficient (Fig. 4.2.2). The calculated transitions for an isolated glycine zwitterion are represented by black vertical bars (shifted by +1.1 eV) below the measured spectrum of solid-state glycine (red curve). One can observe that the MOs with the highest emission intensities are the HOMO-6 to HOMO-11, as indicated in the graph. The respective MOs displayed in panel 4.2.3 all reveal a stronger localization around the nitrogen atom and thus have a bigger wave function overlap with the N 1s core hole than the higher MOs. In addition, especially the orbitals HOMO-8 to HOMO-10 exhibit a strong N 2p character, giving rise to an enhanced emission intensity. The wave function overlap of the higher orbitals with the N 1s core hole is evanescent small, resulting in negligible emission intensities at the N K edge. A convolution of the calculation with Gaussian profiles results in the green curve. Big differences between the calculation and the measurement are observed. After shifting the calculation by +1.1 eV, only the low-energy side of the main emission feature around ≈ 389 eV can partly be described by the calculation. The emission feature at 384 eV, however, is almost not present (a very weak emission line with an energy of 383.9 eV, attributed to the HOMO-12, can be found in the calculation). On the high-energy side of the main emission feature, the discrepancies between calculation and experiment are strongest. Especially the narrow and intense

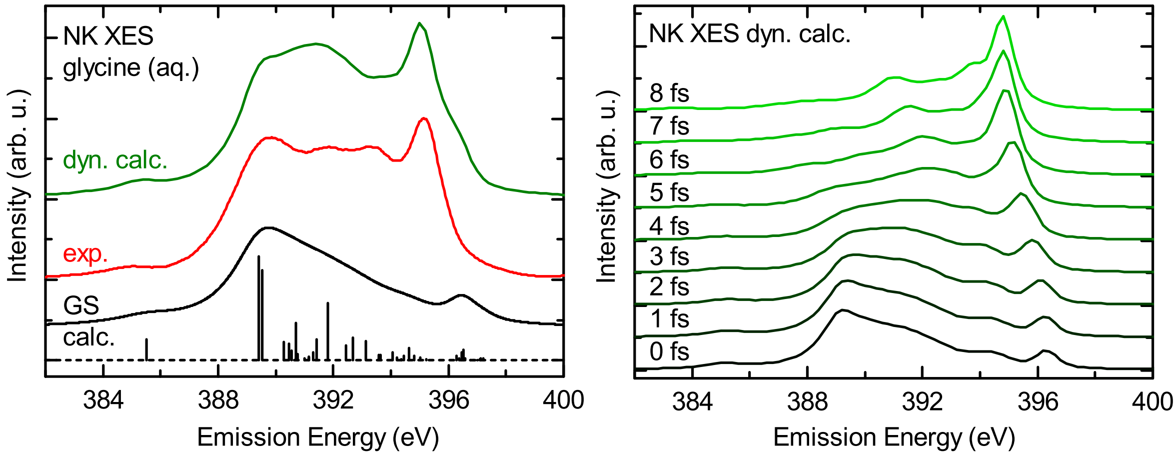

4.3.1

4.3.2

FIGURE 4.3. Left (4.3.1): Non-resonant XES spectrum of glycine in aqueous solution at pH 6.5 (red) in comparison with a static ground state DFT calculation (black) and a dynamic calculation including proton dynamics (green). Right (4.3.2): Calculated "snapshot" spectra for the dynamical calculation. Delay times after the core excitation are given on the left. The graphs are adopted from [60].

peak at ≈ 395 eV is not included in the calculation. In the comprehensive study of aqueous glycine solutions of different pH by Blum *et al.* [60], however, the origin of this distinct peak and the overall spectral shape is very nicely elaborated, corroborated by dynamical DFT calculations of micro-solvated (i.e., surrounded by nine water molecules) glycine molecules. Since the N K x-ray emission spectra of glycine and its derived peptides play a major role in the further course of this thesis, some of the results Blum *et al.* present in Ref. [60] will be recapitulated in the following based on Fig. 4.3.

The spectrum of a half saturated aqueous solution of glycine at pH 6 (measured by Blum *et al.* [60]) is displayed in red in Fig. 4.3.1. At this pH, glycine is in its zwitterionic state (as will be discussed in more detail in Sec. 5.2.1) and thus can serve as a reasonable reference for the solid state. The experimental data is compared to ground state DFT calculations (black bars, labeled "GS calc.") comparable to the ones presented in Fig. 4.2, however, for a glycine molecule which is micro-solvated by nine surrounding water molecules. Accordingly, the calculation exhibits a lot more emission lines due to the larger number of atomic orbitals taking part in the formation of molecular orbitals. The calculation is broadened by Gaussian and Lorentzian profiles for better comparability (black line). As it is the case for the "gas-phase" calculation in Fig. 4.2.2, the agreement with the experimental data is not very good.

To obtain a better description, calculations including dynamical effects were performed. They show that the protonated amino group (NH_3^+) undergoes ultrafast dissociation on the time scale of the x-ray emission process [60], similar to the process described in Sec. 3.2 for gas-phase methanol. Blum *et al.* found that initially the hydrogen-bonded N-H bonds are elongated within the first few femtoseconds, with a proton being detached within 10-20 fs, resulting in a NH_2 group [60]. The changes introduced to the electronic structure by this dissociation process are traced in time by a series of "snapshot" spectra after distinct time intervals after the core excitation. The respective spectra for the first 8 femtoseconds after excitation are displayed in Fig. 4.3.2. The bottom most spectrum represents the ground state calculation shown in Fig. 4.3.1, for the other spectra the passed time intervals are given on the left. Significant changes in the spectral shape can be observed as a function of time. In particular, a high intensity emission feature at ≈ 395 eV develops, which shifts to lower emission energies for increasing delay times. Assuming an exponential decay with a core hole lifetime of 5.7 fs (as determined for the N_2 molecule [136]), a weighted sum of the calculated snapshot spectra is plotted in green in Fig. 4.3.1 ("dyn. calc."), revealing a reasonable agreement with the experimental data. The emission feature at 395 eV is thus attributed to proton dynamics [60]. A similar good agreement with the measured x-ray emission spectrum of the aqueous solution of glycine at pH 6.5 was achieved by a weighted sum of the ground state calculations of glycine at pH 6.5 (NH_3^+) and pH 12.7 (NH_2). With this approach, the emission feature at ≈ 395 eV could be attributed to transitions involving the NH_2 lone pair orbital [60].

With the discussion of the N K edge of solid-state glycine and the O K edge of gas-phase methanol in Sec. 3.2 examples for dynamical effects were given and the consequences they have for the interpretation of the electronic structure with x-ray emission spectroscopy were pointed out. Their significance was already speculated in the pioneering study of glycine by Gråsjö *et al.* [58] and corroborated by other work on a series of different sample systems [59, 60, 77, 79, 172]. In the following section, it will be shown that for glycine and its small derived peptides in the solid state such dynamics are observed in the whole excitation energy region where N K XES intensity is detected. Furthermore, the changes in the electronic structure when going from glycine to its derived peptides are examined by comparing the RIXS maps at the N K and O K edge of glycine, diglycine, and triglycine.

4.2 The electronic structure of glycine's smallest peptides

To get from a single amino acid to peptides and proteins, the individual amino acids are linked together by the formation of “peptide bonds” [173]. These bonds are the result of the connection of the amino group of one amino acid with the carboxyl group of the next amino acid [146, 173]. The actual peptide bond connects the carbon of the former carboxyl group and the nitrogen of the former amino group. A water molecule is set free and a double bond is formed between the carbon and the remaining oxygen atom of the carboxyl group. By repeating this process, bigger peptides and proteins are formed, still having one amino group at the one end and a carboxyl group at the other end of the chain. The schematic chemical structures of glycine, diglycine, and triglycine in their zwitterionic charge state are depicted in Fig. 4.4. Since the two latter can be “built” by combining two or three glycine molecules (being the smallest amino acid), respectively, it is obvious that diglycine is the smallest possible peptide. The amino group of the peptides is protonated (NH_3^+) and the carboxyl group is deprotonated (COO^-) in the zwitterionic state.

In the first part of this section (Sec. 4.2.1), the N K edge emission of the three molecules will be analyzed and compared. In a simple model, the XES spectrum of triglycine will be approximated by using only the measured spectra of glycine and diglycine and combining them in a “building block” approach. Such an approach is widely used in the XAS community [63, 153, 154, 157] and was already successfully applied for XES and RIXS by our group to the amino acid cysteine [61] (and mentioned in an earlier RIXS study of poly(phenylenevinylene)s [174]). It will be shown that the atom- and site-selective character of RIXS can be used to explicitly distinguish between the emission of the nitrogen atoms forming a peptide bond and the nitrogen in the amino group. This opens the door for a more detailed analysis of local changes induced in the electronic structure by the physical surrounding, for example, the localization of the interaction between diglycine molecules in aqueous solution with different dissolved ions in Sec. 5.3.

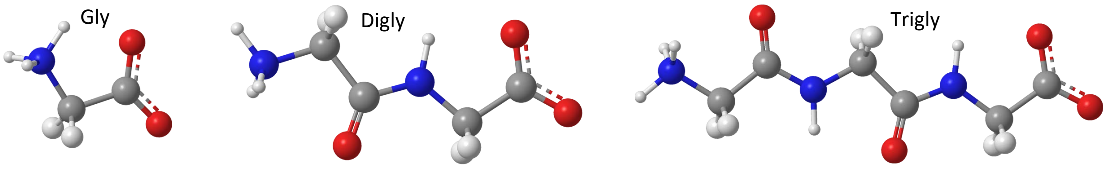

FIGURE 4.4. Chemical structure of the zwitterions of glycine (left), diglycine (middle), and triglycine (right). The amino group is protonated (NH_3^+), the carboxyl group is deprotonated (COO^-), respectively.

4.2.1 The N K x-ray spectra of glycine and its dimer

Non-resonantly excited N K XES spectra of the three molecules are depicted in Fig. 4.5.1. The spectrum of glycine (red) corresponds to the one shown in Fig. 4.2.2. Diglycine is plotted in blue, triglycine in black, respectively. In this chapter, this color code will be used where applicable for the reader's convenience. The spectra were measured using an excitation energy of 419.3 eV and normalized to the integrated emission intensity in the displayed energy range of 380 - 400 eV. Compared to the spectrum of glycine, a new emission feature can be observed for the peptides at 386.8 eV and a very prominent peak arises with a maximum intensity at an energy of 395.8 eV. For Trigly, the two new features exhibit a higher relative intensity than for Digly, corroborating that these two features can be ascribed to transitions into core holes of the nitrogen atoms in the peptide bond [note the bigger fraction of these "peptide nitrogens" for Trigly (2/3) compared to Digly (1/2)]. On the low-energy side, the peak at 395.8 eV exhibits a shoulder, which exactly overlaps with the sharp peak in the glycine emission. Since this peak was attributed to nuclear dynamics in Sec. 4.1, it is very likely (and expected) that the protonated amino group of the two peptides undergoes ultrafast dissociation, too. In his PhD-Thesis [175], Frank Meyer showed that for all 20 naturally occurring amino acids, independently of size and chemical structure of the side chain, a dissociation of the protonated amino group can be observed upon non-resonant excitation, which further strengthens this interpretation.

Assuming that the N K XES spectrum of diglycine can be interpreted as a superposition of transitions into core holes at the amino nitrogen and the peptide nitrogen, respectively, and that the local electronic structure at the amino group does not (or only slightly) change, the peptide contribution can be separated using the spectra of glycine as a reference for the amino nitrogen emission. After normalizing the spectra to the integrated emission intensity in the emission energy range from 380 - 400 eV, the subtraction "Digly - 0.5×Gly" is calculated, resulting in the orange spectrum in Fig. 4.5.2. As it was expected based on the comparison of the spectra in Fig. 4.5.1, the spectra of the "peptide bond" exhibits a very intense feature at 395.8 eV and a distinct peak at 386.8 eV. Another peak can be observed at 391.9 eV which stands out from the otherwise rather featureless emission.

Following the "building block" approach, one should be able to form a reasonable spectrum of triglycine by a superposition of the emission of one amino nitrogen and two peptide nitrogens (see Fig. 4.5.4). Thereby, the emission spectra of the two peptide nitrogens are assumed to be indistinguishable or at least very similar, which seems valid since their chemical environment in the triglycine molecule differs only in the third next neighboring atoms. This superposition is shown in Fig. 4.5.3. The (scaled) sum of "Gly + 2×Peptide bond" is plotted as a green curve in comparison

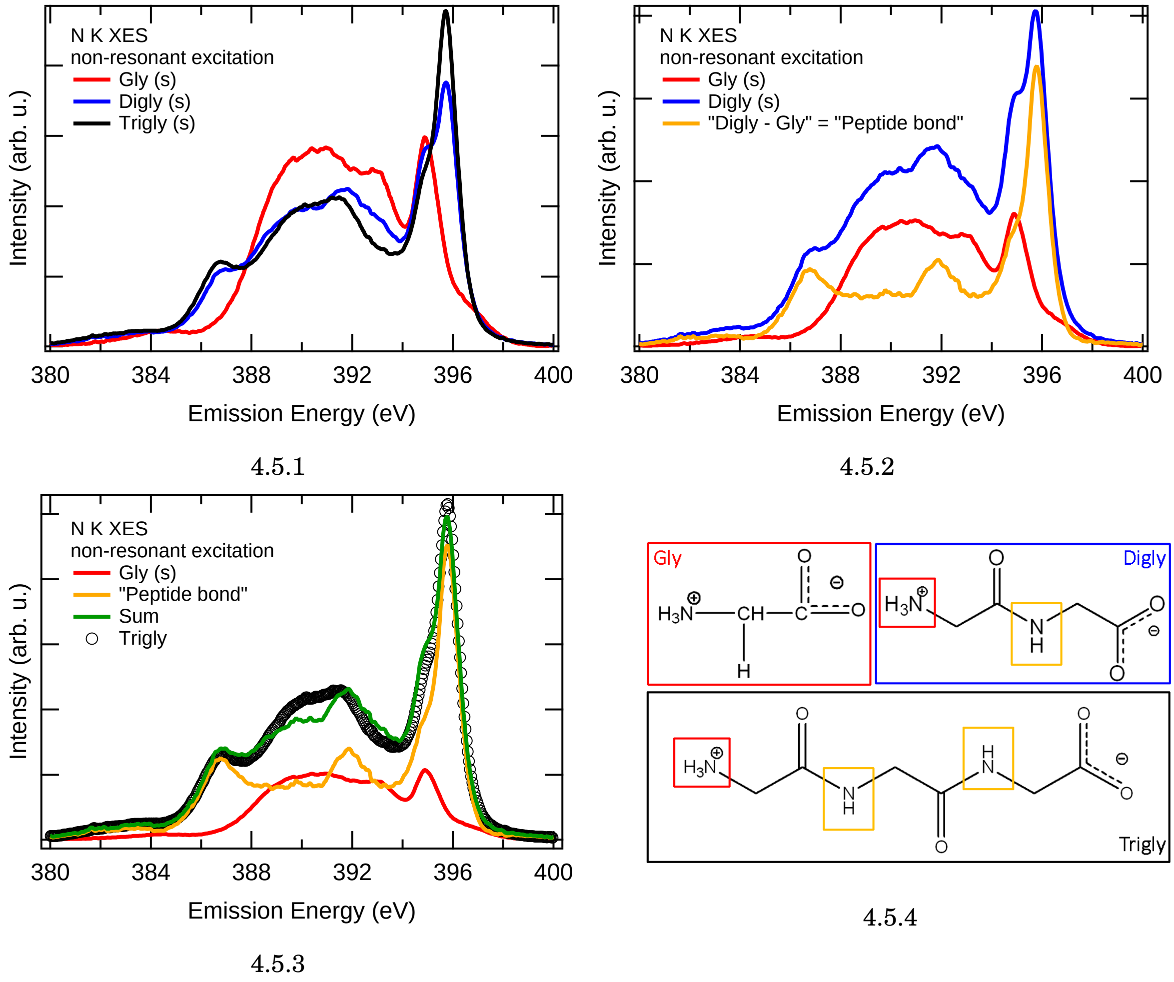

4.5.1

4.5.2

4.5.3

4.5.4

FIGURE 4.5. Non-resonantly excited N K XES spectra of glycine (red), diglycine (blue), and triglycine (black) in solid state. By subtracting the (1:2 weighted) spectrum of glycine from the spectrum of diglycine, the contribution of emission originating from transitions into the nitrogen atom in the peptide bond can be isolated (orange, 4.5.2). A suitable weighted (1:2) linear combination of glycine and the "peptide bond" results in the green spectrum in 4.5.3, reproducing the measured spectrum of triglycine with the exception of the region around 390 eV. Panel 4.5.4 shows the structural formulas of the three molecules with boxes according to the used color code to illustrate this "building block" approach.

to the measured spectrum of triglycine, represented by black circles. The two used contributions are shown as well. As can be seen, even though the applied model seems to be rather simple, the agreement of the calculated spectrum with the measured data is very good. All prominent emission features in the measured spectrum are reproduced by the model spectrum with reasonable relative emission intensities.

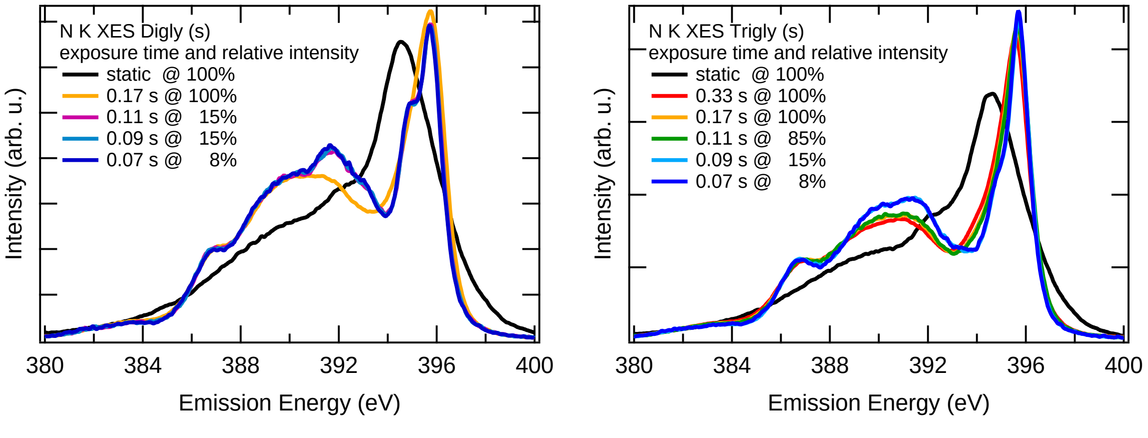

4.6.1

4.6.2

FIGURE 4.6. N K XES spectra of solid-state diglycine (4.6.1) and triglycine (4.6.2), recorded with the given values for exposure time of each sample spot and excitation intensities. The black spectra represent the static measurement, i.e., a completely decomposed sample, whereas the dark blue spectra were recorded with the best possible parameters.

Deviations, however, can be found in the energy region from ≈ 389 - 391.5 eV. There, the modeled spectrum exhibits clearly less emission intensity and more defined emission features than the measured spectra. Potentially, these differences are caused by irradiation induced damage: The intense and highly focused synchrotron beam causes an irreversible decomposition of the molecules. To avoid this, the exposure time and intensity of the exciting beam have to be reduced to a preferably non-destructive amount. How this was done for the studied molecules will be discussed in more detail in the following in conjunction with Fig. 4.6.

The setup described in Sec. 2.3 allows to continuously move the sample in the plane perpendicular to the exciting beam. By doing this, the probed sample volume is continuously replenished. Thereby, the scanning pattern was designed in such a way that every single sample spot is irradiated only once to constantly obtain a completely fresh sample. By varying the scanning speed one can thus reduce the exposure time for each sample spot. With an vertical width of the exciting beam of approx. 30 μm on the sample the exposure time can be estimated based on the used scanning speed. The intensity of the exciting beam can be reduced by closing several apertures in the beamline. In this work, the entrance and exit slit of the monochromator were used to do this. The change in intensity can be estimated based on the photo current measured at a gold-coated mesh in the beam trace downstream of the mentioned slits. Assuming that the intensity of the exciting beam on the sample surface changes proportional to the measured photo current the changes of the intensity can be quantified.

Fig. 4.6 shows a series of N K XES spectra of diglycine (4.6.1) and triglycine (4.6.2), measured with different exposure times (i.e., scanning speeds) and excitation intensities as indicated, respectively. The given values for the intensity relate to the maximum intensity used in the respective measurement series. All spectra were normalized to the integrated emission intensity in the emission energy range of 380 - 400 eV. The black curves represent the spectra recorded without scanning the sample, i.e., static, after an exposure time of more than five minutes. Since the spectra didn't change as a function of time while measuring (not shown), the probed sample volume in these spectra can be regarded as completely decomposed. For diglycine (4.6.1), all "scanned" spectra have a clearly different shape than the static spectrum and look very similar compared to each other, except the spectrum measured with an exposure time of 0.17 s and the maximum intensity (orange). In this spectrum, the low-energy shoulder of the intense peak at 395.8 eV is smeared out and not as pronounced as in the other spectra. On the high-energy side the peak is slightly broader. For emission energies of about 391 - 393 eV, the distinct feature that can be observed for the other spectra is not present. As was mentioned above, the other spectra, recorded with shorter exposure times and especially lower excitation intensities, don't show any trend as a function of the used measurement parameters. The parameters of the dark blue spectrum represent the minimum limits of the setup for feasible scanning speed of the sample and reasonable excitation intensities for recording a XES spectrum.

In the case of triglycine (4.6.2), the situation is quite similar. All scanned spectra differ clearly from the static spectrum, since beam induced degradation effects are reduced. However, a trend in the spectral shape can be observed when going from longer exposure times and higher intensities (e.g., the red spectrum) towards the dark blue spectrum representing the best possible measurement conditions. The high-energy side of the intense peak gets slightly narrower and the low-energy shoulder gets more defined. At the same time, the peak maximum slightly shifts to higher emission energies. Also the feature at 386.8 eV gets sharper. The energy region of approx. 389 - 393 eV gains in relative emission intensity and features start to evolve and get more defined. However, the peak at 391.4 eV does not reach a clear and outstanding shape as it is the case for diglycine, even not at best possible measurement conditions. This might point towards a bigger contribution of emission from at least partially degraded triglycine molecules to the XES spectrum than it is the case for diglycine. This interpretation is corroborated by the optical changes made to the powder samples while measuring. Whereas the sample spots which were irradiated during the measurement of the blue spectra for diglycine could not be distinguished in terms of color, the triglycine sample showed a slightly yellow color (compared to the white, non-irradiated sample areas), even for minimum exposure times and excitation intensity.

The big deviation of the green, modeled spectrum from the measured triglycine spectrum in Fig. 4.5.3 thus can likely be attributed to a bigger contribution of emission of degraded molecules in the case of triglycine. Since it is now clear that especially a reduced excitation intensity helps to improve the quality of the recorded spectra, all measurements performed in this chapter were recorded with low excitation intensities and short exposure times. To find a reasonable balance of time and sample area needed to record a spectrum and the signal-to-noise ratio of the resulting data, the parameters corresponding to the spectra depicted in light blue were used. Note that the best possible measurement parameters (dark blue spectra) did not improve the quality of the data but increased the needed sample area and measurement time significantly.

By comparing the measured spectra of glycine, diglycine, and triglycine some information about the changes in the electronic structure can be gained. To shed more light on the detailed changes, density functional theory calculations were performed for isolated Digly and Trigly molecules in their zwitterionic state. The structures used as an input are taken from Refs. [176, 177]. Prior to the transition calculations, a geometry optimization was performed to achieve convergence in the self-consistent-field iteration. The final structures are shown in Fig. 4.7 adjacent to the experimental spectra depicted in blue and black for diglycine and triglycine, respectively. Vertical bars represent the results of the calculation. Referring to the discussion of the N K XES spectrum of glycine (see Sec. 4.1) and the occurrence of proton dynamics at the amino group, it is clear that these calculations are not able to reproduce the experimental spectra to a satisfying amount. Therefore, broadened spectra as for the glycine molecule in Sec. 4.1 are not shown. Instead, the calculations for the transitions into the different core holes are compared to the spectral contributions from Fig. 4.5. That is, the calculations for the transition into the amino nitrogen core holes (N1, black bars) are compared to the measured Gly spectrum (red curve), whereas the calculations for the peptide nitrogens (red and blue bars) are compared to the difference spectrum of "Digly - 0.5×Gly" (orange). For diglycine, the calculation was shifted by +0.7 eV for both core hole transitions to align it with the experimental data (i.e., with the most prominent peak at approx. 395.8 eV). Selected transitions are labeled with respect to the participating occupied MO. Some selected occupied MOs of the diglycine zwitterion are depicted in Fig. 4.7.3, which will be qualitatively discussed and compared to the molecular orbitals of the glycine zwitterion in the following. A collection showing the 20 highest occupied MOs of diglycine next to the MOs of glycine is given in Fig. A.1 in the appendix.

One can notice that some of diglycine's MOs show a striking resemblance to a specific MO of the glycine zwitterion. For example, the diglycine's HOMO, HOMO-1,

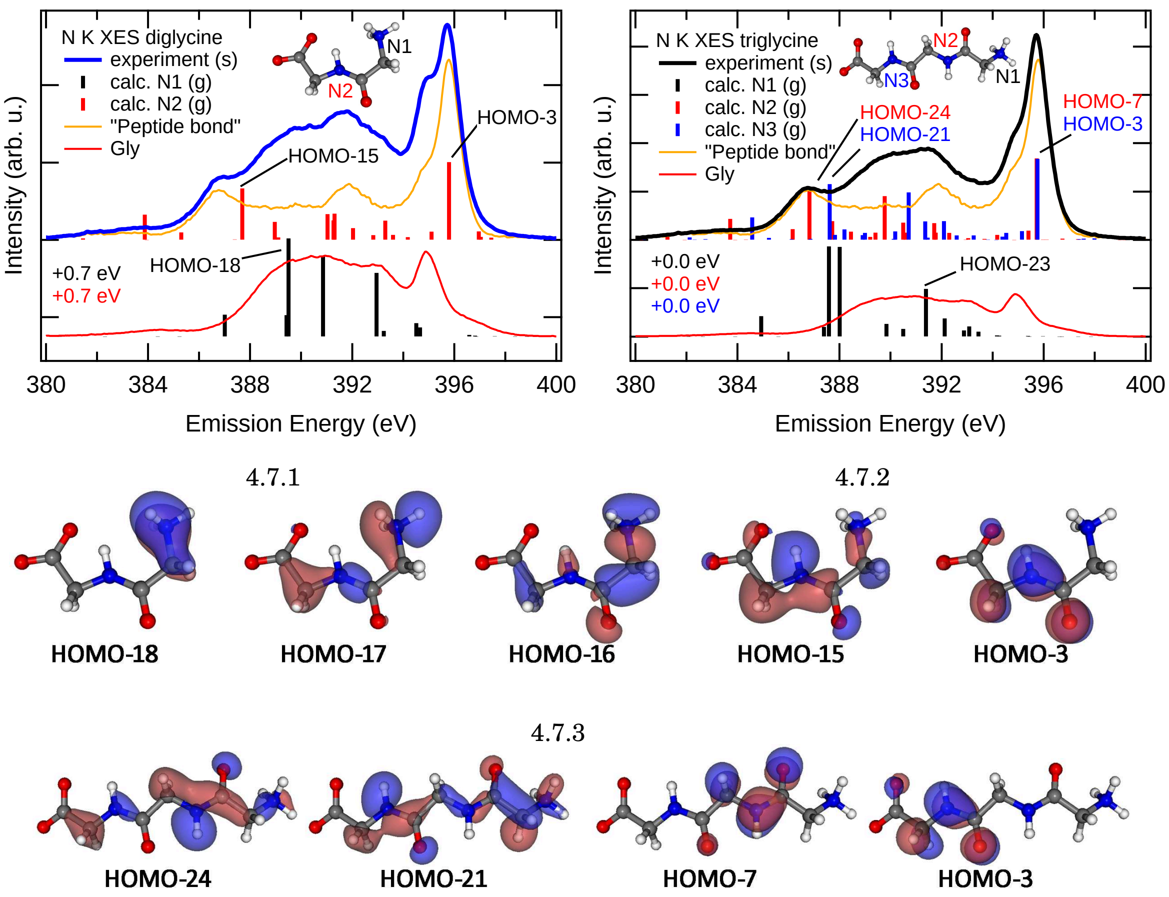

4.7.1

4.7.2

4.7.3

4.7.4

FIGURE 4.7. N K XES spectra of diglycine (blue, panel 4.7.1) and triglycine (black, panel 4.7.2) in comparison to DFT calculations, which are represented by vertical bars. The geometry of the zwitterions used for the calculation are depicted next to the spectra with labels for the different nitrogens (N1-N3). The calculations of the N1 transitions are compared to the experimental spectrum of glycine (red). For the transitions into peptide nitrogen core holes (N2, N3) the difference spectrum of "Digly - 0.5×Gly" (orange) is given as a reference. Selected transitions are labeled with respect to the participating molecular orbital. Panels 4.7.3 and 4.7.4 show isodensity surfaces of selected MOs of diglycine and triglycine, respectively.

and HOMO-2 together with the HOMO-5 to HOMO-7, having a strong O 2p character and being localized at the carboxyl group, have a structure that is very similar to the 6 highest occupied MOs of the glycine zwitterion. Likewise, the orbitals HOMO-13, HOMO-14, and HOMO-16 to HOMO-18 of diglycine bear a strong resemblance to the HOMO-6 to HOMO-10 of glycine in terms of localization at the amino nitrogen and N 2p character. Consequently, the orbitals HOMO-16 to HOMO-18 show high emission intensities in the N K spectrum of diglycine (see bottom spectrum in Fig. 4.7.1). In addition to the MOs with an equivalent for the glycine molecule, a set of new orbitals is found for diglycine. Most of them have a predominant 2p character of either the peptide nitrogen, the peptide oxygen, the peptide carbon, or a combination of these. The MOs with the highest localization at the peptide nitrogen and strongest N 2p character are the HOMO-3 and the HOMO-15. Accordingly, they show the highest emission intensities of all N2 transitions. The HOMO-3 forms the strong feature at 395.8 eV, the HOMO-15 might be the participating orbital leading to the feature at 386.8 eV, albeit the calculation does not exactly reproduce its energetic position.

The assignment of the HOMO-3 to the emission feature at 395.8 eV can be confirmed by comparing with the calculation of the triglycine molecule (Fig. 4.7.2). The number of atoms of course increases the number of molecular orbitals for triglycine. However, similar comparisons as performed for the diglycine MOs can be drawn. For example, the HOMO-7 exhibits an overall shape similar to the HOMO-3, albeit localized at the other peptide bond of the triglycine molecule (see panel 4.7.4). They both have a very similar structure compared to the HOMO-3 of diglycine and lead to transitions of similar emission energy. Likewise, the HOMO-24 and HOMO-21 are very similar. Since their structure is comparable with the HOMO-15 of diglycine and their emission energy is close to the emission feature at 386.8 eV, the assumption made for diglycine regarding its origin is corroborated by the calculation of triglycine as well. Note that the calculation of triglycine was not shifted in energy. The statements given above regarding the character and localization of distinct MOs also apply in a similar way to the O K spectra which are discussed in Sec. 4.2.2.

Having discussed the non-resonant N K XES spectra of glycine and its smallest peptides, the N K RIXS maps of these molecules are now addressed. They are shown in Fig. 4.8. Starting with the RIXS map of glycine (Fig. 4.8.1), one can observe that the overall emission structure does not change significantly with excitation energy. Only small variations in width and relative intensities are found, especially in the absorption onset region from 403 - 406 eV. The distinct feature at an emission energy of ≈ 395 eV is observed throughout the whole map, indicating that nuclear dynamics (as discussed in Sec. 4.1) occur nearly independent of excitation energy. The observation that this peak starts to rise at slightly higher excitation energies than the other

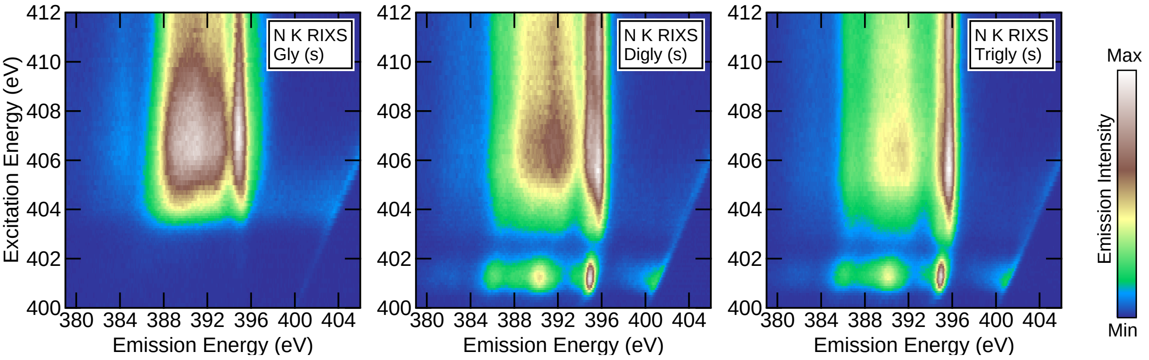

4.8.1 4.8.2 4.8.3

FIGURE 4.8. N K RIXS maps of solid-state glycine, diglycine, and triglycine.

emission features was nicely elaborated by Blum *et al.* for an aqueous solution of glycine [60] for which this is observed equally. The main reason for this "delay" can be attributed to the duration of the scattering process. Reducing the excitation energy below the absorption onset also reduces the duration time of the scattering process [66]. Thus, also the spectral components indicative for dissociation processes decrease. This means that for resonant excitation below the absorption onset, the scattering time is not sufficient for a dissociation of the molecule. This is corroborated by the dynamical calculations in Fig. 4.3.2, showing that the feature at ≈395 eV slowly develops with increasing delay time between the excitation and emission process.

For diglycine and triglycine, the spectral components attributed to proton dynamics at the amino group are also observed throughout the whole excitation energy range starting at the absorption onset of the amino nitrogen. The development of the feature at 395 eV can nicely be followed for excitation energies around ≈ 404.5 eV in the respective RIXS maps. The color code also nicely shows the difference in relative emission intensities when comparing, e.g., the emission at ≈ 395.8 eV with the region from 386 - 394 eV between diglycine and triglycine. Since the feature at 395.8 eV is attributed to transitions into peptide nitrogen core holes, it is clear that this feature exhibits a higher relative emission intensity for the molecule with a bigger portion of peptide nitrogens, i.e., triglycine. When comparing the RIXS maps of diglycine (4.8.2) and triglycine (4.8.3) with glycine a striking difference is observed in the pre-edge. More precisely, emission intensity is observed at an absorption resonance centered at an excitation energy of 401.3 eV with noticeable vibrational loss features at the low-energy side of the Rayleigh line. In addition, the main absorption onset is located at slightly lower excitation energies. Since these features are observed only for the peptides and not for the glycine molecule, they can be attributed to an excitation of a core hole in a peptide nitrogen. This is elaborated in more detail in conjunction with Fig. 4.9.

Panel 4.9.1 shows the N K XAS spectra of the three samples. They were calculated by integrating the spectator emission intensity in the RIXS maps of Fig. 4.8 in the energy range of 384 - 398 eV for each excitation energy. After subtracting a constant background at 399 eV, the spectra were normalized to the maximum. The main resonance at ≈ 406 eV has been assigned to N 1s → σ^* transitions [55, 151, 154]. The pre-edge feature at 401.3 eV, which is present only for the peptides, is attributed to N 1s → $\pi^*_{C=ONH}$ transitions, with "$C = ONH$" indicating the peptide bond [55, 151, 154]. The higher fraction of peptide nitrogen atoms in triglycine leads to a higher relative intensity compared to diglycine in this resonance. Another broad peptide resonance at 413 eV was identified in literature [154], which explains the higher intensity at higher excitation energies for diglycine and triglycine with respect to glycine. For triglycine, a small additional feature at 410.2 eV with a not further defined origin is found.

As can be clearly seen when comparing the three XAS spectra, the onset of the main absorption resonance shifts towards lower excitation energies for an increasing number of peptide bonds. This can be explained by absorption resonances of the peptide nitrogens in this energy region. To support this statement, calculated XAS spectra of the three molecules are compared to the experimental spectra in panels 4.9.2 - 4.9.4. The calculations are represented by vertical bars. The labels N1-N3 correspond to the nomenclature introduced in Figs. 4.2 and 4.7. For a better comparability, the calculated spectra were broadened using Gaussian profiles. To minimize the amount of used parameters, the width of the LUMO transitions are set equal within each set of calculations for diglycine and triglycine. The widths of the higher absorption resonances are increased linearly with excitation energy. The resulting spectra are depicted as green curves. The calculations for the individual core holes were shifted in energy by the given values to fit the main absorption onset and especially the pre-edge feature. Note that for triglycine the three sets of transitions are shifted by the same offset of -1.25 eV whereas for diglycine two different shifts (N1: -1.9 eV, N2: -1.1 eV) are used to describe both the pre-edge feature and the main absorption onset. One can only speculate if this deviation of 0.8 eV can be explained by a physical effect. The calculation is performed for an isolated molecule, thus interactions with the surrounding are not included. Since the molecule is in the zwitterionic charge state in the solid, the interaction with the surrounding predominantly takes place at the charged functional groups rather than at the peptide bond which might explain the shift in energy. As was already elaborated by comparing the XAS spectra of the three samples, the calculation unambiguously confirms that the pre-edge feature can be attributed to excitations at the peptide nitrogens. In addition, both calculations for diglycine and triglycine exhibit absorption resonances related to the peptide nitrogens in the energy region from ≈ 403 - 405 eV, leading to the discussed shift of the main

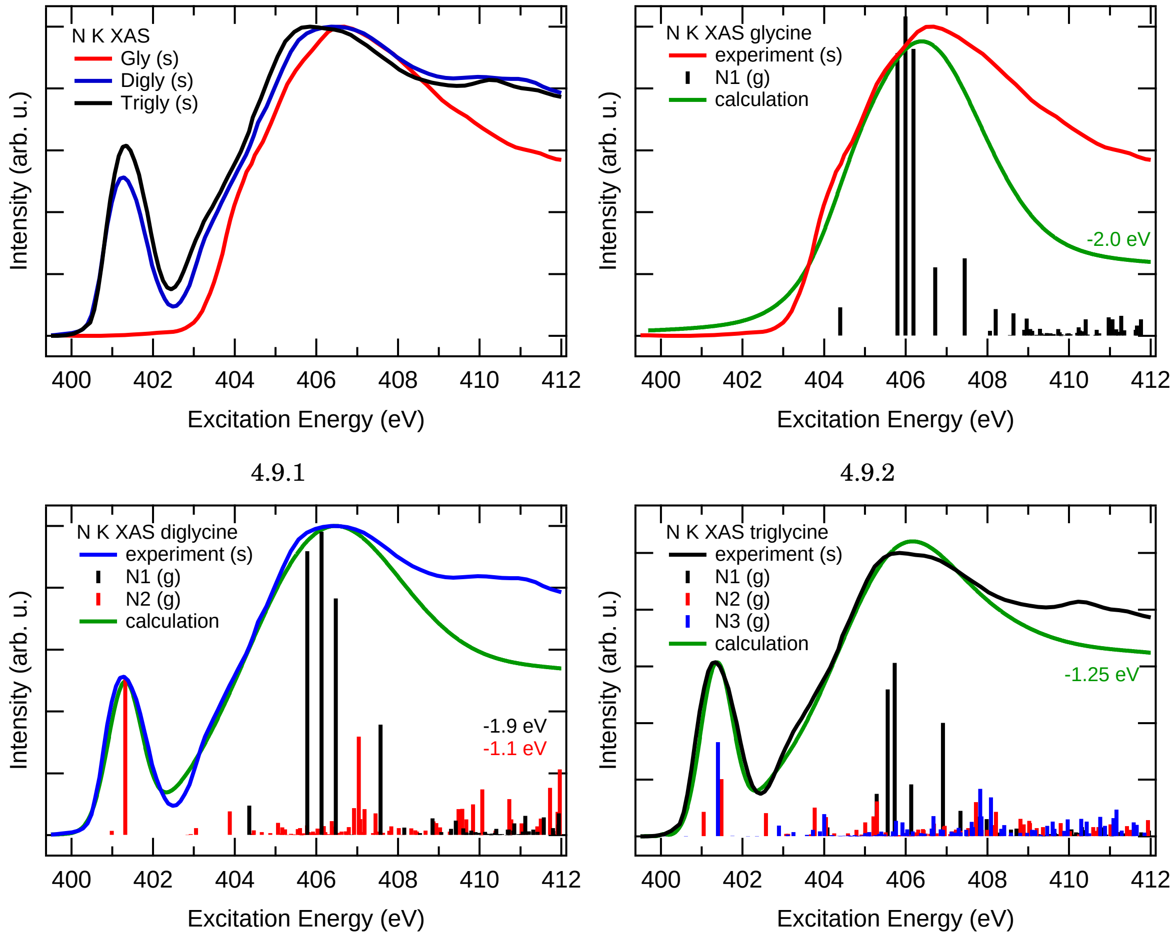

4.9.1

4.9.2

4.9.3

4.9.4

FIGURE 4.9. N K XAS Spectra of solid-state glycine (red), diglycine (blue), and triglycine (black) in comparison with each other (4.9.1) and with DFT calculations (4.9.2-4.9.4). The calculations of the individual core holes (N1-N3) are broadened with Gaussian profiles (dashed lines), resulting in the green curves. The calculations were shifted by the given values to align them with the pre-edge feature and the main absorption onset of the measurement.

absorption onset towards lower excitation energies for the peptides.

Knowing that the pre-edge feature stems from excitations of peptide nitrogens only, the resonant XES spectra at this resonance are analyzed in Fig. 4.10. Supplementary to the measured spectra, the difference spectrum “Digly - 0.5×Gly” is given (orange), however, shifted by -0.8 eV to account for spectator shifts for better comparability. Note that a shift of -0.8 eV leads to the best overall agreement, while the shifts of individual emission features, however, may vary. All spectra (except the one of glycine which does not show any emission intensity) are normalized to the integrated emission intensity

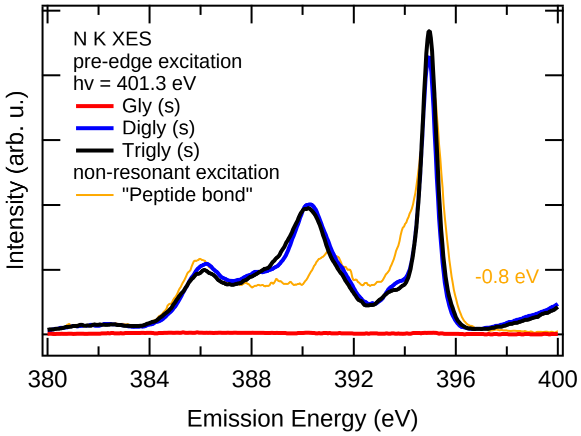

FIGURE 4.10. N K XES spectra of glycine, diglycine, and triglycine, resonantly excited at the pre-edge resonance with 401.3 eV. The difference spectrum representing the peptide bond contribution to the non-resonant spectra is given for comparison and shifted by -0.8 eV to account for spectator shifts.

in the displayed emission energy region for presentation. The spectator emission of the peptides on this absorption feature clearly differs from the non-resonant spectra (Fig. 4.5.1) and the rest of the RIXS maps at higher excitation energies. However, the difference between the spectra of Digly and Trigly is marginal. Keeping spectator shifts and the angular anisotropy of the RIXS process in mind, they both still bear an astonishing resemblance with the difference spectrum calculated for *non-resonant* excitation. Almost every emission feature found in the resonantly excited spectra is also present in the difference spectrum with comparable relative emission intensities. At 390 eV, however, a comparatively high deviation is observed with the resonant spectra exhibiting a significantly higher relative emission intensity.

Concluding the section about the N K emission, one can state that RIXS allows to separate the XES contributions of the chemically non-equivalent N atoms in the peptides. In the present case, the nitrogen atoms in the peptide bonds can be selectively excited by tuning the excitation energy to the first absorption resonance, albeit, a differentiation between the two nitrogen atoms N2 and N3 (for triglycine) is not possible. For non-resonant excitation, the separation of different XES contributions is more difficult. The comparison in Fig. 4.10, however, shows that the building block approach can lead to reasonable results.

4.2.2 O K emission and absorption of glycine and diglycine

The non-resonantly excited XES spectra of glycine, diglycine, and triglycine at the O K edge are shown in Fig. 4.11.1, normalized to the integrated emission intensity in the shown emission energy region from 516 - 530 eV. In contrast to the big differences at the N K edge, the oxygen emission spectra of the peptides show strong similarities to the one of glycine. The highest emission intensity is observed at 526.8 eV, i. e., no shift between the different samples occurs. For the peptides, however, the low-energy side of this feature is slightly broader. Whereas a slightly reduced intensity at ≈ 525 eV is detected for glycine, the peptides both show a similar emission intensity for emission energies from ≈ 522 - 525.8 eV with a minor feature at ≈ 523.8 eV.

Further information for the interpretation of the spectra can be gained by the DFT calculations of the isolated zwitterions shown in panel 4.11.2 (diglycine) and 4.11.3 (triglycine). The results of the calculations are represented by vertical bars. The color code refers to the excitation of different O 1s core holes in the oxygen atoms O1-O4, as they are labeled in the molecule schemes. For a better comparability, the calculation was broadened using Gaussian profiles, resulting in the green curve. To minimize the used parameters for broadening the calculation, the width was increased linearly with decreasing emission energy. The width for the HOMO transitions and the slope are chosen to be identical for every set of core hole transitions. The calculation was aligned by a constant shift in energy of +0.45 eV for diglycine and +0.6 eV for triglycine, respectively. Despite the limited number of parameters, the calculations describe the main features in the spectra. The fine structure in the spectra, however, is not reproduced. The calculations reveal that the origin of the intense feature at 526.8 eV lies in the molecular orbitals which consist mainly of the lone-pair orbitals of the individual oxygen atoms for both molecules. Note that not only the oxygen atoms of the carboxl group, but also the peptide oxygens equally contribute to this emission feature. Also the emission intensity at lower emission energies stems from transitions into all oxygen core holes. Hence, the strong similarities between the three XES spectra of glycine and the two peptides at the O K edge are not surprising.

By comparing the calculations of the peptides with the one for glycine in Fig. 4.2.1 one can notice that the O1 and O2 transitions in the emission energy range from ≈ 521 - 525 eV are shifted to slightly higher emission energies and are not able to reproduce the emission feature at 522.5 eV found in the spectrum of glycine. For a better agreement, the energy scale would have to be stretched by about 20%. Due to this uncertainty it is not possible to attribute further emission features (e.g, at 523.8 eV) to distinct molecular orbitals. Since the density of transitions is rather high in this energy region, a superposition of several transitions leading to this emission feature is likely. Note that the energetic position of each series of transitions into the

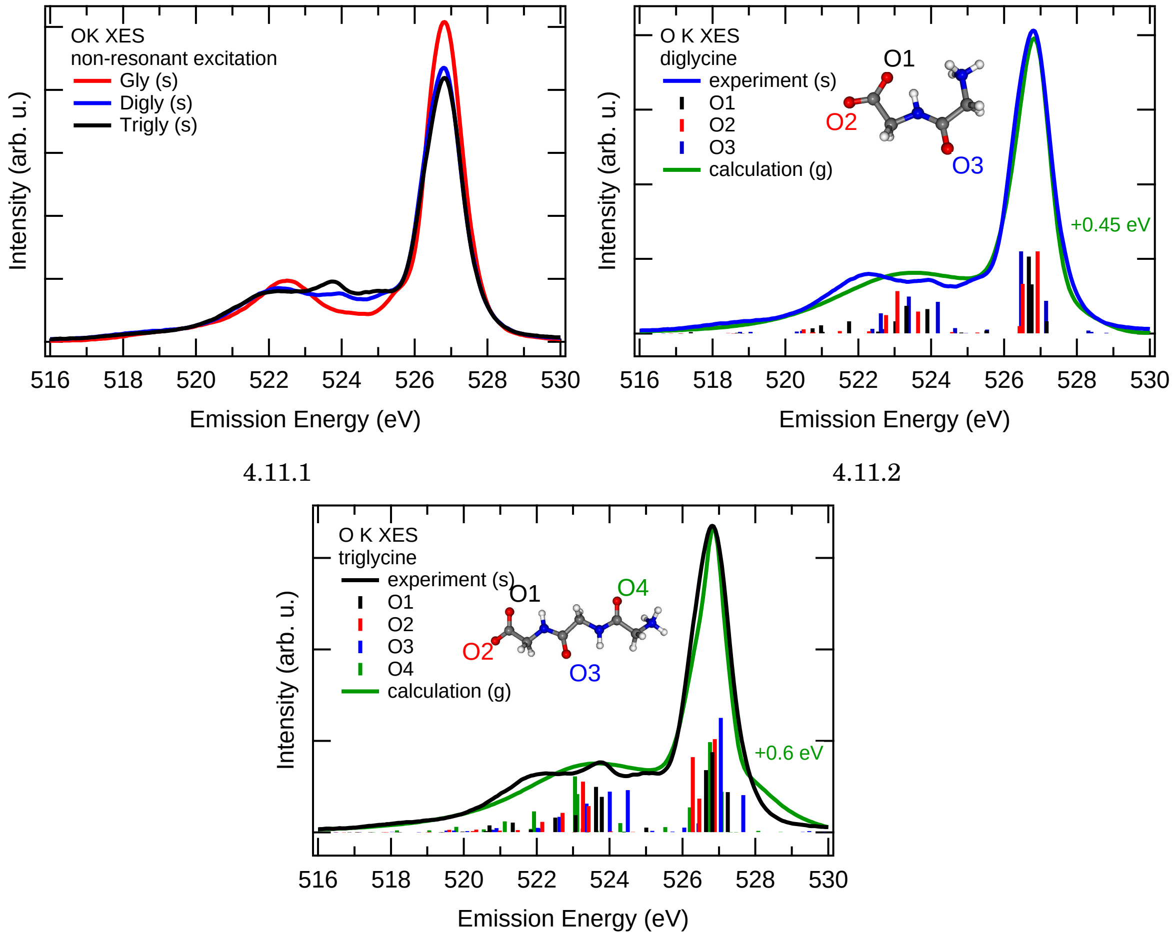

4.11.1

4.11.2

4.11.3

FIGURE 4.11. O K XES spectra of solid-state glycine (red), digylcine (blue), and triglycine (black), excited with 547.4 eV. The spectra of diglycine and triglycine are compared to DFT calculations of the depicted isolated molecules in the zwitterionic state, represented by vertical bars in panels 4.11.2 and 4.11.3, respectively. The calculations were broadened with Gaussian profiles (see text for details) resulting in the green curve and shifted by the given values to align them with the experimental data.

same core hole is determined by the calculated core hole binding energy which differs between the oxygen atoms. For the two oxygen atoms in the deprotonated carboxyl group, the difference in the core hole binding energy of O1 and O2 was calculated to be ≈ 0.2 eV for glycine, which is reproduced in the calculations for diglycine (≈ 0.2 eV) and triglycine (≈ 0.3 eV). The core hole binding energies of the peptide oxygens, however, is calculated to be significantly higher by ≈ 1.6 eV for diglycine and ≈ 2.6 eV (O3) and ≈ 3.7 eV (O4) for triglycine compared to O1, respectively. In XPS experiments, no such differences in core hole binding energies for the different oxygen atoms can be

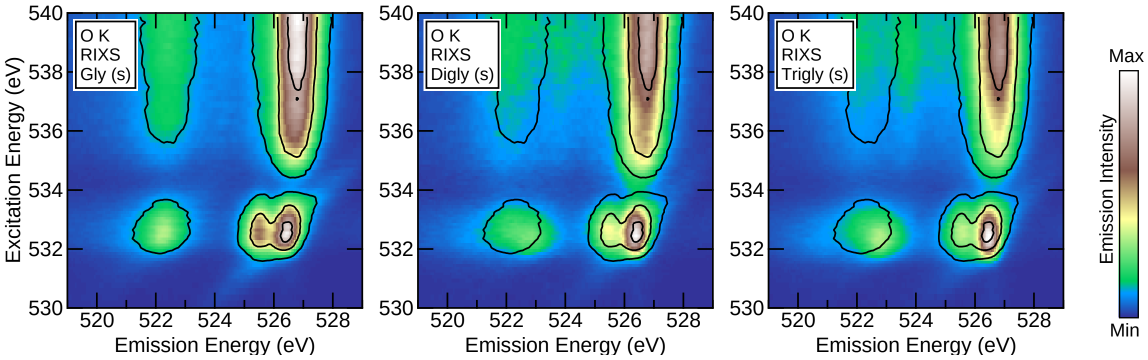

4.12.1 4.12.2 4.12.3

FIGURE 4.12. O K RIXS maps of solid-state glycine (4.12.1), diglycine (4.12.2), and triglycine (4.12.3). Black contours represent the glycine measurement for a better comparability.

observed [161]. Accordingly, the big differences in the core hole binding energies of the individual oxygen atoms can likely be attributed to an artifact of the calculation. Note that the calculation is done for an isolated molecule in the zwitterionic state. Thus, the molecule exhibits a complex charge distribution which is a big challenge for density functional theory calculations. At least the trend between carboxyl and peptide oxygens can be explained. Since the carboxyl group is deprotonated in the zwitterionic state, a positive charge is "removed" from the functional group, leaving an additional negative charge close to the carboxyl oxygens behind. Accordingly, the binding energy of the electrons in this moiety of the molecule is reduced on average and the core hole is lifted in energy.

The results for resonant excitation of the O K edge are displayed in Fig. 4.12. Additionally to the color coded emission intensity, black contours in the RIXS map of glycine (4.12.1) mark regions with the same emission intensity. For comparison of the three RIXS maps, the same contours (for glycine) are also added to the RIXS maps of diglycine and triglycine in panels 4.12.2 and 4.12.3, respectively. Similar to the non-resonant excitation, the RIXS maps of the three molecules bear striking resemblance. For excitation energies above 535 eV, no significant changes as a function of excitation energy are observed in either of the three maps. For excitation energies below the main absorption edge, a pre-edge feature centered at 532.8 eV is found for all samples. For excitation at this absorption resonance, the emission feature with highest intensity is shifted by -0.4 eV, having its maximum at 526.4 eV, and is sharper compared to the non-resonant excitation. An additional emission feature rises at 525.5 eV, albeit with different relative emission intensity for the three samples. Furthermore, the emission feature located at 522.3 eV for glycine changes its shape and the maximum

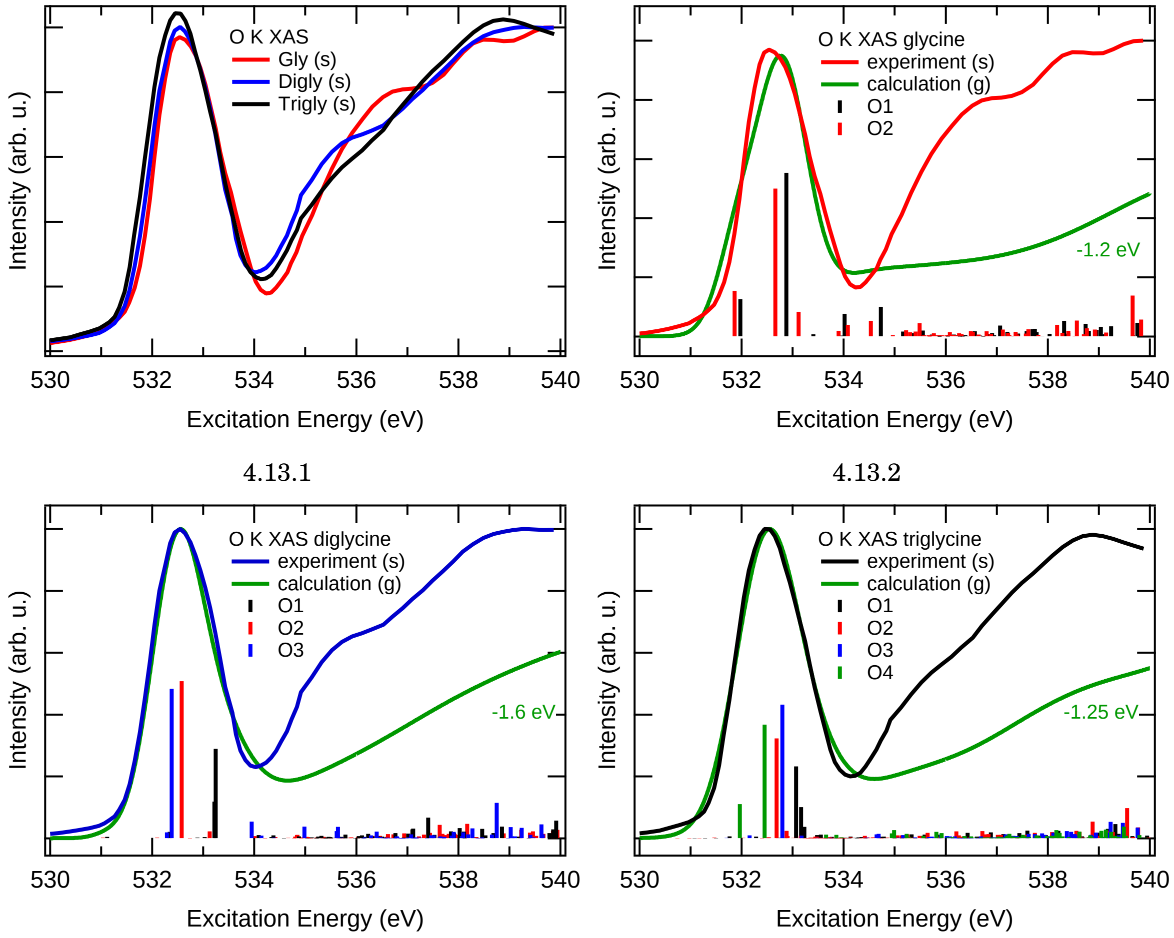

4.13.1

4.13.2

4.13.3

4.13.4

FIGURE 4.13. O K XAS Spectra of solid-state glycine (red), diglycine (blue), and triglycine (black) in comparison with each other (4.13.1) and with DFT calculations (4.13.2-4.13.4). The calculations of the individual core holes (O1-O4, see Figs. 4.2 and 4.11) are broadened with Gaussian profiles resulting in the green curves, respectively. The values on the right represent shifts used to align the calculation with the experiment.

shifts by +0.5 eV to 522.8 eV for triglycine. For diglycine, this feature is rather broad and shows a plateau centered at 522.6 eV, leading to the conclusion that at least one emission feature, which can be attributed to transitions into a peptide oxygen core hole, contributes to this peak emitting at a higher emission energy compared to the carboxyl oxygen transitions observed for glycine.

Upon closer inspection of the RIXS maps shown in Fig. 4.12, the absorption onset slightly shifts towards lower excitation energy with increasing molecular size. To demonstrate this, Fig. 4.13.1 shows O K XAS spectra of the three molecules. They were generated by integrating the intensity for emission energies from 519 - 529 eV for each excitation energy. After subtraction of a constant background they were normalized to the intensity at 539.7 eV. The spectra are dominated by the strong absorption resonance at 532.8 eV, which can be attributed to transitions of O 1s electrons to the C=O π^*-orbitals [151]. As mentioned above, a slight shift of the absorption onset towards smaller excitation energies is observed for increasing molecular, corresponding to additional O 1s → $\pi^*_{C=ONH}$ transitions at the peptide bond located at 531.9 eV [153].

These assignments are reproduced qualitatively by the calculations displayed in panels 4.13.2 - 4.13.4. The results are represented by vertical bars, color coded with respect to the participating core hole. The labels O1-O4 refer to the molecular schemes in Figs. 4.2 and 4.11. Similar to the theoretical XES spectra in Fig. 4.11, the calculations were broadened using Gaussian profiles with widths that linearly increase with excitation energy. The width for the first transition and the slope were chosen to be equal for the individual transition series of each molecule to minimize the number of parameters. The calculated spectra were shifted by the given values to align them with the experimental data. Even though some clear deviations between the calculation and the experimental data can be observed at the pre-edge for glycine (4.13.2), the pre-edge features of the peptides are reproduced very well. The higher intensity for the experimental spectra for energies above 534 eV can be explained by saturation effects, which occur for fluorescence yield detection and are not included in the calculation. As can be seen, each oxygen atom contributes to the broad absorption resonance centered at 532.8 eV to a comparable amount. Thus, a direct spectroscopic separation of the carboxyl oxygens from the peptide oxygens by choosing a suitable excitation energy is not possible.

In the following, the XES spectra resonantly excited at the pre-edge (i.e., with 532.8 eV) are qualitatively discussed. To do this, Fig. 4.14.1 displays the spectra normalized to the integrated intensity for emission energies from 516 - 530 eV. As was already mentioned in the discussion of the RIXS maps in Fig. 4.12, an additional peak (compared to non-resonant excitation) at 525.5 eV is found for all samples. Its relative emission intensity decreases with increasing number of peptide oxygens. Furthermore, the feature at 522.3 eV (for glycine) shifts towards higher emission energies, when going from glycine to triglycine. These trends can be understood when comparing the spectra to XES spectra of suitable reference molecules.

Meyer *et al.* [61] showed that the electronic structure of the amino acid cystein can nicely be described by investigating simple reference molecules which have a similar chemical structure as parts of the amino acid itself. These smaller molecules then can serve as "building blocks", e.g., representing the different functional groups of cysteine. The XES spectra of the original sample can then be comprehensively interpreted by comparing them with the references. This building block approach is commonly used

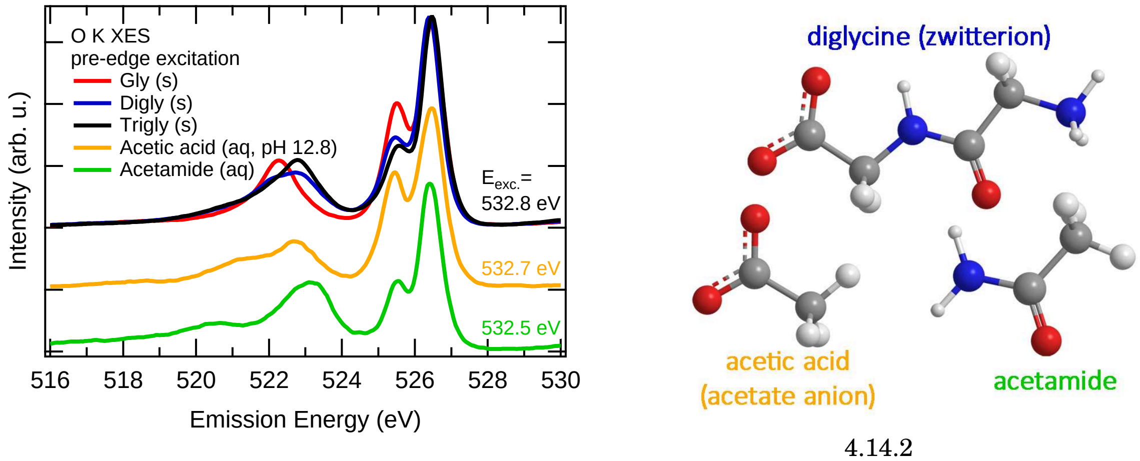

4.14.1

4.14.2

FIGURE 4.14. Resonantly excited XES spectra at the O K edge of glycine, diglycine, and triglycine compared to each other and to reference samples for the different oxygen atoms in these molecules (4.14.1). For the carboxyl group, an aqueous solution of acetic acid at pH 12.8 was used as a reference (orange). The spectrum of an aqueous soultion of acetamide (green) serves as a reference for peptide oxygens. The used excitation energies are given on the right. The schematic molecular structures of the two references are shown in panel 4.14.2 in comparison to the diglycine zwitterion.

in x-ray absorption spectroscopy [63, 153, 154, 157] and was intensively discussed for the XES spectra of the 20 naturally occurring proteinogenic amino acids in Ref. [175].

In the present case, the reference molecules were selected such that the bonding environment of the oxygen atoms is identical up to the second nearest atoms in the molecule. This ensures that the distribution of the electrons in proximity to the excited oxygen atoms is approximated to a high level and thus the local electronic structure and the resulting XES spectrum should be very similar. For the description of the deprotonated carboxyl group, an aqueous solution with 25 wt% of acetic acid (Sigma-Aldrich, ≥99%) was used as reference. To turn it into the right (i.e., deprotonated) charge state, the pH of the solution was set to pH 12.8 by adding NaOH to the solution. As a reference for the peptide oxygen, an aqueous solution of 1 mol/l acetamide (Sigma-Aldrich, ≈99%) was prepared. The chemical structures of the reference molecules is shown in Fig. 4.14.2 in comparison to the diglycine zwitterion. Since both reference molecules are used in aqueous solution, it is obvious that the non-resonant XES spectrum is dominated by the x-ray emission of oxygen atoms in the water molecules (not shown). However, both molecules show a strong absorption resonance below the absorption onset of liquid water. By tuning the excitation energy to this resonance, only the oxygen atoms of the solute are excited and accordingly all detected emission intensity stems from the reference molecules. Note that the addition of NaOH to the solution of acetic acid introduces OH^- ions, which also show emission intensity for pre-edge excitation. However, the spectral influence of these ions is negligibly small for the following, qualitative discussion.

As can be seen in Fig. 4.14.1, the resonantly excited spectra of both acetic acid and acetamide in aqueous solution show very similar spectral shapes compared to the spectra of glycine and its peptides. The excitation energy used to measure the spectra is given on the right and coincides with the maximum of the pre-edge absorption resonance of the samples. All features present for the solid-state samples are also observed for the references, albeit with different relative intensities and slightly different line shapes and peak positions. In particular, the relative emission intensities of the two high-energy features differ between the reference samples. The peak at 525.5 eV is significantly weaker for the acetamide solution compared to the acetic acid sample. At the same time, the spectral weight of the emission features below emission energies of ≈ 524.5 eV is shifted to higher emission energies for acetamide. These findings nicely fit to the changes observed when going from glycine to triglycine. For glycine, the relative emission intensities of the two high-energy features are comparable to the acetic acid solution, being a reference for the carboxyl group. For diglycine and triglycine, the relative emission intensity of the peak at 525.5 eV decreases, resembling the spectral shape of the acetamide sample to an increased degree, being a reference for a peptide oxygen. A similar observation holds for the spectral weight of the low-energy features (below 524.5 eV), which shifts towards higher energies for an increasing number of peptide oxygens.

The discussion of the O K edge of glycine and its small peptides shows that an unambiguously selective excitation of distinct atomic sites is not always possible with RIXS. For the deprotonated carboxyl group, for example, the two oxygen atoms are not distinguishable with soft x-ray spectroscopies. Furthermore, the changes in the O K XES spectra and RIXS maps induced by additional (peptide) oxygens are rather small. However, some distinct trends can be identified. For resonant (pre-edge) excitation, these trends can be qualitatively discussed based on a comparison with suitable reference measurements and a building block approach for soft x-ray emission spectroscopy.

4.3 Summary and discussion

In this chapter, the electronic structure of solid-state glycine, diglycine, and triglycine is discussed by investigating the N K and O K edge, respectively. First, non-resonantly excited XES spectra of glycine are presented and compared to ground state density functional theory calculations of an isolated glycine molecule in the zwitterionic state. At the O K edge, a very good agreement between experiment and theory is found. Hence, one can state that the XES spectra of the solid-state sample is dominated by the electronic structure of the isolated molecule. In contrast to the gas-phase measurements of methanol in the previous chapter, however, the higher number of molecular orbitals for the bigger glycine molecule leads to a broader spectral shape with overlapping emission features. Accordingly, no emission features originating from only one distinct occupied molecular orbital are resolved, making an unambiguous correlation between emission features and their respective molecular orbital difficult.

At the N K edge, significant discrepancies between the experiment and the gas-phase calculations are found. Especially the existence of a distinct emission feature in the measured spectrum can not be explained by the ground-state calculation. Calculations taking nuclear dynamics into account in literature showed previously that this feature can be attributed to proton dynamics on the time scale of the core hole lifetime [60]. More precisely, a proton of the protonated amino group separates from the molecule. In contrast to the findings for resonant excitation of the O K edge of gas-phase methanol, spectral fingerprints of these dynamical processes also are found in the *non-resonant* XES spectrum of glycine. The lack of available XES data of gas-phase glycine hinders a direct comparison between gas-phase and solid-state measurements. If the separation of a proton from the amino group upon non-resonant excitation of the N K edge is also observed for the gas phase is unclear.

After the discussion of the electronic structure of glycine, the sample set is extended by the two smallest glycine-derived peptides. These molecules consist of two respectively three glycine molecules, which are connected via peptide bonds. The formation of these peptide bonds leads to the existence of nitrogen and oxygen atoms with a different chemical environment and bonding to the neighboring atoms in the molecules. By assuming a simple superposition approach for the N K XES spectra, the contributions of peptide and amino nitrogens are separated, leading to a spectrum representative of the peptide nitrogen in diglycine, which is comparable to the results of ground-state calculations of an isolated molecule. Following the building block approach, the spectrum of triglycine can qualitatively be described using the derived peptide nitrogen spectrum and the measured spectrum of glycine representing the amino group.

In the N K XAS spectra, a pre-edge feature is observed for the peptides that is not present for the glycine molecule leading to new emission features in the respective RIXS maps below the main absorption onset. DFT calculations confirm that this pre-edge absorption feature can exclusively be attributed to the excitation of core holes in peptide nitrogens. At this resonance, the N K RIXS spectra of diglycine and triglycine are almost identical. Hence, the local electronic structure at different peptide nitrogens seems to be very similar, which is qualitatively corroborated by DFT calculations of isolated molecules. Furthermore, the derived XES spectrum of the peptide nitrogens for non-resonant excitation is very similar to the resonant spectra. The fact that the local electronic structure at the peptide bond can be probed by resonant excitation of the pre-edge will be utilized to localize the interaction between different salt ions with diglycine in aqueous solution in chapter 5.3. A similar atom and site selective excitation of different oxygen atoms in the studied molecules is not possible. The comparison of non-resonant O K XES spectra of the three samples reveals only minor differences. All spectra are dominated by a very prominent emission feature originating from oxygen lone-pair orbitals from both carboxyl and peptide oxygen atoms. The respective RIXS maps exhibit a strong overall resemblance. For excitation of the pre-edge resonance (which is present for all three molecules), the lone-pair emission feature splits into two distinct peaks with different emission intensities. The relative intensity of these two features, however, changes as a function of the number of peptide oxygens in the molecules. The observed trends in the spectra can be qualitatively understood by comparing them to the x-ray emission spectra of suitable reference molecules.

With the discussion of the electronic structure of solid-state glycine, diglycine, and triglycine in this chapter, a solid basis for the following chapter is now set. It has been shown that RIXS allows for an atom- and especially site selective excitation of the two different nitrogen atoms in the diglycine molecule. Furthermore, the applicability of the building block approach permits in first approximation that the different parts and functional groups of the diglycine molecule can be considered being isolated for the interpretation of the x-ray emission spectra. As a consequence, changes in the XES spectra can eventually be traced back to local changes in the electronic structure. A good example is the identification of the spectral fingerprints of proton dynamics, which are observed for N K edge excitation at the protonated amino group in the XES spectra of glycine and the peptides. With this knowledge, also the non-resonantly excited XES spectra of the peptides can provide valuable information about changes in the local electronic structure in different moieties of the molecule. In the following chapter, the electronic structure of diglycine in its natural environment, i.e., in aqueous solution, is investigated.

CHAPTER 5

X-RAY SPECTROSCOPY OF GLYCINE AND DIGLYCINE IN AQUEOUS SOLUTION

In the previous chapter, the electronic structure of the amino acid glycine and its smallest peptides was discussed based on measurements of the respective molecules in the solid state. However, the native biological environment of amino acids and peptides is the aqueous solution. Instead of being part of an ordered crystal structure in the solid state, the molecules are surrounded by a dynamically changing network of water molecules forming a hydration shell. In addition, many different solutes, e.g., salts or other peptides may be present in the solution which potentially interact with the molecules and influence their chemical and electronic structure.

A prominent example of such hetero-molecular systems are mixed aqueous solutions of proteins with different salts. Thereby, interactions between specific salts and proteins determine phenomena like protein folding, stability, precipitation, and association [11]. Furthermore, the properties of aqueous solutions of electrolytes such as viscosity, refractive index, freezing point depression, and boiling point elevation change significantly with the composition and concentration of the salt [11]. Pioneering studies on the strength of the precipitation effects of different salts to proteins have been performed in the 1880s by Franz Hofmeister [1–3]. Therefore, such ion-specific effects are commonly referred to as "Hofmeister effects" (see, e.g., Ref. [11] and numerous references therein). The ordering of salts with respect to the magnitude of the observed effects has since become known as the "Hofmeister series" [11, 14, 45, 178, 179].

The purpose of this chapter is to shed more light on how different ions in aqueous solution interact with diglycine molecules, which serve as an example for peptides and proteins in general. To disentangle the complex system of interactions between diglycine molecules, the surrounding water, and the dissolved salt, the discussion is separated into three main parts. First, diglycine is dissolved in water to investigate its electronic structure in the aqueous solution with surrounding water molecules in Sec. 5.1. Similar to the solid-state measurements in the previous chapter, aqueous solutions of glycine will be used as a reference for the amino and carboxyl group. The changes induced to the electronic structure by the surrounding water are analyzed by comparing the results to the findings discussed for the solid-state samples.

In Sec. 5.2, the electronic charge state of glycine and diglycine is manipulated via the pH of the aqueous solution. By doing this, the functional groups of the molecules are protonated or deprotonated to monitor the change in the electronic structure caused by the addition or removal of protons at different moieties of the solute. Furthermore, the influence of local changes in the geometric structure on the electronic structure of the whole molecule is discussed, with respect to the applicability of the "building block" model, which is based on a separate analysis of different moieties of a molecule.

Finally, the changes in the electronic structure of diglycine in aqueous solution by adding different salts out of the Hofmeister series are monitored in Sec. 5.3. Thereby, the series for cations is examined using a selection of chlorine salts, whereas the series for anions is investigated using potassium salts. Last, the results of this chapter are summarized.

5.1 Pure aqueous solutions of glycine and diglycine

When dissolving amino acids and/or peptides in water, changes in the electronic structure of the molecules are expected compared to the solid state. The molecular orbitals of neighboring molecules will hybridize and form new orbitals. In the aqueous solution, the type of the neighboring molecules changes and they are not arranged in a ordered crystal structure but in a dynamically changing hydrogen bonded network. Accordingly, dipole-dipole interactions between the (locally charged) peptides and the polar water molecules are expected to deviate from the situation in the homo-molecular crystal structure. As discussed in the previous chapters, dissociation processes on the time scale of the x-ray emission process occur upon x-ray excitation. Since the potential surface governing the dissociation of protons depends on the surrounding, nuclear dynamics can be favored or suppressed in solution compared to gas or the solid state. This was shown, e.g., for ammonia in the gas phase and in aqueous solution [59, 62] and for salt solutions of different concentration and composition [180, 181] in our group. Since glycine and diglycine are present in their zwitterionic charge state in aqueous solution (at neutral pH), the XES and XAS spectra can nicely be compared to the solid-state measurements discussed in the previous chapter to draw conclusions about the influence of the hydrogen bond network. In Sec. 5.1.1, this is done for the N K edge, whereas the O K edge is discussed in Sec. 5.1.2.

5.1.1 The N K edge

The N K edge RIXS maps of glycine, diglycine, and triglycine in aqueous solution are shown in comparison with those of the solid state in Fig. 5.1. The measurements of the aqueous solutions are displayed color-coded, while the data for the solid-state samples are represented as black contour lines on top of the respective RIXS map. The contours hereby mark regions with the same emission intensity, i.e., with the same color in a color-coded RIXS map. Thus, if the displayed contours trace areas with the same color in the displayed RIXS maps, the two data sets are very similar. At first sight, this is the case for the overall shape of all three RIXS maps. A striking difference, however, is the intensity of the elastically scattered light which is very dominant for the aqueous solution (for all three samples). This can be explained by the high reflectivity of the membrane used in the setup to separate the liquid sample from the vacuum of beamline and analysis chamber.

For glycine (Fig. 5.1.1), line positions are found to be comparable for the two data sets (e.g., for the peak at 394.7 eV, which is attributed to dissociation processes). The high-energy shoulder for this feature which is found for excitation beyond the main absorption edge at ≈ 406 eV in the solid-state measurement, however, is not observed in the aqueous solution. Small differences can be identified in the relative emission intensities, which can most easily be seen when following the innermost contour for excitation energies around ≈ 405 eV. For diglycine (Fig. 5.1.2) and triglycine (Fig. 5.1.3), the RIXS maps of the solid-state measurements and the aqueous solutions are very similar as well. The pre-edge feature is centered at 401.3 eV and the main absorption onset is aligned in both data sets. In the case of diglycine, all peaks which are found in the solid-state measurement are also present for the aqueous solution at comparable energy positions. Only slight differences are observed in the relative emission intensities between the two data sets.

For triglycine, the peak maximum of the high-energy feature around 395.5 eV is slightly shifted towards smaller energies for the aqueous solution. This shift, however, might at least partly be caused by an artifact of the measurement using the liquid cell setup with a window membrane. One of the challenges one has to meet when using such a membrane-based setup is to keep the membrane clean throughout the measurement. More specifically, a contamination of the membrane leading to x-ray

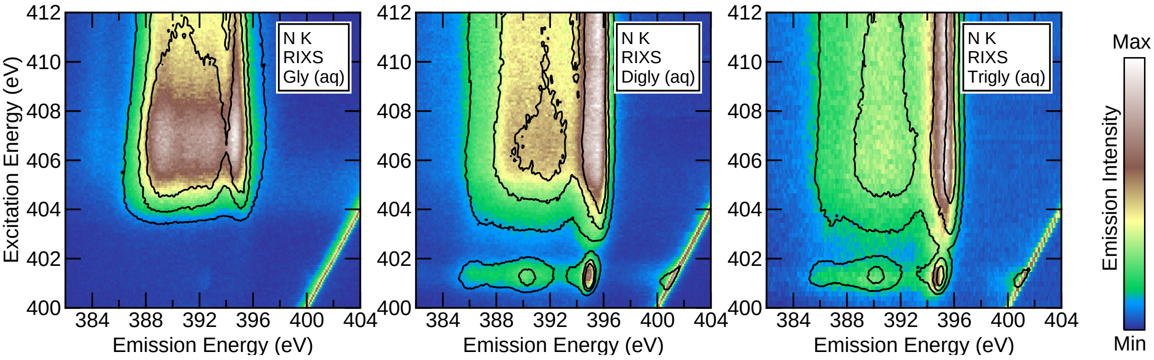

5.1.1 5.1.2 5.1.3

FIGURE 5.1. Color-coded N K RIXS maps of aqueous solutions of glycine (2 M, panel 5.1.1), diglycine (0.5 M, panel 5.1.2), and triglycine (0.25 M, panel 5.1.3). The black contours mark regions with the same emission intensities of the respective solid-state measurements presented in Fig.4.8.

emission intensity in the observed energy region has to be prevented. In the present case, a possible reason for such a contamination might be that fragments of triglycine molecules, which are created by dissociation processes during the measurement adsorb on the membrane leading to a background signal. Possible causes for these fragments are auto-ionization processes induced by auger decays leading to charged and possibly unstable molecules.

In this thesis, big effort was put into minimizing the influence of such a contamination on the measured spectra. First, not fully saturated solutions of the molecules were used for the experiment to increase the chances that possibly created fragments stay dissolved and don't precipitate to form solid residues on the membrane. As a consequence, the intensity of the x-ray emission is reduced especially for the bigger and less soluble peptides. Together with the losses in intensity due to absorption and reflection of the incoming and outgoing photons at the membrane, the strongly reduced density of dissolved molecules leads to a much lower signal-to-noise ratio compared to the solid-state measurements. Second, in between single measurements the complete setup was rinsed with pure water to remove a possibly developed contamination. This cleaning procedure was sufficient for most of the samples used in this thesis. If the cleaning was not successful, the used membrane was replaced by a fresh one. Last, for very sensitive and critical measurements, the irradiated spot on the membrane was moved constantly. This was done by manually moving the complete analysis chamber with the liquid cell attached to it perpendicular to the synchrotron beam using the xyz-stage on which the chamber is mounted. Moving the spot on the membrane, however, can lead to a changing background in the spectra, especially when the edges of the small (0.5 mm × 1 mm) membrane are reached. Correcting these changes is very

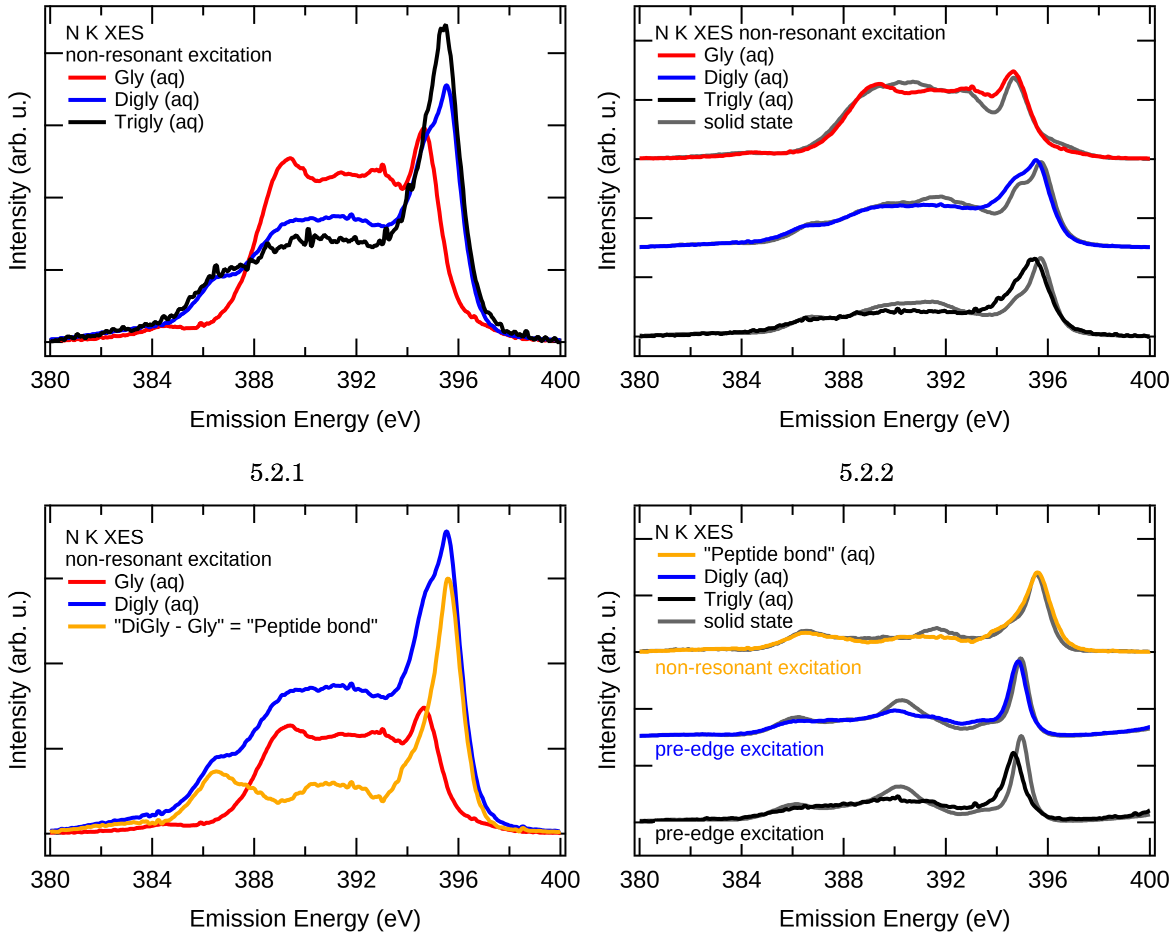

5.2.1

5.2.2

5.2.3

5.2.4

FIGURE 5.2. Non-resonant N K XES spectra of glycine (red), diglycine (blue), and triglycine (black) in aqueous solution (hν = 418.8 eV) compared to each other (panel 5.2.1) and to the solid-state measurements (panel 5.2.2) represented by gray curves. By subtracting the (1:2) weighted spectrum of glycine from diglycine the contribution of peptide nitrogens (orange curve, panel 5.2.3) is isolated from the amino nitrogen emission. This calculated spectrum is compared to its solid-state equivalent in panel 5.2.4 together with spectra of diglycine and triglycine measured after pre-edge excitation with an excitation energy of 401.3 eV.

difficult and several spectra have to be recorded to be able to distinguish between “real” data and background signals. For measuring a complete RIXS map without artifacts one would have to carefully measure several maps with approximately one hour each. Since the RIXS maps and XES spectra of triglycine in aqueous solution only play a minor role for the further course of this thesis these measurements were performed without scanning the membrane for the benefit of the other experiments.

A more detailed analysis of the differences between the x-ray emission of the solid-state measurements and the aqueous solutions is done in conjunction with the non-resonant N K XES spectra shown in Fig. 5.2. The direct comparison between the three molecules is displayed in panel 5.2.1. As for the solid-state measurements displayed in Fig. 4.5, the spectra show some distinct trends. As expected, the relative intensity of the peptide nitrogen related features increases with the number of peptide nitrogens in the sample (e.g., the peak at 395.5 eV). At the same time, the contribution of the amino nitrogen is reduced, leading to big differences in the spectra for emission energies in the range from 388 - 394 eV. The feature attributed to dissociation processes at the amino group at 394.7 eV is present for all three samples. However, whereas this feature leads to a clearly visible shoulder in the spectrum of diglycine (blue), the high-energy feature in the triglycine spectrum does not exhibit a resolved fine structure. In fact, the peak attributed to dissociation processes and the feature of transitions into peptide nitrogen core holes merge to a single peak. The maximum is shifted to slightly lower emission energies compared to diglycine. However, as already mentioned in the discussion of the RIXS maps in Fig. 5.1, this shift might be a consequence of molecule fragments adsorbed on the membrane contributing to the spectrum.

A comparison between the solid state and the aqueous solution is shown in panel 5.2.2. The spectra of the solid state are displayed as gray curves behind the respective aqueous solution data. Every pair of spectra is normalized to the integrated emission intensity in the emission energy region from 380 - 400 eV. Some distinct differences in the spectra are found. The aqueous solution exhibits in general less defined structures compared to the solid-state measurements. A possible explanation for this trend is that in the aqueous solution the molecules are surrounded by a dynamical network of H-bonded water molecules, whereas they are arranged in a defined crystal structure in the solid state. Dependent on the exact arrangement of and bonding conditions between the solute and the surrounding water molecules in the hydration shell, the relative intensity and energetic position of distinct emission features may change. For a spectrum integrated over many emitting molecules, this leads to an inhomogeneous broadening of the spectra.

For the spectra of glycine, the aqueous solution exhibits less signal for emission energies around 390.5 eV compared to the solid state. At ≈ 394 eV, however, more intensity is detected for the aqueous solution. The feature attributed to dissociation processes at the amino group with 394.7 eV is slightly increased and the shoulder at 396 eV which is present for the solid state is strongly reduced. At first sight, this points towards a higher contribution of dissociated molecules to the measured spectrum in the aqueous solution. Note that the dynamical calculation by Blum *et al.* [60] shown in Fig. 4.3.2 reveals that the shoulder at 396 eV is present predominantly in the snapshot spectra calculated shortly after the excitation took place. Thus, this feature rather originates from intact than from dissociated molecules. However, the differences in this energy region between the aqueous solution and the solid state can also be explained by a shift of the contributing lines or features close to the respective energy regions creating a different “background”.

For the spectra of diglycine, similar differences are found. Here, the aqueous solution also exhibits a higher relative intensity for emission energies from 393.5 - 395.6 eV and a slightly reduced relative intensity at the high-energy side of the intense feature at ≈ 396 eV. From 389.0 - 393.3 eV, the spectrum of the aqueous solution shows an almost flat plateau without the maximum at 391.8 eV, which is present in the solid-state spectrum. For triglycine, the observed differences between the aqueous solution and the solid state are qualitatively identical with the ones discussed for diglycine. Due to the likely background by a contaminated membrane, however, a more detailed analysis is omitted.

As for the non-resonant N K XES spectra of the solid-state samples (see Fig. 4.5), one can separate the contributions of the amino nitrogen emission and the peptide nitrogen emission by subtracting the glycine spectrum from the diglycine spectrum to isolate the spectral signature of the peptide nitrogen. This is shown in panel 5.2.3. The calculation procedure was performed identical to the solid-state measurements. After normalizing the spectra to the integrated emission intensity in the emission energy range from 380 - 400 eV, the calculation “Digly - 0.5×Gly” was performed. The obtained spectrum of the peptide nitrogen emission (orange) then can be compared to its solid-state equivalent, which is displayed in panel 5.2.4. The two spectra bear a striking resemblance, all features found in the solid-state spectrum (gray) are also present for the aqueous solution with comparable relative emission intensities. In the energy region where the biggest deviations between the non-resonant spectra of glycine and diglycine are found (≈ 393.5 - 395.6 eV, see panel 5.2.2) only slight differences occur for the “peptide bond” spectra. Keeping the very simple building block approach in mind, one thus can argue that the main changes in the electronic structure between solid and aqueous solution can be related to variations localized near the amino group rather than at the peptide bond.

In addition to the discussed “peptide bond” spectra, panel 5.2.4 shows spectra of the two peptides excited at the pre-edge with 401.3 eV. As was discussed extensively for the solid-state samples in Sec. 4.2.1, only peptide nitrogen core holes are excited at this excitation energy. Thus the local partial density of states at the peptide bond is directly probed. Again, the respective solid-state spectra are depicted in gray and spectra belonging together are normalized to the integrated emission intensity in the displayed energy region and plotted with an offset for a better comparability. Similar to the non-resonant spectra, the resonantly excited spectra of the aqueous samples show less distinct features than in the solid state. The biggest deviations are observed at ≈ 390 eV for both peptides. A shift towards smaller energies of the most intense feature for the aqueous solution is found. For triglycine, this feature also is significantly broader compared to the solid state, which, however, might be due to the mentioned possible contamination of the membrane. Since spectator-shifts can have a significant impact on the shape of the resonantly excited spectra when compared to the non-resonant excited ones, a direct comparison for the two excitation regimes is difficult. However, the deviations between the spectra of the aqueous and solid samples observed at ≈ 391.8 eV for the non-resonant spectra might be of a similar origin as the difference in relative emission intensities at ≈ 390 eV for resonant excitation.

5.1.2 The O K edge

At the O K edge, the investigation of the electronic structure of the dissolved molecules is complicated by the surrounding water molecules. For excitation above the absorption onset of liquid water, the XES spectra are dominated by the emission of water molecules. Fortunately, a pre-edge absorption resonance is found for glycine and its derived peptides that is located below the absorption onset of liquid water. The respective O K RIXS maps of the aqueous solutions are depicted in Fig. 5.3.

In the color-coded RIXS maps, a clearly visible absorption resonance centered at ≈ 532.7 eV is observed for all samples. For excitation energies above ≈ 533.5 eV, the RIXS maps are dominated by the emission of water molecules. O K RIXS maps of pure water can be found in Refs. [54, 133, 180]. The black contours represent the O K RIXS maps of the solid-state measurements discussed in Sec. 4.2.2. One observes a good agreement between the two data sets for all three molecules at the pre-edge. Only small variations in the relative intensity of the visible emission features are found. Peak positions both in the absorption and the emission are identical. This can be more easily seen in Fig. 5.3.4, showing XES spectra resonantly excited at the pre-edge with 532.7 eV, normalized to the maximum intensity. Prior to the normalization, a linear background was subtracted, defined by the intensity on the high-energy side of the elastic peak (at 535 eV) and at 490 eV (i.e., on the low-energy side of a weak O K emission feature located at ≈ 505 eV). As already mentioned above, the spectra of the aqueous solutions and the solid-state samples bear striking similarities. The three main emission features discussed for the solid state in Sec. 4.2.2 are also observed for the aqueous solutions. Hereby, the peak positions are identical for each pair of spectra. However, some changes in the relative emission intensities and line shapes are observed, which follow a qualitative trend. For instance, the emission feature at 525.5 eV exhibits a reduced maximum intensity relative to the main emission feature at 526.5 eV for all aqueous samples compared to their solid-state counterpart. At the same time, the peak shows a broader line shape. This might indicate that the

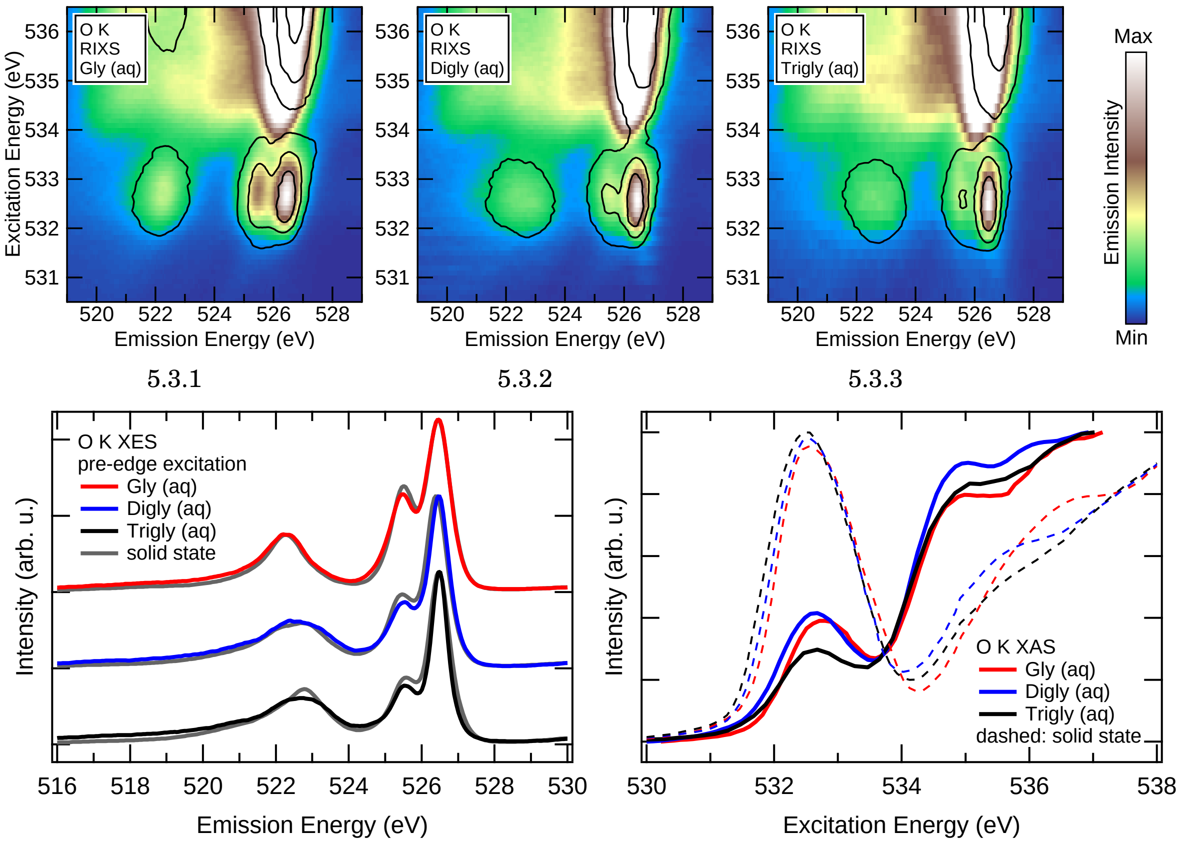

5.3.1 5.3.2 5.3.3

5.3.4 5.3.5

FIGURE 5.3. Color-coded O K RIXS maps of glycine (5.3.1), diglycine (5.3.2), and triglycine (5.3.3) in aqueous solution. Black contours mark regions with constant emission intensities in the respective RIXS maps of the solid-state samples that are discussed in Fig. 4.12. Spectra resonantly excited at the pre-edge ($h\nu = 532.7$ eV) are shown in panel 5.3.4 in comparison to the solid-state measurements depicted in gray. O K XAS spectra of the discussed samples in aqueous solution (solid lines) and solid state (dashed lines) are shown in panel 5.3.5.

molecular orbitals contributing to this emission feature interact with the aqueous environment, leading to an inhomogeneous broadening. Since this trend is observed in all spectra, the interaction with the environment likely takes place rather in proximity to the deprotonated carboxyl group than at the peptide bonds. For the peptides, the width of the peak with highest intensity at 526.5 eV is slightly smaller, the emission feature at ≈ 522.5 eV, however, appears to be broader for the aqueous solution. For emission energies below 521 eV, the spectra of the aqueous solutions show a somewhat increased intensity. Note that this difference most likely can not be attributed to an improperly subtracted background since the spectra were recorded several times and in different experimental runs leading to comparable results.

X-ray absorption spectra of the aqueous solutions at the O K edge are depicted in Fig. 5.3.5 (solid lines) in comparison to the XAS spectra of the solid-state samples discussed in Sec. 4.2.2 (dashed lines). They are normalized to the maximum intensity after subtracting a constant background. The peak position of the pre-edge absorption resonance coincides with the solid-state measurements for all samples, i.e., a small shift towards lower excitation energies for an increasing number of peptide oxygens in the molecule is observed. Thereby, the relative intensity of the pre-edge absorption feature depends on several parameters. First, the concentration (i.e., the molarity) of the solution plays a crucial role, with a higher concentration leading to a higher absorption probability. Second, a higher number of oxygen atoms per dissolved molecule equally enhances the absorption probability. Last, self absorption effects which affect all fluorescence yield XAS measurements lead to an enhanced intensity of the pre-edge features. Their magnitude is described by a complex function of the absorption coefficient and thus also the density of oxygen atoms in the aqueous sample. The combination of all these makes a quantitative discussion of the differences in the absorption intensity difficult.

Concluding this section, one can state that the aqueous environment of the investigated molecules has a measurable effect on the x-ray emission spectra. The observed differences point towards an enhanced interaction of water molecules with the charged functional groups. This seems reasonable when considering the polar character of water molecules and the locally charged moieties of the amino acid and the peptides. In the following section, the functional groups will be manipulated by changing the pH of the aqueous solution.

5.2 The influence of pH on the electronic structure of glycine and diglycine

In the previous sections, the studied molecules in aqueous solution and in the solid state were present in the zwitterionic charge state. In this section, the charge state of the functional groups is manipulated by changing the pH of the aqueous solution. The interplay between the pH value of the solution and the charge state of the functional groups plays a crucial role in nature, since the chemical reactivity of, e.g., an amino acid is determined by the ionic states of its functional groups. Thereby, all possible charge states (anionic, cationic, and zwitterionic) are accessible. The neutral charge state is only favored in the gas phase [149, 150]. Since amino acids and peptides always have an amino group and a carboxyl group, they can function as a base (proton acceptor) or an acid (proton donor), depending on pH.

The pH value is defined as the negative decimal logarithm of the hydrogen proton activity (or "effective concentration"), a_{H^+} [182]. Since the proton activity may vary with the properties of the solution (e.g., temperature), the type of solvent, and the type and concentration of the solute, usually concentrations are used instead of activities to simplify the formalism. The errors introduced by this approximation usually are very small and not relevant for the discussion in this thesis. In aqueous solutions, hydrogen protons do not occur as free radicals but in form of hydronium ions (H_3O^+) and the definition of the pH value can be written as:

$$pH = -\log_{10}(a_{H^+}) \approx -\log_{10}\left(\frac{c(\mathrm{H_3O^+})}{\mathrm{mol/l}}\right) \tag{5.1}$$

For weak ("Brønsted") acids like amino acids, the concentration of ions also depends on the dissociation constant of the functional group (K_a for the *acidic* carboxyl group and K_b for the *basic* amino group), which can be expressed as a pK_a value:

$$pK_a = -\log_{10}(K_a) \text{ with } K_a = \frac{c(\mathrm{A^-})\,c(\mathrm{H^+})}{c(\mathrm{HA})\ \mathrm{mol/l}} \tag{5.2}$$

Here, HA is the generic acid, H^+ is the commonly used short form for H_3O^+, and A^- represents the conjugated base of the acid. Combining equations (5.1) and (5.2) leads to the Henderson-Hasselbalch equation [183–185]:

$$pH = pK_a + \log_{10}\left(\frac{c(A^-)}{c(HA)}\right) \tag{5.3}$$

Since $\log_{10}(1) = 0$, it is clear that when the pH value of the solution is equal to pK_a the concentrations of the deprotonated species (i.e., the conjugated base, $c(A^-)$), and of

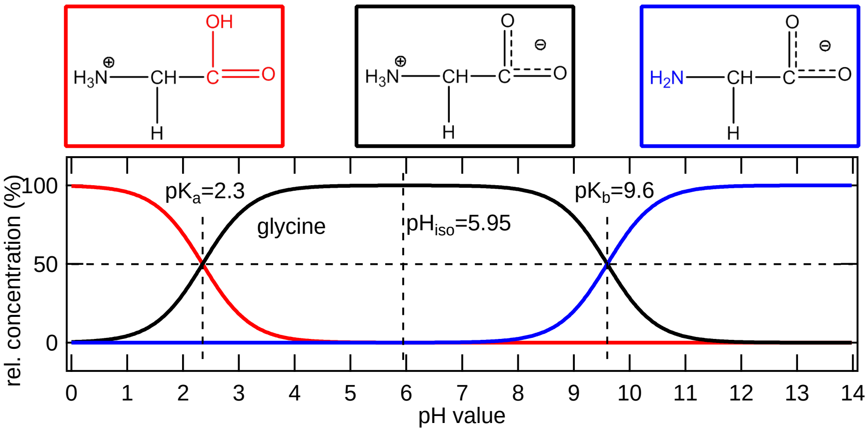

FIGURE 5.4. Relative concentrations of the cationic (red), zwitterionic (black), and anionic (blue) species of glycine molecules in aqueous solution as a function of pH, calculated based on the Henderson-Hasselbalch equation. The Lewis structures of the respective species are depicted at the top.

the protonated species (i.e., the acid, c(HA)), are identical. For molecules with only one (acidic) carboxyl group and one (basic) amino group, the isoelectric point pH_{iso}, i.e., the pH value for which the mean net charge of all molecules in solution is zero, can be calculated by the mean value of pK_a and pK_b. This applies for glycine and its derived peptides. Using equation (5.3) and knowing a molecules pK_a and pK_b values, one can calculate the fraction of neutral (or analogue of protonated or deprotonated) functional groups in solution as a function of pH:

$$\frac{c(HA)}{c(HA)+c(A^-)} = \frac{1}{1+10^{pH-pK_a}} \tag{5.4}$$

The resulting curves are shown for glycine in Fig. 5.4 with given values for pK_a and pK_b [150, 186]. The relative concentration of glycine's zwitterionic species is indicated by a solid black line. For very low and high pH values the concentration decreases whereas it is (almost) constant near 100 percent for medium pH values (around the isoelectric point). The cationic species (i.e., the carboxyl group is protonated) is represented as a red curve. For low pH values its relative concentration is maximized. For increasing pH values the concentration declines, intersects the black line at the pK_a value of glycine's carboxyl group, and vanishes for high pH values. The relative concentration of the anionic species (i.e., with neutral, deprotonated amino group; blue line) behaves the opposite way, with vanishing concentrations for low pH values, intersecting the contribution of the zwitterionic species at glycine's pK_b value, and being maximized for high pH values. The Lewis structures of the three different species are depicted at the top with frames in the colors with respect to the curves in the graph. According to equation (5.4), more than 99.95% of the molecules in the solution are in the zwitterionic charge state at the isoelectric point. The remaining portion is equally divided between the other species. At pH 0.6, slightly more than 98% of the glycine molecules exhibit a protonated carboxyl group (COOH), whereas at pH 12.7, for more than 99.9% of the molecules in solution the amino group is deprotonated (NH_2). This estimation shows that the majority of the molecules is present in the same charge state at these pH values. For XES experiments, the contributions of the molecules in the other charge states to the recorded spectrum can thus be neglected.

5.2.1 Manipulation of glycine's functional groups with pH

Having discussed the charge states of glycine which are present in the aqueous solution as a function of pH, the influence of the pH on the electronic structure of glycine is investigated. Protonation or deprotonation are expected to lead to significant differences in the x-ray emission spectra, as was shown in Sec. 3.2 for gas-phase methanol. Since RIXS probes the *local* partial density of states, however, a change at the carboxyl group is expected to have only a minor influence on the XES spectrum at the N K edge, probing the surrounding of the amino group and vice versa. This local character of RIXS already was used in the previous chapter by applying a building block approach to model, e.g., the non-resonant XES spectrum of triglycine in Sec. 4.2. The applicability of this building block approach for the different ionic species of glycine will by analyzed in more detail in the following.

The N K and O K RIXS maps of glycine in aqueous solution at low, medium, and high pH are depicted in Fig. 5.5. In Sec. 5.1, the RIXS maps at medium pH (middle) have already been discussed and compared to the solid-state measurements. At the N K edge, the RIXS map at low pH (1.5) bears striking resemblance with the medium pH map. Only some minor differences in the relative emission intensities are found. A more detailed discussion of the differences will follow below based on the non-resonant x-ray emission spectra. The strong similarity of the two RIXS maps was expected, since the molecules predominantly exhibit a protonated amino group (NH_3^+) at these pH values (see Fig. 5.4) and thus the electronic structure should be very similar near the excited nitrogen atom. However, big changes occur in the RIXS map when going to high pH. The absorption onset clearly shifts to lower excitation energies and shows two distinct absorption resonances at 401.6 and 402.8 eV, which have been assigned to $1s \rightarrow \sigma^*$ transitions ($\sigma^*_{NH_2}$ and σ^*_{NH}) [55] (considering the difference of 0.3 eV in the energy calibration). Additionally, the overall spectral shape throughout the whole RIXS map changes significantly. A very intense feature with an emission energy of 395.4 eV dominates the spectral shape, whereas comparatively small intensity is observed around 392.6 eV. The N K RIXS maps already have been reported and discussed in the comprehensive study by Blum *et al.* [60], which is in good agreement

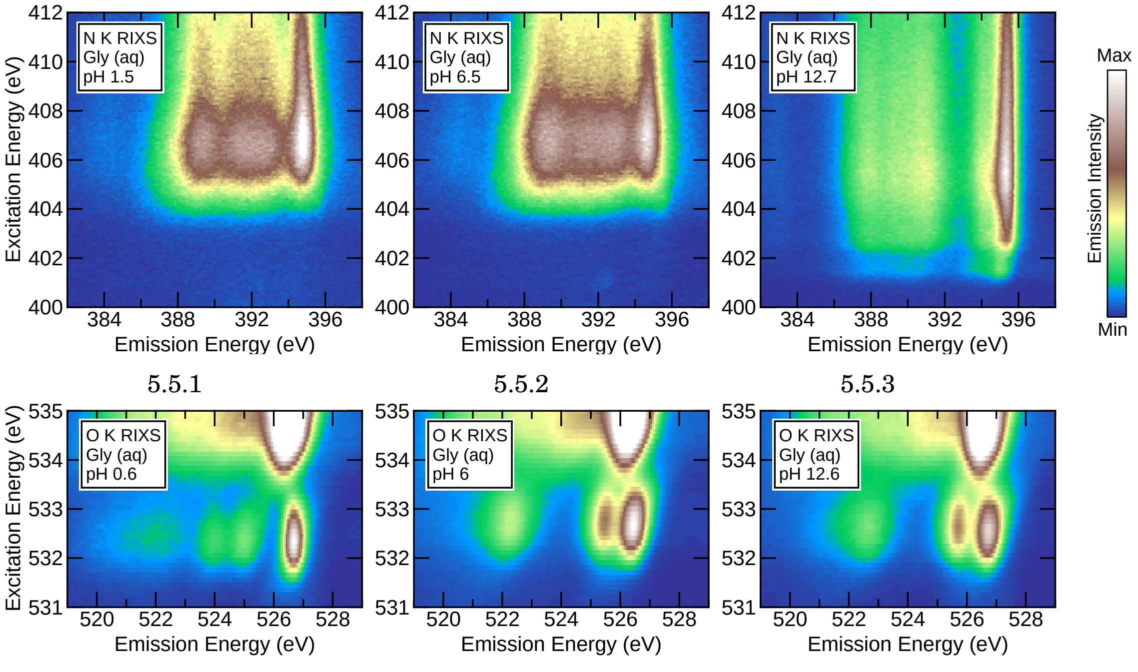

5.5.1 5.5.2 5.5.3

5.5.4 5.5.5 5.5.6

FIGURE 5.5. RIXS maps of glycine in aqueous solution with different pH, excited at the N K edge (top panels) and the O K edge (bottom panels). For excitation energies above ≈ 533.5 eV, the O K RIXS maps are dominated by the emission of water molecules. The RIXS maps at neutral pH (middle) correspond to the maps shown in Figs. 5.1 and 5.3, respectively.

with the spectra published by Gråsjö *et al.* [58] (which, however, bear a much worse signal-to-noise ratio).

For the O K edge, the determining change in the molecular structure is the protonation of the carboxyl group (with a pK_a value of 2.3). Accordingly, the changes in the RIXS map when going from medium to high pH are marginal. Note that the maps are dominated by the emission of water molecules for excitation energies above ≈ 533.3 eV, whereas the pre-edge feature below the absorption onset of water originates from excited glycine molecules. For low pH, the pre-edge feature shows some significant differences compared to the RIXS maps measured at higher pH. The absorption resonance is located at slightly smaller excitation energies centered at ≈ 532.5 eV. This shift was already found by earlier XAS studies of glycine in basic aqueous solution and in the gas phase [56, 154]. In the gas phase, glycine is present in its neutral form [149, 150]. Accordingly, the carboxyl group is protonated as it is the case in the basic aqueous solution. In the gas-phase XAS spectra, two clearly separated absorption features are found, which can be attributed to $1s \rightarrow \pi^*_{C=O}$ and $1s \rightarrow \pi^*_{C-OH}$ transitions, respectively. In the aqueous solution, however, the latter one is obscured by the signal of the water molecules and only the former one can be observed separately.

In the resonantly excited emission spectrum at low pH, the most intense and very sharp peak is shifted to higher emission energies and is now centered at 526.6 eV. Instead of the single feature which is present at the low energy flank of this peak for the solutions of medium and high pH, two distinct new emission features can be observed with similar emission intensities, centered at 524.8 and 523.8 eV, respectively. At even smaller emission energies, a very broad feature centered at ≈ 521.5 eV is found.

The RIXS maps for both the nitrogen and oxygen K edge have been measured at pH values at which the majority of the glycine molecules are in the same electronic charge state. A more detailed analysis of the changes in glycine's XES spectra as a function of pH will be performed based on non-resonant XES spectra at the N K edge, and XES spectra resonantly excited at the pre-edge absorption resonance at the O K edge. On the one hand, the obvious changes in the spectra discussed above will be traced as a function of pH. On the other hand, the effect of protonation of one functional group on the electronic structure in the residual moiety of the molecule will be studied.

The middle panel of Fig. 5.6 shows a series of non-resonantly excited N K XES spectra of glycine in aqueous solution of different pH, normalized to the integrated emission intensity in the displayed emission energy region. All spectra were recorded using an excitation energy in the energy range of 418.8 - 419.3 eV. The small differences in the excitation energy, however, are not expected to have a significant impact on the XES spectrum since they are all far above the absorption onset. The pH values of the solutions are given on the right. In the left panel, the relative concentration of glycine molecules in the three different charge states as a function of pH is given, which was already presented in Fig. 5.4. The protonation and deprotonation of the functional groups are indicated in the middle. The dashed lines give the pH values at which the spectra shown in the central panel have been recorded.

As expected, the N K XES spectrum barely changes for pH values smaller than 6, whereas obvious changes are observed for the spectra measured at higher pH. To simplify the comparison, the panels on the right show the spectra of these two regions of the pH value. In the top right panel, the spectra for pH 6 to pH 12 are displayed, i.e., the pH range where the charge state of the amino group changes. The pH 6 and pH 12 spectra are plotted with solid lines, whereas all spectra in between these two pH values are plotted as dashed lines. As the relative concentration of the two molecular species changes with pH, the XES spectra change accordingly. Thus, the spectra for pH 11.3 and pH 12 are very similar, since almost all glycine molecules are in the anionic charge state at these pH values (see left panel). A similar statement can be made for the spectra at pH 6 and pH 9, however, here the predominant species is the zwitterionic state. For the other pH values, the spectra can be explained by a

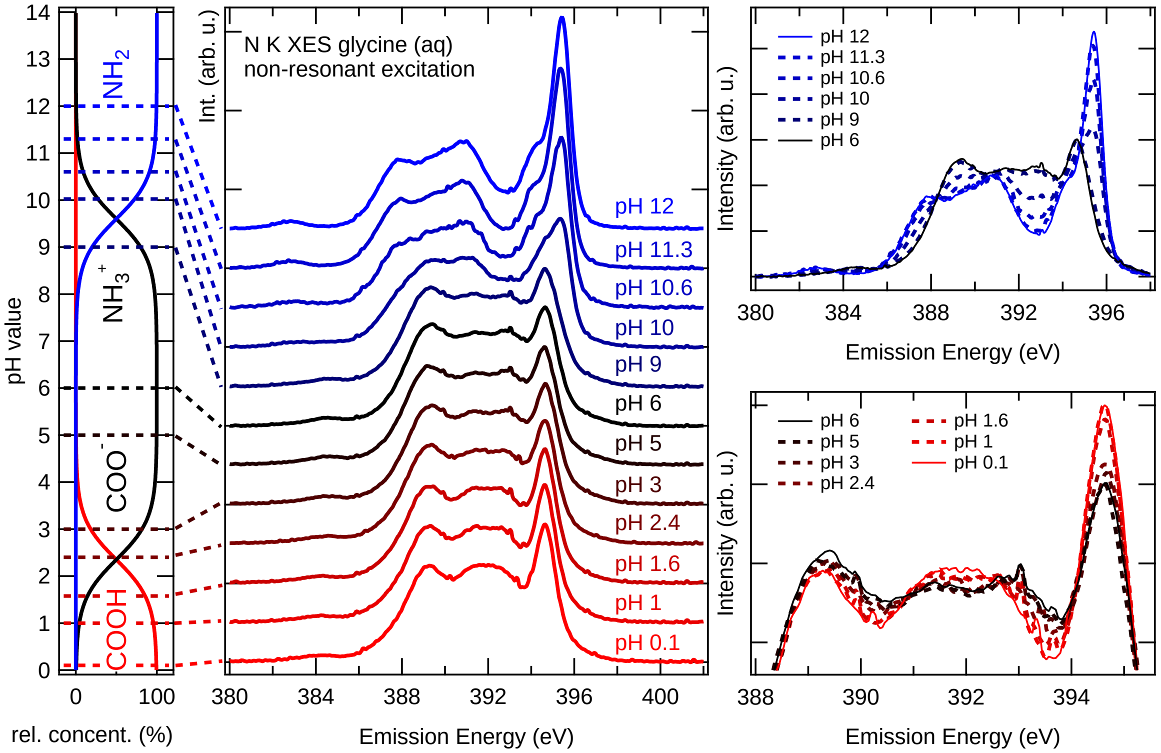

FIGURE 5.6. Left: Relative concentration of glycine molecules in the cationic (red), zwitterionic (black), and anionic (blue) charge state as a function of pH. Middle: Non-resonant N K XES spectra of glycine in aqueous solution at different pH. The pH values are given on the right and indicated by dashed lines in the left panel. Top right: Comparison of the spectra shown in the middle for pH 6 - pH 12. Bottom right: Detail spectra of glycine at pH 0.1 - pH 6.

superposition of the spectrum at pH 6 (zwitterionic) and at pH 12 (anionic), where the weighting factors give a pretty good measure for the relative concentrations of the two species. To demonstrate this, the four spectra for pH 9 - pH 11.3 have been fitted using the pH 6 and pH 12 spectra as components, which is shown in detail in Fig. A.2 in the appendix.

In the bottom right panel, the center region of the spectra for pH 0.1 - pH 6 is shown, with pH 0.1 and pH 6 plotted as solid lines and all other spectra as dashed lines. Despite the fact that the amino group is protonated for all spectra, still some deviations can be observed. For lower pH values, the feature at 394.6 eV increases and the dips in the spectrum on the low-energy side of this peak and at ≈ 390.3 eV get deeper. At the same time, the two emission features in the emission energy range of ≈ 390.3 - 393.5 eV seem to merge and the peak at 389.3 eV gains in intensity. Remarkably, like the spectra for pH 6 - pH 12, all these findings are changing monotonically with pH. A possible explanation for the increase of the peak at 394.6 eV (which is attributed to nuclear dynamics as was shown in Sec. 4.1) can be the presence of Cl^- ions in close proximity to the glycine molecules. Cl was added in form of HCl to manipulate the pH of the solution. The Cl^- ions might create a more attractive potential (compared to water molecules) for the protons in the amino group which then facilitates the dissociation process. The monotonic trend in the spectra might also be caused by the increasing fraction of molecules with a protonated carboxyl group in the solution for lower pH values. Even though this mainly affects the electronic structure at the carboxyl group (as will be shown below with the measurements at the O K edge), also the electronic structure around the nitrogen atom in the amino group might be slightly influenced.

The series of XES spectra of glycine in aqueous solutions of different pH for excitation of the O K pre-edge ($h\nu = 532.5$ eV) is shown in the middle panel of Fig. 5.7. The left panel again shows the theoretical relative concentrations of glycine cations (red), zwitterions (black), and anions (blue) as a function of pH. The changes in the electrical charge state of the functional groups are indicated next to the theoretical curves. The pH values at which the spectra were measured are indicated by dashed lines and given on the left in the middle panel.

As expected based on the electrical charge state of the carboxyl group, the spectra undergo significant changes when going from the pH neutral to the more acidic solutions but are very similar for the more basic solutions. The latter ones are shown in the top right panel without an offset for an easier comparison. The spectra of pH 6 and pH 12 are drawn with solid lines, whereas the spectra for pH values in between are represented by dashed lines. Several small changes can be observed with a clear trend as a function of pH. For higher pH, the most intense feature slightly shifts by up to +0.15 eV towards higher emission energies and loses relative emission intensity. At the same time, the maximum at 522.3 eV (for pH 6) shifts by the same amount. The peak loses in maximum intensity and gets broader, leading to enhanced relative emission intensity for emission energies around ≈ 520.6 eV and ≈ 524.2 eV. The feature at 525.5 eV, however, does not shift in energy.

Due to the protonation of the carboxyl group in the acidic solutions, the spectra undergo significant changes as was already described above. The spectra for pH 0.1 - pH 6 are shown in the bottom right panel. Again, the spectra for the most extreme pH values are represented by solid lines, whereas the remaining spectra are plotted as dashed lines. As one can see, the spectra change monotonically with the pH of the solution. This can be explained by the increasing relative concentration of glycine molecules with a protonated carboxyl group for decreasing pH. Accordingly, all dashed

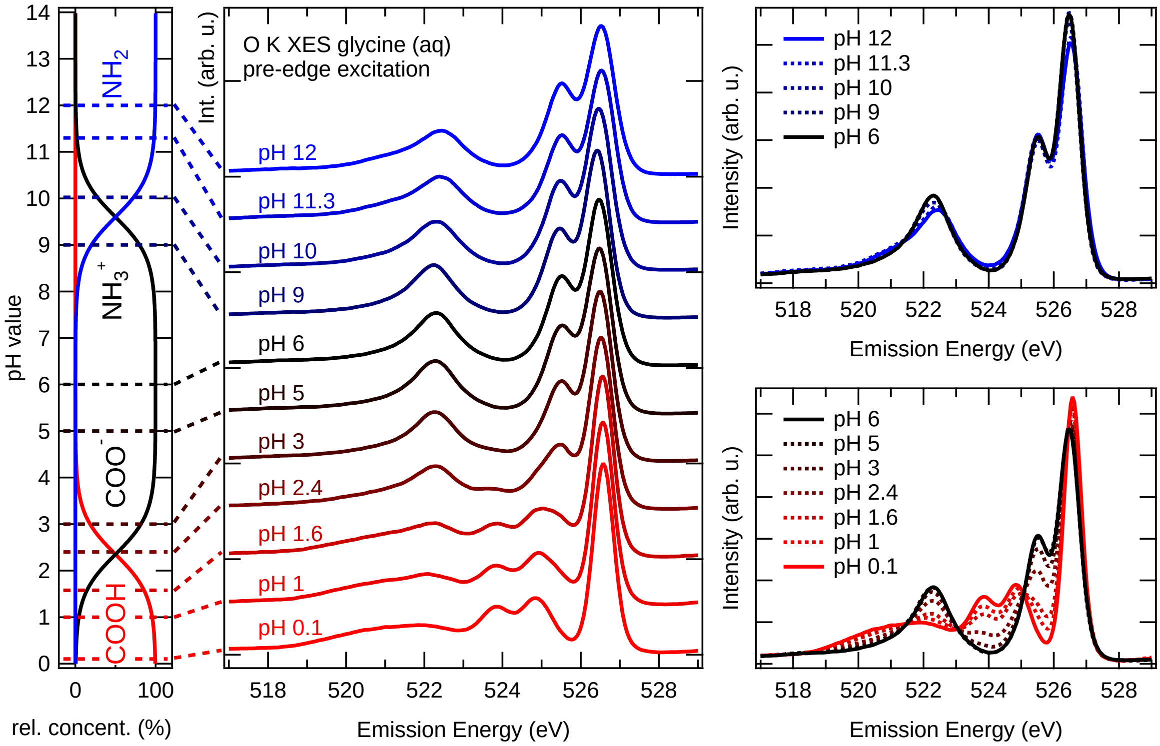

FIGURE 5.7. Left: Relative concentration of glycine molecules in the cationic (red), zwitterionic (black), and anionic (blue) charge state as a function of pH. Middle: O K XES spectra of glycine in aqueous solution at different pH, excited at the pre-edge absorption resonance with hν = 532.5 eV. Dashed lines in the left panel indicate the pH values at which the spectra were measured. Right: Comparison of the spectra shown in the middle for pH 6 - pH 12 (top) and pH 0.1 - pH 6 (bottom).

spectra can be described with an excellent agreement by a weighted superposition of the spectra at pH 0.1 (red) and pH 6 (black). This is shown in detail in Fig. A.3 in the appendix, together with a brief discussion of the small deviations of the resulting weighting factors from the theoretical prediction.

The measurements presented above show that the pH of the solution can have an enormous effect on the electronic structure of molecules with functional groups like glycine or amino acids in general. The pK_a and pK_b values, however, may vary depending on the size and the chemical structure of the side chain by about 2.1±0.3 and 9.5±1.2 for the 20 standard amino acids [187]. As expected, a local change in the chemical structure by adding or removing a proton to or from a functional group has an explicit influence on the partial local density of states which is probed by the RIXS process. In addition, a change in the electrical charge state of one functional group also influences the electronic structure in other moieties of the molecule. For example, a protonation of the carboxyl group for the acidic spectra leads to small but clearly visible changes in the N K XES spectra. Accordingly, the building block approach is only legit in certain limits.

5.2.2 Diglycine in aqueous solutions of different pH

After the effect of pH on the electronic structure of glycine was studied in the previous section, the manipulation of diglycine's functional groups is investigated in the following. Based on the findings for glycine, one can expect similar changes in the XES spectra for diglycine as a function of pH, keeping in mind that the nitrogen and oxygen atoms in the peptide bond equally contribute to the XES spectra. With pK_a=3.1 and pK_b=8.1 [187], the (negative of the logarithm of the) acid dissociation constants of diglycine's functional groups are shifted towards neutral pH. Accordingly, diglycine is a weaker base and weaker acid compared to glycine. The peptide bond, however, is not affected by pH changes and does not dissociate.

The relative concentrations of diglycine cations (red), zwitterions (black), and anions (blue) in aqueous solution as a function of pH as expected based on the Henderson-Hasselbalch equation are shown in Fig. 5.8. The Lewis structures of the different species are given at the top. At pH 5.6, more than 99% of the molecules are in the zwitterionic charge state. The relative concentration of anions at pH 12.1 exceeds 99.9% and more than 99% of the molecules are in the cationic charge state at pH 0.7. Accordingly, it is a reasonable approximation to reduce the following discussion of the RIXS maps and XES spectra of diglycine at these pH values to only the most prominent molecular species.

In Fig. 5.9, RIXS maps of diglycine in acidic (left panels), pH neutral (middle), and basic (right) aqueous solution are depicted. The panels in the top row represent the measurements after excitation of the N K absorption edge, whereas the panels in the bottom row show the measurements at the O K edge. The pH of the solutions is given in the top left corner, respectively. The RIXS maps at pH 5.6 (middle) have already been discussed in Sec. 5.1. Since a low pH value influences mainly the protonation state of the carboxyl group and not the amino group, it is not surprising that the RIXS maps of the N K edge at pH 1 and pH 5.6 are very similar. Only very small differences can be identified in relative emission intensities. The energetic positions of the visible emission features, however, are identical. For high pH, clear changes in the RIXS map can be found as expected due to the deprotonation of the amino group. Hereby, the overall shape of the RIXS map bears striking similarities with the RIXS map of glycine in basic solution shown in Fig. 5.5.3, despite the fact that the x-ray emission intensity of the (deprotonated) amino group overlaps with the emission attributed to peptide nitrogen atoms. For a more detailed analysis of the observed changes, Fig. 5.10 shows XES spectra for non-resonant and resonant pre-edge excitation as well as XAS spectra of the respective solutions.

The spectra of diglycine in aqueous solution at pH 5.6 are displayed in black and correspond to the spectra discussed in Fig. 5.2. The acidic solution is represented in red, the basic solution in blue, respectively. For a comparison, the XES spectra of glycine at pH 12.7 are depicted as dashed green curves. The used excitation energies are given on the right in the color code of the corresponding spectra. All spectra are normalized to the integrated emission intensity in the displayed emission energy region. The spectra after non-resonantly exciting the N K absorption edge are given at the top. For the acidic and the pH neutral solution, the non-resonant XES spectra are very similar. Only some minor differences in the relative emission intensity of the two high-energy features occur. The peak at 394.7 eV, which is attributed to proton dynamics at the (protonated) amino group, is less intense for the acidic solution than for the solution with pH 5.6. Note that the analysis for glycine in conjunction with Fig. 5.6 showed the opposite trend, namely, the spectra with lower pH exhibit a higher intensity of this peak. However, a possible background in the spectrum at neutral pH, which increases the intensity of this peak due to a contamination of the used membrane is possible. Since the solubility of diglycine increases for more acidic (and also basic) solutions [188], a background originating from molecule fragments adsorbed on the membrane is expected to be smaller for the acidic solution.

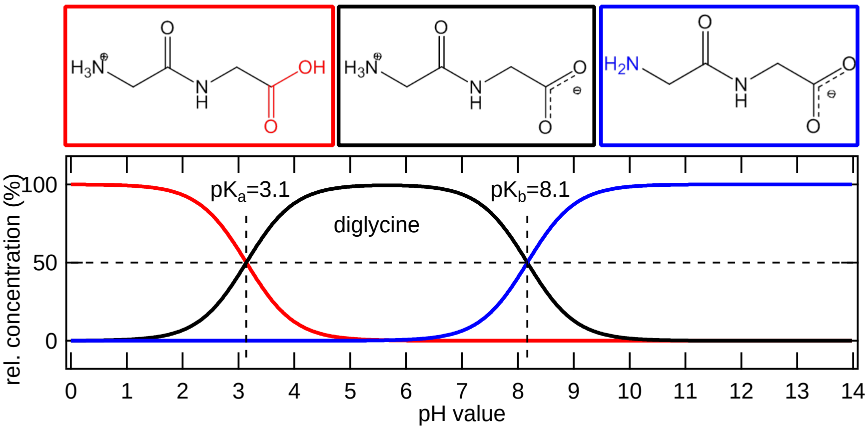

FIGURE 5.8. Relative concentrations of the cationic (red), zwitterionic (black), and anionic (blue) species of diglycine molecules in aqueous solution as a function of pH, calculated based on the Henderson-Hasselbalch equation. The Lewis structures of the respective species are depicted at the top.

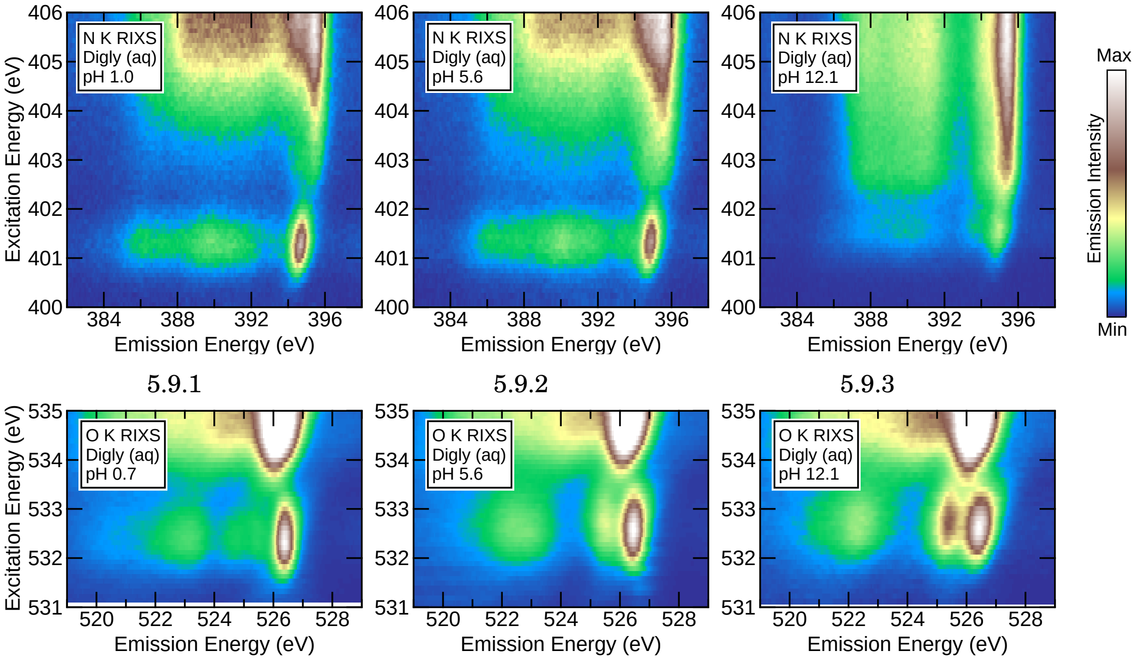

5.9.1 5.9.2 5.9.3

5.9.4 5.9.5 5.9.6

FIGURE 5.9. RIXS maps of diglycine in aqueous solution with different pH, excited at the N K edge (top panels) and the O K edge (bottom panels). For excitation energies above ≈ 533.5 eV, the O K RIXS maps are dominated by the emission of water molecules. The RIXS maps at neutral pH (middle) correspond to the maps shown in Figs. 5.1 and 5.3, respectively.

The spectrum at high pH (blue) is almost identical to the spectrum of glycine in basic solution (green). Hence, the contributions of the peptide nitrogen and the amino nitrogen can also be considered as almost identical for the anionic charge state. The nitrogen atom in the peptide bond has two carbon atoms and one hydrogen atom as its nearest neighbors. In the deprotonated amino group, however, the nitrogen is directly bond to only one carbon but two hydrogen atoms. The different surroundings, however, do not seem to have a crucial effect on the local electronic structure. In fact, the geometry of the bonds seems to play an important role. This becomes clear when considering the XES spectrum of the protonated amino group of glycine, which has a significantly different shape. Here, the nitrogen atom has four nearest neighbors (one carbon and three hydrogen atoms), which changes the bonding geometry to a more tetrahedral form. This finding further justifies the usage of a building block model for the analysis of XES spectra of larger molecules as it was performed, e.g., in Sec. 4.2.2.

For resonant excitation of the N K pre-edge (bottom spectra) the situation is comparable to the findings for non-resonant excitation. The spectra of the molecules with protonated amino group (pH 1 and pH 5.6) are very similar. In the spectrum of the acidic solution, less intensity is observed around ≈ 393.3 eV and the high-energy

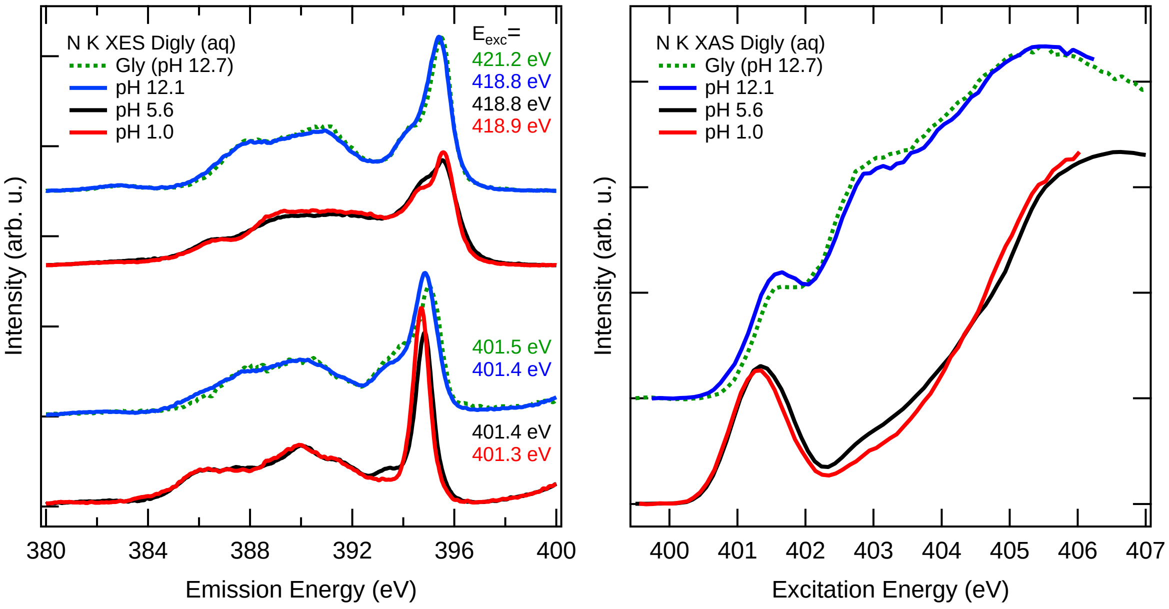

5.10.1

5.10.2

FIGURE 5.10. Panel 5.10.1: N K XES spectra of diglycine in acidic (red), pH neutral (black), and basic (blue) aqueous solution for non-resonant (top) and resonant pre-edge excitation (bottom). The used excitation energies are given on the right, respectively. Spectra of glycine in basic aqueous solution are plotted with dashed green lines for comparison. Panel 5.10.2: N K XAS spectra of the samples described for panel 5.10.1, calculated by integrating the x-ray emission intensity of the RIXS maps shown in Figs. 5.5 and 5.9 for each excitation energy step in the displayed emission energy range.

feature is more intense and shifted by -0.1 eV compared to the pH 5.6 spectrum. The shift, however, can at least partly be attributed to the small difference in the excitation energies (given on the right) since this feature is prone to small shifts in emission energy as a function of the excitation energy as can be seen in the RIXS maps in Fig. 5.9. The spectrum of the basic solution barely shows a different shape compared to the non-resonantly excited spectrum, with the exception that it is shifted by about -0.5 eV, which can be attributed to spectator shifts. Again, the spectrum of glycine in basic solution is given for comparison. As for the non-resonant excitation, the two spectra only differ slightly (note the small difference in the excitation energy). However, some deviations between the spectra at high pH and the spectra for neutral and low pH are observed. This again shows the limitations of the building block approach. Nominally, the chemical structure near the peptide nitrogen does not change when the amino group is deprotonated. Yet, a change in the local electronic structure at the peptide nitrogen (which is probed when resonantly exciting the N K pre-edge) can be observed. The removal of the proton at the amino group obviously leads to a redistribution of the electron density. This also affects the remaining moieties of the molecule, which is in accordance with the findings for glycine in the previous section.

The deprotonation of the amino group also leads to significant changes in the electronic structure of the unoccupied states which are probed by x-ray absorption spectroscopy. The respective N K XAS spectra are shown in Fig. 5.10.2. Whereas the spectra of the basic and the pH neutral solution again have a similar structure with the pre-edge absorption resonance centered at 401.3 eV, the XAS spectrum of the basic solution exhibits a clearly different shape. The pre-edge absorption resonance is shifted by +0.3 eV and another strong absorption resonance at ≈ 402.8 eV can be observed. In literature, no agreement about the correct assignment for this absorption resonance exists for the glycine anion for which the same absorption resonances are found. Based on density functional theory calculations, Messer *et al.* attributed this resonance to a nitrogen 1s $\rightarrow \sigma^*$ transition [56]. By comparing the spectrum to the one of gas-phase glycine [154, 189] and gas-phase ammonia absorbed on Cu [190], Gråsjö *et al.* suggested to assign this feature to CN-π^* antibonding orbitals [58].

The deprotonation of the amino group in the basic solution also leads to some changes in the pre-edge region of the O K RIXS maps in Fig. 5.9. Differences in the relative emission intensity and the linewidth of the observed emission features are found when comparing the RIXS maps at medium and at high pH values. For the acidic solution, the spectral shape changes significantly as expected due to the protonation of the carboxyl group. The relative emission intensity of the narrow peak with an emission energy of 526.5 eV is increased, whereas the feature on its low energy side loses in intensity. An additional peak arises at 524.8 eV and the maximum intensity of the features in the emission energy region from ≈ 518 - 524 eV shifts towards higher emission energies. The absorption resonance is shifted by about -0.2 eV towards smaller excitation energies compared to the pH neutral and basic solution. For excitation energies above ≈ 533.5 eV, the O K RIXS maps are dominated by the emission of water molecules.

The qualitative changes can be seen more quantitatively in Fig. 5.11. In panel 5.11.1, XES spectra resonantly excited at the O K pre-edge with the excitation energies given on the right are shown, normalized to the integrated emission intensity in the displayed energy region. The measurements of diglycine at different pH are represented as solid lines. The bottom spectra show the comparison of diglycine at medium and at high pH with a spectrum of a 6.25 wt% solution of NaOH. The latter one is arbitrarily normalized and indicates the influence of the NaOH (which was added to the aqueous solution to increase the pH) on the XES spectrum. Its maximum

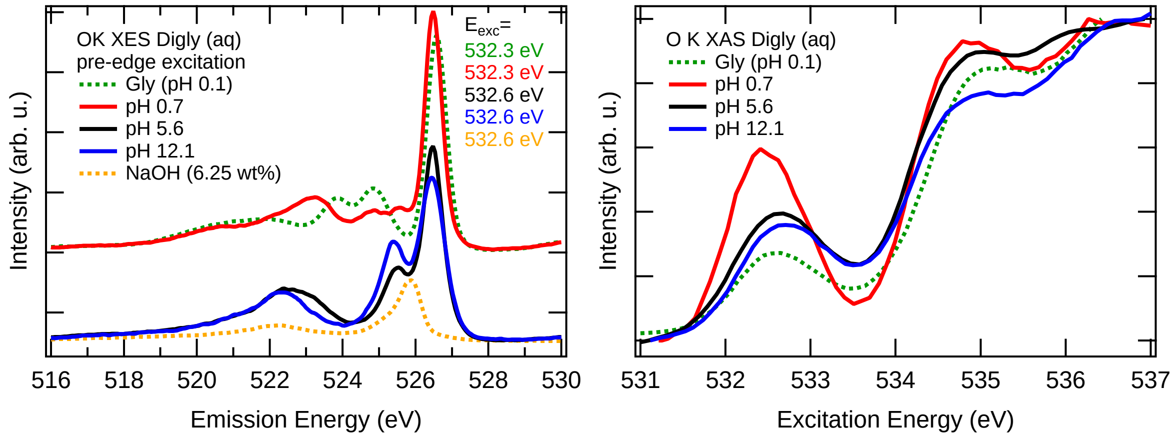

5.11.1

5.11.2

FIGURE 5.11. Panel 5.11.1: O K XES spectra of diglycine in acidic (red), pH neutral (black), and basic (blue) aqueous solution for resonant pre-edge excitation. The used excitation energies are given on the right, respectively. Spectra of glycine in basic aqueous solution (green) and of a 6.25 wt% aqueous solution of NaOH (orange) are plotted with dashed lines. Panel 5.11.2: O K XAS spectra of the samples described for panel 5.11.1, calculated by integrating the x-ray emission intensity of the RIXS maps shown in Figs. 5.5 and 5.9 for each excitation energy step in the displayed emission energy range.

in intensity is reached at 525.9 eV with a broad shoulder on the low energy side. Another broad emission feature is found around 522.3 eV. Hence, the deviations between the black and the blue spectrum can at least be partly explained by the additional emission of OH^- ions in the solution. For the interpretation of the diglycine spectrum in acidic solution, one has to consider that all three oxygen atoms in the diglycine cation have different bonding environments. Since the carboxyl group is protonated in the acidic solution, one of the oxygen atoms in the functional group is double bonded to the carboxyl carbon, whereas the second carboxyl oxygen is single bonded to the carbon atom and single bonded to a hydrogen atom. For excitation energies around 532.3 eV, however, the latter oxygen atom is not excited. XAS measurements of gas-phase glycine and diglycine (i.e., with a protonated carboxyl group) show that its first absorption resonance is located at more than 3 eV higher excitation energies [153, 166]. This is corroborated by XPS measurements of gas-phase glycine [168]. For higher excitation energy, however, the XAS spectrum is dominated by the emission of excited water molecules. The XAS spectra of the aqueous solutions of diglycine and glycine at different pH are displayed in panel 5.11.2. Hence, the resonantly excited XES spectrum can be considered as a superposition of the emission due to transitions into the double bonded carboxyl oxygen and the oxygen atom in the peptide bond which also is double bonded to its neighboring carbon atom. The spectral shape of the double bonded carboxyl oxygen's contribution to the spectrum can be approximated by the resonantly excited spectrum of glycine in acidic solution, which is shown as dashed green line. Accordingly, the emission feature with an emission energy of 524.8 eV can be attributed to transitions at the carboxyl group, whereas the peaks at 523.2 eV and 525.5 eV probably predominantly stem from transitions into the peptide oxygen core hole. The intense feature at 526.5 eV originates from transitions into core holes of both oxygen atoms equally and consists of mainly oxygen lone-pair orbital emission.

Concluding this section, one can state that the addition of NaOH or HCl to aqueous solutions of diglycine can affect the electrical charge state of the dissolved molecules and lead to distinct changes in the x-ray emission spectra. Hereby, the driving force is the increased concentration of OH^- and H_3O^+ ions in the solution, which interact with the functional groups of the dipeptide. The protonation and deprotonation of the functional groups by these ions is very well understood and comprehensively discussed. In the following section, the addition of ions to the solution will be used as a parameter to change the aqueous environment of the dipeptide. Cations and anions will be treated separately by choosing suitably selected salts. The findings will be discussed with regard to the Hofmeister series, which predicts ion-specific interactions with peptides with varying strength. The formalism leading to this ion-specificity and the localization of the interaction between the molecule and the ions in the solution, however, are still not completely understood yet. By applying RIXS to a small example system, new insights can be provided to make the next step on the way to an comprehensive understanding of the Hofmeister series.

5.3 Ion-specific effects on the electronic structure of diglycine

The effects of salts on the hydrogen-bonding structure of water have been intensively investigated with a multitude of experimental techniques such as neutron diffraction [191, 192], Raman [193], infrared [194], femtosecond pump-probe [21, 195], terahertz time-domain [196], and electron spectroscopies [197], as well as with theoretical tools [198–200]. Also x-ray absorption [201–207] and emission spectroscopy [46, 48, 180, 181, 208, 209] was applied frequently after the development of sophisticated experimental setups to make liquids accessible for soft x-rays.

However, only limited work has been published using soft x-ray spectroscopies to investigate the interaction between ions and molecules, especially peptides, in aqueous solution, although these are of fundamental interest for the understanding of the Hofmeister series. Aziz and coworkers focused on aqueous acetate solutions, which serve as a model for carboxylate functional groups of proteins, using XAS as well as XES and RIXS at the O K edge [43, 46, 48]. They came to the conclusion that the interaction strength decreases in the sequence $Na^+ > Li^+ > K^+ > NH_4^+$, i.e., the cations follow the Hofmeister series, with the exception of lithium, which can be explained by Collins law of matching water affinities [37] for the cations and the COO^- group. For aqueous glycine solutions, a more intense interaction for NaCl than for KCl was found [43]. Strong ion pairing of sodium with carboxylate groups was also reported before [210]. In their C K XAS study about acetate and formate solutions, Uejio *et al.* revealed a preferential interaction of Na^+ versus K^+ ions for acetate but not for formate [44]. The same trend is qualitatively also observed a molecular dynamics study for the interaction of Na^+ and K^+ with the negatively charged (deprotonated) carboxyl groups of the amino acids glutamine and asparagine [41]. In this work, also an interaction of cations with the amide bond (the C=O double bond) was identified, again with sodium showing a higher attraction to the electron density around the peptide oxygen than potassium. To mimic the interaction of cations with protein backbones, Okur *et al.* investigated aqueous salt solutions of butyramide via attenuated total reflection Fourier transform infrared and vibrational sum frequency spectroscopy, resulting in an ordering of the cations of $Ca^{2+} > Mg^{2+} > Li^+ > Na^+ \approx K^+$ [211].

Schwartz *et al.* published a first N K XAS study of triglycine in aqueous solution with additional Na_2SO_3 and NaBr. They showed that the kosmotropic sulfite ion is interacting with the protonated amino group while bromide does not show a significant influence on the XAS spectrum [45]. They also support these statements by DFT calculations and claim that kosmotropes can directly interact with the nitrogen backbone of peptides. Molecular dynamics calculations also revealed that weakly hydrated anions such as bromide and iodide interact more strongly with hydrophobic moieties than with the peptide bond [41]. A later molecular dynamics study, corroborated by thermodynamic measurements and NMR experiments, came to the conclusion that large, soft anions like SCN^- and I^- interact with the backbone. The binding site was determined as a combination of the peptide bond and the adjacent α-carbon [212]. This can be understood considering the electron-withdrawing properties of the adjacent N–H and C=O groups. The same group also showed that an NH moiety is not necessary for anion binding to amides in aqueous solution [213]. Interestingly, an NMR and molecular dynamics study of triglycine found a reversal of the Hofmeister series for anions interacting with the protonated amino group of the peptide [39].

Ion-specific effects usually occur when the salt concentration is around or above $\approx 0.1\,\mathrm{M}$, which is a typical range for physiological solutions, pointing out the important role ions play in most biochemical mechanisms [11, 214]. In this section, mixed solutions with a concentration of 0.5 M diglycine and 0.5 M salt are used to study the interaction of different cations and anions with the charged functional groups of the peptide and the peptide bond. The influence of different cations is investigated using a series of Cl^--salts, whereas the interaction of different anions is studied using selected K^+-salts. Both chlorine and potassium are found near the border between kosmotropic and chaotropic ions in the Hofmeister series (with a slight chaotropic character) [215] and thus are excellent candidates for complementary ions for the study of Hofmeister effects of different cations and anions, respectively. The interaction of the salts with the carboxyl group and the peptide oxygen of diglycine is discussed in Sec. 5.3.1, while Sec. 5.3.2 contains the results for the peptide nitrogen and the amino group.

5.3.1 Ions interacting with the oxygen sites of diglycine

The O K XAS spectra of diglycine in aqueous solution with different ions are shown in Fig. 5.12. The spectrum of the 0.5 M diglycine solution is depicted as black curve in both panels. For all other spectra, salt with the given composition was added to the solution such that a salt concentration of 0.5 M was achieved. The left panel (Fig. 5.12.1) includes all measured chlorine salts to investigate the influence of different cations, whereas the impact of different anions is studied in conjunction with Fig. 5.12.2. In the latter panel, a reference measurement of a pure 2 M KNO_3 solution (i.e., without diglycine) is depicted as a dashed line to emphasize the presence of a pre-edge feature at 532 eV which can be attributed to absorption of nitrate ions. Unfortunately, no such a reference spectrum was acquired for K_2SO_4 or found in literature to obtain the same information for sulfate ions, which also contain oxygen. The spectra are sorted according to the appearance of the added ions in the Hofmeister series, with

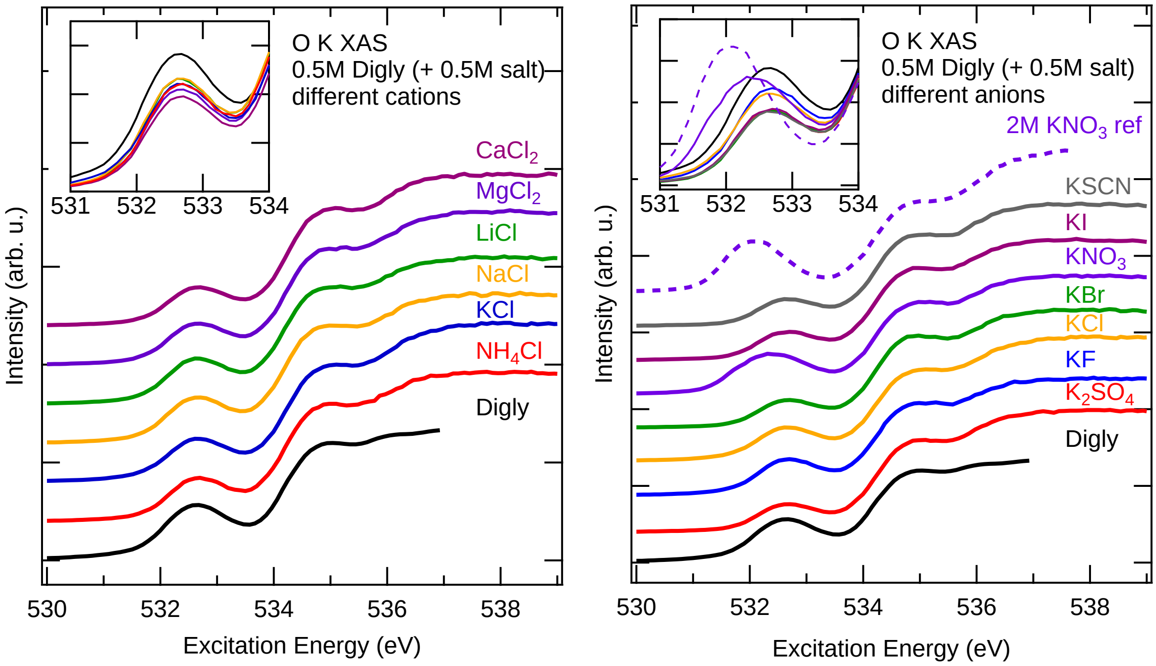

5.12.1 5.12.2

FIGURE 5.12. O K XAS spectra of diglycine in aqueous solution with different additional salts. A series of different cations is shown in Fig. 5.12.1, different anions are used in Fig. 5.12.2, respectively. The dashed spectrum represents a reference measurement of a pure 2 M KNO_3 solution. The insets show the pre-edge feature without an offset between the individual spectra for better comparability.

chaotropes located at the top and kosmotropes at the bottom, respectively. For the pure diglycine solution, only XAS spectra up to an excitation energy of ≈ 537 eV have been acquired, making a normalization to the intensity high above the absorption onset (e.g., at 539 eV) impossible. Thus, to be consistent, all spectra are normalized to the maximum intensity of the absorption resonance around 535 eV.

For excitation energies above ≈ 533.6 eV, all spectra are dominated by the absorption of water molecules. The effects of different ions on the hydrogen-bonding structure of liquid water and how these effects change the relative intensities of the main features in the absorption spectrum have been thoroughly investigated in literature [201–207] and is beyond the scope of this thesis. The insets in Fig. 5.12 show a magnified view of the pre-edge feature at 532.6 eV, which probes the carboxyl group and the peptide oxygen of diglycine, as was shown in the previous sections.

For the series of cations (Fig. 5.12.1), clear changes in the intensity of the pre-edge feature are observed. For sodium and lithium, the peak exhibits the highest intensity of all salts, for calcium the lowest, while potassium, magnesium, and ammonium lay in between. Based on the intensities of the pre-edge absorption resonance, the cations can be ordered as follows: $Na^+ \approx Li^+ > NH_4^+ > K^+ \approx Mg^{2+} > Ca^{2+}$. In their study of aqueous glycine solutions with additional KCl and NaCl, Aziz *et al.* also found a higher intensity of the pre-edge feature for sodium than for potassium [43]. They attribute the changes in the peak intensity to a “change of the local density of unoccupied states at the oxygen site of COO^-_{aq}, induced by interaction with the cations” [43]. Accordingly, a higher peak intensity is claimed to “result from electron withdrawal from the carboxyl group by the cations, which [...] scales with the strength of the COO^-_{aq} to cation interaction” [43]. However, the divalent cations Ca^{2+} and Mg^{2+}, which one would expect to have an even stronger ability to withdraw electron density from the carboxyl group due to their double positive charge, lead to the smallest peak intensities.

Also for salts with the same cation (potassium) and different anions, differences in the peak intensity at the pre-edge absorption resonance are observed (Fig. 5.12.2). The shift towards smaller excitation energies and the broadening of the pre-edge absorption resonance for the solution with KNO_3 can be explained by an additional absorption resonance of nitrate ions at 532.0 eV (dashed spectrum), which also affects the relative intensity of the pre-edge feature in the mixed solution. Out of the remaining anions, fluorine leads to the highest peak intensity at the pre-edge, followed by chlorine. For the anions SCN^-, I^-, Br^-, and SO_4^{2-}, the lowest peak intensity is observed. The variations in the XAS spectra for different anions (with the same cation, i.e., potassium) can not be explained only with the model of different interaction strengths between cations and the carboxyl group, as proposed by Aziz *et al.* [43]. The O K XAS spectrum of diglycine of course also exhibits intensity at the pre-edge that can be attributed to the excitation of peptide oxygens (in contrast to glycine investigated by Aziz *et al.*). However, a more important effect which leads to a compression of the XAS spectra is an artifact of the fluorescence yield detection mode used by Aziz *et al.* and in this thesis. This effect was already briefly mentioned in Sec. 5.1.2 and is called “self absorption” or “saturation” in literature [216–219]. To qualitatively estimate how the addition of different salts to the diglycine solution changes the strength of this effect, the principle physics behind it are addressed in the following.

For a sample with a thickness z and an absorption coefficient κ_{in}, which is illuminated with an intensity I_0 at a photon energy $h\nu_{\text{in}}$, the transmitted intensity $I_T(h\nu_{\text{in}})$ is according to Lambert-Beer’s law:

$$I_T(h\nu_{\text{in}}) = I_0 \cdot e^{-z \cdot \kappa_{\text{in}}}. \tag{5.5}$$

For an infinitely thick sample, assumed normal incidence and detection geometry, the negative derivative of equation (5.5) describes the amount of radiation in the depth z, $\delta I_{\text{in}}(h\nu_{\text{in}}, z)$:

$$\delta I_{\text{in}}(h\nu_{\text{in}}, z) = I_0 \cdot \kappa_{\text{in}} \cdot e^{-z \cdot \kappa_{\text{in}}}. \tag{5.6}$$

If A is a constant factor describing the probability per absorbed photon of emitting a photon in the direction of the detector, the detected intensity $I_{\text{out}}(h\nu_{\text{in}})$ is:

$$I_{\text{out}}(h\nu_{\text{in}}) = \int_0^\infty A \cdot \delta I_{\text{in}}(h\nu_{\text{in}}, z) \cdot e^{-z \cdot \kappa_{\text{out}}} = A \cdot I_0 \cdot \frac{\kappa_{\text{in}}}{\kappa_{\text{in}} + \kappa_{\text{out}}}. \tag{5.7}$$

In the limit of $\kappa_{\text{in}} \ll \kappa_{\text{out}}$, the measured intensity thus is proportional to the absorption coefficient for the incoming light, κ_{in}. In the limit of $\kappa_{\text{in}} \gg \kappa_{\text{out}}$, however, the measured intensity is equal to the upper limit $A \cdot I_0$, which is a constant and the spectrum is saturated. For absorption measurements in fluorescence yield detection mode, the situation is unfavorable: for excitation above the absorption edge, the emitted photons have an emission energy below the investigated absorption edge and thus a lower absorption coefficient κ_{out} than that of the incident light. When now adding more absorbing atoms (or ions) to the solution with absorption edges below the investigated one (in this case, the O K absorption edge), both the absorption coefficient for the incoming and the outgoing photons, κ_{in} and κ_{out}, are increased. Assuming, that the change of the two coefficients is very similar (e.g., $\Delta\kappa$), which is the case for photons high above the additionally introduced absorption edge, the measured intensity I_{out} can be estimated as:

$$I_{\text{out}}(h\nu_{\text{in}}, \Delta\kappa) = A \cdot I_0 \cdot \frac{\kappa_{\text{in}} + \Delta\kappa}{\kappa_{\text{in}} + \kappa_{\text{out}} + 2\Delta\kappa}. \tag{5.8}$$

For $\Delta\kappa \geq 0$, this function is decreasing monotonically, i.e., the higher the change in the absorption coefficient $\Delta\kappa$ by the additionally introduced absorption edge, the smaller the measured intensity at the pre-edge (below the absorption edge of water).

In the present case, $\Delta\kappa$ is determined by the absorption coefficients of the added salts for photon energies near the O K absorption edge. For example, for salts containing chlorine, the Cl L absorption edge, and for salts containing potassium, the K L absorption edge at energies below the investigated O K absorption edge are relevant for an increase of the absorption coefficients. Likewise, all other elements which occur in the list of salts used in this thesis can absorb photons and thus increase the absorption coefficients. Using equation (5.8), it is obvious that independently of the type of salt added to the diglycine solution, the pre-edge feature in the absorption spectrum should lose intensity, which is observed in the experiment.

For a qualitative estimation of $\Delta\kappa$, tabulated values can be used for the absorption coefficients of the individual salts [220]. Henke *et al.* implemented these tables into an open source script, which calculates the inverse of the absorption coefficient for compounds with given chemical composition and density [221]. This script was used to obtain absorption coefficients for salts with a density as expected for 0.5 M aqueous solutions in the relevant energy range. They can be ordered by size as

$\kappa(\mathrm{CaCl_2}) > \kappa(\mathrm{KCl}) > \kappa(\mathrm{MgCl_2}) > \kappa(\mathrm{NH_4Cl}) > \kappa(\mathrm{NaCl}) \approx \kappa(\mathrm{LiCl})$ for the series of different cations and $\kappa(\mathrm{KBr}) \approx \kappa(\mathrm{KSCN}) > \kappa(\mathrm{KI}) \approx \kappa(\mathrm{KCl}) > \kappa(\mathrm{KF})$ for the series of different anions (not containing oxygen). Noticeably, these trends are qualitatively also observed (in reversed order) in the intensity of the pre-edge feature in the XAS spectra in Fig. 5.12. One thus can state that already the effect the added salts have on the characteristics of the self absorption can explain the observed intensity variations, challenging the interpretations by Aziz *et al.* [43].

To obtain absorption spectra that are not or only very weakly affected by saturation effects, one can either use a transmission measurement setup (limited to thin samples), partial electron yield, or ion yield detection with its extremely short escape depth of a few Å. Another bulk sensitive method using soft x-rays is the so-called "inverse partial fluorescence yield detection" [222], where the absorption edge is scanned and emitted photons originating from a lower lying absorption edge are detected to then calculate the desired absorption spectrum. In principle, this technique is also applicable in the present case using the N K emission that is simultaneously measured with the spectrometer described in Sec. 2.3 and [108]. However, the N K yield is very low for an excitation above the O K edge. Since it would require considerably longer measurement times to achieve a reasonable signal-to-noise ratio, in turn leading to experimental issues such as an oxidation of the used membrane, this kind of analysis was not performed in the present case.

The spectral shape of the x-ray emission spectra, however, is not affected by saturation effects, making a salt-specific analysis of the changes feasible. XES spectra of the mixed solutions, excited at the pre-edge absorption resonance with an excitation energy of 532.7 eV, are shown in Fig. 5.13. The series of chlorine salts with different cations is displayed in panel 5.13.1 and panel 5.13.2 depicts the series of the potassium salts with different anions. Again, the spectra are ordered with respect to the appearance of the salts in the Hofmeister series, with chaotropes being located at the top and kosmotropes at the bottom, respectively. To emphasize the changes to the spectrum of pure diglycine induced by the addition of the salts, difference spectra are shown in the respective color code below the spectrum of the pure diglycine solution. After normalizing the spectra to the integrated emission intensity in the displayed emission energy region, the difference spectra were obtained by subtracting the black spectrum (representing the pure diglycine solution) from the spectra of the mixed solutions, respectively. Since the emission spectrum of nitrate ions in aqueous solution overlaps with the emission of diglycine, a reference spectrum of a 2 M $\mathrm{KNO_3}$ solution was acquired and subtracted from the the spectrum of the mixed solution to try to eliminate this contribution to the measured spectrum. The resulting spectrum bears a reasonable spectral shape. For details, see Fig. A.4 in the appendix. Unfortu-

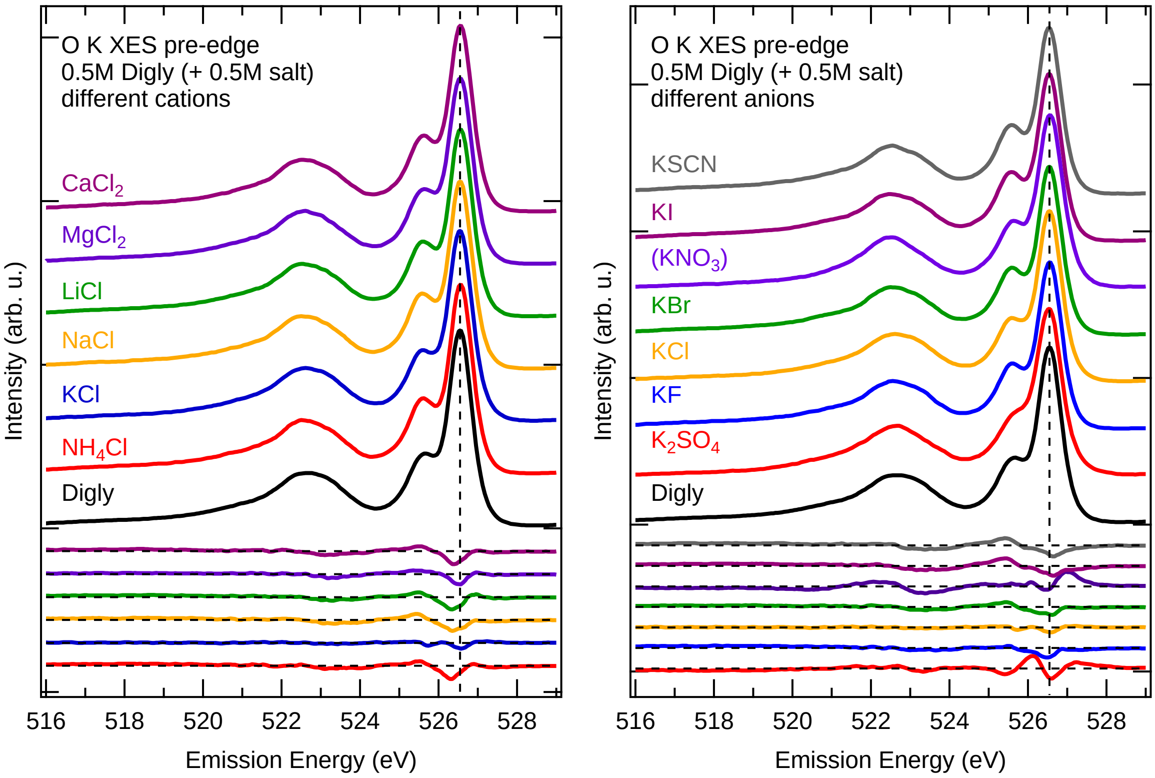

5.13.1

5.13.2

FIGURE 5.13. O K XES spectra of diglycine in aqueous solution with additional salt, resonantly excited at the pre-edge absorption resonance with hν=532.7 eV. The spectra are normalized to the integrated emission intensity in the displayed emission energy region. Below, difference spectra of “Digly with salt - pure Digly” are given. The influence of different cations on the spectrum of diglycine is depicted in Fig. 5.13.1, the situation for different anions is shown in Fig. 5.13.2, respectively. For KNO$_3$, a reference spectrum of a pure 2 M KNO$_3$ solution was subtracted of the measured spectrum, see also Fig. A.4 in the appendix.

nately, no such a reference spectrum for K$_2$SO$_4$ was acquired or available in literature. Hence, the observed changes in the spectrum for the mixed K$_2$SO$_4$ solution might also originate from emission of sulfate ions.

A possible background signal in the spectra which originates from an oxidation of the used membrane can be excluded. Special care was taken to prevent an oxidation of the membrane by changing the illuminated spot on the membrane after each individual solution. In addition, spectra of pure water were measured on each spot afterwards, which did not show any differences which would point towards an oxidation of the membrane. Furthermore, the spectra were measured in an order explicitly not following the Hofmeister series and were reproduced in parts to exclude any other effects which might change the spectral shape over time in the best possible way.

For the cations (panel 5.13.1), the difference spectra are all very similar. The biggest deviation from the pure diglycine solution is observed for the emission feature at 526.5 eV, which decreases in emission intensity when salt is added to the solution. Also on the low-energy flank of this feature, adding salt leads to a decrease in intensity. Even if the variations in the spectra are small, an ordering qualitatively following the Hofmeister series can be identified. The addition of NH_4^+ leads to the highest maximum intensity (but lower than for pure diglycine) and the lowest intensity on the low-energy flank. For the remaining salts, the maximum intensity decreases and the low-energy flank gains in intensity in the order $NH_4^+ > Na^+ \approx Li^+ > Mg^{2+} \approx Ca^{2+}$. At the same time, the peak at 525.5 eV slightly gains in intensity and the maximum shifts by up to ≈ 0.1 eV to lower emission energies with small differences between the individual salts, albeit, not showing a specific trend with respect to the Hofmeister series. The spectrum for KCl, in contrast, shows a slight intensity decrease for this peak. Also some changes in the low-energy region of the emission spectrum below ≈ 524 eV occur for most of the salts (except for KCl, which is very similar to the pure diglycine spectrum in this energy region). The broad feature around 522.7 eV loses some intensity at the high-energy side, leading to a shift of its maximum to slightly smaller emission energies. Furthermore, the small feature around 517 eV increases. These changes, however, are almost identical in (their small) size and no ion-specificity is observed.

For the series of anions (Fig. 5.13.2) the situation is similar, except for the spectra of the oxygen containing salts KNO_3 and K_2SO_4, which bear significantly different structures. This can easily be explained by the emission of excited nitrate and sulfate ions, which overlaps with the emission of the diglycine molecules. Despite the subtraction of a reference spectrum (for KNO_3), the shape of the difference spectrum still reveals some deviations from the general trend observed for the other salts. For the high-energy flank of the most intense peak (around 527 eV), a higher intensity is observed in the KNO_3 spectrum, whereas the other salts exhibit a reduced intensity in this energy region compared to the diglycine spectrum. Similarly, the KNO_3 spectrum exhibits a higher emission intensity around 522 eV. Unfortunately, no reference spectrum was acquired or available for K_2SO_4, which hinders a potential correction. The following analysis is thus reduced to the remaining anions SCN^-, I^-, Br^-, and F^-.

The features observed in the respective difference spectra are very similar to the ones discussed for the different cations. The peak at 526.5 eV and its low-energy flank loses intensity to a comparable degree for all anions. The feature at 525.5 eV increases and slightly shifts to lower emission energies. The intensity increase describes a trend following the Hofmeister series with the chaotropic anions I^- and SCN^- leading to the highest (and comparable) intensity, followed by Br^- and finally the slightly kosmotropic F^-, which exhibits almost the same maximum intensity as pure diglycine ($I^- \approx SCN^- > Br^- > F^-$). This trend can likely be attributed to an increasing interaction strength for anions with a higher chaotropic character with the nitrogen moieties of the molecule. This will be discussed in more detail in Sec. 5.3.2. The high-energy flank of the feature around 522.7 eV decreases to a similar amount for all anions, leading to a shift of the maximum to lower emission energies. The weak feature around 517 eV gains in intensity for all anions, without any mentionable variations between the different anionic species.

Due to the limited available experimental data and theoretical work on mixed solutions of peptides and ions, the interpretation of what kind of interaction causes the observed changes in the emission spectrum of diglycine is difficult and has to remain speculative at the moment. For the interpretation, one has to keep in mind that all oxygen atoms of the diglycine molecule are excited at the O K pre-edge. Accordingly, it is not possible to specify the oxygen site where a possible interaction between ion and diglycine takes place. In general, one would expect that the positively charged cations prefer moieties of the molecule with a high electron density or negative charge. In the case of diglycine in aqueous solution, such moieties are found at the deprotonated carboxyl group and in proximity of the peptide oxygen, due to its strong electronegative character and electron-withdrawing properties. In contrast, the negatively charged anions are rather expected to interact at sites with more positively charged character such as the protonated amino group.

A good starting point for the interpretation are the spectra shown for diglycine at different pH values in Sec. 5.2. In conjunction with Fig. 5.11, the changes in the XES spectrum after excitation of the O K pre-edge for diglycine in basic solution are elaborated. For the readers convenience, Fig. 5.14.1 again shows the spectra of diglycine in aqueous solution at neutral (black) and high pH (blue). To recapitulate the observed changes when going from medium to high pH, these are: a decrease of the most intense feature at 526.5 eV, an increase of the feature at 525.5 eV accompanied by a small shift towards lower emission energies, and a decrease in intensity at the high-energy side of the broad feature centered at 522.7 eV. These changes are qualitatively identical (yet much stronger) to the ones observed for the salt containing mixed solutions, as is displayed exemplarily for NaCl (orange) in Fig. 5.14.1.

As described in Sec. 5.2, the main effect causing these variations for diglycine in basic solution is the change of the electrical charge state of the molecule. At high pH, diglycine is in its negatively charged, anionic state with a deprotonated carboxyl (COO^-) and a deprotonated amino (NH_2) group. The supply of OH^- ions by

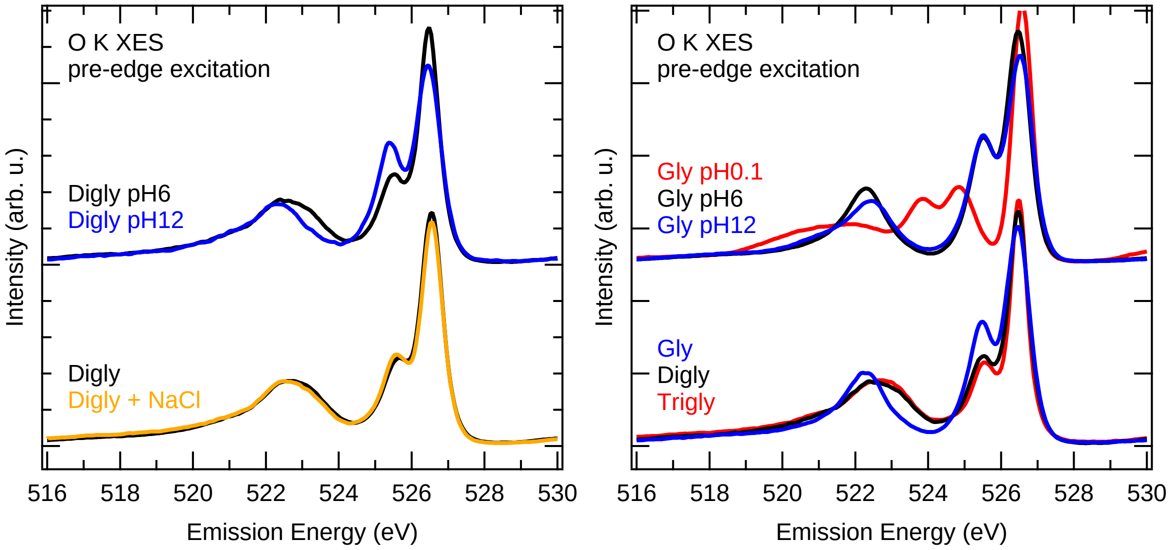

5.14.1

5.14.2

FIGURE 5.14. XES spectra after resonant excitation of the O K pre-edge. Panel 5.14.1: spectra of diglycine at medium and high pH (top, see also Fig. 5.11) and in mixed aqueous salt solution, exemplarily shown for NaCl (bottom). Panel 5.14.2: spectra of glycine at different pH (top, see also Fig. 5.7) and comparison of the spectra for glycine, diglycine, and triglycine in aqueous solution (bottom, see also Fig. 5.3.4).

adding NaOH to the solution thus leads to the removal of the additional proton at the amino group with a strong impact on the electronic structure. However, sodium cations (which, according to the results in this section, also interact with the diglycine molecule) are also added to the solution in form of NaOH for high pH. Hence, an unambiguous attribution of the changes in the XES spectrum of diglycine to either of those possibilities is not feasible.

To further narrow down the number of potential interaction sites, one can take a look at the spectra measured for glycine (which does not have a peptide oxygen) at different pH, which are presented in Figs. 5.7 and 5.14.2. They reveal that for increasing pH values, i.e., more Na^+ and OH^- ions in the solution, the feature at 526.5 eV loses intensity, but the feature at 525.5 eV is basically not affected. For lower pH values and thus a protonation of the carboxyl group, the spectral shape changes significantly. The peak at 526.5 eV gains in intensity (and shifts to higher emission energies), whereas the peak at 525.5 eV loses intensity and even disappears for a complete protonation of all carboxyl groups in the solution. A trend concerning the interaction strength between different cations and the peptide can be derived from the magnitude of the intensity decrease for the feature at 526.5 eV, albeit, the observed effect is very small. For the more kosmotropic cations the loss is bigger than for the chaotropes. The intensity at the peak maximum qualitatively follows the Hofmeister series $NH_4^+ \approx K^+ > Na^+ \approx Li^+ > Mg^{2+} \approx Ca^{2+}$.

In their RIXS study of different acetate solutions, which show a similar spectral shape at the O K pre-edge (see also Fig. 4.14), Petit *et al.* conclude that "an increasing interaction strength between acetate and counter-ion leads to an intensity decrease of the peak at 525.8 eV" [48], in agreement with previous work performed on zinc acetate solutions [46]. Furthermore, they assign this feature to the emission of out-of-plane lone-orbitals located at the carboxyl group of the acetate ion. The observed increase in intensity for the feature at 525.5 eV, which is observed for most of the salts, thus rather questions a direct interaction between cations and the carboxyl group and points towards an interaction of the cations with the high electron density around the peptide oxygen.

An observation which strengthens this interpretation is the decrease in intensity at the high-energy flank of the feature at 522.7 eV when salt is added to the solution. The comparison of the XES spectra of glycine, diglycine, and triglycine in Figs. 4.14 and 5.14.2 show that an increasing number of peptide bonds in the molecule leads to a higher emission intensity in this energy region. Hence, the decrease in intensity observed for the salt containing solutions suggests a deformation of the molecular orbitals or redistribution of the electron density in proximity of the peptide oxygen, potentially induced by the presence of close-by ions in the solution.

With the interpretation given above, almost all changes in the O K XES spectra have been explained. Only the very small increase in intensity for emission energies around 517 eV is not discussed yet. In a XES study of water molecules confined in a micelle lattice [223], the authors identify a faint structure at 517.5 eV in the XES spectrum, which they attribute to complex interactions of water molecules with Cl^- ions in presence of a micelle head-group. Furthermore, the authors claim that this feature is "due to states of primarily Cl^- 3s character forming bonding combinations with the $1b_2$ orbital of H_2O" [223]. An explanation for the increased intensity in the spectra presented in this thesis might thus be hybridization of distinct molecular orbitals of diglycine with states derived from ions in the solution.

5.3.2 Ions interacting with the nitrogen sites of diglycine

In Fig. 5.15, N K XES spectra of diglycine in aqueous salt solutions are shown, resonantly excited at the N K pre-edge. All spectra are normalized to the integrated emission intensity in the displayed energy region and ordered with respect to the appearance of the respective salt in the Hofmeister series, with chaotropes located at the top and kosmotropes at the bottom, respectively. For the nitrogen containing salts, reference spectra of pure NH_4Cl (2 M), KSCN (1 M), and KNO_3 (1 M) solutions were

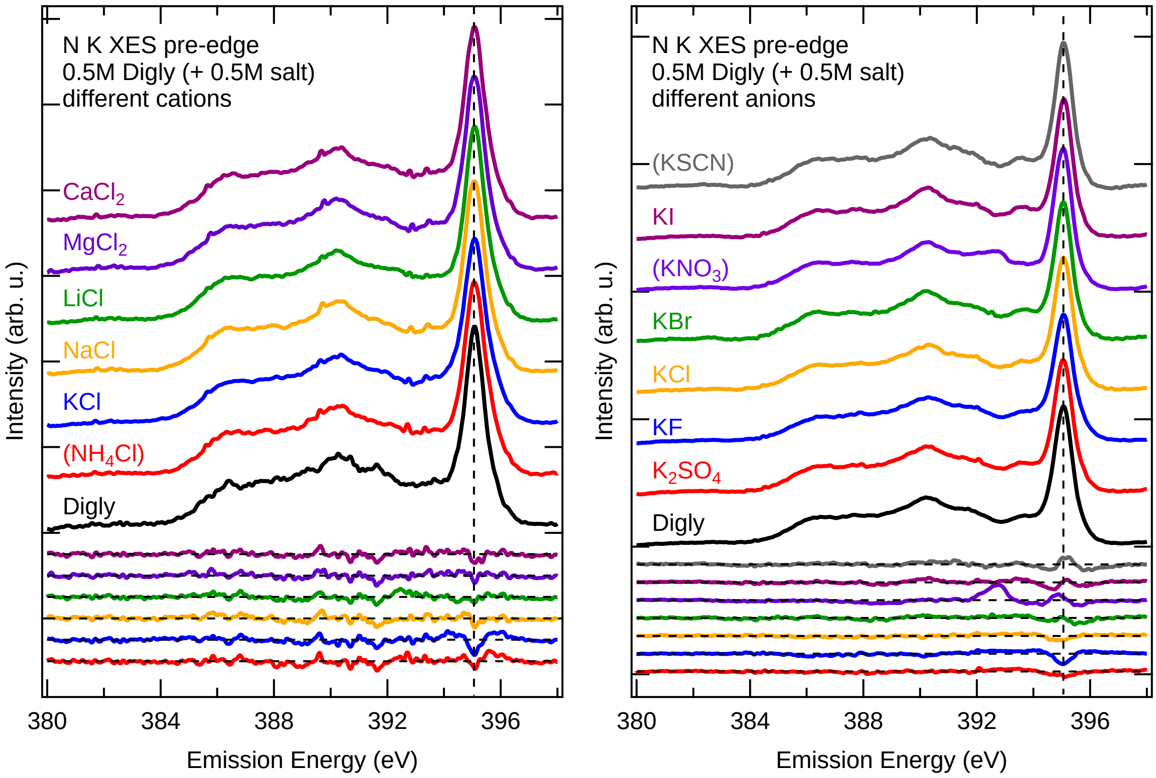

5.15.1

5.15.2

FIGURE 5.15. N K XES spectra of diglycine in aqueous solution with additional salt, resonantly excited at the pre-edge absorption resonance with hν=401.9 eV for the series of different cations (5.15.1) and hν=401.6 eV for the series of different anions (5.15.2), respectively. The spectra are normalized to the integrated emission intensity in the displayed emission energy region. Below, difference spectra of "Digly with salt - pure Digly" are given. For the nitrogen containing salts, reference spectra of pure salt solutions were subtracted, see also Fig. A.5 in the appendix.

recorded. They were subtracted from the spectra of the mixed solutions to eliminate the contribution of excited salt ions to the measured XES spectra. This subtraction procedure, however, is potentially erroneous since the weighting factor used had to be chosen arbitrarily. For more details, see Fig. A.5 in the appendix. The series for salts with different cations is displayed in the left panel (5.15.1), whereas the right panel (5.15.2) shows the series of salts with different anions. The two series were recorded in two different experimental runs with slightly different excitation energies, i.e., with hν= 401.8 eV for the different cations and with hν= 401.6 eV for the different anions. This explains the somewhat different relative emission intensities at emission energies around $\approx$393 eV and for the prominent feature at 395 eV, as can be seen also in the N K RIXS map of diglycine in Fig. 5.1.2. Since no single spectrum with sufficient exposure times for pure diglycine was measured using the same excitation energy as the complete series of the mixed solutions for different cations, the diglycine spectrum shown in the left panel was extracted from the RIXS map. To improve the signal-to-noise ratio, however, the spectra spectra with hν= 401.7 - 401.9 eV were added. Below the spectrum of the pure diglycine solution, difference spectra are shown that were calculated by subtracting the spectrum of pure diglycine from the shown spectra of the mixed solutions, respectively. Overall, all spectra are very similar and only a small change in the intensity at $\approx$ 395 eV can be seen. This, however, can be related to the integration of spectra excited at different excitation energies to obtain the diglycine spectrum, since the feature at 395 eV is prone to strong intensity changes in this excitation energy region. Performing the subtraction using a single spectrum extracted from the RIXS map leads to difference spectra with a much worse signal-to-noise ratio but no significant dip at 395 eV.

For the series of different anions the situation is different. Here, the maximum intensity of the feature at 395 eV significantly changes with the type of salt and an order of KSCN > KNO_3 > KI > KBr > KCl $\approx$ K_2SO_4 > KF is found. However, the observed variations in relative emission intensity are rather small. For emission energies below 394 eV no significant differences in the spectra are found, except for KNO_3 where clearly more intensity is observed at 392.6 eV and at the low-energy side of the elastic peak at 400.2 eV (not shown) compared to the spectrum of pure diglycine. As was already mentioned above, the spectrum shown in Fig. 5.15.2 was derived by subtracting a reference spectrum of a pure KNO_3 solution from the spectrum of the mixed solution containing diglycine and KNO_3. However, since the reference spectrum does not exhibit a distinct emission feature at 392.6 eV (see Fig. A.5.5 in the appendix), the origin of this feature is not related to the emission of nitrate ions. In this case, the additional intensity can be attributed to gas-phase nitrogen from an air bubble behind the membrane during the measurement. Gas-phase nitrogen has a strong absorption resonance at 400.88 eV with a fairly broad vibrational progression [224]. The spectator emission at the first absorption resonance consists of a single line which is centered at 392.3 eV [129] and slightly shifts to higher emission energies for higher excitation energies. In addition, a vibrational progression in the participant emission is observed for higher excitation energies, which explains the distinct peak next to the Rayleigh line at 400.2 eV [129].

As was thoroughly discussed in the previous sections, only the peptide nitrogen is excited at the N K pre-edge absorption resonance. For a more comprehensive understanding what causes the observed changes in the spectra, it is helpful to also consider the spectra taken with higher excitation energies where also the amino nitrogen is excited. For this thesis, two more sets of spectra were recorded. One using an excitation energy approximately 20 eV above the pre-edge absorption resonance, i.e.,

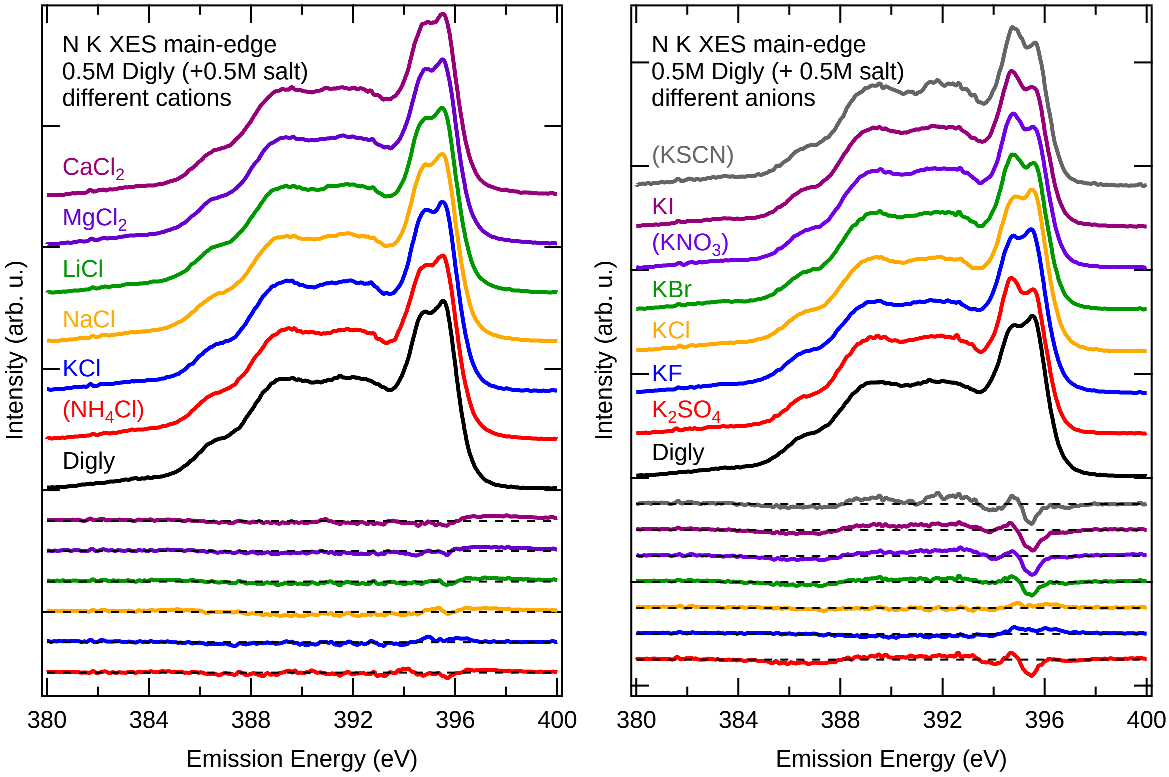

5.16.1

5.16.2

FIGURE 5.16. N K XES spectra of diglycine in aqueous solution with additional salt, resonantly excited at the main absorption resonance with hν=406.5 eV for the series of different cations (5.16.1) of different anions (5.16.2), respectively. The spectra are normalized to the integrated emission intensity in the displayed emission energy region. Below, difference spectra of "Digly with salt - pure Digly" are given. For the nitrogen containing salts, reference spectra of pure 2M salt solutions were subtracted, see also Fig. A.5 in the appendix.

non-resonantly excited, and one series using an excitation energy which corresponds to an excitation of the main absorption resonance at ≈ 406.5 eV (see, for example, Fig. 4.9). As the RIXS map of diglycine shown in Fig. 5.1.2 reveals, the overall spectral shape of the emission does not change for excitation energies above the main-edge. Accordingly, the changes in the spectrum induced by the additional salts in the solution are qualitatively the same for both sets of spectra. However, the observed changes are more clearly visible in the spectra recorded at the main-edge, which are thus used for the following discussion.

Note that the mixed solutions have been measured using an excitation energy of 406.5 eV, whereas the spectrum of the pure diglycine solution was excited with

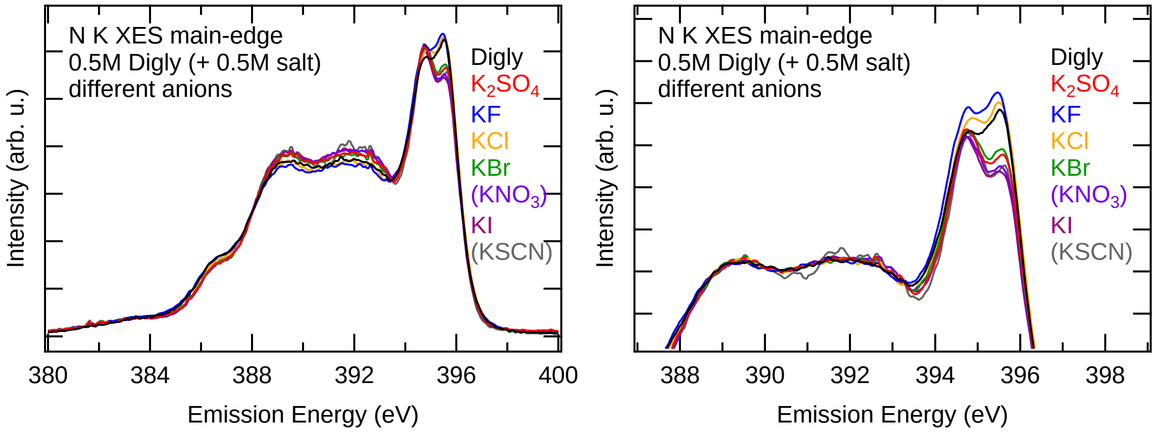

5.17.1

5.17.2

FIGURE 5.17. Spectra of diglycine with salts with different anions shown in Fig. 5.16.2, displayed without constant offsets (5.17.1), and zoomed view with the spectra being normalized to the integrated emission intensity in the energy region from 388 - 393.5 eV (5.17.2).

406.1 eV (in a different experimental run). Since the spectral shape of the emission spectrum does not change significantly in this excitation energy region this does not affect the following discussion. The series of spectra for salts with different cations are depicted in Fig. 5.16.1. Only very small changes in the spectra can be identified. A barely visible trend, however, can be observed in the intensity of the foot at the high-energy side of the spectrum at ≈ 398 eV, which follows the Hofmeister series with the kosmotropic cations such as Ca^{2+} showing slightly higher intensities than the chaotropes such as NH_4^+ and K^+.

The situation for the series of different anions is much more interesting. Here, strong variations can be identified, especially in the intensity ratio of the two peaks in the double peak feature at high emission energies. To show the variations more clearly, the spectra are plotted without constant offsets in Fig. 5.17.1, normalized to the integrated emission intensity in the displayed emission energy region. As one can learn from the spectra, not only the peak ratio at high emission energies changes, but also the relative intensity of the energy region of ≈ 384 - 394 eV is prone to variations as a function of the anion. This is more clearly highlighted in Fig. 5.17.2, which shows a zoomed view of the relevant emission energy region. Here, the spectra are normalized to the integrated emission intensity in the energy region from 388 - 393.5 eV.

Regarding the peak ratio at higher emission energies, Fig. 5.17 shows that for KF and KCl the double peak feature resembles the situation for pure diglycine, whereas for the other salts the peak at 394.7 eV has a significantly higher relative emission intensity compared to the peak at 395.5 eV. The spectral shape for lower emission energies (≈ 388 - 393.5 eV), however, is comparable for all mixed solutions. Yet, the relative emission intensity observed in this energy region changes with respect to the intensity of the high-energy features above 393.5 eV. When sorting the spectra according to the ratio of the relative emission intensities in these two energy regions, one obtains the order KF > KCl > KBr ≈ K_2SO_4 > KNO_3 ≈ KI ≈ KSCN. This sequence qualitatively describes the Hofmeister series of anions and is also found in the intensity of the emission feature at 386.6 eV in reversed order. Note, that the subtraction of the background signal originating from the nitrogen containing salt anions for the spectra of KNO_3 and KSCN is mainly based on a subjective evaluation of the overall spectral shape of the resulting difference spectrum. Whereas the spectrum of pure KSCN exhibits two clearly visible emission features at 391.4 eV and 394.8 eV (Fig. A.5.4), facilitating the background subtraction, the spectrum of the KNO_3 solution is rather broad with its maximum emission intensity around ≈ 395 eV (Fig. A.5.6). Hence, for KNO_3 the subjective character of the subtraction procedure may easily lead to changing relative emission intensities for the energy regions discussed above, which in turn can influence the positioning of KNO_3 in the observed ordering of the individual anions.

The only spectrum that is clearly not following the trend in the Hofmeister series for anions is the spectrum for K_2SO_4. Instead of a strong resemblance with the spectrum of pure diglycine based on the kosmotropic character as it is the case for KF and KCl, the peak ratio of the high-energy features and their combined relative emission energy compared to the low-energy region is very similar to the spectra of the chaotropic anions. A possible explanation for this might be that the sulfate ion is divalent, whereas all other anions investigated here carry only a single charge. Why this might have such a strong influence on the emission spectrum will be discussed in more detail below.

The only marginal changes in the spectra shown in Figs. 5.15.1 and 5.16.1 lead to the conclusion that the interaction between diglycine molecules and different cations in the mixed solutions does not affect the local electronic structure in proximity of the nitrogen sites of diglycine. The variations in the interaction strength for different cations with the diglycine molecule, which were derived based on the interpretation of the O K XES spectra given in the previous section, are not found in the N K emission spectra.

In contrast, strong ion-specific effects are observed in the spectra for the series of different anions and a trend which follows the Hofmeister series is found. Whereas the changes induced in the spectra resonantly excited at the N K pre-edge absorption resonance (probing the peptide nitrogen) are very small, considerable variations in the spectra excited at the N K main-edge absorption resonance are found. On first sight, this implies an interaction of the negatively charged anions with the positively charged amino group of diglycine. Thereby, a concrete indication of different interaction strengths can be found in the peak ratios of the two high emission energy features at 394.7 and 395.5 eV. As was thoroughly shown in the previous sections of this thesis, the emission feature at 394.7 eV can be attributed to a dissociation of a proton from the protonated amino group on the time scale of the x-ray emission process, with a subsequent emission of the lone-pair orbital of the amino nitrogen. In contrast, the peak at 395.5 eV is ascribed to the emission of the lone-pair orbital of the peptide nitrogen, similarly to the peak at 394.7 eV for resonant pre-edge excitation. Yet, the isolated contributions to the measured spectrum containing these emission features consist not only of one single feature but also exhibit more emission lines. In first approximation, the spectral shape of these emission spectra for non-resonant excitation has been derived in Sec. 5.1.1 using the emission spectrum of glycine as a reference for the amino nitrogen. Subtracting the weighted spectrum of glycine from the spectrum of diglycine then results in an approximated spectrum of the peptide nitrogen. To check whether the variations in the spectra in Fig. 5.16.2 can be traced back to a specific contribution, Fig. 5.18 shows these spectra with a different normalization. Since the strongest deviations are observed for the chaotropes Br^-, NO_3^-, I^-, and SCN^-, as well as the divalent $K_2SO_4^{2-}$, the discussion is reduced to these anions.

In the left panel, the spectra of the mixed solutions are normalized to the maximum intensity of the feature at 395.5 eV. Interestingly, this normalization leads to almost identical intensities for the weak emission feature at 386 eV (including the spectra for KCl and KF, which are not shown here). Since the peak at 395.5 eV is attributed to the emission of peptide nitrogens, this indicates that also the feature at 386 eV is part of this contribution to the spectrum. This is in accordance with the findings in conjunction with the comparison of the XES spectra of glycine, diglycine, and triglycine in Fig. 5.2. Assuming the peptide nitrogen contribution is identical for all spectra (no matter which kind of salt is added to the solution), the calculation of difference spectra using this normalization reveals the changes in the amino nitrogen contribution induced by the interaction with the added salts. Accordingly, the spectrum of diglycine was subtracted from the spectra of the mixed solutions to obtain the difference spectra shown below. Thereby, a weighting factor of 0.9 was used to obtain difference spectra with a reasonable shape. Note, that the best results were obtained when shifting the spectrum of pure diglycine by about 20 - 60 meV to higher emission energies prior to the subtraction. This can be justified by small deviations in the calibration of the different spectra. Since the flank of the spectrum is very steep at ≈ 396 eV, without this energetic offset, a comparatively high feature is observed in the difference spectra

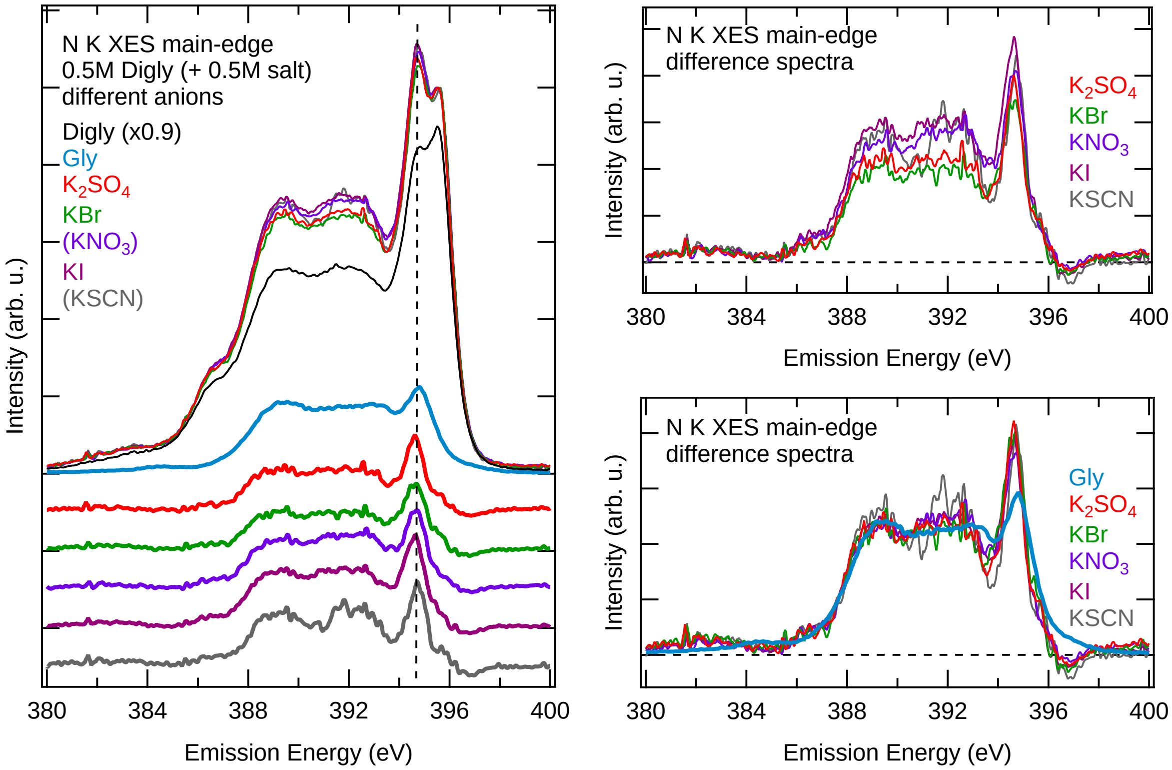

FIGURE 5.18. Left: Spectra normalized to the maximum of the peak at 395.5 eV. The spectrum of diglycine additionally has been scaled by a factor of 0.9. Difference spectra are depicted at the bottom (see text for details). Right: Calculated difference spectra, plotted without constant offsets (top) and normalized to the integrated emission intensity in the displayed energy region (bottom). For comparison, a spectrum of glycine is shown in blue.

at this energy. In turn, this shift leads to a dip in the resulting difference spectra with slightly negative intensities in the energy region around ≈ 397 eV.

All calculated difference spectra are very similar, with a prominent feature at 394.6 eV and less pronounced emission features for lower emission energies. Overall, the spectra resemble the spectrum of glycine shown in blue, taken at the same excitation energy. This spectrum was generated by integrating the emission spectra in the RIXS map of glycine (Fig. 5.1.1) for excitation energies from 406.3 - 406.7 eV to improve the signal-to-noise ratio. The integrated emission intensity of the difference spectra for the slightly chaotropic KBr thereby is smaller than for the stronger chaotropic salts such as KSCN or KI. This can be more easily seen in the top right panel, which shows the calculated difference spectra in direct comparison without constant offsets. In the bottom right panel, the difference spectra are normalized to the integrated emission intensity and compared to the spectrum of glycine shown in blue, emphasizing the strong resemblance of the spectra.

Yet, some differences compared to the spectrum of glycine can be spotted. The weak emission feature at 386.4 eV appears somewhat more pronounced and a broad feature at ≈ 382 eV is observed in the difference spectra, which is comparable in intensity with the peak at ≈ 384 eV in the spectrum of glycine. Most noticeable, the peak at 394.6 eV is sharper and more intense for the difference spectra than for the glycine spectrum. The increased intensity and the deeper dip at 394.6 and 393.7 eV, respectively, are also found for non-resonantly excited spectra of glycine at lower pH values (see Fig. 5.6). Possible reasons for the difference between the N K XES spectra of glycine at medium and low pH have been discussed in the previous sections.

In literature only limited work is found about potential interaction sites of anions with peptides. A molecular dynamics study of Heyda *et al.* showed that none of the investigated halide anions (F^-, Cl^-, Br^-, I^-) showed any appreciable attraction to the peptide bond or the hydrogen atom attached to the nitrogen [41]. They also found indication that bromide and iodide interact more strongly with hydrophobic moieties than with the peptide bond. However, a later study including molecular dynamics simulations, NMR experiments, and thermodynamic measurements determined a combination of the peptide bond and the neighboring α-carbon as binding sites for strongly chaotropic anions such as SCN^- and I^- [212]. Schwartz *et al.* claim to have identified an interaction of sulfite (SO_3^{2-}) and sulfate (SO_4^{2-}) ions with the protonated amino group in the N K XAS spectra of triglycine, which is not observed for bromide. However, a similar effect of bromide and sulfate ions on the XES spectra shown in this thesis is observed. A better agreement between the results presented here and molecular dynamics calculations in literature is found for the work of Paterová *et al.*, which shows that the binding of anions is dominated by the influence of the positively charged amino group of the peptide (triglycine) [39].

As was shown above, the main changes in the spectra of diglycine in aqueous solution for different anions can be approximated by a stronger relative contribution of the amino nitrogen to the emission spectrum. In principle, this could be explained by differences in the absorption cross-sections for the two nitrogen atoms of diglycine at the main-edge induced by the presence of salt ions in the solution (assuming the emission cross-section is not affected), or by changes in the emission cross-section of at least one of the two nitrogen atoms. An effect of different absorption cross-sections, however, seems to be unlikely. For non-resonant excitation, qualitatively the same approximate observation can be made, namely that the contribution of the amino nitrogen to the emission spectrum is increased in the presence of chaotropic anions. The respective measured data and calculated difference spectra can be found in

Fig. A.6 in the appendix. Since in the non-resonant, ionizing case the absorption cross-section does not depend on the symmetry and localization of a distinct intermediate state, a potential influence of ions on the absorption probability at the main-edge (showing qualitatively the same results as observed for the non-resonant spectra) can be neglected.

To achieve a bigger contribution of the amino nitrogen to the emission spectrum based on different emission cross-sections two scenarios are possible, namely an enhanced emission of the amino nitrogen or a reduced emission of the peptide nitrogen. On first thought, normalizing the measured spectra with respect to the measurement time and photon flux should reveal whether the total intensity increases or decreases, and thus which possible interpretation is more likely. However, the presence of different salt ions in the solution complicates the analysis. Indeed, the integrated measured emission intensity changes monotonically with the absorption coefficients of the salt solutions already used in Sec. 5.3.1 to discuss the effect of saturation effects, with a higher absorption coefficient leading to a lower nitrogen emission intensity (not shown). Thus, an unambiguous determination is not possible based on the total emission intensity.

Yet, an increase of the relative emission intensity of the amino nitrogen can potentially be derived from the negative charge of the anions, making it likely that the anions interact with the positively charged, protonated amino group via ion-dipole interactions. The presence of a negatively charged ion in proximity to the amino group would lead to an increased negative charge around the amino nitrogen and the hydrogen atoms with covalent bonds to it. An increase in the electron density around the amino nitrogen consequently would lead to an enhanced emission intensity. The additional charge will at the same time influence the shape and localization of the molecular orbitals of the molecule. Thus, it is not surprising that the relative emission intensity of different emission features slightly changes. This in turn might explain the observed variations in the spectral shape of the difference spectra compared to the reference spectrum of glycine in the simple building block approach.

Concluding this section, one can state that ion-specific effects are observed for diglycine in aqueous solution containing potassium salts with different anions. Whereas chlorine and fluorine ions don't show a noticeable effect on the electronic structure of diglycine, the chaotropic anions Br^-, NO_3^-, I^-, and SCN^-, as well as the strongly kosmotropic (divalent) anion SO_4^{2-} induce very strong changes. The type and site of interaction can not be determined unambiguously, however, an interaction with the protonated amino group of diglycine seems to be very likely. The interaction strength thereby changes with the type of salt in the sequence $KBr \approx K_2SO_4 > KNO_3 \approx KI \approx KSCN$, qualitatively following the Hofmeister series for anions. The exceptional behavior of

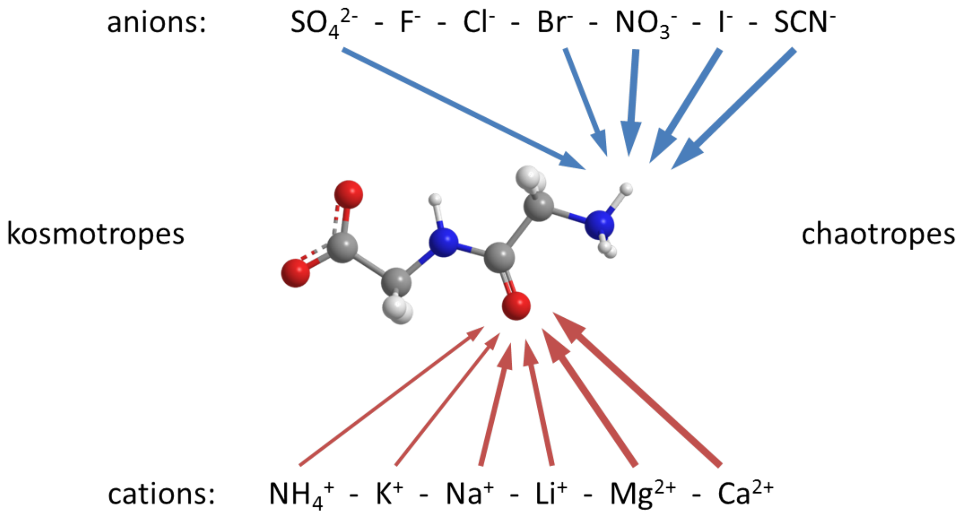

FIGURE 5.19. Schematic overview of the interaction of different anions and cations with diglycine in aqueous solution. The thicknesses of the arrows indicate differences the interaction strength (not to scale).

the sulfate ion, however, can not be explained without a doubt but likely be traced back to its divalent charge.

A schematic overview of the results about ion-specific effects for the studied anions and cations with diglycine in aqueous solution based on the O K and N K XES and XAS spectra discussed in this thesis is displayed in Fig. 5.19. Here, a stronger interaction with the diglycine molecule is indicated by a thicker arrow, pointing towards the site where the interaction likely takes place, namely the protonated amino group for the anions and the electron density around the peptide oxygen for the cations.

5.4 Summary

In this chapter, the electronic structure of diglycine in different aqueous environments has been studied. Starting in Sec. 5.1, the influence of the surrounding water molecules in a pure aqueous solution of glycine and diglycine was investigated. By comparing the RIXS maps of the aqueous solution with the solid state discussed in chapter 4, some differences have been found, which likely can be attributed to dipole-dipole interactions between the locally charged functional groups of the amino acid and the peptide on the one side, and the polar water molecules on the other side. Furthermore, hybridization of the molecular orbitals of the studied molecules with the surrounding water molecules might occur, which in turn also would have an effect on the electronic structure and thus the x-ray emission spectra. However, the identified variations between the solid state and aqueous solutions are not very pronounced.

In Sec. 5.2, it is shown that the electronic structure of glycine and diglycine (and peptides in general) can intentionally be manipulated by changing the pH of the aqueous solution. In the detailed discussion of the XES spectra of glycine at various pH values ranging from strongly acidic to strongly basic solutions, the changes in the local electronic structure by protonating or deprotonating the functional groups has been addressed. The spectra also provide evidence that the local change of the protonation state of a functional group also has an effect on the local electronic structure in other moieties of the molecule. The obtained results are then used for the interpretation of the XES spectra of diglycine in solutions of different pH.

Finally, after the electronic structure of diglycine was thoroughly discussed in the previous sections, Sec. 5.3 studies the interaction of a multitude of salts with diglycine in aqueous solution. To investigate both the influence of anions and cations related to the respective Hofmeister series, a set of chlorine salts with different cations and a set of potassium salts with different anions are used. For both series, ion-specific effects on the electronic structure of diglycine are identified. For the cations, an increase in the interaction strength in the sequence $NH_4^+ \approx K^+ > Na^+ \approx Li^+ > Mg^{2+} \approx Ca^{2+}$ is found, qualitatively following the Hofmeister series. The interaction site more likely can be found in proximity to the peptide oxygen rather than at the carboxyl group of the peptide. However, an unambiguous assignment is not possible based on the collected data.

For the series of anions, even more distinct ion-specific effects are observed. Whereas chlorine and fluorine do not effect the electronic structure of diglycine significantly, pronounced changes are observed for the chaotropic anions Br^-, NO_3^-, I^-, and SCN^-, as well as for the divalent SO_4^{2-}. An ordering in the interaction strength of $KBr \approx K_2SO_4 > KNO_3 \approx KI \approx KSCN$ is found, following the chaotropic part of the Hofmeister series for anions. The data suggests that the interaction likely takes place at the amino group and not in proximity to the peptide nitrogen. The exceptional behavior of the sulfate ion, however, can not be explained without doubt. Since it is divalent (in contrast to all other anions studied in this thesis), the positive charge of the functional group might lead to an enhanced interaction strength.

CHAPTER 6

CONCLUSION AND OUTLOOK

In this thesis, soft x-ray spectroscopic methods are used to gain an improved understanding of the influence different physical environments have on the electronic structure of small molecules. Especially the interaction between salts and small peptides in aqueous solution is studied to try to unravel some of the mysteries of the Hofmeister series. Thereby, x-ray emission (XES) and absorption spectroscopy (XAS), as well as resonant inelastic x-ray scattering (RIXS) are employed to probe both the occupied and unoccupied electronic states and develop a comprehensive picture of the electronic structure of the studied molecules. Additional information is gathered by density functional theory (DFT) calculations. To disentangle the complex system of the peptide, the surrounding water, and the additional salt ions, a firm basis for the interpretation of the collected data is set in a step-by-step manner.

In a first step, molecules without any interactions with the surrounding are investigated, using the example of gas-phase methanol as a model system. Thereby, the local character of RIXS is demonstrated and applied to separately probe the local electronic structure of methanol's hydroxyl and methyl group, respectively. The attribution of the observed emission features to distinct molecular orbitals is confirmed by density functional theory calculations, which also quantitatively explain the different relative intensities of the emission features. For resonant excitation of the O K pre-edge absorption resonance, strong isotope effects are found that are explained by proton dynamics on the time scale of the x-ray emission process. This serves as a good example for the tremendous consequences a local change in the geometric structure can have on the electronic structure.

For the further studies in this thesis, the sample system is expanded to more complex molecules, namely the amino acid glycine and its smallest derived peptides diglycine and triglycine, at first in their crystalline form in solid state. Again, using functional theory calculations for modeling the XES and XAS spectra of the three molecules and measuring RIXS maps at the oxygen and nitrogen K absorption edge, a comprehensive picture of the electronic structure is developed. The occurrence of nuclear dynamics at the protonated amino group is highlighted. Furthermore, it is shown that RIXS can be used to selectively excite the peptide nitrogen to probe the local electronic structure. For higher excitation energies, a simple building block approach is applied to separate the contribution of the emission attributed to transitions into core holes at the peptide and the amino nitrogen, respectively.

In the aqueous solution, the surrounding water molecules slightly change the electronic structure, probably via dipole-dipole interactions with the charged functional groups and potentially also by hybridization of molecular orbitals. The consequences for the x-ray emission spectra, however, are rather small. Much bigger changes are observed when manipulating the protonation state of the functional groups by adjusting the pH value of the solution. A protonation of the carboxyl group at low pH values, as well as a deprotonation of the amino group at high pH values, lead to striking changes in the shape of the O K and N K RIXS maps, respectively. In a comprehensive study of glycine's XES spectra at varying pH values, changes in the local electronic structure are not only observed in the immediate surrounding of the manipulated functional groups but also in more distant moieties of the molecule.

Finally, the study is extended to mixed aqueous solutions of diglycine and a variety of different salts. To investigate the influence of different cations, a series of chlorides is used, whereas a collection of different potassium salts probes the impact anions have on the electronic structure of diglycine. Ion-specific effects are identified for both cases. Some of the changes in the x-ray emission spectra of diglycine in the mixed solutions qualitatively follow the Hofmeister series as a function of the used salt. The observed trends thereby indicate an increased interaction between the electron density around the peptide oxygen and the cations, whereas some anions seem to interact with the amino group of the peptide more than others.

The results presented in this thesis give valuable new input into the discussion about ion-specific effects and the Hofmeister series. However, there is a lot of more work to be done to develop a generally valid explanation for the observed effects. The comparatively young methods of x-ray spectroscopy might play a major role in the future to reach a molecular understanding of the interactions, which are the driving forces for ion-specific effects to occur. Some of the questions still open, e.g., where the interaction between ions and peptides takes place, can probably be answered by extended experiments similar to those performed in this thesis. For instance, one could eliminate a possible interaction with the peptide bond by turning to glycine or other small amino acids in mixed salt solutions. Analogue, the number of peptide bonds can also be increased in experiments using triglycine or even bigger molecules as a model peptide. However, the maximum solubility of such substances decreases with growing size, which limits the feasibility of such experiments due to increasing measurement times needed to record meaningful x-ray emission spectra. One possible workaround to investigate the effects of ions on the peptide bond could be to use suitable, smaller reference molecules. For the double bonded oxygen in the peptide bond, acetamide might be a proimsing candidate, whereas the peptide nitrogen could be represented by N-vinylformamide.

Furthermore, only a very small part of the big variety of ions, which are relevant for physiological solutions, is covered in this thesis. Thus, the experiments can easily be expanded with more and different salts, e.g., salts with a strongly kosmotropic anion and a highly chaotropic cation. It is also conceivable that the concentration of the salt ions in the solution might play a major role. Especially for higher concentrations, the simplifying concept of separate anionic and cationic Hofmeister series might break down, when ions not only interact with the peptides but also amongst themselves in the solution.

APPENDIX A

APPENDIX

Fig. A.1 shows a comparison of the calculated electronic isodensity surfaces of the 20 highest occupied molecular orbitals of diglycine and the 12 highest occupied molecular orbitals of glycine, both in their zwitterionic charge state, respectively. Some MOs show a striking resemblance between the two molecules, whereas a set of diglycine's MOs (which are localized to a big amount near the peptide bond) don't have a counterpart for glycine. A more detailed discussion of similarities and differences between the MOs of the two molecules can be found in Sec. 4.2.1 in the main part of this thesis.

Fig. A.2 shows non-resonantly excited N K XES spectra of glycine in aqueous solution at different pH (gray circles, see also Fig. 5.6). Each spectrum is fitted using the spectra of glycine at pH 6 (black) and pH 12 (blue) that represent the contributions of glycine in its zwitterionic (i.e., with protonated amino group, NH_3^+) and in its anionic charge state (i.e., with deprotonated amino group, NH_2), respectively. After normalizing all spectra to the area in the displayed emission energy region, the weighing factors of the two components were the only parameters for the fitting routine. The residua of the fits are displayed in red, showing a very good agreement with the measured spectra. The biggest (but still very small) deviations are observed for emission energies of ≈ 395.3 - $396.3\,\mathrm{eV}$, i.e., near the most intense feature in the spectrum with very steep flanks. There, a small deviation in the line position between the fit and the measured spectrum leads to a comparatively large residuum.

Fig. A.3 shows O K XES spectra of glycine in aqueous solution at different pH (gray circles, see also Fig. 5.7), excited at the pre-edge absorption resonance. Each spectrum is fitted using the spectra of glycine at pH 0.1 (red) and pH 6 (black) that represent

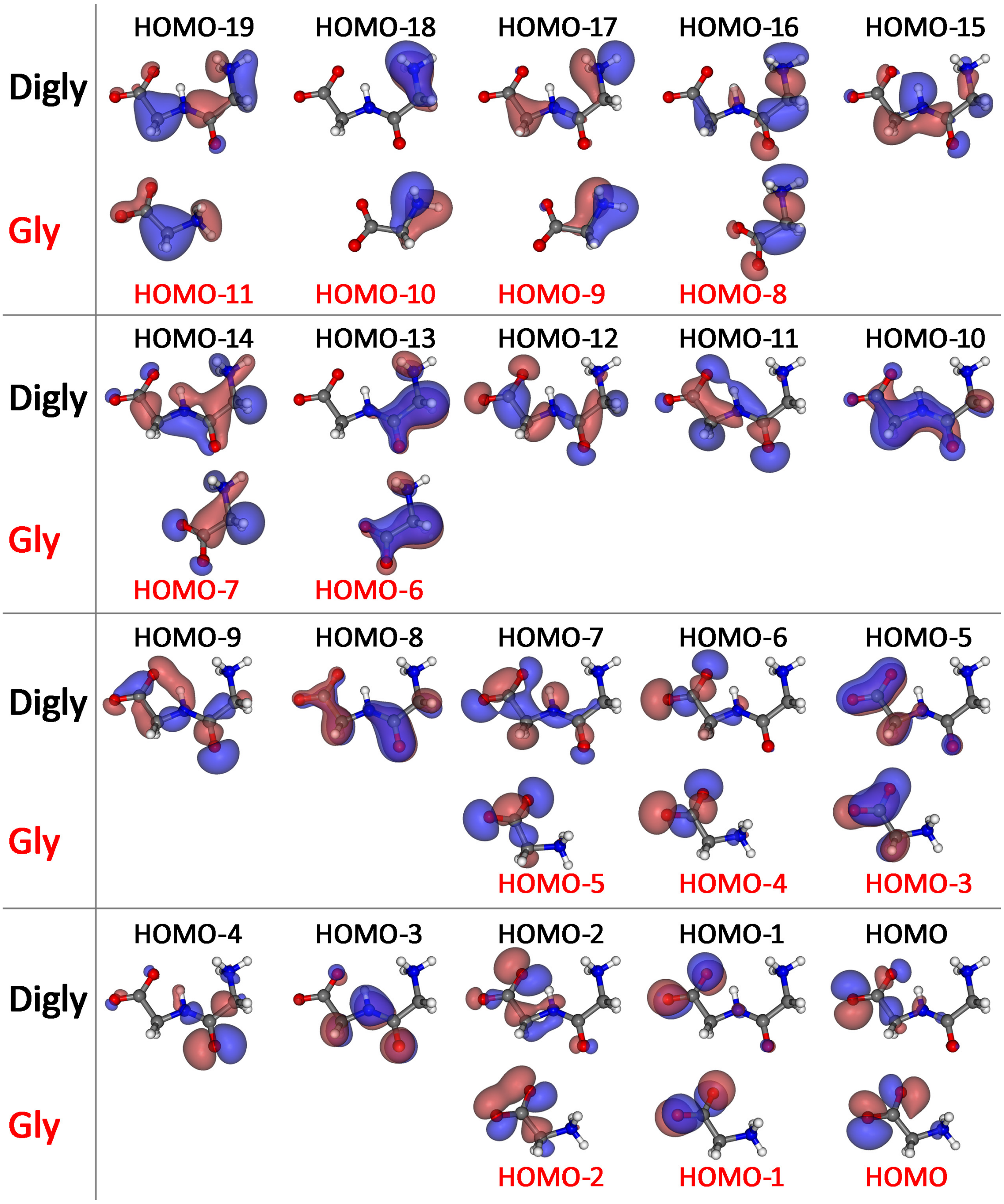

FIGURE A.1. Comparison of the calculated electronic isodensity surfaces of glycine and diglycine molecules in the zwitterionic charge state.

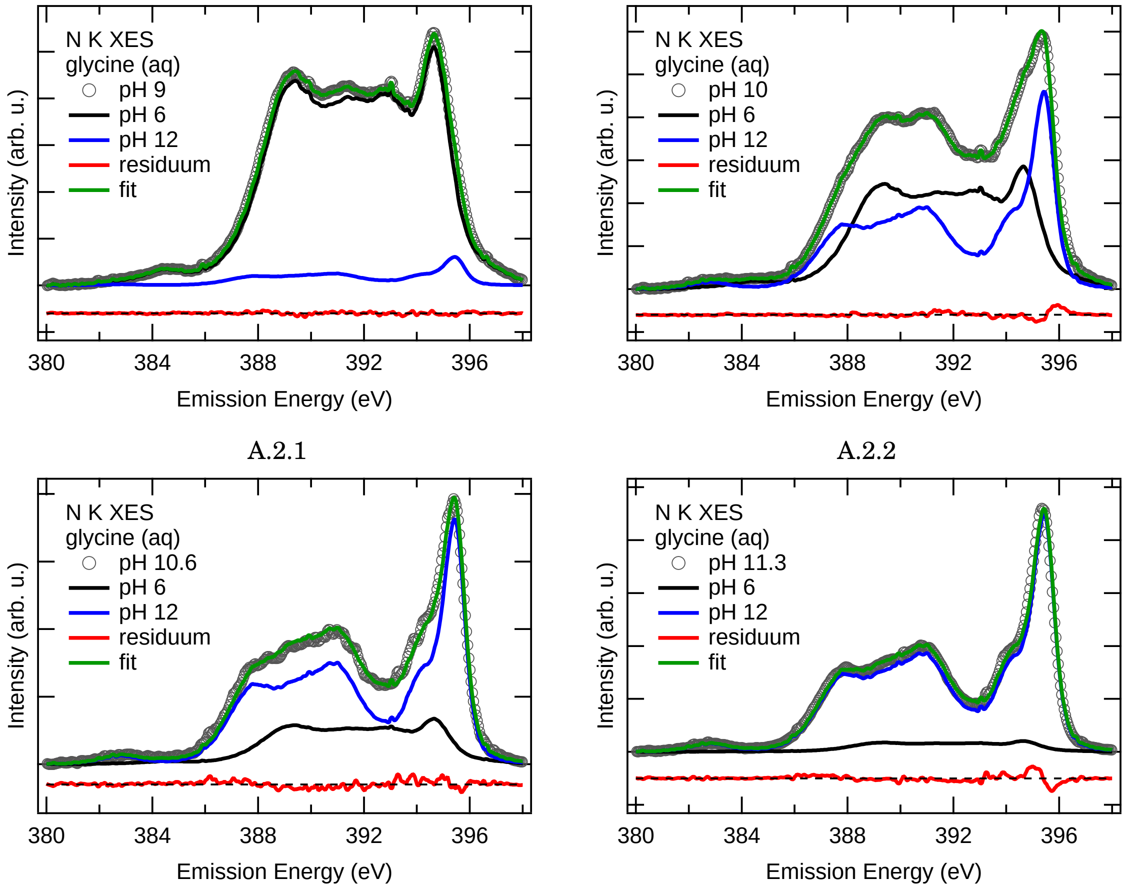

A.2.1

A.2.2

A.2.3

A.2.4

FIGURE A.2. Fits (green curves) of the non-resonantly excited N K XES spectra of glycine in aqueous solution at different pH (gray circles) using the spectra at pH 12 (blue) and pH 6 (black) as components. The residua are given in red.

the contributions of glycine in its cationic (i.e., with protonated carboxyl, COOH) and in its zwitterionic charge state (i.e., with deprotonated carboxyl group, COO^-), respectively. Similar to the N K XES spectra in Fig. A.2, the weighing factors of the two components were the only fitting parameters. The residua of the fits are displayed in blue, confirming the excellent agreement between the fit and the measured spectra.

In Fig. A.3.6, the results of the fits performed for the O K pre-edge spectra and the non-resonant N K XES spectra are summarized. The solid lines represent the predicted relative concentrations of glycine in the different electrical charge states (see also Fig. 5.4 in the main text). The weighting factors for the fits are given by circles in the same color code. For acidic pH values (smaller than 6), the circles origin from the fits of the O K edge, whereas the circles at basic pH (bigger than 6) belong to the fits of the N K edge. The used weighting factors clearly follow the theoretical

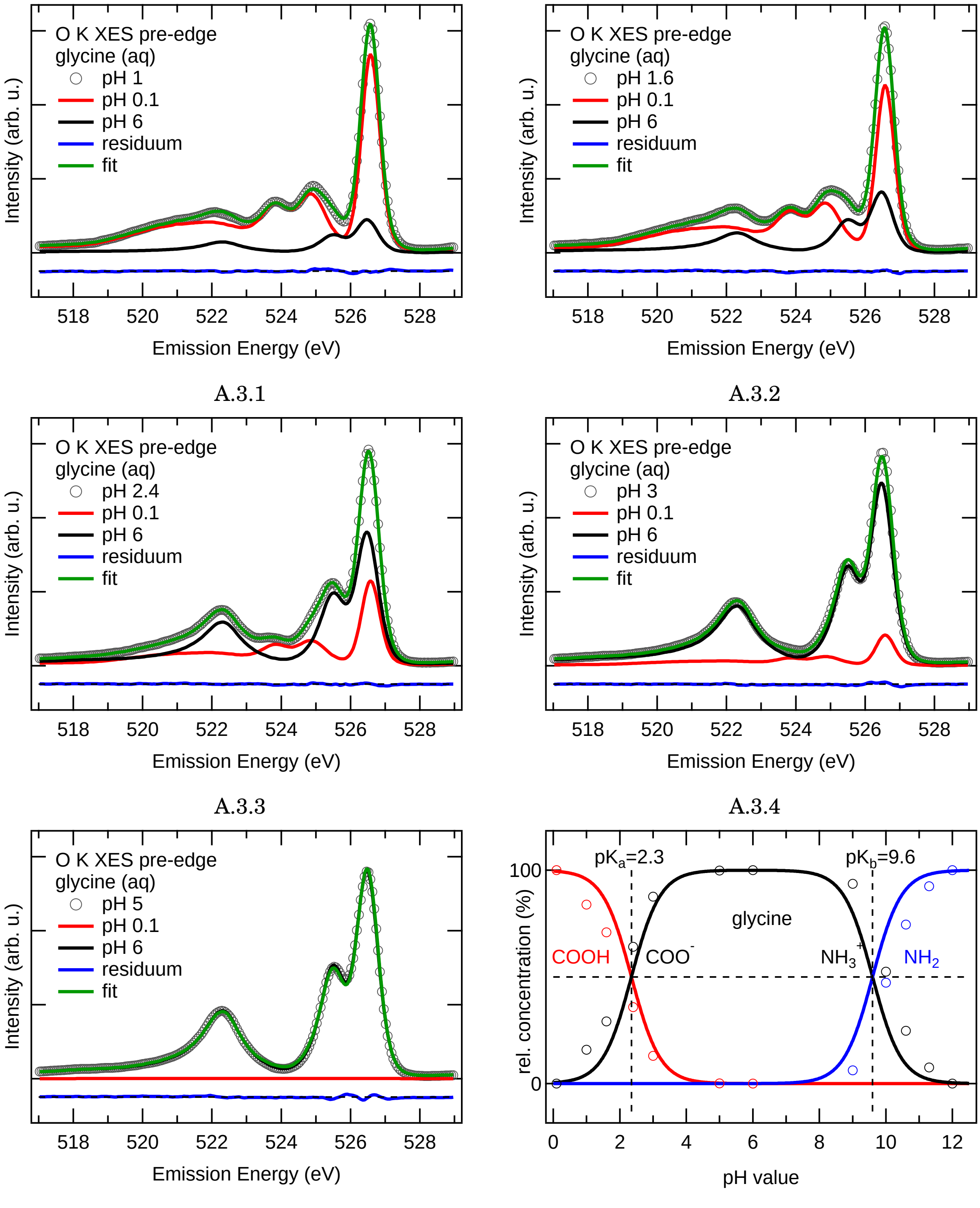

A.3.1

A.3.2

A.3.3

A.3.4

A.3.5

A.3.6

FIGURE A.3. Fits (green spectra) of the O K pre-edge spectra of glycine in aqueous solution at different pH (gray circles) using the spectra at pH 0.1 (red) and pH 6 (black) as components. The residua are given in blue. The resulting contributions are compared to the theoretical relative concentrations of the respective molecular species in panel A.3.6.

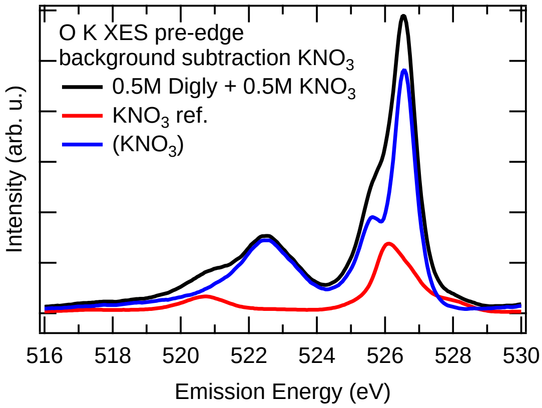

FIGURE A.4. Subtraction of the background signal originating from emission of excited nitrate ions in the O K XES spectrum of a mixed solution with 0.5M diglycine and 0.5 M KNO_3, measured with an excitation energy of 532.7 eV. The red curve represents a reference measurement of a 2 M KNO_3 solution, which is subtracted from the measured spectrum for the mixed solution (black) to obtain the blue spectrum which is shown in Fig. 5.13 in the main part of this thesis.

prediction, however, with a systematic deviation for both pH regimes. For all fits, the used weighting factors for the zwitterionic species (black) are bigger than the theory predicts. A possible reason for this can be an enhanced XAS and XES cross-section for the zwitterionic species. Moreover, an offset in the calibration of the used pH meter may explain the systematic deviation. The pH meter was calibrated separately for acidic (using buffer solutions of pH 1 and pH 6) and basic solutions (using buffer solutions of pH 6 and pH 10). This can lead to the observed change of sign of the deviation. The mean deviation is ≈ -0.3 for the acidic solutions and ≈ +0.5 for the basic solutions. Furthermore, the exact values for pK_a and pK_b are subject to uncertainties, which of course effects the theoretical curves (see equation (5.3) in Sec. 5.2). However, this uncertainty is negligible small since glycine as the smallest amino acid has been in the focus of numerous biochemical studies, making its pK_a and pK_b values very well known.

The measured spectrum for resonant excitation of the O K pre-edge with $h\nu = 532.7$ eV of a mixed aqueous solution of 0.5 M diglycine and 0.5 M KNO_3 is depicted in Fig. A.4 as black curve. The spectrum can be considered as a superposition of the emission of diglycine molecules and nitrate ions. The latter one is plotted in red and was acquired for a pure 2 M KNO_3 solution. The emission of diglycine molecules is then isolated by subtracting the KNO_3 reference measurement from the spectrum of the mixed solution with a suitable weighing factor. This factor was subjectively chosen in a way that the peaks originating from nitrate ions are not visible in the blue difference spectrum any more. At the same time it was tried to obtain a difference spectrum with a spectral shape similar to the respective spectrum of a pure 0.5 M diglycine solution (black curve in Fig. 5.13 in the main part.

Fig. A.5 shows the measured spectra for mixed aqueous solutions containing 0.5 M diglycine and 0.5 M salt (NH_4Cl, KSCN, and KNO_3, respectively), excited at the N K pre-edge absorption resonance with hν = 401.6 eV (left) and at the N K main-edge with 406.5 eV (right), respectively. To try to eliminate the contribution of the emission of excited (nitrogen containing) salt ions, difference spectra are calculated. Therefor, reference measurements of pure salt solutions with a concentration of 1 M (panels A.5.3 and A.5.5) and 2 M (remaining panels) have been recorded at the same excitation energies, which are shown as red curves. They then were subtracted with suitable weighing factors from the measured spectra of the mixed solutions, resulting in the blue curves, which are used for the discussion in Sec. 5.3.2 of this thesis. Note, that the determination of the weighing factors for the subtraction procedure is mainly based on a subjective evaluation of the resulting difference spectra concerning their overall spectral shape. Especially for the cases where the spectrum of the salt solution does not exhibit distinct emission features, which can also be identified in the spectra of the mixed solutions, this has to be kept in mind for the interpretation of the resulting spectra.

In Fig. A.6, non-resonantly (hν = 418.9 eV) excited spectra at the N K edge of mixed aqueous solutions of diglycine with different potassium salts are shown in the top left panel. They are normalized to the intensity at 395.5 eV. The spectrum of the pure diglycine solution and the solutions containing KCl and KF are additionally scaled by a factor 0.93. Difference spectra calculated with the subtraction “Digly with salt - Digly” are shown below. The spectra for the salts KCl and KF are very similar to the spectrum of pure diglycine. For the other salts, the difference spectra can be approximatively described by a spectrum of glycine in aqueous solution, excited at the same excitation energy, which is shown in the top right panel. For the nitrogen containing salts KSCN and KNO_3, a reference spectrum of a pure 2 M solution of the salts was subtracted from the measured spectrum of the mixed solution to try to eliminate the contribution of the emission of ions. This is shown in the bottom panels. The measured spectra of the mixed solution are displayed as black lines, the reference spectra of the pure salt solutions in red, and the resulting difference spectra in blue, respectively.

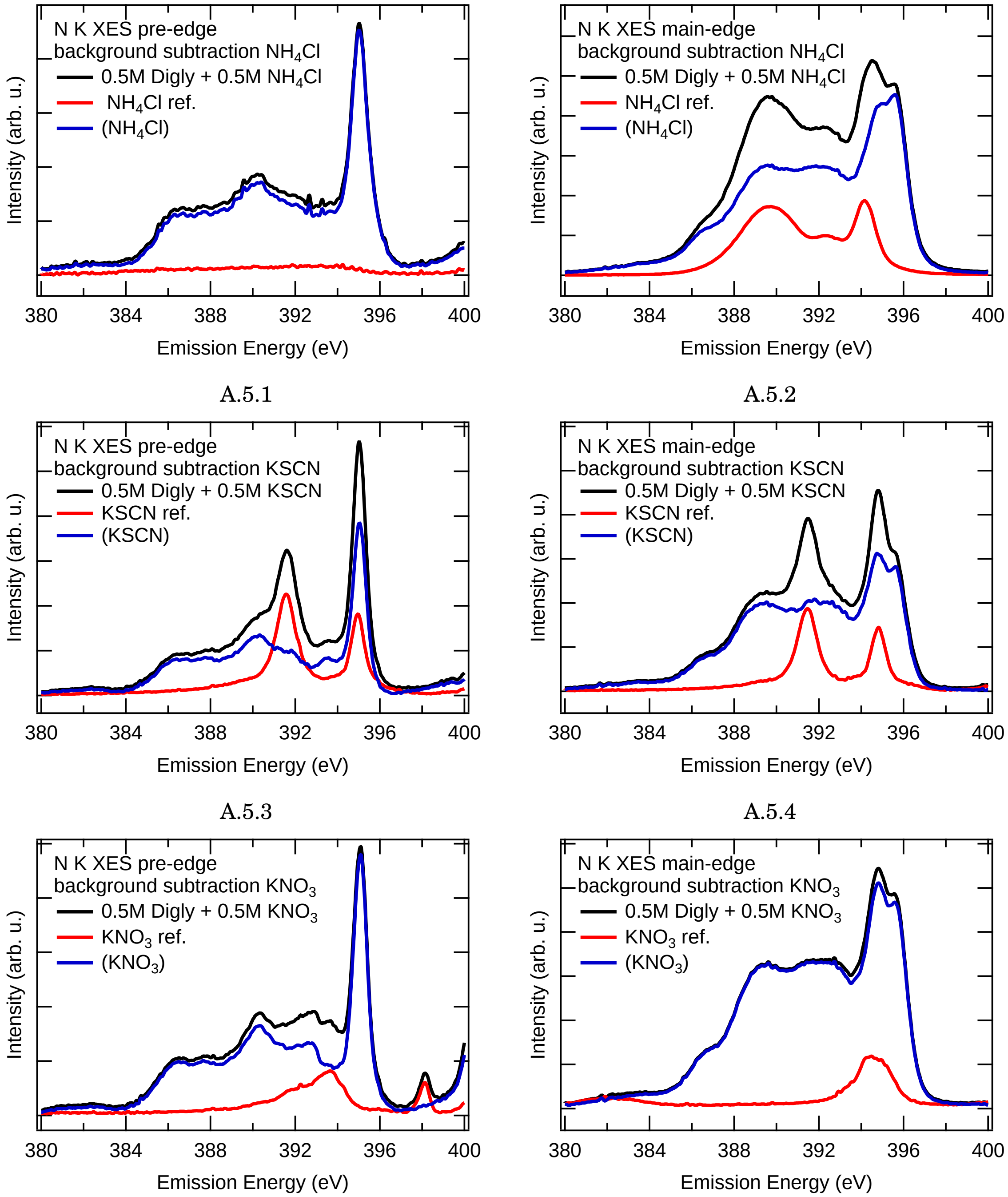

A.5.1

A.5.2

A.5.3

A.5.4

A.5.5

A.5.6

FIGURE A.5. Background subtraction for nitrogen containing salts in mixed aqueous solution with diglycine. The measured spectra are displayed as black lines. As a reference for the emission attributed to excited ions, spectra of pure salt solutions (red) have been subtracted from the measured spectra. The resulting blue spectra are shown and discussed in Sec. 5.3.2 in the main text.

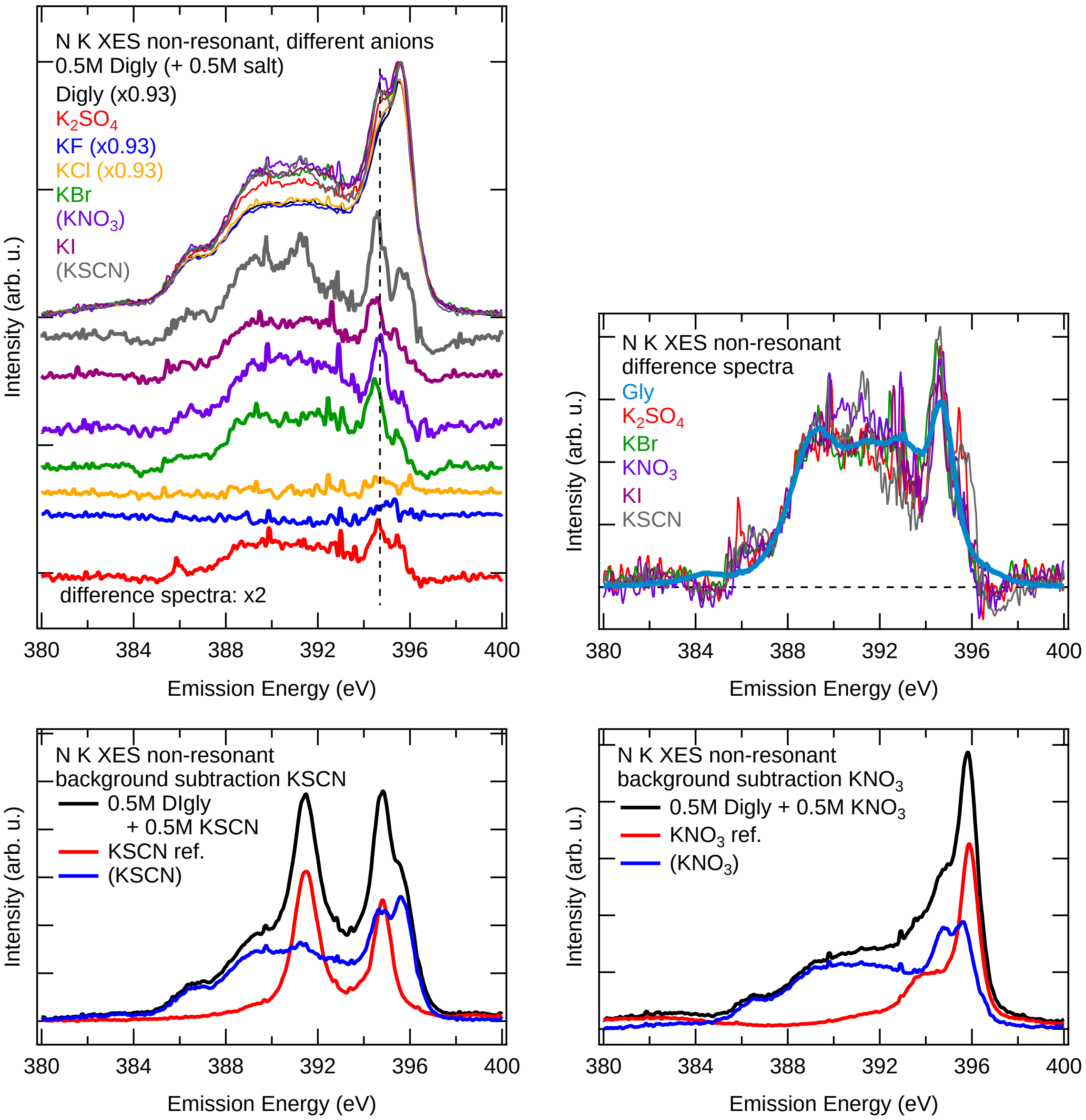

FIGURE A.6. Non-resonant N K XES spectra of diglycine in mixed aqueous solution. Top: Spectra normalized to the peak maximum at 395.5 eV. The spectra of the pure diglycine solution, KF, and KCl have been scaled additionally by a factor 0.93. The difference spectra shown below ("Digly with salt - Digly") have been scaled with a factor 2 and are compared to a spectrum of glycine (blue) on the right, normalized to the integrated emission intensity in the displayed energy region. Bottom: Background subtraction for KSCN (left) and KNO_3 (right) in mixed solution with diglycine. The measured spectra are displayed in black, reference spectra of pure salt solutions in red, and the resulting difference spectra in blue, respectively.

BIBLIOGRAPHY

[1] F. Hofmeister. “Zur Lehre von der Wirkung der Salze”. *Archiv f. experiment. Pathol. u. Pharmakol.* **25** (1888), pp. 1–30.

[2] F. Hofmeister. “Zur Lehre von der Wirkung der Salze”. *Archiv f. experiment. Pathol. u. Pharmakol.* **24** (1888), pp. 247–260.

[3] W. Kunz, J. Henle, and B. W. Ninham. “‘Zur Lehre von der Wirkung der Salze’ (about the science of the effect of salts): Franz Hofmeister’s historical papers”. *Curr. Opin. Colloid Interf. Sci.* **9** (2004), pp. 19–37.

[4] G. Jones and M. Dole. “The viscosity of aqueous solutions of strong electrolytes with special reference to barium chloride”. *J. Am. Chem. Soc.* **51** (1929), pp. 2950–2964.

[5] S. Murgia, G. Palazzo, M. Mamusa, S. Lampis, and M. Monduzzi. “Aerosol-OT in water forms fully-branched cylindrical direct micelles in the presence of the ionic liquid 1-butyl-3-methylimidazolium bromide”. *Phys. Chem. Chem. Phys.* **13** (2011), pp. 9238–9245.

[6] S. Rossi, P. Lo Nostro, M. Lagi, B. W. Ninham, and P. Baglioni. “Specific Anion Effects on the Optical Rotation of α-Amino Acids”. *J. Phys. Chem. B* **111** (2007), pp. 10510–10519.

[7] R. L. Baldwin. “How Hofmeister ion interactions affect protein stability.” *Biophys. J.* **71** (1996), pp. 2056–2063.

[8] A. Salis, D. Bilanicova, B. W. Ninham, and M. Monduzzi. “Hofmeister Effects in Enzymatic Activity: Weak and Strong Electrolyte Influences on the Activity of Candida rugosa Lipase”. *J. Phys. Chem. B* **111** (2007), pp. 1149–1156.

[9] J. Rubin, A. San Miguel, A. S. Bommarius, and S. H. Behrens. “Correlating Aggregation Kinetics and Stationary Diffusion in Protein-Sodium Salt Systems Observed with Dynamic Light Scattering”. *J. Phys. Chem. B* **114** (2010), pp. 4383–4387.

[10] A. Salis and B. W. Ninham. “Models and mechanisms of Hofmeister effects in electrolyte solutions, and colloid and protein systems revisited”. *Chem. Soc. Rev.* **43** (2014), pp. 7358–7377.

[11] P. Lo Nostro and B. W. Ninham. “Hofmeister Phenomena: An Update on Ion Specificity in Biology”. *Chem. Rev.* **112** (2012), pp. 2286–2322.

[12] W. Kunz, P. Lo Nostro, and B. W. Ninham. “The present state of affairs with Hofmeister effects”. *Curr. Opin. Colloid Interf. Sci.* **9** (2004), pp. 1–18.

[13] W. Kunz. “Specific ion effects in colloidal and biological systems”. *Curr. Opin. Colloid Interf. Sci.* **15** (2010), pp. 34–39.

[14] Y. Zhang and P. S. Cremer. “Interactions between macromolecules and ions: the Hofmeister series”. *Cur. Op. Chem. Biol.* Model systems / Biopolymers **10** (2006), pp. 658–663.

[15] J. Song, T. H. Kang, M. W. Kim, and S. Han. “Ion specific effects: decoupling ion–ion and ion–water interactions”. *Phys. Chem. Chem. Phys.* **17** (2015), pp. 8306–8322.

[16] B. W. Ninham and P. Lo Nostro. *Molecular Forces and Self Assembly*. Colloid, Nano Sciences and Biology. Cambridge, U.K.: Cambridge University Press, 2010.

[17] W. M. Cox and J. H. Wolfenden. “The Viscosity of Strong Electrolytes Measured by a Differential Method”. *Proc. Royal Soc. London A: Mathematical, Physical and Engineering Sciences* **145** (1934), pp. 475–488.

[18] R. W. Gurney. *Ionic Processes In Solution*. eng. McGraw-Hill Book Company, Inc, 1953.

[19] R. Zangi. “Can Salting-In/Salting-Out Ions be Classified as Chaotropes/ Kosmotropes?” *J. Phys. Chem. B* **114** (2010), pp. 643–650.

[20] Y. Marcus. “Effect of Ions on the Structure of Water: Structure Making and Breaking”. *Chem. Rev.* **109** (2009), pp. 1346–1370.

[21] A. W. Omta, M. F. Kropman, S. Woutersen, and H. J. Bakker. “Negligible Effect of Ions on the Hydrogen-Bond Structure in Liquid Water”. *Science* **301** (2003), pp. 347–349.

[22] S. Funkner, G. Niehues, D. A. Schmidt, M. Heyden, G. Schwaab, K. M. Callahan, D. J. Tobias, and M. Havenith. “Watching the Low-Frequency Motions

in Aqueous Salt Solutions: The Terahertz Vibrational Signatures of Hydrated Ions". *J. Am. Chem. Soc.* **134** (2012), pp. 1030–1035.

[23] F. A. Long and W. F. McDevit. "Activity Coefficients of Nonelectrolyte Solutes in Aqueous Salt Solutions." *Chem. Rev.* **51** (1952), pp. 119–169.

[24] N. Schwierz, D. Horinek, and R. R. Netz. "Anionic and Cationic Hofmeister Effects on Hydrophobic and Hydrophilic Surfaces". *Langmuir* **29** (2013), pp. 2602–2614.

[25] A. Salis, M. Cristina Pinna, D. Bilanicova, M. Monduzzi, P. L. Nostro, and B. W. Ninham. "Specific Anion Effects on Glass Electrode pH Measurements of Buffer Solutions: Bulk and Surface Phenomena". *J. Phys. Chem. B* **110** (2006), pp. 2949–2956.

[26] Y. Zhang and P. S. Cremer. "The inverse and direct Hofmeister series for lysozyme". *PNAS* **106** (2009), pp. 15249–15253.

[27] M. M. Ries-Kautt and A. F. Ducruix. "Relative effectiveness of various ions on the solubility and crystal growth of lysozyme." *J. Biol. Chem.* **264** (1989), pp. 745–748.

[28] J. Bello and H. R. Bello. "Interaction of Model Peptides with Water and Lithium Bromide". *Nature* **190** (1961), pp. 440–441.

[29] J. Bello and H. R. Bello. "Evidence from Model Peptides relating to the Denaturation of Proteins by Lithium Salts". *Nature* **194** (1962), pp. 681–682.

[30] D. R. Robinson and W. P. Jencks. "The Effect of Concentrated Salt Solutions on the Activity Coefficient of Acetyltetraglycine Ethyl Ester". *J. Am. Chem. Soc.* **87** (1965), pp. 2470–2479.

[31] P. K. Nandi and D. R. Robinson. "Effects of salts on the free energies of nonpolar groups in model peptides". *J. Am. Chem. Soc.* **94** (1972), pp. 1308–1315.

[32] P. K. Nandi and D. R. Robinson. "Effects of salts on the free energy of the peptide group". *J. Am. Chem. Soc.* **94** (1972), pp. 1299–1308.

[33] T. Arakawa and S. N. Timasheff. "Preferential interactions of proteins with salts in concentrated solutions". *Biochemistry* **21** (1982), pp. 6545–6552.

[34] T. O. Street, D. W. Bolen, and G. D. Rose. "A molecular mechanism for osmolyte-induced protein stability". *PNAS* **103** (2006), pp. 13997–14002.

[35] L. M. Pegram and M. T. Record. "Thermodynamic Origin of Hofmeister Ion Effects". *J. Phys. Chem. B* **112** (2008), pp. 9428–9436.

[36] I. Kalcher, D. Horinek, R. R. Netz, and J. Dzubiella. "Ion specific correlations in bulk and at biointerfaces". *J. Phys.: Condens. Matter* **21** (2009), p. 424108.

[37] K. D. Collins. "Charge density-dependent strength of hydration and biological structure." *Biophys. J.* **72** (1997), pp. 65–76.

[38] J. Heyda, T. Hrobárik, and P. Jungwirth. "Ion-Specific Interactions between Halides and Basic Amino Acids in Water". *J. Phys. Chem. A* **113** (2009), pp. 1969–1975.

[39] J. Paterová, K. B. Rembert, J. Heyda, Y. Kurra, H. I. Okur, W. R. Liu, C. Hilty, P. S. Cremer, and P. Jungwirth. "Reversal of the Hofmeister Series: Specific Ion Effects on Peptides". *J. Phys. Chem. B* **117** (2013), pp. 8150–8158.

[40] B. Hess and N. F. A. van der Vegt. "Cation specific binding with protein surface charges". *PNAS* **106** (2009), pp. 13296–13300.

[41] J. Heyda, J. C. Vincent, D. J. Tobias, J. Dzubiella, and P. Jungwirth. "Ion Specificity at the Peptide Bond: Molecular Dynamics Simulations of N-Methylacetamide in Aqueous Salt Solutions". *J. Phys. Chem. B* **114** (2010), pp. 1213–1220.

[42] N. Vlachy, B. Jagoda-Cwiklik, R. Vácha, D. Touraud, P. Jungwirth, and W. Kunz. "Hofmeister series and specific interactions of charged headgroups with aqueous ions". *Advances in Colloid and Interface Science* **146** (2009), pp. 42–47.

[43] E. F. Aziz, N. Ottosson, S. Eisebitt, W. Eberhardt, B. Jagoda-Cwiklik, R. Vácha, P. Jungwirth, and B. Winter. "Cation-Specific Interactions with Carboxylate in Amino Acid and Acetate Aqueous Solutions: X-ray Absorption and ab initio Calculations". *J. Phys. Chem. B* **112** (2008), pp. 12567–12570.

[44] J. S. Uejio, C. P. Schwartz, A. M. Duffin, W. S. Drisdell, R. C. Cohen, and R. J. Saykally. "Characterization of selective binding of alkali cations with carboxylate by x-ray absorption spectroscopy of liquid microjets". *PNAS* **105** (2008), pp. 6809–6812.

[45] C. P. Schwartz, J. S. Uejio, A. M. Duffin, A. H. England, D. N. Kelly, D. Prendergast, and R. J. Saykally. "Investigation of protein conformation and interactions with salts via X-ray absorption spectroscopy". *PNAS* **107** (2010), pp. 14008–14013.

[46] R. Golnak, K. Atak, E. Suljoti, K. F. Hodeck, K. M. Lange, M. A. Soldatov, N. Engel, and E. F. Aziz. “Local electronic structure of aqueous zinc acetate: oxygen K-edge X-ray absorption and emission spectroscopy on micro-jets”. *Phys. Chem. Chem. Phys.* **15** (2013), pp. 8046–8049.

[47] K. M. Lange and E. F. Aziz. “Electronic structure of ions and molecules in solution: a view from modern soft X-ray spectroscopies”. *Chem. Soc. Rev.* **42** (2013), pp. 6840–6859.

[48] T. Petit, K. M. Lange, G. Conrad, K. Yamamoto, C. Schwanke, K. F. Hodeck, M. Dantz, T. Brandenburg, E. Suljoti, and E. F. Aziz. “Probing ion-specific effects on aqueous acetate solutions: Ion pairing versus water structure modifications”. *Struc. Dyn.* **1** (2014), p. 034901.

[49] M. Lund, L. Vrbka, and P. Jungwirth. “Specific Ion Binding to Nonpolar Surface Patches of Proteins”. *J. Am. Chem. Soc.* **130** (2008), pp. 11582–11583.

[50] S. Myneni, Y. Luo, L. Näslund, M. Cavalleri, L. Ojamäe, H. Ogasawara, A. Pelmenschikov, P. Wernet, P. Väterlein, C Heske, Z. Hussain, L. Pettersson, and A. Nilsson. “Spectroscopic probing of local hydrogen-bonding structures in liquid water”. *J. Phys.: Condens. Matter* **14** (2002), p. L213.

[51] J.-H. Guo, Y. Luo, A. Augustsson, J.-E. Rubensson, C. Såthe, H. Ågren, H. Siegbahn, and J. Nordgren. “X-Ray Emission Spectroscopy of Hydrogen Bonding and Electronic Structure of Liquid Water”. *Phys. Rev. Lett.* **89** (2002), p. 137402.

[52] P. Wernet, D. Nordlund, U. Bergmann, M. Cavalleri, M. Odelius, H. Ogasawara, L. A. Näslund, T. K. Hirsch, L. Ojamäe, P. Glatzel, L. G. M. Pettersson, and A. Nilsson. “The Structure of the First Coordination Shell in Liquid Water”. *Science* **304** (2004), pp. 995–999.

[53] M. Odelius, M. Cavalleri, A. Nilsson, and L. G. M. Pettersson. “X-ray absorption spectrum of liquid water from molecular dynamics simulations: Asymmetric model”. *Phys. Rev. B* **73** (2006), p. 24205.

[54] L. Weinhardt, M. Blum, O. Fuchs, A. Benkert, F. Meyer, M. Bär, J. D. Denlinger, W. Yang, F. Reinert, and C. Heske. “RIXS investigations of liquids, solutions, and liquid/solid interfaces”. *J. Electr. Spectr. Rel. Phenom.* Progress in Resonant Inelastic X-Ray Scattering **188** (2013), pp. 111–120.

[55] B. M. Messer, C. D. Cappa, J. D. Smith, W. S. Drisdell, C. P. Schwartz, R. C. Cohen, and R. J. Saykally. “Local Hydration Environments of Amino Acids and

Dipeptides Studied by X-ray Spectroscopy of Liquid Microjets". *J. Phys. Chem. B* **109** (2005), pp. 21640–21646.

[56] B. Messer, C. Cappa, J. Smith, K. Wilson, M. Gilles, R. Cohen, and R. Saykally. "pH Dependence of the Electronic Structure of Glycine". *J. Phys. Chem. B* **109** (2005), pp. 5375–5382.

[57] D. Nolting, E. Aziz, N. Ottosson, M. Faubel, I. Hertel, and B. Winter. "pH-Induced Protonation of Lysine in Aqueous Solution Causes Chemical Shifts in X-ray Photoelectron Spectroscopy". *J. Am. Chem. Soc.* **129** (2007), pp. 14068–14073.

[58] J. Gråsjö, E. Andersson, J. Forsberg, L. Duda, E. Henke, W. Pokapanich, O. Björneholm, J. Andersson, A. Pietzsch, F. Hennies, and J.-E. Rubensson. "Local Electronic Structure of Functional Groups in Glycine As Anion, Zwitterion, and Cation in Aqueous Solution". *J. Phys. Chem. B* **113** (2009), pp. 16002–16006.

[59] L. Weinhardt, M. Weigand, O. Fuchs, M. Bär, M. Blum, J. Denlinger, W. Yang, E. Umbach, and C. Heske. "Nuclear dynamics in the core-excited state of aqueous ammonia probed by resonant inelastic soft x-ray scattering". *Phys. Rev. B* **84** (2011), p. 104202.

[60] M. Blum, M. Odelius, L. Weinhardt, S. Pookpanratana, M. Bär, Y. Zhang, O. Fuchs, W. Yang, E. Umbach, and C. Heske. "Ultrafast Proton Dynamics in Aqueous Amino Acid Solutions Studied by Resonant Inelastic Soft X-ray Scattering". *J. Phys. Chem. B* **116** (2012), pp. 13757–13764.

[61] F. Meyer, M. Blum, A. Benkert, D. Hauschild, S. Nagarajan, R. G. Wilks, J. Andersson, W. Yang, M. Zharnikov, M. Bär, C. Heske, F. Reinert, and L. Weinhardt. ""Building Block Picture" of the Electronic Structure of Aqueous Cysteine Derived from Resonant Inelastic Soft X-ray Scattering". *J. Phys. Chem. B* **118** (2014), pp. 13142–13150.

[62] L. Weinhardt, E. Ertan, M. Iannuzzi, M. Weigand, O. Fuchs, M. Bär, M. Blum, J. D. Denlinger, W. Yang, E. Umbach, M. Odelius, and C. Heske. "Probing hydrogen bonding orbitals: resonant inelastic soft X-ray scattering of aqueous NH3". *Phys. Chem. Chem. Phys.* **17** (2015), pp. 27145–27153.

[63] J. Stöhr. *NEXAFS spectroscopy*. Springer, 1992.

[64] F. Gel'mukhanov and H. Ågren. "X-ray resonant scattering involving dissociative states". *Phys. Rev. A* **54** (1996), p. 379.

[65] F. Gel'mukhanov and H. Ågren. "Raman, non-Raman, and anti-Raman dispersion in resonant x-ray scattering spectra of molecules". *Phys. Rev. A* **54** (1996), pp. 3960–3970.

[66] F. Gel'mukhanov and H. Ågren. "Resonant X-ray Raman scattering". *Phys. Rep.* **312** (1999), pp. 87–330.

[67] P. a. M. Dirac. "The Quantum Theory of the Emission and Absorption of Radiation". *Proc. Royal Soc. London A: Mathematical, Physical and Engineering Sciences* **114** (1927), pp. 243–265.

[68] E. Fermi. *Nuclear Physics*. Uniersity of Chicago Press, 1950.

[69] D. Attwood. *Soft X-Rays And Extreme Ultraviolet Radiation: Principles And Applications*. Cambridge University Press, 2007.

[70] H. A. Kramers and W. Heisenberg. "Über die Streuung von Strahlung durch Atome". de. *Z. Physik* **31** (1925), pp. 681–708.

[71] Y. Ma, N. Wassdahl, P. Skytt, J. Guo, J. Nordgren, P. D. Johnson, J.-E. Rubensson, T. Boske, W. Eberhardt, and S. D. Kevan. "Soft-x-ray resonant inelastic scattering at the C K edge of diamond". *Phys. Rev. Lett.* **69** (1992), pp. 2598–2601.

[72] T. A. Callcott. "Soft x-ray fluorescence spectroscopy". *Experimental Methods in the Physical Sciences* **32** (1998), pp. 279–300.

[73] L. Weinhardt, O. Fuchs, D. Batchelor, M. Bär, M. Blum, J. Denlinger, W. Yang, A. Schöll, F. Reinert, E. Umbach, and C. Heske. "Electron-hole correlation effects in core-level spectroscopy probed by the resonant inelastic soft x-ray scattering map of C60". *J. Chem. Phys.* **135** (2011), p. 104705.

[74] M. O. Krause. "Atomic radiative and radiationless yields for K and L shells". *J. Phys. Chem. Ref. Data* **8** (1979), p. 307.

[75] O. Björneholm, A. Nilsson, A. Sandell, B. Hernnäs, and N. Mrtensson. "Determination of time scales for charge-transfer screening in physisorbed molecules". *Phys. Rev. Lett.* **68** (1992), pp. 1892–1895.

[76] O. Björneholm, S. Sundin, S. Svensson, R. Marinho, A. Naves de Brito, F. Gel'mukhanov, and H. Ågren. "Femtosecond Dissociation of Core-Excited HCl Monitored by Frequency Detuning". *Phys. Rev. Lett.* **79** (1997), pp. 3150–3153.

[77] O. Fuchs, M. Zharnikov, L. Weinhardt, M. Blum, M. Weigand, Y. Zubavichus, M. Bär, F. Maier, J. D. Denlinger, C. Heske, M. Grunze, and E. Umbach. "Isotope and Temperature Effects in Liquid Water Probed by X-Ray Absorption and Resonant X-Ray Emission Spectroscopy". *Phys. Rev. Lett.* **100** (2008), p. 027801.

[78] L. Weinhardt, A. Benkert, F. Meyer, M. Blum, R. Wilks, W. Yang, M. Bär, F. Reinert, and C. Heske. "Nuclear dynamics and spectator effects in resonant inelastic soft x-ray scattering of gas-phase water molecules". *J. Chem. Phys.* **136** (2012), p. 144311.

[79] S. Schreck, A. Pietzsch, K. Kunnus, B. Kennedy, W. Quevedo, P. Miedema, P. Wernet, and A. Föhlisch. "Dynamics of the OH group and the electronic structure of liquid alcohols". *Struct. Dyn.* **1** (2014), p. 054901.

[80] J.-L. Calais. "Density-functional theory of atoms and molecules. R.G. Parr and W. Yang, Oxford University Press, New York, Oxford, 1989. IX + 333 pp. Price £45.00". *Int. J. Quantum Chem.* **47** (1993), pp. 101–101.

[81] R. M. Dreizler and E. K. U. Gross. *Density Functional Theory*. Berlin, Heidelberg: Springer Berlin Heidelberg, 1990.

[82] T. Ziegler. "Approximate density functional theory as a practical tool in molecular energetics and dynamics". *Chem. Rev.* **91** (1991), pp. 651–667.

[83] R. G. Parr. "Density Functional Theory". *Ann. Rev. Phys. Chem.* **34** (1983), pp. 631–656.

[84] R. O. Jones and O. Gunnarsson. "The density functional formalism, its applications and prospects". *Rev. Mod. Phys.* **61** (1989), p. 689.

[85] U. von Barth. "Basic density-functional theory—an overview". *Phys. Scr.* **2004** (2004), p. 9.

[86] W. Kohn. "Nobel Lecture: Electronic structure of matter\char22{}wave functions and density functionals". *Rev. Mod. Phys.* **71** (1999), pp. 1253–1266.

[87] P. Hohenberg and W. Kohn. "Inhomogeneous Electron Gas". *Phys. Rev.* **136** (1964), B864–B871.

[88] W. Kohn and L. J. Sham. "Self-Consistent Equations Including Exchange and Correlation Effects". *Phys. Rev.* **140** (1965), A1133–A1138.

[89] D. R. Hartree. “The Wave Mechanics of an Atom with a Non-Coulomb Central Field. Part I. Theory and Methods”. *Mathematical Proceedings of the Cambridge Philosophical Society* **24** (1928), pp. 89–110.

[90] E. Wigner. “Effects of the electron interaction on the energy levels of electrons in metals”. *Trans. Faraday Soc.* **34** (1938), pp. 678–685.

[91] D. M. Ceperley and B. J. Alder. “Ground state of the electron gas by a stochastic method”. *Phys. Rev. Lett.* **45** (1980), p. 566.

[92] J. P. Perdew, K. Burke, and M. Ernzerhof. “Generalized Gradient Approximation Made Simple”. *Phys. Rev. Lett.* **77** (1996), pp. 3865–3868.

[93] A. Becke. “Density-functional exchange-energy approximation with correct asymptotic behavior”. *Phys. Rev. A* **38** (1988), pp. 3098–3100.

[94] C. Lee, W. Yang, and R. G. Parr. “Development of the Colle-Salvetti correlation-energy formula into a functional of the electron density”. *Phys. Rev. B* **37** (1988), pp. 785–789.

[95] J. P. Perdew. “Density-functional approximation for the correlation energy of the inhomogeneous electron gas”. *Phys. Rev. B* **33** (1986), pp. 8822–8824.

[96] K. Hermann, L.G.M. Pettersson, M. E. Casida, C. Daul, A. Goursot, A. Koester, E. Proynov, A. St-Amant, D.R. Salahub, Contributing authors: V. Carravetta, H. Duarte, C. Friedrich, N. Godbout, J. Guan, C. Jamorski, M. Leboeuf, M. Leetmaa, M. Nyberg, S. Patchkovskii, L. Pedocchi, F. Sim, L. Triguero, and A. Vela. *StoBe-deMon version 3.1 (2011)*. 2011.

[97] D. R. Salahub, M. Castro, R. Fournier, P. Calaminici, N. Godbout, A. Goursot, C. Jamorski, H. Kobayashi, A. Martínez, I. Pápai, E. Proynov, N. Russo, S. Sirois, J. Ushio, and A. Vela. “Density Functional Description of Metal-Metal and Metal-Ligand Bonds”. *Theoretical and Computational Approaches to Interface Phenomena*. Ed. by H. L. Sellers and J. T. Golab. DOI: 10.1007/978-1-4899-1319-7_11. Springer US, 1994, pp. 187–218.

[98] D. R. Salahub, M. Castro, and E. I. Proynov. “Density Functional Theory, Its Gaussian Implementation and Applications to Complex Systems”. *Relativistic and Electron Correlation Effects in Molecules and Solids*. Ed. by G. L. Malli. NATO ASI Series. DOI: 10.1007/978-1-4899-1340-1_14. Springer US, 1994, pp. 411–445.

[99] J. P. Perdew. “Erratum: Density-functional approximation for the correlation energy of the inhomogeneous electron gas”. *Phys. Rev. B* **34** (1986), pp. 7406–7406.

[100] L. Triguero, L. G. M. Pettersson, and H. \AAgren. “Calculations of near-edge x-ray-absorption spectra of gas-phase and chemisorbed molecules by means of density-functional and transition-potential theory”. *Phys. Rev. B* **58** (1998), p. 8097.

[101] L. Triguero, L. G. M. Pettersson, and H. Ågren. “Calculations of X-ray Emission Spectra of Molecules and Surface Adsorbates by Means of Density Functional Theory”. *J. Phys. Chem. A* **102** (1998), pp. 10599–10607.

[102] L. Triguero and L. G. M. Pettersson. “MO and DFT approaches to the calculation of X-ray absorption/emission spectra of nitrogen atom adsorbed on Cu(100)”. *Surface Science* **398** (1998), pp. 70–83.

[103] H. Öström, L. Triguero, K. Weiss, H. Ogasawara, M. G. Garnier, D. Nordlund, M. Nyberg, L. G. M. Pettersson, and A. Nilsson. “Orbital rehybridization in n-octane adsorbed on Cu(110)”. *J. Chem. Phys.* **118** (2003), pp. 3782–3789.

[104] A. Föhlisch, J. Hasselström, P. Bennich, N. Wassdahl, O. Karis, A. Nilsson, L. Triguero, M. Nyberg, and L. G. M. Pettersson. “Ground-state interpretation of x-ray emission spectroscopy on adsorbates: CO adsorbed on Cu(100)”. *Phys. Rev. B* **61** (2000), pp. 16229–16240.

[105] N. Godbout, D. R. Salahub, J. Andzelm, and E. Wimmer. “Optimization of Gaussian-type basis sets for local spin density functional calculations. Part I. Boron through neon, optimization technique and validation”. *Can. J. Chem.* **70** (1992), pp. 560–571.

[106] W. Kutzelnigg, U. Fleischer, and M. Schindler. “The IGLO-Method: Ab-initio Calculation and Interpretation of NMR Chemical Shifts and Magnetic Susceptibilities”. *Deuterium and Shift Calculation*. NMR Basic Principles and Progress. DOI: 10.1007/978-3-642-75932-1_3. Springer Berlin Heidelberg, 1990, pp. 165–262.

[107] L. Pettersson, U. Wahlgren, and O. Gropen. “Effective core potential parameters for first- and second-row atoms”. *J. Chem. Phys.* **86** (1987), pp. 2176–2184.

[108] O. Fuchs, L. Weinhardt, M. Blum, M. Weigand, E. Umbach, M. Bär, C. Heske, J. Denlinger, Y.-D. Chuang, W. McKinney, Z. Hussain, E. Gullikson, M. Jones,

P. Batson, B. Nelles, and R. Follath. “High-resolution, high-transmission soft x-ray spectrometer for the study of biological samples”. *Rev. Sci. Instr.* **80** (2009), p. 063103.

[109] M. Blum, L. Weinhardt, O. Fuchs, M. Bär, Y. Zhang, M. Weigand, S. Krause, S. Pookpanratana, T. Hofmann, W. Yang, J. D. Denlinger, E. Umbach, and C. Heske. “Solid and liquid spectroscopic analysis (SALSA)–a soft x-ray spectroscopy endstation with a novel flow-through liquid cell”. *Rev. Sci. Instrum.* **80** (2009), p. 123102.

[110] O. Fuchs. “Soft x-ray spectroscopy of organic molecules and liquids”. PhD thesis. Würzburg: Julius-Maximilians-Universität Würzburg, 2009.

[111] V. S. Lusvardi, M. A. Barteau, J. G. Chen, J. Eng Jr., B. Frühberger, and A. Teplyakov. “An NEXAFS investigation of the reduction and reoxidation of TiO2(001)”. *Surf. Sci.* **397** (1998), pp. 237–250.

[112] C. T. Chen, Y. Ma, and F. Sette. “K-shell photoabsorption of the N2 molecule”. *Phys. Rev. A* **40** (1989). Copyright (C) 2009 The American Physical Society; Please report any problems to prola@aps.org, p. 6737.

[113] B. Watts and H. Ade. “A simple method for determining linear polarization and energy calibration of focused soft X-ray beams”. *J. Electr. Spectr. Rel. Phenom.* **162** (2008), pp. 49–55.

[114] A. Benkert, M. Blum, F. Meyer, R. Wilks, W. Yang, M. Bär, F. Reinert, C. Heske, and L. Weinhardt. “Setup for in situ investigation of gases and gas/solid interfaces by soft x-ray emission and absorption spectroscopy”. *Rev. Sci. Instrum.* **85** (2014), p. 015119.

[115] M. Blum. “Electronic and Chemical Properties of Liquids and Solutions”. PhD thesis. Würzburg: Julius-Maximilians-Universität Würzburg, 2009.

[116] R. G. Wilks, J. B. MacNaughton, H.-B. Kraatz, T. Regier, R. I. R. Blyth, and A. Moewes. “Comparative Theoretical and Experimental Study of the Radiation-Induced Decomposition of Glycine”. *J. Phys. Chem. A* **113** (2009), pp. 5360–5366.

[117] P. S. Johnson, P. L. Cook, X. Liu, W. Yang, Y. Bai, N. L. Abbott, and F. J. Himpsel. “Universal mechanism for breaking amide bonds by ionizing radiation”. *J. Chem. Phys.* **135** (2011), p. 044702.

[118] R. Bayer. “Die Dampfdrücke des binären Systems Methylalkohol-Wasser”. *Z. Phys. Chem.* **130** (1927), pp. 1–14.

[119] A. Benkert, F. Meyer, D. Hauschild, M. Blum, W. Yang, R. G. Wilks, M. Bär, F. Reinert, C. Heske, and L. Weinhardt. “Isotope Effects in the Resonant Inelastic Soft X-ray Scattering Maps of Gas-Phase Methanol”. *J. Phys. Chem. A* **120** (2016), pp. 2260–2267.

[120] A. Benkert. “Röntgenspektroskopische Untersuchungen von Wasser und Methanol in der Gasphase”. Master thesis. Würzburg, 2012.

[121] K. Prince, R. Richter, M. de Simone, M. Alagia, and M. Coreno. “Near Edge X-ray Absorption Spectra of Some Small Polyatomic Molecules”. *J. Phys. Chem. A* **107** (2003), pp. 1955–1963.

[122] A. Hempelmann, M. N. Piancastelli, F. Heiser, O. Gessner, A. Rüdel, and U. Becker. “Resonant photofragmentation of methanol at the carbon and oxygen K-edge by high-resolution ion-yield spectroscopy”. *J. Phys. B: At. Mol. Opt. Phys.* **32** (1999), p. 2677.

[123] L. Tröger, D. Arvanitis, K. Baberschke, H. Michaelis, U. Grimm, and E. Zschech. “Full correction of the self-absorption in soft-fluorescence extended x-ray-absorption fine structure”. *Phys. Rev. B* **46** (1992), pp. 3283–3289.

[124] S. Kashtanov, A. Augustsson, J.-E. Rubensson, J. Nordgren, H. Ågren, J.-H. Guo, and Y. Luo. “Chemical and electronic structures of liquid methanol from x-ray emission spectroscopy and density functional theory”. *Phys. Rev. B* **71** (2005), p. 104205.

[125] J.-E. Rubensson, N. Wassdahl, R. Brammer, and J. Nordgren. “Local electronic structure in simple alcohols studied in x-ray emission”. *J. Electr. Spectr. Rel. Phenom.* **47** (1988), pp. 131–145.

[126] V. D. Yumatov, A. V. Okotrub, L. N. Mazalov, G. S. Belikova, and T. M. Okhrimenko. “X-ray spectra and electronic structure of the CH3OH molecule”. *J. Struct. Chem.* **26** (1985), pp. 540–545.

[127] F. P. Larkins and A. J. Seen. “Ab initio studies of molecular X-ray emission processes: methanol”. *Phys. Scr.* **41** (1990), p. 827.

[128] P. Skytt, P. Glans, K. Gunnelin, J. Guo, J. Nordgren, Y. Luo, and H. Ågren. “Role of screening and angular distributions in resonant x-ray emission of CO”. *Phys. Rev. A* **55** (1997), pp. 134–145.

[129] P. Glans, P. Skytt, K. Gunnelin, J. Guo, and J. Nordgren. “Selectively excited X-ray emission spectra of N2”. *J. Electr. Spectr. Rel. Phenom.* **82** (1996), pp. 193–201.

[130] H. Ågren, Y. Luo, F. Gelmukhanov, and H. J. A. Jensen. “Screening in resonant X-ray emission of molecules”. *J. Electr. Spectr. Rel. Phenom.* **82** (1996), pp. 125–134.

[131] Y. Luo, H. Ågren, and F. Gel’mukhanov. “Polarization anisotropy in resonant x-ray emission from molecules”. *Phys. Rev. A* **53** (1996), pp. 1340–1348.

[132] M. Neeb, J.-E. Rubensson, M. Biermann, and W. Eberhardt. “Coherent excitation of vibrational wave functions observed in core hole decay spectra of O2, N2 and CO”. *J. Electr. Spectr. Rel. Phenom.* **67** (1994), p. 261.

[133] L. Weinhardt, O. Fuchs, M. Blum, M. Bär, M. Weigand, J. D. Denlinger, Y. Zubavichus, M. Zharnikov, M. Grunze, C. Heske, and E. Umbach. “Resonant X-ray emission spectroscopy of liquid water: Novel instrumentation, high resolution, and the "map" approach”. *J. Electr. Spectr. Rel. Phenom.* Water and Hydrogen Bonds **177** (2010), pp. 206–211.

[134] A. de Brito, A. de Brito, O. Björneholm, J. Neto, A. Machado, S. Svensson, A. Ausmees, S. Osborne, L. Sæthre, H. Aksela, O. Sairanen, A. Kivimäki, E. Nõmmiste, and S. Aksela. “Fast dissociation of resonantly core excited H2S studied by vibrational and temporal analysis of the Auger spectra”. *J. Mol. Struct.: THEOCHEM*. Proceedings of the Eighth Brazilian Symposium of Theoretical Chemistry **394** (1997), pp. 135–145.

[135] I. Hjelte, M. Piancastelli, C. Jansson, K. Wiesner, O. Björneholm, M. Bässler, S. Sorensen, and S. Svensson. “Evidence of ultra-fast dissociation in ammonia observed by resonant Auger electron spectroscopy”. *Chem. Phys. Let.* **370** (2003), pp. 781–788.

[136] K. Prince, M. Vondráček, J. Karvonen, M. Coreno, R. Camilloni, L. Avaldi, and M. de Simone. “A critical comparison of selected 1s and 2p core hole widths”. *J. Electr. Spectr. Rel. Phenom.* **101–103** (1999), pp. 141–147.

[137] K. R. Wilson, M. Cavalleri, B. S. Rude, R. D. Schaller, T. Catalano, A. Nilsson, R. J. Saykally, and L. G. M. Pettersson. “X-ray Absorption Spectroscopy of Liquid Methanol Microjets: Bulk Electronic Structure and Hydrogen Bonding Network”. *J. Phys. Chem. B* **109** (2005), pp. 10194–10203.

[138] L. Pauling. *The Nature of the Chemical Bond and the Structure of Molecules and Crystals: An Introduction to Modern Structural Chemistry*. Cornell University Press, 1960.

[139] J.-H. Guo, Y. Luo, A. Augustsson, S. Kashtanov, J.-E. Rubensson, D. K. Shuh, H. Ågren, and J. Nordgren. “Molecular Structure of Alcohol-Water Mixtures”. *Phys. Rev. Lett.* **91** (2003), p. 157401.

[140] J. H. Guo, Y. Luo, A. Augustsson, S. Kashtanov, J. E. Rubensson, D. Shuh, V. Zhuang, P. Ross, H. Ågren, and J. Nordgren. “The molecular structure of alcohol-water mixtures determined by soft-X-ray absorption and emission spectroscopy”. *J. Electr. Spectr. Rel. Phenom.* **137–140** (2004), pp. 425–428.

[141] K. Lin, X. Zhou, Y. Luo, and S. Liu. “The Microscopic Structure of Liquid Methanol from Raman Spectroscopy”. *J. Phys. Chem. B* **114** (2010), pp. 3567–3573.

[142] S. K. Allison, J. P. Fox, R. Hargreaves, and S. P. Bates. “Clustering and microimmiscibility in alcohol-water mixtures: Evidence from molecular-dynamics simulations”. *Phys. Rev. B* **71** (2005), p. 024201.

[143] M. Pagliai, G. Cardini, R. Righini, and V. Schettino. “Hydrogen bond dynamics in liquid methanol”. *J. Chem. Phys.* **119** (2003), pp. 6655–6662.

[144] J. Lehtola, M. Hakala, and K. Hämäläinen. “Structure of Liquid Linear Alcohols”. *J. Phys. Chem. B* **114** (2010), pp. 6426–6436.

[145] A. S. Koster. “Oxygen emission spectra of ice, solid carbon dioxide, and solid alcohols”. *Appl. Phys. Lett.* **18** (1971), pp. 170–171.

[146] J. D. Bryngelson and E. M. Billings. “From Interatomic Interactions to Protein Structure”. *Physics of Biological Systems*. Ed. by H. Flyvbjerg, J. Hertz, M. H. Jensen, O. G. Mouritsen, and K. Sneppen. Lecture Notes in Physics. DOI: 10.1007/978-3-540-49733-2_5. Springer Berlin Heidelberg, 1997, pp. 80–116.

[147] I. Wagner and H. Musso. “New Naturally Occurring Amino Acids”. *Angew. Chem. Int. Ed. Engl.* **22** (1983), pp. 816–828.

[148] Y. Zubavichus, A. Shaporenko, M. Grunze, and M. Zharnikov. “Solid-State Near-Edge X-ray Absorption Fine Structure Spectra of Glycine in Various Charge States”. *J. Phys. Chem. B* **110** (2006), pp. 3420–3427.

[149] I. D. Reva, A. M. Plokhotnichenko, S. G. Stepanian, A. Ivanov, E. D. Radchenko, G. G. Sheina, and Y. P. Blagoi. “The rotamerization of conformers of glycine isolated in inert gas matrices. An infrared spectroscopic study”. *Chem. Phys. Let.* **232** (1995), pp. 141–148.

[150] M. J. Locke and R. T. McIver. “Effect of solvation on the acid/base properties of glycine”. *J. Am. Chem. Soc.* **105** (1983), pp. 4226–4232.

[151] Y. Zubavichus, M. Zharnikov, A. Schaporenko, and M. Grunze. “NEXAFS study of glycine and glycine-based oligopeptides”. *J. Electr. Spectr. Rel. Phenom.* **134** (2004), pp. 25–33.

[152] J. Boese, A. Osanna, C. Jacobsen, and J. Kirz. “Carbon edge XANES spectroscopy of amino acids and peptides”. *J. Electr. Spectr. Rel. Phenom.* **85** (1997), pp. 9–15.

[153] G. Cooper, M. Gordon, D. Tulumello, C. Turci, K. Kaznatcheev, and A. P. Hitchcock. “Inner shell excitation of glycine, glycyl-glycine, alanine and phenylalanine”. *J. Electr. Spectr. Rel. Phenom.* ICESS-9 Proceedings of the 9th International Conference on Electronic Spectroscopy and Structure **137–140** (2004), pp. 795–799.

[154] M. L. Gordon, G. Cooper, C. Morin, T. Araki, C. C. Turci, K. Kaznatcheev, and A. P. Hitchcock. “Inner-Shell Excitation Spectroscopy of the Peptide Bond: Comparison of the C 1s, N 1s, and O 1s Spectra of Glycine, Glycyl-Glycine, and Glycyl-Glycyl-Glycine”. *J. Phys. Chem. A* **107** (2003), pp. 6144–6159.

[155] E. Otero and S. Urquhart. “Nitrogen 1s Near-Edge X-ray Absorption Fine Structure Spectroscopy of Amino Acids: Resolving Zwitterionic Effects”. *J. Phys. Chem. A* **110** (2006), pp. 12121–12128.

[156] Y. Zubavichus, A. Shaporenko, M. Grunze, and M. Zharnikov. “Innershell Absorption Spectroscopy of Amino Acids at All Relevant Absorption Edges”. *J. Phys. Chem. A* **109** (2005), pp. 6998–7000.

[157] K. Kaznacheyev, A. Osanna, C. Jacobsen, O. Plashkevych, O. Vahtras, Ågren, V. Carravetta, and A. P. Hitchcock. “Innershell Absorption Spectroscopy of Amino Acids”. *J. Phys. Chem. A* **106** (2002), pp. 3153–3168.

[158] C. R. Wu, J. O. Nilsson, and W. R. Salaneck. “Photoelectron Spectroscopy of the Adsorption of Amino Acids on Surfaces: Glycine on Si(O 2)”. *Phys. Scr.* **35** (1987), p. 586.

[159] P. H. Cannington and N. S. Ham. “The photoelectron spectra of amino-acids : A survey”. *J. Electr. Spectr. Rel. Phenom.* The International Journal on Theoretical and Experimental Aspects of Electron Spectroscopy **15** (1979), pp. 79–82.

[160] P. Löfgren, A. Krozer, J. Lausmaa, and B. Kasemo. “Glycine on Pt(111): a TDS and XPS study”. *Surf. Sci.* **370** (1997), pp. 277–292.

[161] A. Chatterjee, L. Zhao, L. Zhang, D. Pradhan, X. Zhou, and K. T. Leung. “Core-level electronic structure of solid-phase glycine, glycyl-glycine, diglycyl-glycine, and polyglycine: X-ray photoemission analysis and Hartree–Fock calculations of their zwitterions”. *J. Chem. Phys.* **129** (2008), p. 105104.

[162] D. T. Clark, J. Peeling, and L. Colling. “An experimental and theoretical investigation of the core level spectra of a series of amino acids, dipeptides and polypeptides”. *Biochimica et Biophysica Acta (BBA) - Protein Structure* **453** (1976), pp. 533–545.

[163] J. Hasselström, O. Karis, M. Nyberg, L. G. M. Pettersson, M. Weinelt, N. Wassdahl, and A. Nilsson. “The Bonding and Electronic Structure Changes upon Adsorption of Important Functional Groups: Glycine on Copper”. *J. Phys. Chem. B* **104** (2000), pp. 11480–11483.

[164] M. Nyberg, J. Hasselström, O. Karis, N. Wassdahl, M. Weinelt, A. Nilsson, and L. G. M. Pettersson. “The electronic structure and surface chemistry of glycine adsorbed on Cu(110)”. *J. Chem. Phys.* **112** (2000), pp. 5420–5427.

[165] M. Nyberg, M. Odelius, A. Nilsson, and L. G. M. Pettersson. “Hydrogen bonding between adsorbed deprotonated glycine molecules on Cu(110)”. *J. Chem. Phys.* **119** (2003), pp. 12577–12585.

[166] V. Feyer, O. Plekan, R. Richter, M. Coreno, K. Prince, and V. Carravetta. “Photoemission and Photoabsorption Spectroscopy of Glycyl-Glycine in the Gas Phase”. *J. Phys. Chem. A* **113** (2009), pp. 10726–10733.

[167] A. Slaughter and M. Banna. “Core-photoelectron binding energies of gaseous glycine: correlation with its proton affinity and gas-phase acidity”. *J. Phys. Chem.* **92** (1988), pp. 2165–2167.

[168] O. Plekan, V. Feyer, R. Richter, M. Coreno, M. de Simone, K. Prince, and V. Carravetta. “Investigation of the Amino Acids Glycine, Proline, and Methionine by Photoemission Spectroscopy”. *J. Phys. Chem. A* **111** (2007), pp. 10998–11005.

[169] O. Plekan, V. Feyer, R. Richter, M. Coreno, M. de Simone, K. Prince, and V. Carravetta. “Photoemission and the shape of amino acids”. *Chem. Phys. Let.* **442** (2007), pp. 429–433.

[170] N. Ottosson, K. J. Børve, D. Spångberg, H. Bergersen, L. J. Sæthre, M. Faubel, W. Pokapanich, G. Öhrwall, O. Björneholm, and B. Winter. “On the Origins of Core-Electron Chemical Shifts of Small Biomolecules in Aqueous Solution: Insights from Photoemission and ab Initio Calculations of Glycineaq”. *J. Am. Chem. Soc.* **133** (2011), pp. 3120–3130.

[171] M. Schreyer, L. Guo, S. Thirunahari, F. Gao, and M. Garland. “Simultaneous determination of several crystal structures from powder mixtures: the combination of powder X-ray diffraction, band-target entropy minimization and Rietveld methods”. *J. Appl. Cryst.* **47** (2014), pp. 659–667.

[172] F. Hennies, A. Pietzsch, M. Berglund, A. Föhlisch, T. Schmitt, V. Strocov, H. O. Karlsson, J. Andersson, and J.-E. Rubensson. “Resonant Inelastic Scattering Spectra of Free Molecules with Vibrational Resolution”. *Phys. Rev. Lett.* **104** (2010), p. 193002.

[173] S. Doonan. “The covalent structures of peptides and proteins”. *The covalent structures of peptides and proteins*. 2002.

[174] J.-H. Guo, M. Magnuson, C. Såthe, J. Nordgren, L. Yang, Y. Luo, H. Ågren, K. Z. Xing, N. Johansson, W. R. Salaneck, R. Daik, and W. J. Feast. “Resonant and nonresonant x-ray scattering spectra of some poly(phenylenevinylene)s”. *J. Chem. Phys.* **108** (1998), pp. 5990–5996.

[175] F. Meyer. “Soft X-ray Spectroscopic Study of Amino Acid and Salt Solutions”. PhD thesis. Würzburg: Julius-Maximilians-Universität Würzburg, 2015.

[176] S. A. Moggach, D. R. Allan, S. Parsons, and L. Sawyer. “Effect of pressure on the crystal structure of α-glycylglycine to 4.7 GPa; application of Hirshfeld surfaces to analyse contacts on increasing pressure”. *Acta Crystallographica Section B Structural Science* **62** (2006), pp. 310–320.

[177] V. Pichon-Pesme and C. Lecomte. “Experimental Charge Density and Electrostatic Potential of Triglycine”. *Acta Crystallographica Section B Structural Science* **54** (1998), pp. 485–493.

[178] P. Jungwirth. “Hofmeister Series of Ions: A Simple Theory of a Not So Simple Reality”. *J. Phys. Chem. Lett.* **4** (2013), pp. 4258–4259.

[179] D. J. Tobias and J. C. Hemminger. “Getting Specific About Specific Ion Effects”. *Science* **319** (2008), pp. 1197–1198.

[180] Y. L. Jeyachandran, F. Meyer, S. Nagarajan, A. Benkert, M. Bär, M. Blum, W. Yang, F. Reinert, C. Heske, L. Weinhardt, and M. Zharnikov. “Ion-Solvation-Induced Molecular Reorganization in Liquid Water Probed by Resonant Inelastic Soft X-ray Scattering”. *J. Phys. Chem. Lett.* **5** (2014), pp. 4143–4148.

[181] Y. L. Jeyachandran, F. Meyer, A. Benkert, M. Bär, M. Blum, W. Yang, F. Reinert, C. Heske, L. Weinhardt, and M. Zharnikov. “Investigation of the Ionic Hydration in Aqueous Salt Solutions by Soft X-ray Emission Spectroscopy”. *J. Phys. Chem. B* **120** (2016), pp. 7687–7695.

[182] A. K. Covington and R. G. Bates. “Definition of pH scales, standard reference values, measurement of pH, and related terminology (IUPAC Recommendations 1984)”. *Pure Appl. Chem.* **57** (1985), pp. 531–542.

[183] L. J. Henderson. “Concerning the relationship between the strength of acids and their capacity to preserve neutrality”. *American Journal of Physiology-Legacy Content* **21** (1908), pp. 173–179.

[184] L. J. Henderson. “The theory of neutrality regulation in the animal organism”. *American Journal of Physiology- Legacy Content* **21** (1908), pp. 427–448.

[185] H. N. Po and N. M. Senozan. “The Henderson-Hasselbalch Equation: Its History and Limitations”. *J. Chem. Educ.* **78** (2001), p. 1499.

[186] M. J. Locke, R. L. Hunter, and R. T. McIver. “Experimental determination of the acidity and basicity of glycine in the gas phase”. *J. Am. Chem. Soc.* **101** (1979), pp. 272–273.

[187] R. C. Weast. *CRC handbook of chemistry and physics*. CRC Press, 1988.

[188] J. Lu, X.-J. Wang, X. Yang, and C.-B. Ching. “Solubilities of Glycine and Its Oligopeptides in Aqueous Solutions”. *J. Chem. Eng. Data* **51** (2006), pp. 1593–1596.

[189] O. Plekan, V. Feyer, R. Richter, M. Coreno, M. de Simone, K. C. Prince, and V. Carravetta. “An X-ray absorption study of glycine, methionine and proline”. *J. Electr. Spec. Rel. Phenom.* Scattering, Coincidence and Absorption Studies of MoleculesSCASM **155** (2007), pp. 47–53.

[190] J. Hasselström, A. Föhlisch, O. Karis, N. Wassdahl, M. Weinelt, A. Nilsson, M. Nyberg, L. G. M. Pettersson, and J. Stöhr. "Ammonia adsorbed on Cu(110): An angle resolved x-ray spectroscopic and ab initio study". *J. Chem. Phys.* **110** (1999), pp. 4880–4890.

[191] R. Mancinelli, A. Botti, F. Bruni, M. A. Ricci, and A. K. Soper. "Hydration of Sodium, Potassium, and Chloride Ions in Solution and the Concept of Structure Maker/Breaker". *J. Phys. Chem. B* **111** (2007), pp. 13570–13577.

[192] R. Mancinelli, A. Botti, F. Bruni, M. A. Ricci, and A. K. Soper. "Perturbation of water structure due to monovalent ions in solution". *Phys. Chem. Chem. Phys.* **9** (2007), pp. 2959–2967.

[193] J. D. Smith, R. J. Saykally, and P. L. Geissler. "The Effects of Dissolved Halide Anions on Hydrogen Bonding in Liquid Water". *J. Am. Chem. Soc.* **129** (2007), pp. 13847–13856.

[194] J.-J. Max and C. Chapados. "IR spectroscopy of aqueous alkali halide solutions: Pure salt-solvated water spectra and hydration numbers". *J. Chem. Phys.* **115** (2001), pp. 2664–2675.

[195] K. J. Tielrooij, N. Garcia-Araez, M. Bonn, and H. J. Bakker. "Cooperativity in Ion Hydration". *Science* **328** (2010), pp. 1006–1009.

[196] M. Kondoh, Y. Ohshima, and M. Tsubouchi. "Ion effects on the structure of water studied by terahertz time-domain spectroscopy". *Chem. Phys. Lett.* **591** (2014), pp. 317–322.

[197] B. Winter, E. F. Aziz, N. Ottosson, M. Faubel, N. Kosugi, and I. V. Hertel. "Electron Dynamics in Charge-Transfer-to-Solvent States of Aqueous Chloride Revealed by Cl- 2p Resonant Auger-Electron Spectroscopy". *J. Am. Chem. Soc.* **130** (2008), pp. 7130–7138.

[198] I.-F. W. Kuo, C. J. Mundy, B. L. Eggimann, M. J. McGrath, J. I. Siepmann, B. Chen, J. Vieceli, and D. J. Tobias. "Structure and Dynamics of the Aqueous Liquid-Vapor Interface: A Comprehensive Particle-Based Simulation Study". *J. Phys. Chem. B* **110** (2006), pp. 3738–3746.

[199] T. D. Kühne, T. A. Pascal, E. Kaxiras, and Y. Jung. "New Insights into the Structure of the Vapor/Water Interface from Large-Scale First-Principles Simulations". *J. Phys. Chem. Lett.* **2** (2011), pp. 105–113.

[200] S. J. Irudayam and R. H. Henchman. “Long-range hydrogen-bond structure in aqueous solutions and the vapor-water interface”. *J. Chem. Phys.* **137** (2012), p. 034508.

[201] C. D. Cappa, J. D. Smith, K. R. Wilson, B. M. Messer, M. K. Gilles, R. C. Cohen, and R. J. Saykally. “Effects of Alkali Metal Halide Salts on the Hydrogen Bond Network of Liquid Water”. *J. Phys. Chem. B* **109** (2005), pp. 7046–7052.

[202] C. D. Cappa, J. D. Smith, B. M. Messer, R. C. Cohen, and R. J. Saykally. “Effects of Cations on the Hydrogen Bond Network of Liquid Water: New Results from X-ray Absorption Spectroscopy of Liquid Microjets”. *J. Phys. Chem. B* **110** (2006), pp. 5301–5309.

[203] L.-A. Näslund, D. C. Edwards, P. Wernet, U. Bergmann, H. Ogasawara, L. G. M. Pettersson, S. Myneni, and A. Nilsson. “X-ray Absorption Spectroscopy Study of the Hydrogen Bond Network in the Bulk Water of Aqueous Solutions”. *J. Phys. Chem. A* **109** (2005), pp. 5995–6002.

[204] C. D. Cappa, J. D. Smith, B. M. Messer, R. C. Cohen, and R. J. Saykally. “The Electronic Structure of the Hydrated Proton: A Comparative X-ray Absorption Study of Aqueous HCl and NaCl Solutions”. *J. Phys. Chem. B* **110** (2006), pp. 1166–1171.

[205] E. F. Aziz. “The solvation of ions and molecules probed via soft X-ray spectroscopies”. *J. Electr. Spectr. Rel. Phenom.* Water and Hydrogen Bonds **177** (2010), pp. 168–180.

[206] I. Waluyo, C. Huang, D. Nordlund, U. Bergmann, T. M. Weiss, L. G. M. Pettersson, and A. Nilsson. “The structure of water in the hydration shell of cations from x-ray Raman and small angle x-ray scattering measurements”. *J. Chem. Phys.* **134** (2011), p. 064513.

[207] I. Waluyo, D. Nordlund, U. Bergmann, D. Schlesinger, L. G. M. Pettersson, and A. Nilsson. “A different view of structure-making and structure-breaking in alkali halide aqueous solutions through x-ray absorption spectroscopy”. *J. Chem. Phys.* **140** (2014), p. 244506.

[208] Z. Yin, I. Rajkovic, K. Kubicek, W. Quevedo, A. Pietzsch, P. Wernet, A. Föhlisch, and S. Techert. “Probing the Hofmeister Effect with Ultrafast Core–Hole Spectroscopy”. *J. Phys. Chem. B* **118** (2014), pp. 9398–9403.

[209] Z. Yin, I. Rajkovic, V. S. Thekku, S. Deinert, D. Raiser, R. Jain, H. Fukuzawa, S.-i. Wada, W. Quevedo, B. Kennedy, S. Schreck, A. Pietzsch, P. Wernet, K. Ueda, A. Föhlisch, and S. Techert. "Ionic Solutions Probed by Resonant Inelastic X-ray Scattering". *Z. Phys. Chem.* **229** (2015), pp. 1855–1867.

[210] L. Vrbka, J. Vondrasek, B. Jagoda-Cwiklik, R. Vacha, and P. Jungwirth. "Quantification and rationalization of the higher affinity of sodium over potassium to protein surfaces". *PNAS* **103** (2006), pp. 15440–15444.

[211] H. I. Okur, J. Kherb, and P. S. Cremer. "Cations Bind Only Weakly to Amides in Aqueous Solutions". *J. Am. Chem. Soc.* **135** (2013), pp. 5062–5067.

[212] K. B. Rembert, J. Paterová, J. Heyda, C. Hilty, P. Jungwirth, and P. S. Cremer. "Molecular Mechanisms of Ion-Specific Effects on Proteins". *J. Am. Chem. Soc.* **134** (2012), pp. 10039–10046.

[213] K. B. Rembert, H. I. Okur, C. Hilty, and P. S. Cremer. "An NH Moiety Is Not Required for Anion Binding to Amides in Aqueous Solution". *Langmuir* **31** (2015), pp. 3459–3464.

[214] L. Medda, C. Carucci, D. F. Parsons, B. W. Ninham, M. Monduzzi, and A. Salis. "Specific Cation Effects on Hemoglobin Aggregation below and at Physiological Salt Concentration". *Langmuir* **29** (2013), pp. 15350–15358.

[215] Z. Yang. "Hofmeister effects: an explanation for the impact of ionic liquids on biocatalysis". *J. Biotech.* Industrial Biotechnology: Current Status and Future Development for the Sustainability of Human Society **144** (2009), pp. 12–22.

[216] H. C. Burger and P. H. Cittert. "Verbreiterung von Spektrallinien durch Selbstabsorption". *Z. Physik* **51** (1928), pp. 638–651.

[217] S. Gota, M. Gautier-Soyer, and M. Sacchi. "Fe 2p absorption in magnetic oxides: Quantifying angular-dependent saturation effects". *Phys. Rev. B* **62** (2000), pp. 4187–4190.

[218] R. Nakajima, J. Stöhr, and Y. U. Idzerda. "Electron-yield saturation effects in L-edge x-ray magnetic circular dichroism spectra of Fe, Co, and Ni". *Phys. Rev. B* **59** (1999), pp. 6421–6429.

[219] T. J. Regan, H. Ohldag, C. Stamm, F. Nolting, J. Lüning, J. Stöhr, and R. L. White. "Chemical effects at metal/oxide interfaces studied by x-ray-absorption spectroscopy". *Phys. Rev. B* **64** (2001), p. 214422.

[220] B. L. Henke, E. M. Gullikson, and J. C. Davis. “X-Ray Interactions: Photoabsorption, Scattering, Transmission, and Reflection at E = 50-30,000 eV, Z = 1-92”. *Atomic Data and Nuclear Data Tables* **54** (1993), pp. 181–342.

[221] B. L. Henke, E. M. Gullikson, and J. C. Davis. *CXRO X-Ray Interactions With Matter*. http://henke.lbl.gov/optical_constants/, 2016.

[222] A. J. Achkar, T. Z. Regier, H. Wadati, Y.-J. Kim, H. Zhang, and D. G. Hawthorn. “Bulk sensitive x-ray absorption spectroscopy free of self-absorption effects”. *Phys. Rev. B* **83** (2011), p. 081106.

[223] J. Gråsjö, E. Andersson, J. Forsberg, E. F. Aziz, B. Brena, C. Johansson, J. Nordgren, L. Duda, J. Andersson, F. Hennies, J.-E. Rubensson, and P. Hansson. “Electronic Structure of Water Molecules Confined in a Micelle Lattice”. *J. Phys. Chem. B* **113** (2009), pp. 8201–8205.

[224] J.-E. Rubensson, M. Neeb, M. Biermann, Z. Xu, and W. Eberhardt. “Electronic decay of vibrationally selected core excited states in molecular N2”. *J. Chem. Phys.* **99** (1993), pp. 1633–1636.

OWN PUBLICATIONS

- **A. Benkert**, F. Meyer, D. Hauschild, M. Blum, W. Yang, R. G. Wilks, M. Bär, F.Reinert, C. Heske, and L. Weinhardt. “Isotope Effects in the Resonant Inelastic Soft X-ray Scattering Maps of Gas-Phase Methanol”. *J. Phys. Chem. A* **120** (2016), pp. 2260–2267.
- **A. Benkert**, M. Blum, F. Meyer, R. G. Wilks, W. Yang, M. Bär, F. Reinert, C.Heske, and L. Weinhardt. “Setup for in situ investigation of gases and gas/solid interfaces by soft x-ray emission and absorption spectroscopy”. *Rev. Sci. Instrum.* **85** (2014), p. 015119
- A. Léon, A. Fiedler, M. Blum, **A. Benkert**, F. Meyer, W. Yang, M. Bär, F. Scheiba, H. Ehrenberg, L. Weinhardt, and C. Heske. “Valence Electronic Structure of Li_2O_2, Li_2O, Li_2CO_3, and LiOH Probed by Soft X-ray Emission Spectroscopy”. *J. Phys. Chem. C* **121** (2017), pp. 5460-5466.
- L. Weinhardt, O. Fuchs, A. Fischer, M. Weigand, F. Meyer, **A. Benkert**, M. Blum, M. Bär, S. Pookpanratana, J. Denlinger, C. Heske, and E. Umbach. “Site- and Symmetry-Resolved Resonant X-ray Emission Study of a Highly Ordered PTCDA Thin Film”. *J. Phys. Chem. C* **120** (2016), pp. 8607–8615.
- Y. L. Jeyachandran, F. Meyer, **A. Benkert**, M. Bär, M. Blum, W. Yang, F. Reinert, C. Heske, L. Weinhardt, and M. Zharnikov. "Investigation of the Ionic Hydration in Aqueous Salt Solutions by Soft X-ray Emission Spectroscopy". *J. Phys. Chem. B* **120** (2016), pp. 7687-7695
- D. Hauschild, E. Handick, S. Göhl-Gusenleitner, F. Meyer, H. Schwab, **A. Benkert**, S. Pohlner, J. Palm, S. Tougaard, C. Heske, L. Weinhardt, and F. Reinert. "Band-Gap Widening at the Cu(In,Ga)$(S,Se)_2$ Surface - A Novel Determination Approach Using Reflection Electron Energy Loss Spectroscopy". *Appl. Mater. Interfaces* **8(32)** (2016), pp. 21101–21105
- D. Hauschild, F. Meyer, **A. Benkert**, D. Kreikemeyer-Lorenzo, S. Pohlner, J. Palm, M. Blum, W. Yang, R. G. Wilks, M. Bär, C. Heske, L. Weinhardt, and F.

Reinert. “Annealing-Induced Effects on the Chemical Structure of the In_2S_3/$CuIn(S,Se)_2$ Thin-Film Solar Cell Interface”. *J. Phys. Chem. C* **119** (2015), pp. 10412–10416.

- F. Meyer, M. Blum, **A. Benkert**, D. Hauschild, S. Nagarajan, R. G. Wilks, J. Andersson, W. Yang, M. Zharnikov, M. Bär, C. Heske, F. Reinert, and L. Weinhardt. ““Building Block Picture” of the Electronic Structure of Aqueous Cysteine Derived from Resonant Inelastic Soft X-ray Scattering”. *J. Phys. Chem. B* **118** (2014), pp. 13142–13150.

- Y. L. Jeyachandran, F. Meyer, S. Nagarajan, **A. Benkert**, M. Bär, M. Blum, W. Yang, F. Reinert, C. Heske, L. Weinhardt, and M. Zharnikov. “Ion-Solvation-Induced Molecular Reorganization in Liquid Water Probed by Resonant Inelastic Soft X-ray Scattering”. *J. Phys. Chem. Lett.* **5** (2014), pp. 4143–4148.

- L. Weinhardt, M. Blum, O. Fuchs, **A. Benkert**, F. Meyer, M. Bär, J. D. Denlinger, W. Yang, F. Reinert, and C. Heske. “RIXS investigations of liquids, solutions, and liquid/solid interfaces”. *J. Electr. Spectr. Rel. Phenom.* **188** (2013), pp. 111–120.

- L. Weinhardt, **A. Benkert**, F. Meyer, M. Blum, R. G. Wilks, W. Yang, M. Bär, F. Reinert, and C. Heske. “Nuclear dynamics and spectator effects in resonant inelastic soft x-ray scattering of gas-phase water molecules”. *J. Chem. Phys.* **136** (2012), p. 144311.

- R. G. Wilks, R. Caballero, X. Song, R. Felix, **A. Benkert**, D. Gerlach, L. Weinhardt, M. Blum, W. Yang, C. Kaufmann, C. Heske, H. Schock, and M. Bar. “X-ray spectroscopic analysis of the growth of CBD-CdS buffers on flexible $Cu(In,Ga)Se_2$ thin-film solar cell structures”. *38th IEEE Photovoltaic Specialists Conference (PVSC)*. 2012, pp. 001682–001687.

DANKSAGUNG

Zu guter Letzt möchte ich mich bei allen bedanken, die auf unterschiedlichste Art und Weise zum Gelingen dieser Arbeit beigetragen haben.

An erster Stelle gilt mein Dank meinem Doktorvater an der Universität Würzburg Prof. Dr. Friedrich Reinert für die Möglichkeit, meine Promotion in seiner Arbeitsgruppe anfertigen zu können, sozusagen als letztes Überbleibsel der einstigen Röntgenemissions-Gruppe in einem ansonsten hauptsächlich von Photoemission geprägten Lehrstuhl. Besonders die Diskussionen in der Phase des Schreibens der Arbeit haben dazu beigetragen, dass ich den nötigen Weitblick über den Inhalt meiner Arbeit hinaus nicht verloren habe. Das große Vertrauen, das er meiner Arbeit entgegen gebracht hat, schätze ich sehr.

Darüber hinaus hatte ich das große Glück, in Prof. Dr. Clemens Heske quasi einen zweiten Doktorvater zu besitzen, der mir am Karlsruher Institut für Technologie (KIT) eine zweite wissenschaftliche Heimat gab. Ihn als weiteren Rückhalt hinter mir zu wissen hat vieles erleichtert. Vielen Dank auch für die kritischen Diskussionen meiner Ergebnisse und die unzähligen Korrekturen und Anmerkungen, die ich beim Paper Schreiben nicht hätte missen wollen.

Ohne einen Zweitgutachter geht es nicht, weswegen ich mich bei Prof. Dr. Jean Geurts für die Erstellung des Gutachtens und das damit verbundene Interesse an meiner Arbeit bedanken möchte.

Einen sehr großen Anteil an der Entstehung dieser Arbeit hat Dr. Lothar Weinhardt (KIT) in Form einer hervorragenden Betreuung trotz der Entfernung zwischen Würzburg und Karlsruhe und seines viel zu vollen Terminkalenders. Ohne seine unerschöpflichen Ideen, die unzähligen Diskussionen über Experimente und Daten, die Ermutigung neue Wege zu gehen und die fachliche Anleitung zu allem, was auch nur ansatzweise mit RIXS zu tun hat (und darüber hinaus), würde diese Arbeit so nicht existieren. Auch die Freude an der Programmierung von allerhand IGOR Prozeduren sprang von ihm auf mich über.

Die grundlegenden Vorarbeiten zur Messung von Molekülen in Lösung und insbesondere Glycin wurden von Dr. Monika Blum (Universität Las Vegas) durchgeführt. Viel wertvoller war jedoch ihr unermüdlicher Einsatz, bei jeder Messzeit in Berkeley eine Wohlfühlatmosphäre für die große Messzeitfamilie zu schaffen. Dazu gehörten die

Organisation vorab, der Auf- und Abbau von SALSA und der unermüdliche Einsatz sich jeden auftretenden Problems anzunehmen (und zur Not auch mal stundenlang ein Stück Edelstahl zu polieren). Das mehr oder weniger große Chaos, das nach Messzeiten typischerweise herrschte, war dank ihr bis zur nächsten Messzeit wenige Monate später wieder komplett beseitigt, alle Reparaturen und Umbauten erledigt und SALSA bereit für eine neue Runde (um nur ein paar Beispiele zu nennen). Die auch aus zahlreichen gemeinsamen Tag- und Nachtschichten entstandene Freundschaft ist mir unglaublich viel Wert, nicht nur wegen der vielen lieben Worte und Aufmunterungen wenn es mal nicht so gut lief. Der obligatorische, selbstgebackene Geburtstagskuchen während der Messzeit soll hier nicht unerwähnt bleiben.

Mein direkter Vorstreiter in vielerlei Hinsicht war Dr. Frank Meyer. Er hat durch seine Vorarbeiten zur Spektroskopie von Aminosäuren nicht nur die nötigen Erfahrungen geliefert, sondern hat mich auch in die Welt der Dichtefunktionaltheorie eingeführt und die ersten, mühseligen Schritte von der batch–Datei basierten Bedienung von StoBe hin zur IGOR–Prozedur mit Benutzeroberfläche gemacht. Unvergessen bleiben auch die zahlreichen Messzeiten, die wir zusammen bestritten haben, auch wenn wir es selten schafften auf einer Schicht zu landen.

Deutlich mehr gemeinsame (Nacht-) Schichten durfte ich mit Dr. Dagmar Kreikemeyer-Lorenzo (KIT) bewältigen, nicht nur weil wir es beide nicht so mit dem Aufstehen früh um 5 haben ;-). Ihrer Unterstützung konnte ich mir immer sicher sein, auch wenn es darum ging unermüdlich die Kammer per Hand hoch und runter zu kurbeln, um die Membran während der Messung zu scannen. Dass die Spaßkomponente an der Messzeit nicht zu kurz kam galt mit ihr als gesetzt. Die Zusammenarbeit mit ihr und die regelmäßigen (natürlich nur dienstlichen) Telefonate während der Arbeitszeit werde ich vermissen.

Darüber hinaus hatte ich weitere zahlreiche Unterstützung auf Messzeiten. Hier dürfen Prof. Dr. Marcus Bär und Dr. Regan Wilks vom Helmholtz-Zentrum Berlin nicht fehlen, die mit Rat und Gelassenheit zur Seite standen wenn man sie brauchte und die mit ihrem trockenen Humor auch die verzwicktesten Situationen erträglich erschienen ließen. Viele helfende Hände, vor allem beim Zusammenrühren meiner Lösungen im Chemielabor aber auch beim Nerv tötenden Kalibrieren des Spektrometers, kamen aus der Gruppe der Universität Las Vegas. Hier möchte ich besonders Dr. Michelle Mezher nennen, die unter anderem auch oft beim Auf- und Abbau von SALSA kräftig mit anpackte. Seitens der Advanced Light Source kam mir besonders die Unterstützung durch Dr. Doug Taube zu Gute, der immer irgendwo noch ein bisschen passendes Salz für mich aufgetrieben hat, wenn ich spontan noch etwas ausprobieren wollte.

Zwischen den Messzeiten in Berkeley war ich in der EP7 von einer super Gruppe mit allerhand hilfsbereiten und witzigen Kollegen umgeben, die ein tolles Arbeitsklima geschaffen haben. Ein paar Leute möchte ich hier noch gesondert nennen, allen voran meine langjährigen Bürokollegen Dr. Frank Meyer, Dr. Dirk Hauschild und Holger Schwab, die nicht nur in sondern auch neben der Uni für allerhand Späße und Aktionen zu haben waren und zu echten Freunden geworden sind. Der wissenschaftliche Austausch ist dabei natürlich nicht zu kurz gekommen. Die von den Jungs auf meinen Schreibtisch geklebte Klaviertastatur hat mich zumindest etwas früher in die Uni kommen lassen. Holger war auch immer der perfekte Ansprechpartner, wenn es darum ging, die nächste Wanderung oder sonstige Freizeitaktivitäten zu planen. Dirk hat Frank und mich unzählige Male nach Karlsruhe chauffiert, um mit Lothar über Experimente und Daten zu diskutieren und hat sich außerdem auch der Korrektur meiner Arbeit mit angenommen. Nach seinem Weggang nach Karlsruhe hat er mir zudem seinen Doppelkeksrollenspender überlassen, der mir weiterhin treue Dienste geleistet hat und nie leer war.

Als die drei Jungs schließlich alle in Süddeutschland verstreut waren, haben der Keksspender und ich eine neue Bleibe gesucht und bei Katharina Treiber und (bald Dr.) Henriette Maaß Unterschlupf gefunden, in der es zum Glück nicht nur "Mädchengequatsche" gab, wie der Nikolaus vorhersagte. Von Henriette durfte ich viel über Spinpolarisation in der Photoemission lernen und sie sorgte dafür, dass ich den roten Faden nicht aus den Augen verloren habe. Sie war es auch, die mehr Abwechslung in den Keksspender brachte (sehr zur Verwunderung eines alltäglichen Stammgastes, der mit so viel Abwechslung nicht wirklich zurecht kam). Als der Keksspender immer größere Konkurrenz von einem stetigen Nachschub an frischem Obst bekam, waren letztendlich Wohlfühlbedingungen für die ausgedehnten Nachtschichten in der Zeit des Schreibens geschaffen. Als Patrick Bayersdorfer dann auch noch in unserem Büro landete, war ich zumindest zu Beginn meiner Nachtschichten öfters nicht ganz alleine. Dabei konnte ich auch viele Einblicke in die mir bisher eher fremde Welt der Oberflächenröntgenbeugung gewinnen und noch etwas mehr über den Tellerrand blicken. Für tiefgreifendere Diskussionen zu RIXS, XAS und XES konnte ich dabei immer auf telefonische Unterstützung aus Karlsruhe zurückgreifen. Neben Lothar und Dirk hat dabei insbesondere auch Dr. Marc Häming die ein oder andere Idee geliefert und mir einen Schubs in die richtige Richtung gegeben, vor allem wenn es um die Diskussion von Absorptionskoeffizienten und Wirkungsquerschnitten ging.

Meine Familie und meine Freunde haben mich vermutlich mehr unterstützt als sie selbst denken und sollen deshalb auch nicht ungenannt bleiben. Das sind vor allem meine Eltern Petra und Norbert Benkert und meine Brüder Matthias und Max mit meinen Schwägerinnen (in spe) Marina und Pauline. Es ist einfach wahnsinnig toll zu wissen, dass man sich immer auf euch verlassen kann und ihr voll hinter einem steht. Super, dass wir uns alle so gut verstehen. Ganz besonders stolz bin ich, dass ich Pate von meiner Nichte Lia werden durfte. Vielen Dank für dieses riesengroße Vertrauen und Geschenk!

Diejenige, die mich wohl am meisten motiviert und alle meine Sorgen aber auch Erfolge mit mir geteilt hat, ist meine Freundin Sabrina Keith. Ich bin wahnsinnig dankbar für ihre Engelsgeduld mit mir und meiner Arbeit, auch wenn wir unter anderem meinen Geburtstag in den letzten vier Jahren nie gemeinsam feiern konnten, weil ich immer auf Messzeit war oder gerade noch im Flieger saß. Sie ist und bleibt mein größter Rückhalt und Antrieb.

EUCH ALLEN ein riesengroßes ***DANKE!***